THE UNIVERSITY
of ADELAIDE

The Origin of Galactic TeV Gamma Ray Sources

Kirsty Mia Feijen

Faculty of Sciences
School of Physical Sciences
The University of Adelaide

Supervisors:
Dr. Sabrina Einecke
Prof. Gavin Rowell

A thesis submitted for the degree of
Doctor of Philosophy

April, 2022

Contents

Abstract

The High Energy Stereoscopic System (H.E.S.S.) is a ground-based telescope which detects gigaelectronvot (GeV) and teraelectronvolt (TeV) γ-rays. Many TeV γ-ray sources are associated with high-energy environments such as pulsar wind nebulae (PWNe) and supernova remnants (SNRs). However, the majority of these TeV γ-ray sources are 'unidentified' or 'dark' sources as no clear counterpart to be powering the γ-rays has been discovered. One of these 'unidentified' TeV γ-ray sources is HESS J1804$-$216, which is the focus of this thesis. HESS J1804$-$216 has several plausible counterparts investigated in detail in this thesis.

It is vital to have an understanding of the interstellar medium (ISM) surrounding a very high energy (VHE) Galactic γ-ray source as it can lead to constraining the nature of the source. Several scenarios for the origin of VHE γ-ray emission from HESS J1804$-$216 have been considered. For a hadronic scenario, SNR G8.7$-$0.1 is a plausible candidate for the acceleration of CR protons. Sufficient interstellar gas as a target for CR collisions and γ-ray production is present in the corresponding velocity component. Assuming an isotropic diffusion model, the CR proton spectra from SNR G8.7$-$0.1 showed that this interpretation requires slow diffusion to match the observed values. For an alternate hadronic scenario, the undetected progenitor SNR of PSR J1803$-$2137 is another promising candidate. This is due to the derived CR enhancement factors for this case matching the γ-ray observations well. For a leptonic scenario, the TeV emission is produced by highly energetic electrons from PSR J1803$-$2137 as a PWNe. A TeV γ-ray efficiency of 3% supports the PWN scenario from an energetics point of view.

Expanding on this further, modelling of the diffusive energy-dependent escape of CR protons and interaction with the surrounding ISM in the hadronic scenario is performed for the two plausible SNR counterparts. The spatial and spectral distributions of CRs are generated for a range of model parameters, describing, amongst others, the diffusion and the injection spectrum of CRs. Gamma-ray morphology maps and spectral distributions are created based on these CR distributions and the ISM distribution for the two nearby plausible CR accelerators: SNR G8.7$-$0.1 and the progenitor SNR of PSR J1803$-$2137.

Finally, all the available H.E.S.S. data is analysed to produce spatial morphology maps and spectral distributions. The analysis shows that the spectrum of HESS J1804$-$216 extends up to tens of TeV with a cutoff of $E_{\mathrm{cutoff}} = 24.7 \pm 18.4\,\mathrm{TeV}$. This is indicative of a PeVatron source. The morphology of γ-ray emission towards HESS J1804$-$216 is investigated over different energy bands to perform an energy-dependent morphology study. Both PWNe and SNR scenarios are investigated for any energy-dependent morphology. The PWNe scenario is expected to exhibit clear energy-dependent morphology, which is not consistent with the morphology from this study. No clear evidence of energy-dependent morphology was found, as supported by statistical tests. The observations for the SNR scenarios showed no compelling evidence of energy-dependence. The modelled γ-ray emission, however, indicated the presence of energy-dependent morphology. Therefore, the observations and model for the SNR scenario were significantly different from one another.

Declaration of Originality

I, Kirsty Mia Feijen, certify that this work contains no material which has been accepted for the award of any other degree or diploma in my name, in any university or other tertiary institution and, to the best of my knowledge and belief, contains no material previously published or written by another person, except where due reference has been made in the text. In addition, I certify that no part of this work will, in the future, be used in a submission in my name for any other degree or diploma in any university or other tertiary institution without the prior approval of the University of Adelaide and where applicable, any partner institution responsible for the joint award of this degree.

I acknowledge that copyright of published works contained within this thesis resides with the copyright holder(s) of those works.

I also give permission for the digital version of my thesis to be made available on the web, via the University's digital research repository, the Library Search and also through web search engines, unless permission has been granted by the University to restrict access for a period of time.

Published works in this thesis:

K. Feijen et al. (2022), "Modelling the Gamma-Ray Morphology of HESS J1804−216 from Two Supernova Remnants in a Hadronic Scenario" *MNRAS*, 511, 5915-5926

K. Feijen et al. (2020), "Arcminute-scale studies of the interstellar gas towards HESS J1804−216: Still an unidentified TeV γ-ray source" *PASA*, 37, E056

1st April 2022

_____   _____

Date   Signature

Acknowledgments

A PhD is like a roller-coaster with plenty of ups and downs, twists and turns, and many people rode this crazy roller-coaster with me.

I would like to firstly thank my supervisors, Prof. Gavin Rowell and Dr. Sabrina Einecke, for all their advice and guidance, in helping me navigate through the past four years. Both Gavin and Sabrina gave much of their time and knowledge in helping me finish this thesis. They also gave me multiple opportunities to attend conferences and workshops, along with the amazing opportunity to work a shift at the H.E.S.S. site in Namibia. I'd like to extend my gratitude to all my colleagues and co-authors interstate and overseas. Especially for their guidance and peer review of our papers.

I would also like to thank all my office-mates, who have been friendly and a much needed distraction at times throughout my PhD. In particular, thank you to both James and Fabien who took time out of their work to provide me with help and extremely useful input, especially at the start of my PhD when I was trying to find my footing. It has been a delight to work with all other members of the High Energy Astrophysics Group. The environment they have created is such a friendly and productive one. A special thanks to Ella and Ryan for the many lunch, coffee and chat breaks to keep me sane.

A special thanks to my family and friends who provided ongoing support, patience, and encouragement during these intense years of doing a PhD. Last but not least, I would like to thank my partner Brayden for his endless support. Thanks for keeping me motivated and for all your encouragement, especially during the last stages of my PhD. I couldn't have completed this without you.

In memory of my grandma, who was a shining light when all things seemed grey. She always provided constant support, coffee, and plenty of biscuits.

1 Introduction

Curiosity is the essence of our existence.

— Gene Cernan, *American Astronaut*

For thousands of years humans have gazed into the skies and marvelled at what lay before them. Driven by our deeply curious nature, humans have continually questioned the unknown, searching for the answers to the many unanswered questions about our universe. The field of astronomy is an ever changing one, advancing at astronomical speeds. We once relied only on the naked eye for observation of the night sky, however, with technological advances we can now detect light across the entire electromagnetic spectrum.

Gamma rays are the most energetic form of electromagnetic radiation, found at the farthest end of the electromagnetic spectrum. The highest energy γ-rays, often having energy in the TeV (Tera-electron Volt $\equiv 10^{12}$ eV) range, are generally produced by particles with a non-thermal energy distribution, in the most extreme and violent processes in our universe. Hence, γ-rays become a useful probe in the study of non-thermal astrophysical environments.

Very-high-energy (VHE) γ-rays are produced when accelerated "charged" cosmic rays (hereafter cosmic rays or CRs refers to "charged" cosmic rays) collide with matter. Earth is constantly bombarded by these CR particles from space. One of the most intriguing mysteries in modern astrophysics is the origin of these CRs (protons, nuclei). Since their discovery by Austrian physicist Victor Hess in the early 20th century (Hess, 1912), they have become one of the most researched topics. Unveiling the origin of CRs allows us to learn about high-energy astrophysical environments, and hence γ-ray sources. By studying TeV γ-rays, an impact can be made on the understanding of the extreme universe.

The state of the art facility to detect TeV γ-rays is the High Energy Stereoscopic System (H.E.S.S.). H.E.S.S. has identified numerous sources in our Milky Way galaxy (or 'Galactic sources'), however, the exact nature of over 30% of these sources still remains unknown (H.E.S.S. Collaboration et al., 2018). A significant portion of these sources are classified as 'unidentified', meaning no convincing counterpart to power the γ-ray source has been discovered.

TeV γ-rays are produced via two pathways in astrophysical environments; hadronically and leptonically. The hadronic production of γ-rays involves neutral pion decay, when an accelerated CR collides with the interstellar medium (ISM). Leptonic γ-rays are produced dominantly via inverse-Compton scattering, the upscattering of background photons by high-energy electrons. Morphological matches between the ISM gas and γ-ray emission are an indication of hadronic interactions, whilst for a leptonic accelerator the ISM gas is expected to anti-correlate with the γ-ray source. Mapping the ISM surrounding a TeV γ-ray source can therefore help to determine the nature of the source. Radio telescopes are used to detect these molecular and

atomic clouds in space.

This thesis makes use of radio telescopes to investigate the ISM to gain an understanding of the unidentified Galactic TeV γ-ray source HESS J1804−216. HESS J1804−216 is one of the brightest and most mysterious γ-ray sources discovered by H.E.S.S.. It has several potential counterparts which are investigated throughout this thesis to place limits on the object that is powering the source. This is done by using multi-wavelength data, in particular that from the ISM to gain an understanding of the target material for cosmic rays. Modelling of the γ-ray emission towards HESS J1804−216 using the ISM data will help to constrain the nature.

The thesis is structured as follows:

Chapter 2 gives an overview of high-energy astrophysics with a focus on γ-ray astronomy and the instruments used to detect these high-energy particles.

Chapter 3 summarises the techniques used to detect γ-rays, along with a brief explanation of the instruments used throughout this thesis.

Chapter 4 gives a review of the basic theory behind tracing the ISM, including explanations on molecular line emission physics, as well as the gas tracers utilised within this thesis.

Chapter 5 is the first journal publication paper: K. Feijen et al. (2020), "Arcminute-scale studies of the interstellar gas towards HESS J1804−216: Still an unidentified TeV γ-ray source" *PASA*, 37, E056.

Chapter 6 is the second journal publication paper: K. Feijen et al. (2022), "Modelling the Gamma-Ray Morphology of HESS J1804−216 from Two Supernova Remnants in a Hadronic Scenario" *MNRAS*, 511, 5915-5926.

Chapter 7 describes the background and methods required to model the γ-ray emission from SNRs and to create the Python code '`mario`: **m**odelling g**a**lactic gamma-**r**ay emiss**io**n'.

Chapter 8 presents the methods used to analyse the H.E.S.S. data using the Python package `gammapy`. This chapter involves looking for any indication of energy-dependent morphology and the evidence for acceleration of particles to PeV energies.

2   High-Energy Astrophysics

Somewhere, something incredible is waiting to be known.

— Carl Sagan, *American Astronomer*
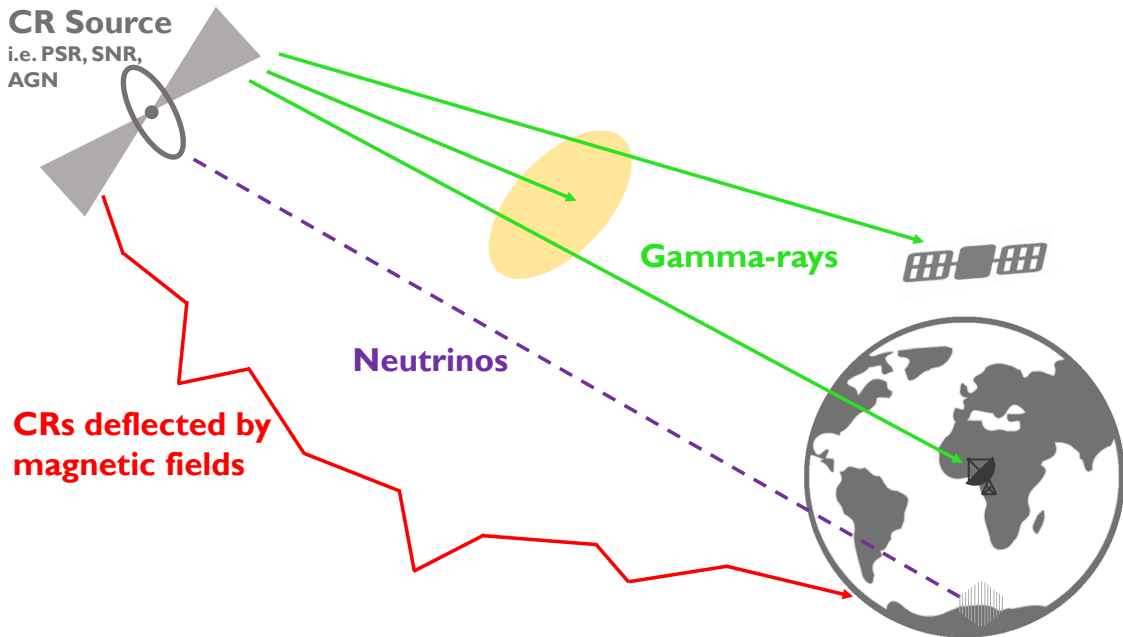
Figure 2.1: High-energy astrophysical messengers: CRs, neutrinos and γ-rays, as they propagate from their source (i.e. PSR, SNR, AGN) to Earth. Each messenger has different properties and therefore may or may not interact with magnetic fields, the interstellar medium or the Earths atmosphere as they propagate to Earth. They can be detected by various instruments both in space and by ground-based techniques. Image adapted from Einecke, 2017.

High-energy astrophysics is the study of highly energetic phenomena in the Universe. There are three types of messengers from high-energy astrophysical objects: neutrinos, cosmic rays (CRs) and γ-rays (as shown in Figure 2.1). CRs are affected by magnetic fields as they travel to Earth, resulting in a direction change (Berezinskii et al., 1990). This makes tracing their origin difficult, except at the highest energies (10^{19} eV). As a CR enters the Earth's upper atmosphere it interacts leading to a shower of particles. These particles are detected with ground-based methods such as the Pierre Auger Observatory (The Pierre Auger Collaboration, 2015) which is a CR observatory in Argentina that aims to decipher their origin and existence. Gamma rays and neutrinos are however uncharged particles, so their paths are not altered by magnetic fields. Gamma rays are detected by both space-based (i.e. *Fermi*-LAT, Atwood et al., 2009) and ground-based techniques. The primary γ-ray can interact with the Earths upper atmosphere inducing an air shower. The Cherenkov light originating from these showers can be detected with Imaging Atmospheric Cherenkov Telescopes, such as H.E.S.S. (High Energy Stereoscopic System, Aharonian et al., 2005) and CTA (Cherenkov Telescope Array, CTA Consortium

et al., 2018). Neutrinos have a low chance of interacting, so are not affected as they travel through the Universe. This, however, means that large detector volumes are required to increase the chance of interaction within the detector. IceCube is a neutrino detector at the South Pole which utilises the ice to detect the Cherenkov light from neutrino induced interactions (Aartsen et al., 2017).

The following chapter describes the high-energy astrophysical events which lead to the production of γ-rays. An overview of CR protons and electrons, including how they are accelerated to high energies is presented. Finally, the production pathways of high-energy γ-rays are described.

2.1   Galactic TeV Gamma-ray Sources

In 1989, the first detection of TeV γ-rays was achieved, with observations of the Crab Nebula by ground-based methods (Weekes et al., 1989). Since then, many different sources of γ-rays have been established using both space-based (at GeV energies) and ground-based γ-ray observatories. The H.E.S.S. Galactic Plane Survey (HGPS, H.E.S.S. Collaboration et al., 2018) provides the most extensive list of VHE Galactic γ-ray sources to date, with 78 catalogued sources. VERITAS (Very Energetic Radiation Imaging Telescope Array System, Weekes et al., 2002) is another γ-ray telescope array which has surveyed the Cygnus region in depth at γ-ray energies (Abeysekara et al., 2018). HAWC (High Altitude Water Cherenkov, Abeysekara et al., 2012) is a very high-energy γ-ray observatory which maps the northern sky. The 3HWC catalog (Albert et al., 2020) provides an all-sky survey of point-like and extended sources. LHAASO (Large High Altitude Air Shower Observatory) will provide information on the highest energy γ-rays, with a particular focus on accelerating particles to PeV energies (Cao et al., 2019; Cao et al., 2021).

Particles are accelerated to high energies by various events which are both Galactic and extragalactic in origin. This thesis focuses on Galactic sources such as supernova remnants, pulsar wind nebulae, massive stars, and stellar clusters. The majority of these sources are located along the Galactic plane, as shown in Figure 2.2. Figure 2.3 shows the distribution of Galactic TeV γ-ray sources from the HGPS, note the large fraction of unidentified sources.

2.1.1   Unidentified Sources

A significant portion (over 30%) of the Galactic TeV sources discovered to date are classified as 'unidentified'. This means no convincing candidate has yet been found to power the source. It is often the case that these source candidates lack emission in multiple wavelengths, making them difficult to identify (Hinton and Hofmann, 2009). Numerous unidentified sources have several plausible candidates which could be powering the γ-ray source. As the particle acceleration mechanism is unclear, they are frequently referred to as 'dark accelerators'. It is often suggested that these γ-ray sources are hadronic in origin as they lack X-ray synchrotron emission which limits the presence of multi-TeV electrons (Hinton and Hofmann, 2009).
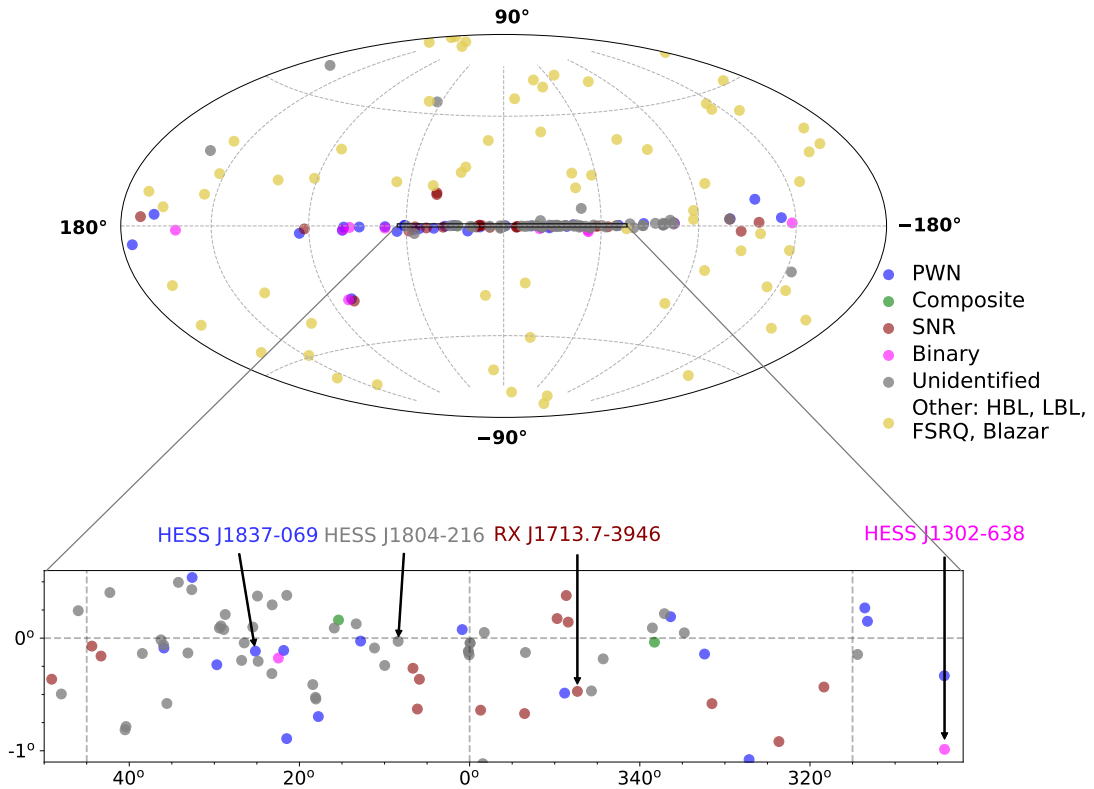
Figure 2.2: Sky map of the TeV γ-ray sources as of June 2021, plotted in Galactic coordinates. The lower bar shows a zoomed in image of a portion of the Galactic plane. Image adapted from the online source catalogue, TeVCat (Wakely and Horan, 2021).
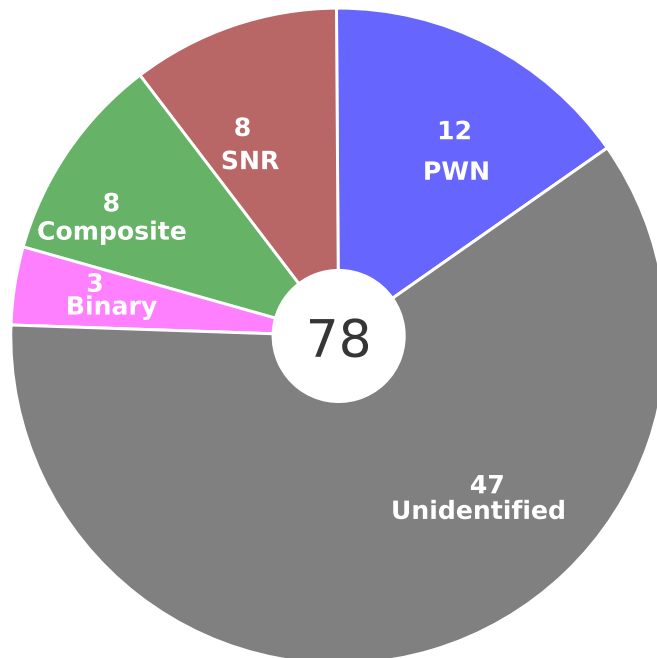
Figure 2.3: Pie chart showing the Galactic TeV γ-ray sources from the HGPS (H.E.S.S. Collaboration et al., 2018), noting that a large population of sources remains unidentified.

A promising method used for investigating and potentially determining the nature of these unidentified sources is by studying the interstellar gas which surrounds the TeV γ-ray source. By analysing the morphology of the gas using different tracers (i.e. hydrogen, carbon monoxide, carbon monosulfide, see Chapter 4), in conjunction with spectral line absorption and emission, it is possible to distinguish between hadronic and leptonic acceleration, and between different source types. Multiple authors (Moriguchi et al., 2005; Fukui et al., 2012; Lau et al., 2017; de Wilt et al., 2017; Voisin et al., 2019; Sano et al., 2019) have investigated the distribution and morphology of the ISM towards Galactic TeV γ-ray sources (in particular the unidentified ones) using radio observations (described in Chapter 3).

2.1.2   Supernova Remnants

A prominent candidate for accelerating CRs are supernova remnants (SNRs, Baade and Zwicky, 1934). During a supernova the gravitational collapse overcomes electron degeneracy pressure causing atoms to break into their constituent nuclides. The core then reaches nuclear density. Neutron degeneracy pressure stops this collapse, allowing the neutrinos that were trapped in the core to be released causing an intense explosion. The initial object is known as the 'progenitor' star.

Supernova are observationally classified by two types: Type I or Type II. Type I are divided into three or more subtypes: Ia, Ib, and Ic. Type Ia are of interest in the thesis. Type Ia supernova occur in a binary system in which the companion star accretes matter onto a white dwarf. When the mass of the white dwarf exceeds the Chandrasekhar limit ($1.44\,M_\odot$) the core collapses causing a thermonuclear explosion. Type II supernova (or core-collapse supernova) occur in stars with mass $\geq 8 M_\odot$. The star burns through layers of fuel as the core contracts and heats which causes ignition of heavier elements in the star. Once the star burns through most of its fuel, it is left as an iron core surrounded by shell burning materials. These outer layers of the star fall towards the core, and bounce back causing a supernova explosion. For further details on both types of supernova explosion see e.g. Woosley and Weaver, 1986; Leibundgut, 2000.

The evolution of SNRs is described by three main stages: the free expansion phase, Sedov-Taylor phase and radiative phase (Chevalier, 1977). Free expansion occurs for age less than $\sim$300 yr. As a supernova explodes its shock wave expands into the surrounding ISM creating a forward shock which moves into the ISM and a reverse shock travelling back into the ejecta (see Figure 2.4). During this phase (free expansion) the ISM has no influence on the expansion of the shock. The shock radius scales as $R_{\mathrm{sh}} = v_{\mathrm{sh}} t$, where the shock velocity, v_{sh}, is constant. The SNR accelerates CRs to the highest energies in the transition between this phase and the Sedov-Taylor phase (Ptuskin and Zirakashvili, 2005). The reverse shock continues to travel inwards, whilst continuing to cool adiabatically. The initial shock velocity remains constant until the Sedov-Taylor phase is initiated in which the mass of the swept up material exceeds the mass of the supernova ejecta (Sedov, 1959; Taylor, 1950; Truelove and McKee, 1999).
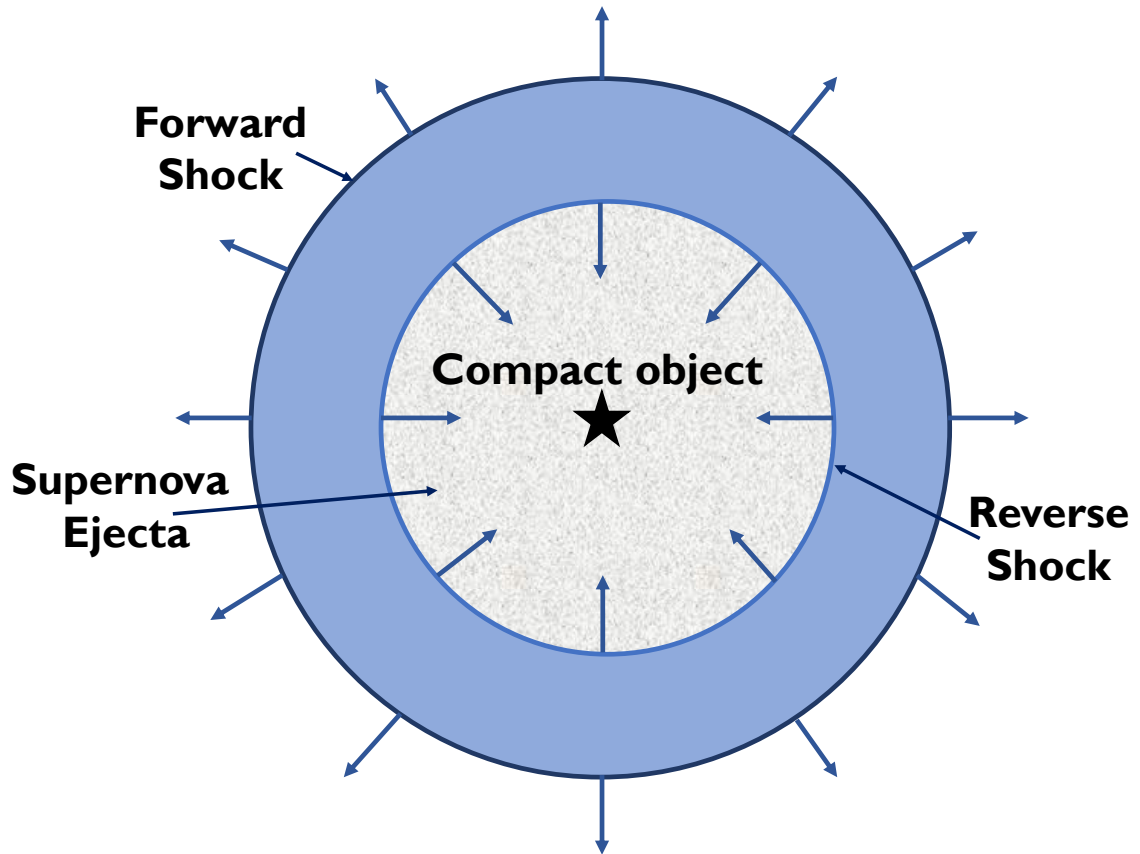
Figure 2.4: Schematic of supernova structure (Truelove and McKee, 1999).

In Sedov-Taylor phase the shock radius and velocity are given by Equations 2.1 and 2.2, respectively (Truelove and McKee, 1999).

$$R_{\text{sh}} = \left(\xi_0 \frac{E_{\text{SN}}}{\rho_0} \right)^{1/5} t^{2/5} \tag{2.1}$$

$$v_{\text{sh}} = \frac{2}{5} \left(\xi_0 \frac{E_{\text{SN}}}{\rho_0} \right)^{1/5} t^{-3/5} \tag{2.2}$$

where E_{SN} is the kinetic energy released in the supernova explosion, ρ_0 is the density of the ISM and $\xi_0 = 2.026$ (Taylor, 1950; Sedov, 1959). Equations 2.1 and 2.2 assume the shock is expanding into a uniform medium. The Sedov-Taylor phase occurs until an SNR age of $\sim$20 kyr. The shock begins to slow down as it continues to expand and cool adiabatically until temperatures of $\sim 10^6$ K, when it enters the radiative phase (Blondin et al., 1998). The radiative phase has a shock radius of $R_{\text{sh}} \propto t^{1/4}$ and shock velocity of $v_{\text{sh}} \propto t^{-3/4}$ (Cioffi et al., 1988). Ionised atoms start to capture free electrons and lose their energy by radiation. When these radiative losses become significant, the adiabatic expansion of the SNR ends (Reynolds, 2008) allowing the shock to cool further. The SNR will then dissipate into the surrounding ISM. The evolution of the SNR described here is depicted in Figure 2.5.
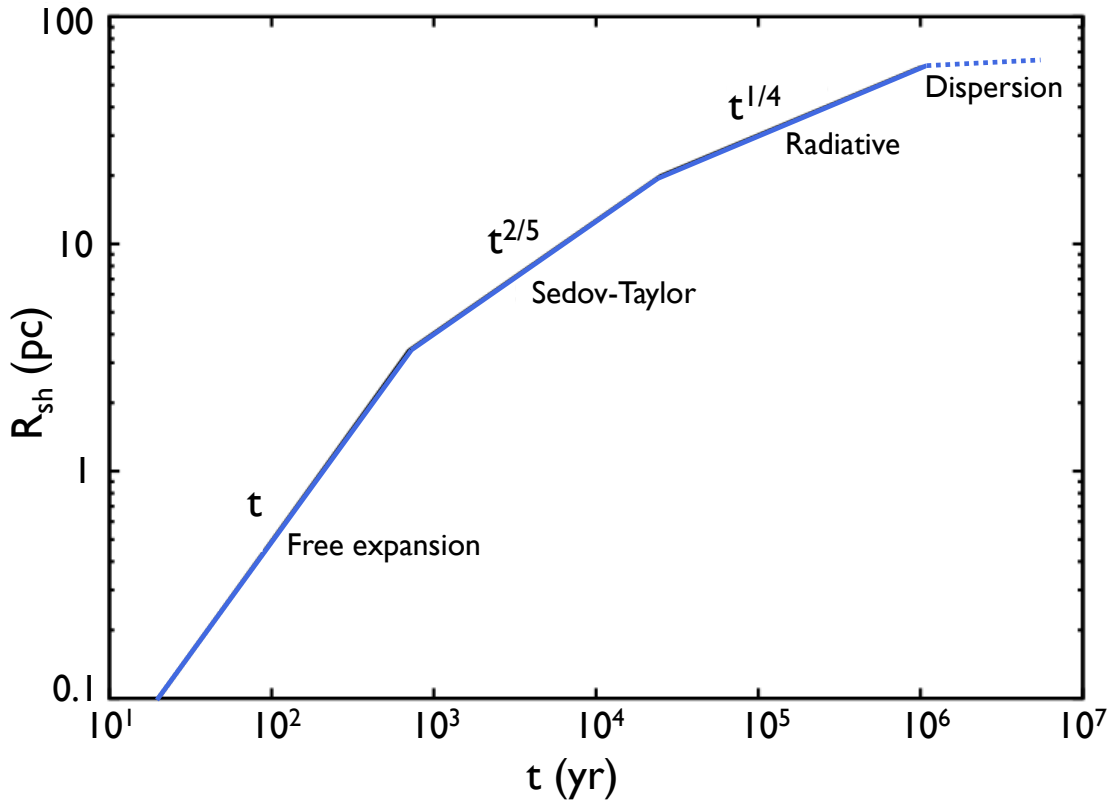
Figure 2.5: Evolution phases of SNRs as described in the text. Image adapted from Padmanabhan, 2001.

For a typical supernova explosion, several solar masses of material are released at initial speeds of $\sim 10^4$ km/s. The matter ejected in this process has a total canonical kinetic energy of more than 10^{51} erg. Of this $\sim 10 - 50\%$ is expected to be converted into CRs (Chevalier, 1977; Canto, 1977; Drury et al., 1989; Berezhko and Völk, 1997). The expanding shock wave interacts with the ISM. This creates an expanding nebula structure which is known as a SNR. The particles, often protons, are accelerated as they are deflected back and forth across the shock wave by magnetic fields. These conditions allow diffusive shock acceleration (DSA) to occur (Fermi, 1949, see Section 2.2.2). Particles gain enough energy to escape the shock front and interact with molecular clouds to create γ-rays.

SNRs are believed to accelerate both CR protons and electrons at their shock front (Blandford and Ostriker, 1978). In an SNR environment TeV γ-rays can therefore be produced either via hadronic processes (proton-proton collisions) or leptonic (electron interactions) processes. Evidence of proton acceleration is seen at multiple SNR sites, for example SNR W28, SNR W44 and IC 443 (H. Li and Chen, 2010; Ackermann et al., 2013; H.E.S.S. Collaboration et al., 2018). X-ray observations of various SNRs show the acceleration of electrons to high energies is plausible at the shock front (Koyama et al., 1995; Keohane et al., 1997; Slane et al., 1999; Slane et al., 2001; Ohira et al., 2012). It is likely that SNRs produce γ-rays through a combination of both accelerated CR protons and electrons.

2.1.3 Pulsar Wind Nebulae

Another dominant source of TeV γ-rays are pulsar wind nebulae (PWNe, H.E.S.S. Collaboration et al., 2018). A pulsar is a highly magnetised, rapidly-rotating neutron star, resulting from the collapse of the progenitor star's compact core during a supernova explosion. The spin period of a pulsar slows down due to the magnetic axis being misaligned to the rotation axis, causing the loss of rotational energy. The rate of rotational energy loss is described through the spin-down power given by:

$$\dot{E} = \frac{4\pi^2 I \dot{P}}{P^3} \,,$$

(2.3)

where I is the moment of inertia of the pulsar, P is the spin period and $\dot{P}$ is the period derivative. The strong rotating magnetic field causes an electric field to be produced hence allowing charged particles, commonly electrons, to be accelerated to very high energies. This creates a plasma around the pulsar region, which forms a dense magnetosphere defined by the closed magnetic field lines. Figure 2.6 shows a schematic of pulsar with its magnetic field lines.
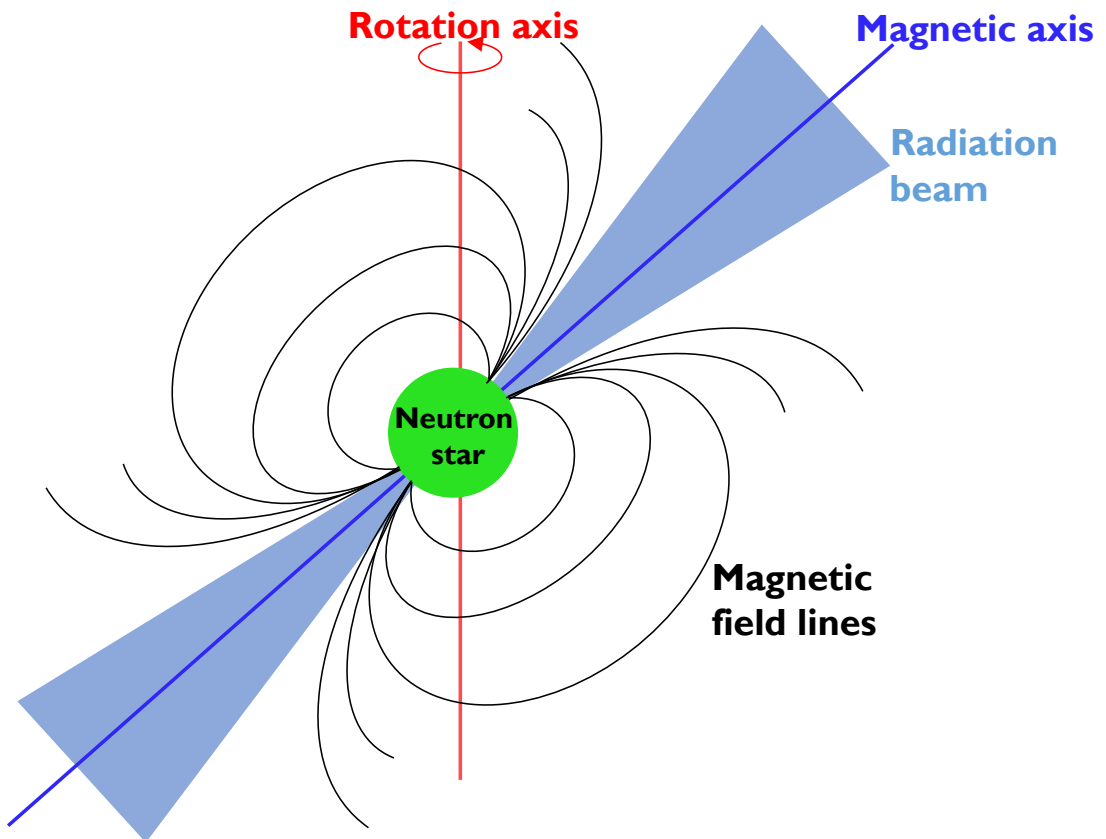
Figure 2.6: Structure of pulsar environment with its magnetic fields lines, showing the magnetic field is misaligned to the rotation axis. Image adapted from Kaspi et al., 2006.

The strong magnetic field lines lead to particles being accelerated to relativistic speeds. As these particles emanate from the pulsar, a shock front is created as they

interact with the ISM. This results in relativistic winds of charged particles, often comprised of electrons and positrons. These winds form a pulsar wind nebula as they travel radially outwards.

Figure 2.7 shows the different stages of PWNe evolution as described here. Stage 1 occurs when the age of the pulsar is less than 10 kyr, in which the pulsar is still positioned close to its birthplace. It is surrounded by the electron-positron wind. In this stage, the PWNe is still surrounded by the expanding SNR, which creates a forward shock. (FS) as the supernova ejecta moves outwards into the surrounding ISM. A reverse shock (RS) is also present in which the ejecta is decelerated. The contact discontinuity (CD) is the region between the two shocks. At later times where $t \sim$ 10-100 kyr (Stage 2), the reverse shock meets the PWNe leading to disruption and compression of the PWNe. This compression leads to an increase in pressure causing the PWN to rapidly expand again. The system repeats this behaviour several times (Blondin et al., 2001), resulting in a distorted nebula. This is typically 'crushed' on one side and the pulsar is offset from the central position of the nebula. After $\sim$100 kyr (Stage 3) the pulsar escapes its SNR interior and propagates through the ISM. A bow shock is formed, allowing high energy particles to be accelerated and form a 'TeV halo'. Further information on the evolution of PWNe see e.g. Blondin et al., 2001; Gaensler and Slane, 2006; Giacinti et al., 2020.
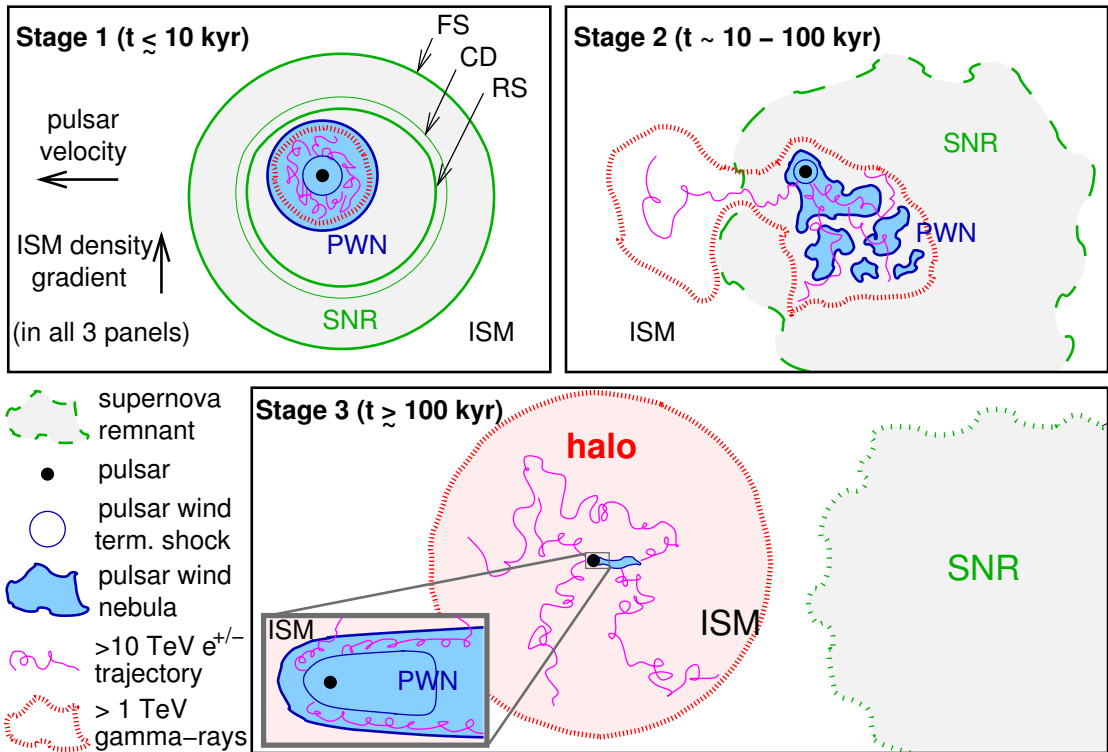
Figure 2.7: Sketch of the stages of PWNe evolution. Stage 1: the pulsar is close to its birth position and the PWN is contained in the SNR. RS, CD and FS indicate the reverse shock, contact discontinuity and forward shock, respectively, as described in text. Stage 2: the PWN has been disrupted leading to an irregular nebula. Stage 3: the pulsar leaves the SNR interior as high-energy electrons interact with the surrounding ISM forming a 'TeV halo'. Image from Giacinti et al., 2020.

TeV γ-rays may be produced by these PWNe. Emission of γ-rays from PWNe is plausible via two main mechanisms: inverse Compton scattering of low-energy photons by accelerated electrons, or non-thermal synchrotron radiation (typically observed in the radio to X-ray band). The Crab pulsar is a well-studied example of a pulsar producing high-energy γ-rays (Bogovalov and Aharonian, 2000).

2.1.4 Stellar Clusters

Stellar clusters are believed to be another source of TeV γ-rays. These clusters contain a large number of energetic stars, with high-velocity stellar winds. These strong winds collide with one another to form a termination shock, which is able to accelerate particles to high energies (Abramowski et al., 2012). Two stellar clusters detected with H.E.S.S. are Westerlund 1 and Westerlund 2, which are young clusters containing evolved high-mass stars such as Wolf-Rayets and OB supergiants and hypergiants (Abramowski et al., 2012; Aharonian et al., 2007). Given that these clusters can contain many different CR accelerators such as SNRs and pulsars, this makes the emission mechanism difficult to determine.

2.2 Cosmic-ray Protons and Electrons

CRs are highly energetic protons, electrons and heavier nuclei which travel through the universe at speeds close to the speed of light, until they collide with other particles or convert their energy to photons in the cosmic microwave background (CMB). Due to their charged nature, their direction is altered as they travel through Galactic magnetic fields, making CR directional analysis difficult.

2.2.1 The Origin of Cosmic Rays

Victor Hess performed various experiments on a hot air balloon flight, to find that the atmospheric ionisation rate increases with altitude (Hess, 1912). He concluded that this radiation comes from outer space, which led to the discovery of CRs. One of the most intriguing mysteries in modern astrophysics is the origin of these CRs.

These highly energetic CRs are constantly incident upon Earth with a large range of energies from 10^7 eV to as high as 10^{20} eV. The CR energy distribution at Earth is described by the power law:

$$\frac{dN}{dE} \propto E^{-\alpha} \,, \tag{2.4}$$

where N is the number of particles incident upon the Earth's atmosphere, E is the energy of CRs and α is the spectral index which varies with energy (Thoudam et al., 2016). The behaviour of a power law means the CR flux decreases rapidly as energy increases, as shown by the energy spectrum of CRs in Figure 2.8. At CR energies of

$\sim 10^{13}\,\mathrm{eV}$ there is approximately 1 particle/m^2/s, whilst at higher energies ($10^{19}\,\mathrm{eV}$) this is dramatically reduced to only 1 particle/km^2/year.
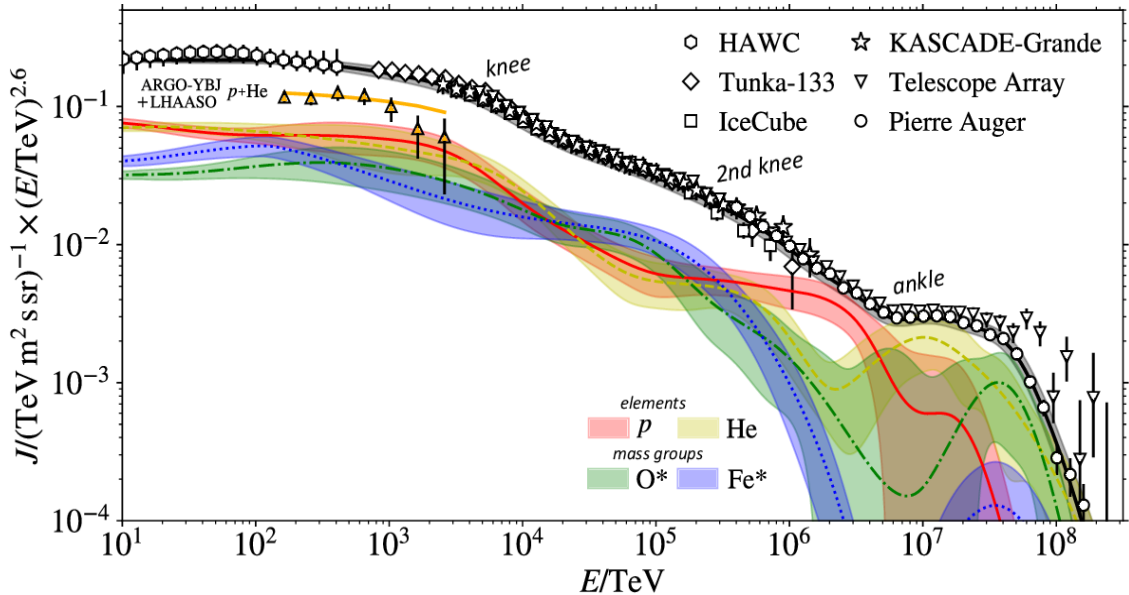
Figure 2.8: The CR energy spectrum (and mass composition) as viewed at Earth with data points from numerous CR experiments. Image from Schröder et al., 2019.

The energy spectrum of CRs in Figure 2.8 exhibits the power law behaviour from Equation 2.4, however, there are four areas in which the spectrum varies. These are known as the 'knee', 'second knee', 'ankle' and the high-energy cut-off. At an energy of $\sim 3 \times 10^{15}\,\mathrm{eV}$ the flux of the CRs begins to steepen from a spectral index of $\alpha \sim 2.7$ to $\alpha \sim 3.1$, at $\sim 10^{18}\,\mathrm{eV}$ the flux steepens again to $\alpha \sim 3.3$, then at $\sim 4 \times 10^{18}\,\mathrm{eV}$ the flux begins to flatten out with a spectral index of $\alpha \sim 2.7$, these are the 'knee', 'second knee' and 'ankle' respectively (Thoudam et al., 2016). The flux decreases rapidly at energies above $\sim 6 \times 10^{19}\,\mathrm{eV}$ which is known as the Greisen-Zatsepin-Kuzmin (GZK) cut-off. CRs above this energy can no longer reach us directly due to losing energy through interactions with CMB photons as they propagate to Earth (Greisen, 1966; Zatsepin and Kuz'min, 1966) or due to the limits on the available energy of the accelerator (Hillas, 1984).

CRs with energies below $10^{10}\,\mathrm{eV}$ have strong evidence of being solar CRs (Kotera and Olinto, 2011). For GeV ($10^9\,\mathrm{eV}$) and TeV ($10^{12}\,\mathrm{eV}$) energies, CRs are believed to originate from Galactic sources, for example SNR shock environments or PWNe (Thoudam et al., 2016). The SNR population is believed to have sufficient power ($\sim 10^{41}\,\mathrm{erg/s}$) to support the total Galactic CRs up to the knee (Blandford and Eichler, 1987). The higher energy CRs are believed to originate from extragalactic sources such as clusters of galaxies, Active Galactic Nuclei (AGN) or γ-ray bursts. The exact origin of CRs in the energy region between the 'knee' and 'ankle' is still unclear, as this region involves a mixture of both galactic and extragalactic origins (Swordy, 2001; Jokipii and Morfill, 1987; Protheroe and Szabo, 1992).

2.2.2 Cosmic-ray Acceleration

As discussed previously CRs are accelerated by various extreme astrophysical objects (see Section 2.1). The following section discusses the method for accelerating CRs to high energies. In 1949, Fermi proposed a model to explain the acceleration of low-energy particles to ultra-high energies. Fermi acceleration is the acceleration of low-energy CRs by the interaction of such particles with the magnetic fields inside interstellar clouds (Fermi, 1949). This mechanism is believed to be the primary way in which particles gain energy in a shock environment. There are two classifications of Fermi acceleration: first-order and second-order.

Second-Order Fermi Acceleration
Molecular clouds have regular motion around the galaxy. In addition, these clouds also exhibit turbulence in their magnetic fields caused by the local random velocities of $\sim$15 km/s (Fermi, 1949; Protheroe and Clay, 2004). As a CR enters a molecular cloud, it is deflected by turbulent magnetic fields within the cloud, leading to either a gain or loss in energy. The energy change is dependent on the type of collision; a head-on collision results in an energy gain, whilst a tail-on collision ends in an energy loss. A charged particle with energy E_i enters a cloud at an angle of θ_i with respect to the clouds velocity, v_{cloud}. The particle is scattered by the turbulent magnetic fields inside the cloud and escapes at an angle of θ_f with energy E_f. This process is depicted in Figure 2.9. Two frames are considered for this scenario; the cloud frame (primed) and the laboratory frame (unprimed). It is possible to move between these frames using Lorentz transformations.
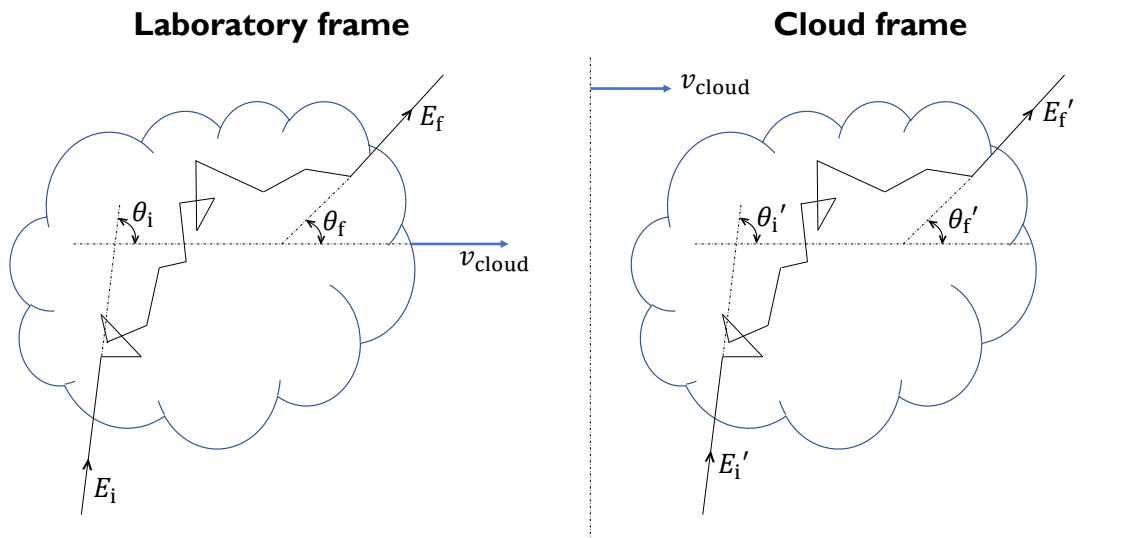
Figure 2.9: Illustration of Fermi acceleration. *Left*: The laboratory frame, the particle of energy E_i enters the cloud, with velocity v_{cloud}, at an angle of θ_i. This particle exits the cloud, after being scattered by the magnetic field, at an energy of E_f and angle of θ_f. *Right*: The cloud frame (primed frame), which is described by the same process. Image adapted from Protheroe and Clay, 2004.

The initial energy in the cloud frame is given by:

$$E'_i = \gamma_{\text{cloud}} E_i (1 - \beta_{\text{cloud}} \cos\theta_i) \,, \tag{2.5}$$

where $\beta_{\text{cloud}} = v_{\text{cloud}}/c$ and $\gamma_{\text{cloud}} = 1/\sqrt{1 - \beta_{\text{cloud}}^2}$. The scattering of the CR by the cloud is collisionless, hence there is no change in energy in this frame:

$$
\begin{aligned}
E'_f &= E'_i \\
&= \gamma_{\text{cloud}} E_i (1 - \beta_{\text{cloud}} \cos\theta_i) \,.
\end{aligned}
\tag{2.6}
$$

In the laboratory frame, the energy of the particle exiting the cloud is:

$$
\begin{aligned}
E_f &= \gamma_{\text{cloud}} E'_f (1 + \beta_{\text{cloud}} \cos\theta'_f) \\
&= \gamma_{\text{cloud}}^2 E_i (1 - \beta_{\text{cloud}} \cos\theta_i)(1 + \beta_{\text{cloud}} \cos\theta'_f) \,.
\end{aligned}
\tag{2.7}
$$

In this frame there is a fractional change in the energy entering and exiting the cloud, as shown by Equation 2.8.

$$
\begin{aligned}
\frac{\Delta E}{E} &= \frac{E_f - E_i}{E_i} \\
&= \frac{1 - \beta_{\text{cloud}} \cos\theta_i + \beta_{\text{cloud}} \cos\theta'_f - \beta_{\text{cloud}}^2 \cos\theta_i \cos\theta'_f}{1 - \beta_{\text{cloud}}^2} - 1 \,.
\end{aligned}
\tag{2.8}
$$

To determine the average fractional energy change per crossing the average values for $\cos\theta_i$ and $\cos\theta'_f$ need to be determined. Inside the cloud, the direction of the CR is randomized as it scatters off the magnetic field irregularities, hence $\langle \cos\theta'_f \rangle = 0$. Calculating the average of $\cos\theta_i$ however depends on the collision rate of CRs with the cloud at different angles. The probability of collision is $P_{\text{coll}} \propto (1 - \beta_{\text{cloud}} \cos\theta_i)$ for $-1 < \cos\theta_i < 1$. Therefore, the average of the cosine of the incident angle is

$$\langle \cos\theta_i \rangle = \frac{\int \cos\theta_i \, P_{\text{coll}} \, d(\cos\theta_i)}{\int P_{\text{coll}} \, d(\cos\theta_i)} = -\frac{\beta_{\text{cloud}}}{3} \,. \tag{2.9}$$

Using the above results, the average fractional energy change is obtained from Equation 2.8.

$$\left\langle \frac{\Delta E}{E} \right\rangle = \frac{4}{3} \beta_{\text{cloud}}^2 \tag{2.10}$$

Equation 2.10 shows that the average change in energy is positive. This means a head-on collision is more probable than a tail-on collision and so on average the CRs gain energy, i.e. the CRs are accelerated on average. It is important to note,

however, that this average energy gain is very small due to $\beta_{\text{cloud}} \ll 1$. This process would later be called 'second-order Fermi acceleration', due to the proportionality to the square of β_{cloud}. There are almost as many head-on collisions (energy gains) as tail-on collisions (energy loss) in this system in addition to a very small energy gain, therefore it is not possible for this process to account for the observed flux of accelerated CRs.

First-Order Fermi Acceleration

In the 1970s a new theory was suggested (Bell, 1978; Blandford and Ostriker, 1978; Axford et al., 1977), to modify Fermi's original model to include a description of the acceleration at astrophysical shock fronts. In this scenario, CRs are able to pass the shock front where they are scattered off the magnetic field existing within the medium on the opposite side of the shock, allowing the CR to return to the other side of the shock. As this can occur a number of times and the collisions are head-on, the CR particle gains energy after each crossing. This process is known as 'first-order Fermi acceleration' or more commonly 'diffusive shock acceleration'.

A shock front is created as the ISM and associated magnetic field pile up in front of the matter ejected from a violent astrophysical event, such as a supernova explosion. This shock front travels at a very high velocity (v_{shock}) compared to the velocity of the surrounding medium. The magnetic field irregularities on either side of the shock cause the CRs to be scattered. These magnetic irregularities can be visualised as magnetised clouds which move at a velocity of v_{ejecta} (see Figure 2.10). A CR can be scattered off a magnetised cloud to pass the shock front from downstream (behind the shock) to upstream (ahead of the shock), and back. This CR will cross the shock multiple times before it escapes the system.

For non-relativistic shocks ($v_{\text{ejecta}} \ll c$) the rate at which CRs cross the shock from upstream to downstream ($R_{\text{U} \to \text{D}}$) and downstream to upstream ($R_{\text{D} \to \text{U}}$) with respect to the CR number density, n_{CR}, and CR speed, v_{CR} is given by:

$$
\begin{aligned}
R_{\text{U} \to \text{D}} &\sim -n_{\text{CR}} \, v_{\text{CR}} \, \cos \theta_{\text{i}} \\
R_{\text{D} \to \text{U}} &\sim n_{\text{CR}} \, v_{\text{CR}} \, \cos \theta_{\text{f}}' \, .
\end{aligned}
\tag{2.11}
$$

Here, θ_{i} is the angle between the direction of the CR and the shock ($90° < \theta_{\text{i}} < 180°$) in the laboratory frame as the particle moves downstream and θ_{f}' is the angle between the direction of the CR and the shock ($0° < \theta_{\text{f}}' < 90°$) in the shock frame as the particle moves upstream. The average values for $\cos \theta_{\text{i}}$ and $\cos \theta_{\text{f}}'$, provided the distribution of CRs is isotropic, are given in Equation 2.12. The probability of $\cos \theta_{\text{i}}$ on shock crossing is $P(\cos \theta_{\text{i}}) \propto - \cos \theta_{\text{i}}$ and for $\cos \theta_{\text{f}}'$ on shock crossing is $P(\cos \theta_{\text{f}}') \propto \cos \theta_{\text{f}}'$.
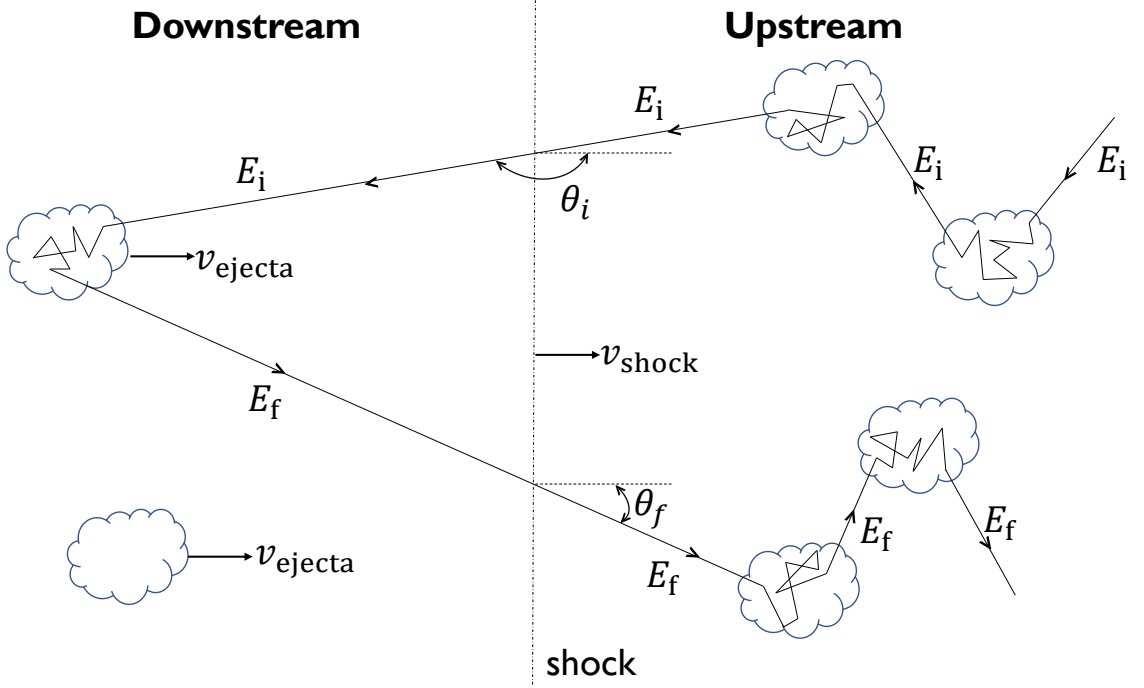
Figure 2.10: Particles being scattered off magnetised clouds on either side of a shock. The velocity of the shock and eject are, v_{shock} and v_{ejecta}, respectively. In this simplified schematic the particle crosses the shock only twice, but in reality this would occur multiple times. Image adapted from Protheroe and Clay, 2004.

$$
\begin{aligned}
\langle \cos \theta_{\text{i}} \rangle &= \frac{\int_{-1}^{0} P(\cos \theta_{\text{i}}) \cos \theta_{\text{i}} \, d(\cos \theta_{\text{i}})}{\int_{-1}^{0} P(\cos \theta_{\text{i}}) \, d(\cos \theta_{\text{i}})} = \frac{\int_{-1}^{0} \cos^2 \theta_{\text{i}} \, d(\cos \theta_{\text{i}})}{\int_{-1}^{0} \cos \theta_{\text{i}} \, d(\cos \theta_{\text{i}})} = -\frac{2}{3} \\
\langle \cos \theta_{\text{f}}' \rangle &= \frac{\int_{0}^{1} P(\cos \theta_{\text{f}}') \cos \theta_{\text{f}}' \, d(\cos \theta_{\text{f}}')}{\int_{0}^{1} P(\cos \theta_{\text{f}}') \, d(\cos \theta_{\text{f}}')} = \frac{\int_{0}^{1} \cos^2 \theta_{\text{f}}' \, d(\cos \theta_{\text{f}}')}{\int_{0}^{1} \cos \theta_{\text{f}}' \, d(\cos \theta_{\text{f}}')} = \frac{2}{3}
\end{aligned}
\tag{2.12}
$$

The average fractional change per crossing is found by combining Equation 2.8 (where $v_{\text{cloud}} = v_{\text{ejecta}}$) and Equation 2.12, and assuming $\beta_{\text{ejecta}} = v_{\text{ejecta}}/c$.

$$
\left\langle \frac{\Delta E}{E} \right\rangle = \frac{1 - \beta_{\text{ejecta}} \langle \cos \theta_{\text{i}} \rangle + \beta_{\text{ejecta}} \langle \cos \theta_{\text{f}}' \rangle - \beta_{\text{ejecta}}^2 \langle \cos \theta_{\text{i}} \rangle \langle \cos \theta_{\text{f}}' \rangle}{1 - \beta_{\text{ejecta}}^2} - 1
\tag{2.13}
$$

For $\beta_{\text{ejecta}} \ll 1$:

$$
\left\langle \frac{\Delta E}{E} \right\rangle \sim \frac{4}{3} \beta_{\text{ejecta}} = \frac{4}{3} \frac{v_{\text{ejecta}}}{c} \, .
\tag{2.14}
$$

The compression ratio, $R \equiv \rho_{\text{shocked}}/\rho_{\text{unshocked}}$, is used to relate the velocity of the shock v_{shock} and the velocity of the ejecta v_{ejecta} (see Equation 2.15). For strong shocks, such as a supernova shock, the ratio of the density of the shocked and unshocked gas is $R = 4$ (Reynolds, 2008).

$$\frac{v_{\text{shock}}}{v_{\text{ejecta}}} = \frac{R}{R-1} = \frac{4}{3} \tag{2.15}$$

Applying this to Equation 2.13, the average fractional change in energy is

$$\left\langle \frac{\Delta E}{E} \right\rangle \sim \frac{4}{3} \frac{v_{\text{ejecta}}}{c} = \frac{v_{\text{shock}}}{c} \, . \tag{2.16}$$

The fractional energy change per collision for this process is higher than Fermi's original theory due to being first order in $\beta_{\text{shock}} = v_{\text{shock}}/c$. Thus, diffusive shock acceleration is more efficient at accelerating particles than second-order Fermi acceleration and is more likely to accelerate CRs to the observed energies.

Diffusive shock acceleration leads to a differential CR spectrum of

$$\frac{dN}{dE} \propto E^{-\frac{R+2}{R-1}} \, . \tag{2.17}$$

See Appendix A for further information. The well-known result of $dN/dE = E^{-2}$ is obtained assuming a strong shock ($R = 4$) and that the particles do not effect the shock. Variation of the spectral index is expected between different models due to uncertainty in the shock dynamics. For example, Marcowith et al., 2006 obtain a spectral index of $\alpha \sim 2.3$. Energy-losses are significant during propagation of the particles from their source to Earth. Heavier CR nuclei (e.g. Fe, C, O) are expected to experience spallation from collisions during their propagation to Earth, which would create secondary (lighter) CR nuclei (e.g. Li, Be, B, Cheng and Romero, 2004). These factors result in a steepening of the CR energy spectrum, which could explain the spectral index of $\alpha \sim 2.7$ in the observed CR spectrum at Earth.

2.3   Production of Gamma Rays

Throughout the universe, thermal radiation is observed across most of the electromagnetic spectrum. The radiation from these thermal sources obey Planck's law, which describes the emission from a black-body. This black-body radiation is characteristic to the source, where the temperature is proportional to the peak frequency emitted. These thermal sources, however, cannot account for all radiation detected. Non-thermal processes can produce electromagnetic radiation from low-energy radio emission to the highest energy photons in our universe, γ-rays. There are two pathways in which γ-rays are produced in astrophysical environments; hadronically (from protons and nuclei) and leptonically (from electrons). Figure 2.11 shows these scenarios. This section outlines the common processes in which high-energy γ-rays are produced.
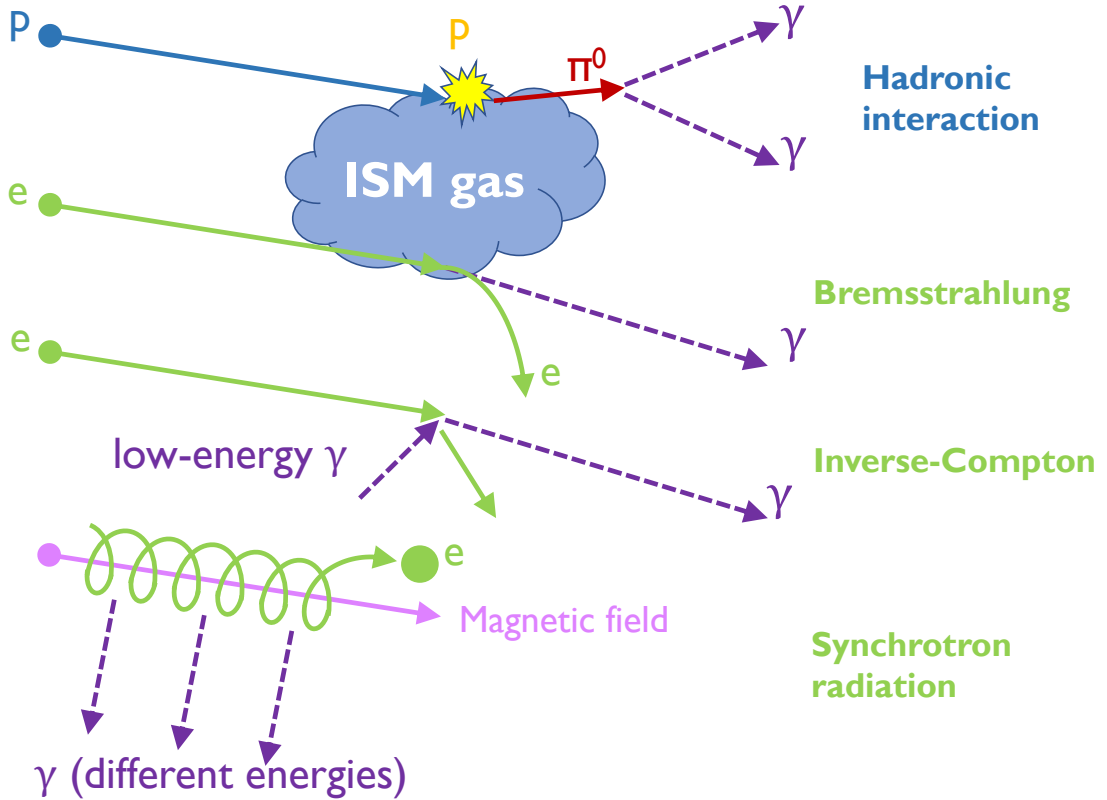
Figure 2.11: The different production mechanisms of high-energy γ-rays.

2.3.1 Hadronic Origin of Gamma Rays

The hadronic mechanism of γ-ray production occurs when a CR collides with the nuclei of matter. This is most commonly a proton-proton interaction (the same as in the Large Hadron Collider at CERN) which results in γ-rays being produced via pion decay (see e.g. Ginzburg and Syrovatskii, 1964). There are three different channels; neutral pion decay and charged pion decay (positive and negative). The mean lifetime of a neutral pion $\sim 10^{-16}$ s is much shorter than a charged pions mean lifetime $\sim 10^{-8}$ s (Martin and Shaw, 2009). These pions are produced in roughly equal quantities at high energies.

$$p + p \rightarrow \begin{cases} \pi^0 + p + p \\ \pi^+ + \pi^- + p + p \\ \pi^+ + n + p \end{cases} \tag{2.18}$$

where p represents a proton in the form of a CR and a proton from the ISM. Neutral pions, π^0, decay to produce a pair of γ-ray photons.

$$\pi^0 \rightarrow 2\gamma \tag{2.19}$$

Charged pions, $\pi^\pm$, decay to produce muons, muon neutrinos and muon anti-neutrinos. These products then go on to decay to produce electrons and positrons, as shown by Equations 2.20 and 2.21 (see e.g. Martin and Shaw, 2009, for an overview).

$$\pi^+ \to \mu^+ + \nu_\mu$$
$$\pi^- \to \mu^- + \overline{\nu}_\mu$$

(2.20)

$$\mu^+ \to e^+ + \nu_e + \overline{\nu}_\mu$$
$$\mu^- \to e^- + \overline{\nu}_e + \nu_\mu$$

(2.21)

In a proton-proton interaction, the primary proton loses approximately half of its energy to the leading proton or nuclei. The rest of the energy is used in the production of pions. Due to this, a significant amount of the energy from the primary proton is given to the γ-rays produced ($E_\gamma \sim 0.17 E_\mathrm{p}$, Kelner et al., 2006). The energy loss rate of protons for proton-proton interactions depends on the ambient medium number density, n, the total cross section of proton-proton collisions, σ_pp, and the inelasticity for a single interaction, $f \sim 0.5$ (Gaisser, 1990), shown in Equation 2.22.

$$\frac{dE_\mathrm{p}}{dt} = n\,\sigma_\mathrm{pp}\,f\,c\,E_\mathrm{p}\,,$$

(2.22)

where E_p is the energy of the initial proton.

The cooling time is described as the time taken for a particle to radiate all its energy through a single process, given by $\tau_\mathrm{i} \sim E_\mathrm{i}/(dE_\mathrm{i}/dt)$ (Rybicki and Lightman, 1986). The radiative cooling time of protons through proton-proton collisions is (Aharonian and Atoyan, 1996):

$$\tau_\mathrm{pp} = (n\,\sigma_\mathrm{pp}\,f\,c)^{-1} \approx 6 \times 10^7\,(n/\mathrm{cm}^{-3})^{-1}\,\mathrm{yr}\,,$$

(2.23)

where σ_pp and κ are the cross-section and inelasticity of proton-proton collisions, respectively. These parameters are approximated by the mean values of $\sigma_\mathrm{pp} \approx 40\,\mathrm{mb}$ and $\kappa \approx 0.45$ from Gaisser, 1990.

2.3.2 Leptonic Origin of Gamma Rays

Leptonic γ-rays are produced through electron interactions. There are three main processes; inverse Compton scattering, Bremsstrahlung and synchrotron radiation. As electrons are less massive than CRs, they lose energy faster and are more influenced by different effects, such as synchrotron losses.

Inverse Compton Scattering

Inverse Compton scattering is a process in which high-energy electrons and positrons $(e_{\mathrm{LE}}^{\pm})$ scatter low-energy photons (γ_{LE}) to produce γ-rays in the MeV energy range and above, shown by Equation 2.24 (Blumenthal and Gould, 1970). These low-energy photons are generated in a number of different ways, such as radio, infrared, optical, however, they are most commonly from the CMB which is spread throughout the universe.

$$e_{\mathrm{HE}}^{\pm} + \gamma_{\mathrm{LE}} \rightarrow e_{\mathrm{LE}}^{\prime\pm} + \gamma_{\mathrm{TeV}} \qquad (2.24)$$

The energy loss rate of electrons for the inverse Compton scenario is given by (Blumenthal and Gould, 1970):

$$\left.\frac{dE_{\mathrm{e}}}{dt}\right|_{\mathrm{IC}} = \frac{4}{3}\, U_{\mathrm{rad}}\, c\, \gamma^2\, \sigma\,, \qquad (2.25)$$

where U_{rad} is the radiation energy density, c is the speed of light and γ is the electron Lorentz factor. The interaction cross-section, σ, can be approximated by the Thomson cross-section, σ_{T} (Equation 2.26), when the rest mass energy is much greater than the electron energy.

$$\sigma_T = \frac{8\pi}{3}\frac{q^2}{4\pi\,\epsilon_0\,m_{\mathrm{e}}\,c^2} \qquad (2.26)$$

The charge and mass of the electron is q and m_{e}, respectively. The permittivity of free space is $\epsilon_0 \sim 8.86 \times 10^{-12}\,\mathrm{m^{-3}\,kg^{-1}\,s^4\,A^2}$ (Longair, 2011). For electrons, the Thomson cross-section is $\sigma_T = 6.65 \times 10^{-29}\,\mathrm{m^2}$. For higher electron energies, where the electron energy is much greater than the rest mass energy, the inverse Compton scattering emission is suppressed. This causes a cut-off in the photon spectra at an energy of $\sim$50 TeV. Above this energy is the Klein-Nishina regime (Moderski et al., 2005). The Klein-Nishina cross-section is

$$\sigma_{\mathrm{KN}} = \pi r_{\mathrm{e}}^2 \frac{1}{x}\left(\left[1 - \frac{2(x+1)}{x^2}\right]\ln(2x+1) + \frac{1}{2} + \frac{4}{x} - \frac{1}{2(2x+1)^2}\right), \qquad (2.27)$$

where the electron radius is $r_{\mathrm{e}} = e^2/(4\pi\epsilon_0 m_{\mathrm{e}}c^2)$ and $x = \hbar\omega/m_{\mathrm{e}}c^2$. Here $\hbar = h/2\pi$, where $h = 6.626 \times 10^{-24}\,\mathrm{J\,s}$ is Planck's constant and ω is the frequency of the incoming photon. The Klein-Nishina cross-section in the ultra-relativistic limit $(\gamma \gg 1)$ can be approximated by:

$$\sigma_{\mathrm{KN}} = \pi r_{\mathrm{e}}^2 \frac{1}{x}\left[\ln(2x) + \frac{1}{2}\right]. \qquad (2.28)$$

An initial photon of energy, ϵ_{i}, undergoes inverse Compton scattering with an electron of energy, E_{e}, where the resulting energy of the photon produced, E_γ, is:

$$E_\gamma \approx \left(\frac{E_\mathrm{e}}{mc^2}\right)\epsilon_\mathrm{i} = \gamma_\mathrm{e}^2\epsilon_\mathrm{i}\,. \tag{2.29}$$

The inverse Compton cooling time t_IC is given by (Aharonian, 2004):

$$\tau_\mathrm{IC} \approx 3 \times 10^8 (U_\mathrm{rad}/\mathrm{eV}/\mathrm{cm}^3)^{-1}(E_\mathrm{e}/\mathrm{GeV})^{-1}\,\mathrm{yr}\,, \tag{2.30}$$

where U_rad is $0.26\,\mathrm{eV}/\mathrm{cm}^3$ (the energy density of the CMB) and E_e is the electron energy. For any given H.E.S.S. source $100\,\mathrm{GeV}$ γ-rays (the lower limit detectable by H.E.S.S.) are expected to be produced by inverse Compton scattering to correspond to electron of energies of $E_\mathrm{e} \sim 6\,\mathrm{TeV}$ ($E_\mathrm{e} \sim 20\sqrt{E_\gamma}$ for the Thomson scattering regime).

Bremsstrahlung
Bremsstrahlung (German for 'braking radiation') is a process in which electrons convert their energy to photons after being scattered within the field of a nucleus in interstellar gas. When the mass of the electron is much smaller than the mass of the nucleus, it causes the deceleration of the atomic nucleus when deflected by the electron and Bremsstrahlung radiation to be emitted (Blumenthal and Gould, 1970). The γ-ray energy is equal to the difference in the initial and final energy of the electron.

$$e^- + N \rightarrow e^{'-} + \gamma\,, \tag{2.31}$$

where e^- is the initial electron, N is the nucleus of the molecule, $e^{'-}$ is the deflected electron and γ is Bremsstrahlung radiation.

The energy loss rate of electrons due to Bremsstrahlung radiation is

$$\left.\frac{dE_\mathrm{e}}{dt}\right|_\mathrm{Brems} = c\,m_\mathrm{p}\,n_\mathrm{p}\,\frac{E_\mathrm{e}}{X_0}\,, \tag{2.32}$$

where c is the speed of light, m_p is the proton mass, n_p is the ambient matter density and $X_0 = \frac{7}{9}\frac{\rho}{n_\mathrm{p}\,\sigma_0}$ is the radiation length, where the matter density is $\rho = m_\mathrm{p}\,n_\mathrm{p}$ and σ_0 is the pair production cross section (Aharonian, 2004).

The Bremsstrahlung cooling time τ_brem is given by (Aharonian, 2004):

$$\tau_\mathrm{brem} \approx 4 \times 10^7 (n/\mathrm{cm}^3)^{-1}\,\mathrm{yr}\,, \tag{2.33}$$

where n is the ambient matter number density.

Synchrotron Radiation

Synchrotron radiation is the most prominent process to produce non-thermal radio to X-ray radiation. The photons are produced when an electron traverses a magnetic field (B). The force from the magnetic field causes the electron to spiral around the magnetic field lines, slowly accelerating, and producing synchrotron radiation (Blumenthal and Gould, 1970). For TeV electrons, the radiation generated is in the X-ray energy range, whilst GeV electrons produce radio, optical or UV radiation, as seen by Equation 2.34.

$$
\begin{aligned}
e^-_{\text{TeV}} + B_{\mu\text{G}} &\rightarrow e^{'-} + \gamma_{\text{keV}} && \text{X-rays} \\
e^-_{\text{GeV}} + B_{\mu\text{G}} &\rightarrow e^{'-} + \gamma_{\text{eV}} && \text{Radio/optical/UV}
\end{aligned}
\tag{2.34}
$$

The energy loss rate of charged particles through synchrotron radiation is (Rybicki and Lightman, 1986)

$$
\left.\frac{dE_{\text{e}}}{dt}\right|_{\text{sync}} = \frac{4}{3}\,\sigma_{\text{T}}\,c\,U_{\text{B}}\,\gamma^2\,,
\tag{2.35}
$$

where σ_{T} is the Thomson cross section in Equation 2.26, c is the speed of light, $U_{\text{B}} = B^2/2\mu_0$ is the magnetic energy density, and $\gamma = E_{\text{e}}/m_{\text{e}}c^2$ is the Lorentz factor.

The synchrotron cooling time τ_{sync} is given by:

$$
\tau_{\text{sync}} \approx 1.2 \times 10^7 (B/\mu\text{G})^{-2}(E_{\text{e}}/\text{TeV})^{-1}\,\text{yr}\,,
\tag{2.36}
$$

where B is the magnetic field strength which is commonly described by Equation 2.37 (Crutcher et al., 2010).

$$
B = \begin{cases}
B_0 & \text{for } n < 300\,\text{cm}^{-3} \\
B_0 \left(\dfrac{n}{300\,\text{cm}^{-3}}\right)^{0.65} & \text{for } n > 300\,\text{cm}^{-3}\,,
\end{cases}
\tag{2.37}
$$

where the average number density is n and $B_0 = 10\,\mu\text{G}$.

In many γ-ray and X-ray sources (e.g. PWNe) the synchrotron and inverse Compton emission occur within a population of electrons and hence the two processes compete for the energy. The ratio of energy loss from inverse Compton scattering (F_{IC}) of CMB photons in the Thomson regime and synchrotron radiation (F_{sync}) is dependent on the magnetic field strength B (see Equation 2.38, Aharonian et al., 1997a).

$$
\frac{F_{\text{IC}}}{F_{\text{sync}}} = \frac{1}{10(B/10\,\mu\text{G})^2}
\tag{2.38}
$$

As the magnetic field increases ($B > 10\,\mu\mathrm{G}$), the synchrotron emission will dominate over the emission from inverse Compton processes. This is also shown through the timescales of the synchrotron and inverse Compton cooling in Equations 2.30 and 2.36 respectively. The synchrotron cooling time decreases with magnetic field as it is proportional to B^{-2}, allowing high energy electrons to emit X-rays via synchrotron radiation for strong magnetic fields.

3   Detecting TeV Gamma Rays and the Interstellar Medium

> *I'm comfortable with the unknown – that's the point of science. There are places out there, billions of places out there, that we know nothing about. And the fact that we know nothing about them excites me, and I want to go out and find out about them. And that's what science is.*
>
> — Brian Cox, *English Astrophysicist*

The sky has been observed for decades by both ground-based and space-based telescopes. Radio astronomy is utilised in the study of specific γ-ray investigations, such as SNRs in the hadronic scenario, as this production method relies on the presence of molecular clouds. This chapter briefly discusses high-energy γ-ray detection methods, as well as the various telescopes which have contributed data to this thesis (i.e. H.E.S.S., Mopra, ATCA and Parkes). Figure 3.1 shows the location of each telescope discussed in this chapter.
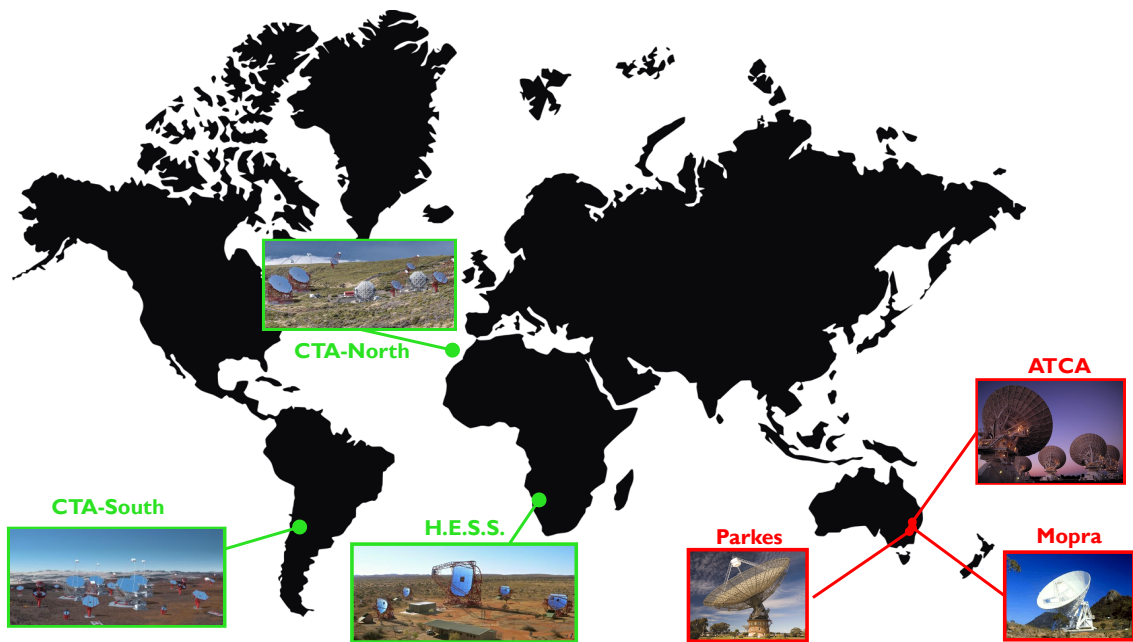
Figure 3.1: The location of various telescopes discussed throughout this chapter. Image credit for each telescope is found within this chapter.

3.1   Gamma-ray Astronomy

One of the long-standing mysteries in astrophysics is the origin of cosmic rays (CRs). Due to their charged nature, CRs are deflected by both Galactic and extragalactic magnetic fields, meaning we cannot trace these particles back to their origin. To overcome this, various astronomical messengers such as γ-rays are used as they are not affected by magnetic fields. These messengers provide information about high-energy astrophysical environments.

γ-rays cannot be directly observed from the Earth's surface, due to atmospheric attenuation. Space-based detectors are also limited in detecting TeV γ-rays as the low flux of these γ-rays would require a large collection area which is impractical in space (Aharonian et al., 2008). Various γ-ray techniques are employed in order to overcome these issues. The concept for ground-based detection is to detect the Cherenkov light which originates from secondary particles created when a γ-ray interacts with the Earth's atmosphere, which creates a showering effect of particles (discussed further in Sections 3.1.1 and 3.1.2, see Engel et al., 2011 for a review). This creates a cone of light on the ground which can be detected using large telescopes with segmented mirrors to reflect the Cherenkov light to the photon detector. From this detection, the arrival direction and energy of the primary particle can be determined. This method is known as the imaging air Cherenkov technique (Porter and Weekes, 1977). These Imaging Atmospheric Cherenkov Telescopes (IACTs, i.e. H.E.S.S., MAGIC, VERITAS, CTA) have a field of view of a few degrees and can only be operated at night time, but provide high resolution. Another technique involves using water tanks at high altitude (Weekes, 1988; Amenomori et al., 1990). As particles pass through the water they emit Cherenkov light which is recorded by photon detectors. These detectors (i.e. HAWC) have a wide field of view and are used over a 24 hour period, with sensitivity to γ-rays in the GeV to TeV energy range, however, have a poorer resolution than IACTs (Sinnis, 2009).

A shower is also produced when a CR enters the Earth's atmosphere. Figure 3.2 shows the lateral spread is larger and more irregular for hadronic air showers, compared to a shower initiated by a γ-ray. This is due to secondary particles in the hadronic component receiving a higher transverse momentum leading to a larger lateral extent (Hillas, 1996). Air showers initiated by hadrons contain various secondary particles such as pions, muons and neutrinos which are not present in γ-ray initiated showers (as shown in Section 3.1.1 and Section 3.1.2). These multi-particle processes lead to further fluctuations and makes them irregular compared to γ-ray air showers which are dominated by three particle types. These differences allow γ-ray and hadron initiated showers to be distinguished from one another with use of computer simulations i.e. Monte Carlo simulations with CORSIKA (Heck et al., 1998).

Gamma-ray shower   **Hadronic shower**
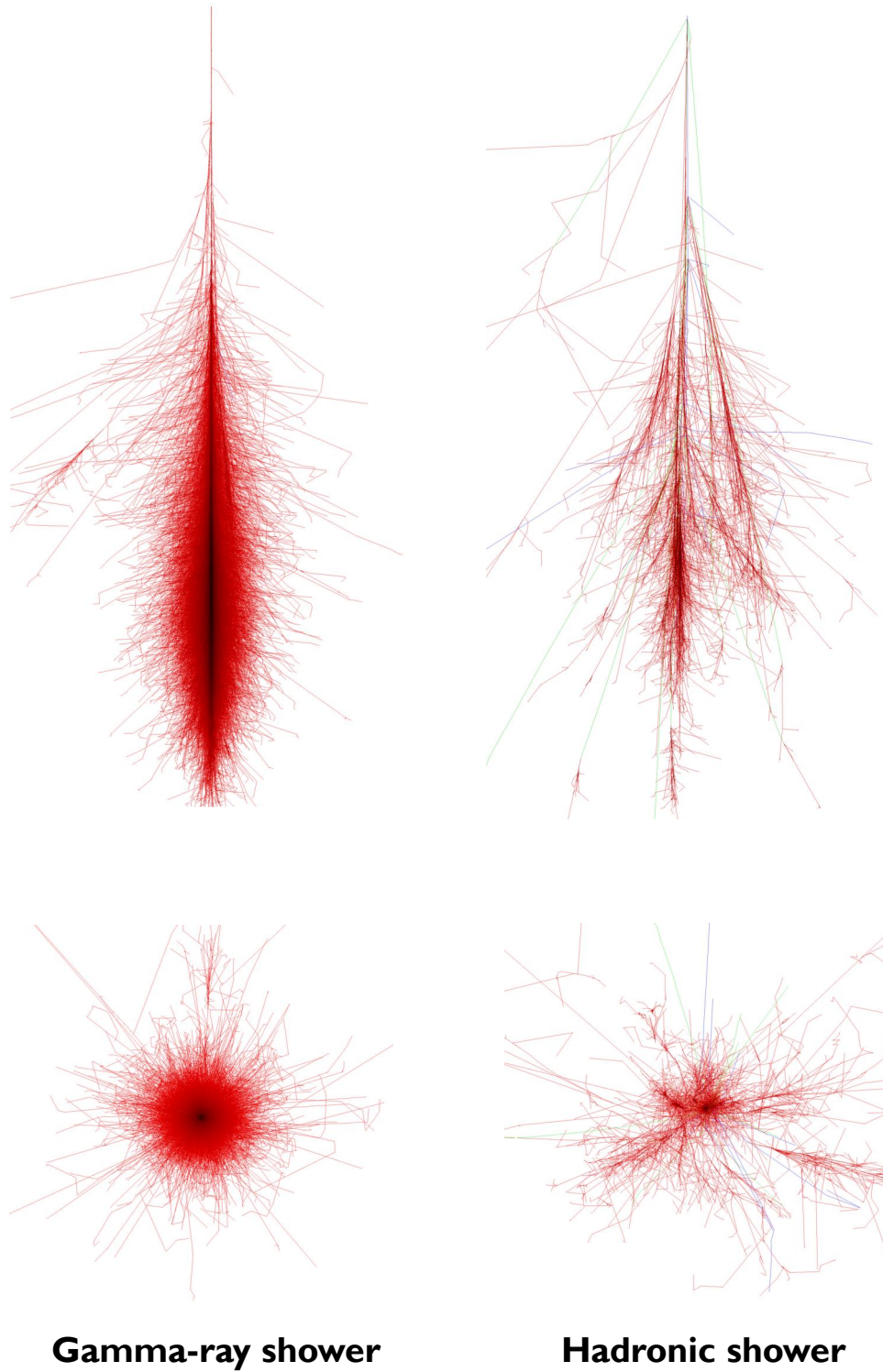
Figure 3.2: Simulated extensive air showers initiated by a 1 TeV γ-ray (left) and 100 GeV proton (right). The particle type is shown by its track colour. Red is for electrons, positrons and γ-rays, green is for muons and blue is for hadrons (i.e. protons). *Top*: the x-z plane showing the vertical axis of the shower. *Bottom*: the x-y plane, where the x and y axes are perpendicular to the shower direction. Image from Schmidt, 2021.

3.1.1   Electromagnetic Extensive Air Showers

Many ground-based telescope systems, such as H.E.S.S., are classified as IACTs which employ the use of the stereoscopic atmospheric imaging technique to detect TeV γ-rays (Porter and Weekes, 1977). As a primary γ-ray enters and interacts with the Earth's upper atmosphere, it undergoes pair production to create a positron-electron pair. Over the next radiation length these particles undergo Bremsstrahlung from the interaction of the positron-electron pair with atmospheric nuclei to create more secondary photons (γ-rays), which in turn allows pair production to occur again, restarting the whole process and creating a cascade of particles, known as an electromagnetic cascade (see Equation 3.1). This process continues to grow exponentially, deep into the atmosphere, until the energy of the particles reaches some critical energy, E_c. At this energy the ionisation losses begin to dominate over the Bremsstrahlung energy loss, and the number of photons will no longer increase, hence terminating the shower (see Heitler, 1954; Matthews, 2005 for further information). Electromagnetic air showers can also be initiated by an electron/positron, in which γ-rays are produced through Bremsstrahlung as described by Equation 3.1.

$$
\begin{aligned}
e^{\pm} + N &= e^{\pm} + N + \gamma \\
\gamma + N &= e^{+} + e^{-} + N
\end{aligned}
\tag{3.1}
$$

A simplified model of an electromagnetic cascade was introduced by Heitler, 1954. In his model, it is assumed that the cascade of particles consists of only Bremsstrahlung and positron-electron pair production, and the interaction length of these is equal. In reality, the interaction length of Bremsstrahlung is equal to 7/9 th's of the interaction length of pair production. The Heitler model is therefore within approximately 20% of the true case. The Heitler model ensures that both pair production and Bremsstrahlung grow at the same rate, making it possible to clearly see each interaction in the shower, as shown in Figure 3.3.

The number of particles, N, in the electromagnetic cascade is (Heitler, 1954):

$$
N = 2^n \, ,
\tag{3.2}
$$

where the number of interaction lengths is n. The energy of a particle in the cascade, E_n, is calculated using the energy, E_0, of the particle which initiated the Extensive Air Shower (EAS, see Equation 3.3).

$$
E_n = E_0/N
\tag{3.3}
$$
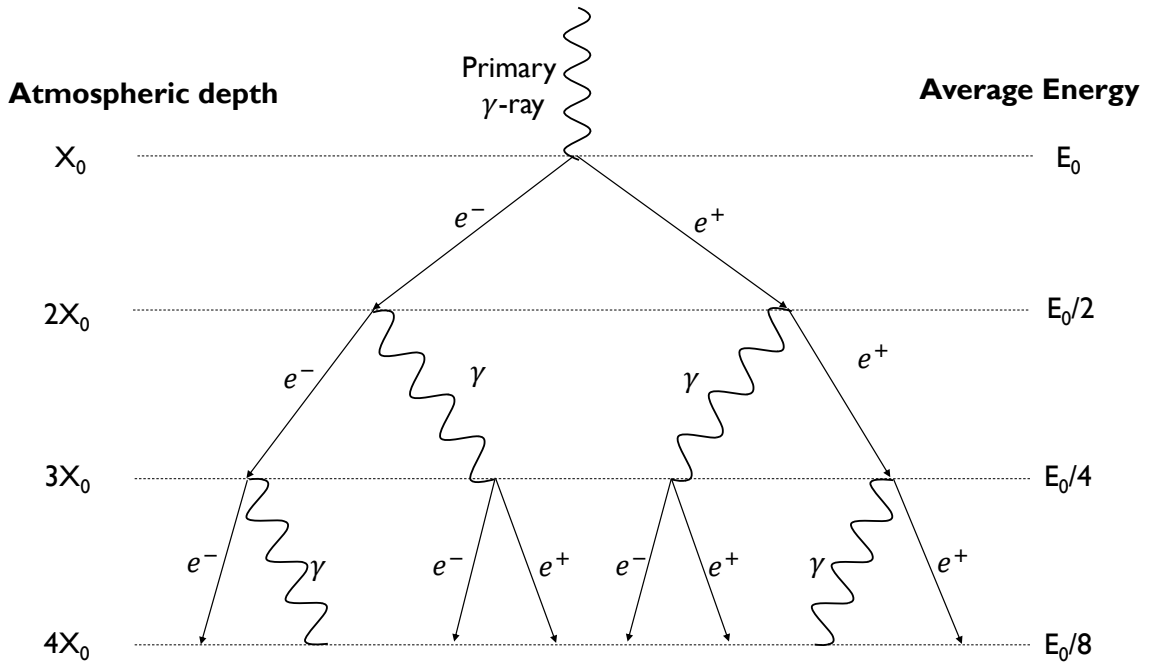
Figure 3.3: Sketch of an electromagnetic cascade according to the Heitler model (Heitler, 1954). The interaction length is given by X_0, four interaction lengths are shown here. The primary γ-ray has initial energy, E_0. The average energy of each particle changes according to this initial energy.

The maximum depth of particles in the shower is $X_{\mathrm{max}} = nX_0$, where X_0 is the interaction length. Using this information, along with Equation 3.2, gives the maximum number of particles in the cascade in terms of the maximum depth (Heitler, 1954):

$$N_{\mathrm{max}} = 2^{\frac{X_{\mathrm{max}}}{X_0}} \; . \tag{3.4}$$

The maximum number of particles can also be expressed as:

$$N_{\mathrm{max}} = \frac{E_0}{E_{\mathrm{c}}} \tag{3.5}$$

Combining these gives an expression for the maximum shower depth (Equation 3.6), in terms of the initial γ-ray energy, E_0, and critical energy, $E_{\mathrm{c}} = 86\,\mathrm{MeV}$ in air (Engel et al., 2011).

$$X_{\mathrm{max}} = \frac{X_0 \ln\left(\frac{E_0}{E_{\mathrm{c}}}\right)}{\ln\left(2\right)} \tag{3.6}$$

3.1.2   Hadronic Extensive Air Showers

In addition to EAS initiated by γ-rays, the initial particle interacting with the Earth's upper atmosphere could be hadronic in nature. Air showers initiated by a hadron lead to further secondary particles such as muons, pions, and nucleons, which differ from the electromagnetic air showers discussed previously (see Matthews, 2005, for the generalised Heitler model for hadronic showers). The initial hadron interacts with protons in the atmosphere, leading to a proton-proton interaction which produces neutral and charged pions. The neutral pions, π^0, go on to create γ-rays, which decay to produce an electron-positron pair, known as the electromagnetic component (see Figure 3.4 and Equation 2.19, Martin and Shaw, 2009). The charged pions, $\pi^{\pm}$, decay into a pair of muons and neutrinos, these decay again to produce neutrinos, positrons, and electrons (see Equations 2.20 and 2.21) this is called the mesonic component. The hadronic component comes from the primary hadron colliding with a nucleon in the atmosphere and creating a high-energy nucleon, N, which decays into protons and neutrons. These hadronic components have a longer interaction length than the electromagnetic air showers, so the sub-shower can reach a deeper point in the atmosphere.
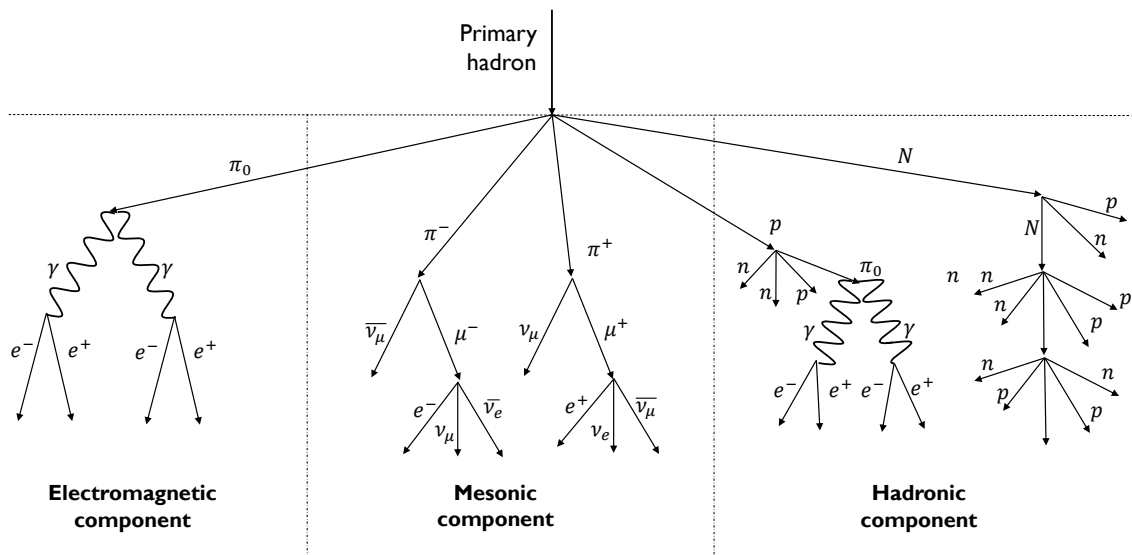
Figure 3.4: Sketch of a hadronic extended air shower. This shower contains three components: electromagnetic, mesonic and hadronic. Image adapted from Haungs et al., 2003.

3.1.3   Cherenkov Radiation and Imaging

The shower of charged particles described in Sections 3.1.1 and 3.1.2 move faster than the local velocity of light, and emit Cherenkov radiation (Čerenkov, 1934). This radiation peaks in the UV band to create a faint blue light. As the charged particles propagate, they temporarily polarise the atoms in the medium. Pulses of electromagnetic radiation are emitted as the polarised molecules oscillate to restore equilibrium. If the velocity of the charged particles is less than the local speed of

light ($v < c/n$, where n is the refractive index of the medium, in this case air) radiation is not detected as the pulses interfere with one another destructively. If the velocity is greater than the speed of light in the medium ($v > c/n$), then the pulses constructively interfere. This effect is analogous to a sonic boom (Jennings, 1962). The Cherenkov light from a single particle creates a forward cone, which is demonstrated through the Huygens construction of the track pulse (wavelet) in Figure 3.5.
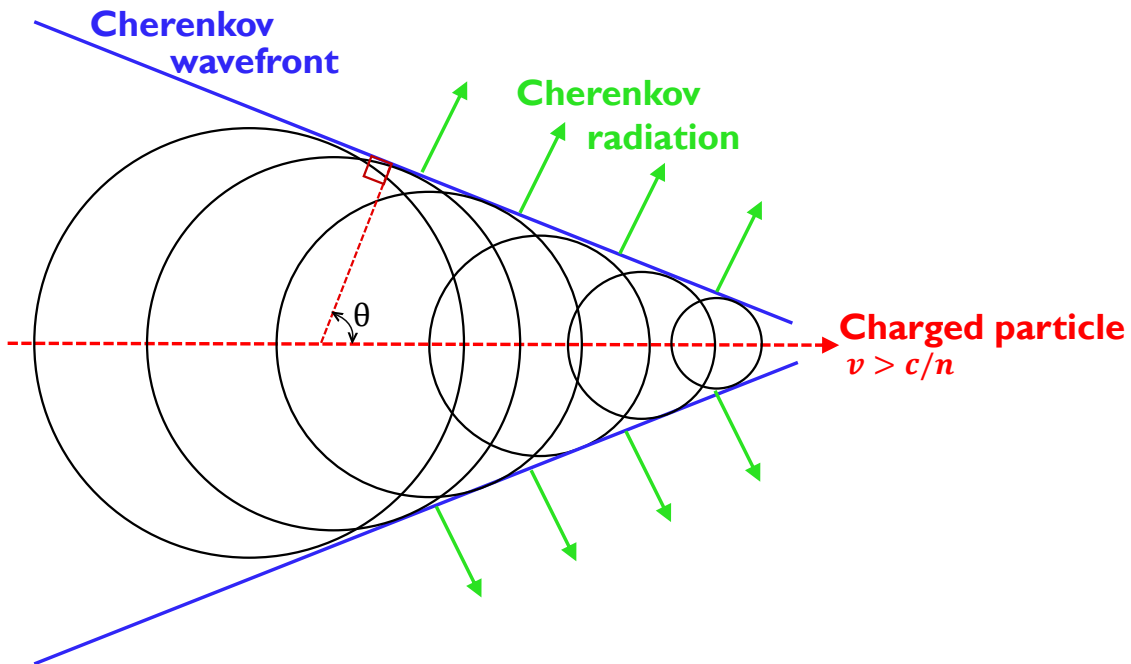
Figure 3.5: Sketch of Huygens construction of wavelets to show how the Cherenkov light wave-front forms due to constructive interference, where the charged particle moves at a velocity of $v > c/n$. The angle between the charged particle's propagation direction and the Cherenkov wavefront is θ. Image adapted from Jelley, 1958.

The cosine of angle of the Cherenkov light cone relative to the particles trajectory, θ, for $v > c/n$ is (Čerenkov, 1934):

$$\cos(\theta) = \frac{1}{\beta\,n}\,, \tag{3.7}$$

where $\beta = v/c$, c is the speed of light, n is the refractive index of the medium and v is the velocity of the particle. In the ultra-relativistic limit ($\beta \to 1$) we find $\theta_{\max} = \arccos(1/n)$. For the atmosphere, where the refractive index is roughly $n \sim 1.0003$ at sea-level, the maximum angle is $\theta \sim 1.3°$ (Jennings, 1962).

For a single particle that emits Cherenkov radiation, it will have a forward light cone covering an angle of $\sim 1°$, slowly increasing as the particle travels downwards (Völk and Bernlöhr, 2009). The amount of Cherenkov light generated by the electromagnetic cascade illuminates the ground below to create a light pool. This often has a radius of approximately $125\,\mathrm{m}$ for a primary γ-ray of $\sim 100\,\mathrm{GeV}$ (Hofmann, 2012a,

as depicted in Figure 3.6). As the primary particle energy increases so too does the radius of the light pool. The light pool can be up to 1 km in radius, achieved with high energy particles and a large zenith angle. For an initial γ-ray of TeV energy, there are approximately one hundred photons per square metre arriving at ground level.
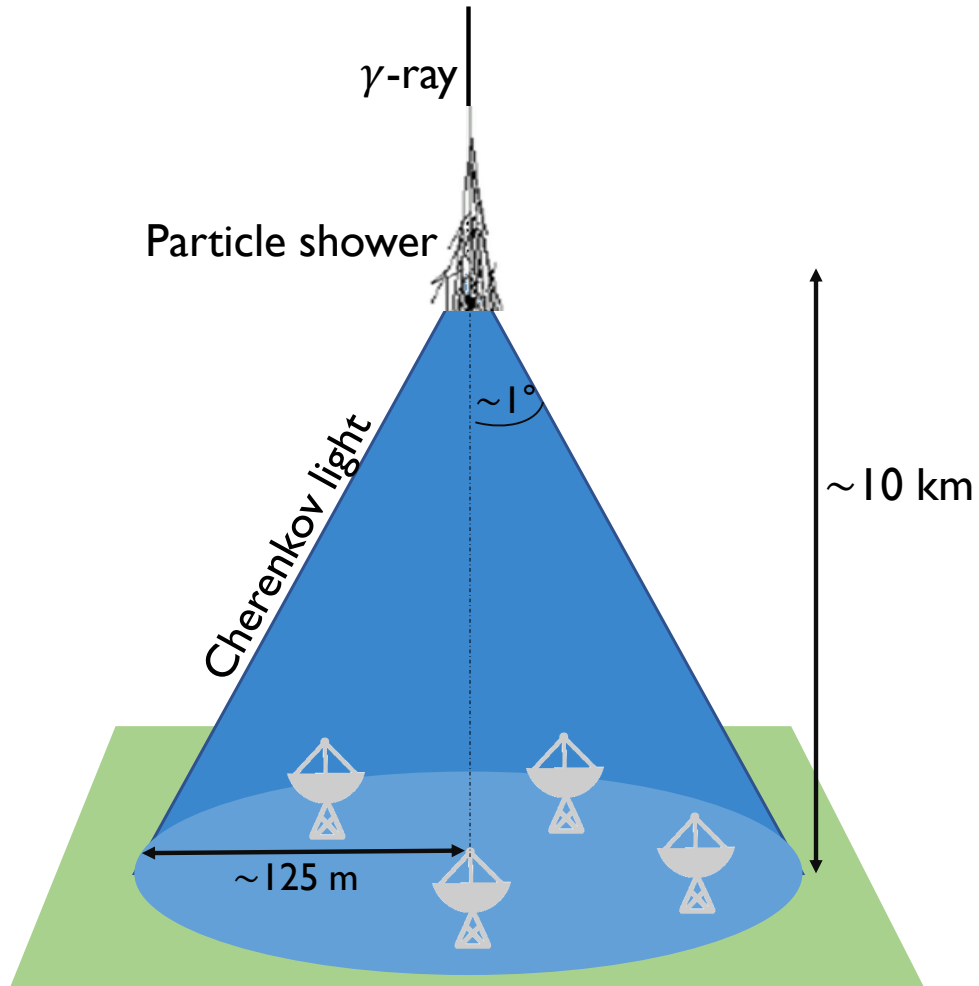
Figure 3.6: Cherenkov light pool with diameter of 250 m, as generated by a $\sim$100 GeV γ-ray entering the Earth's atmosphere. The telescopes detect any γ-ray events which fall within the light pool. Image adapted from Hofmann, 2012a.

The optical/UV component of Cherenkov radiation emitted can be viewed at ground level by the telescope (Völk and Bernlöhr, 2009). IACTs use spherical or parabolic reflectors which are comprised of mirrors to focus the light to an array of photon detectors (e.g. photomultiplier tubes, PMTs), to form an image at the focal plane (camera position, see Figure 3.7). This is known as the camera image. The PMTs convert the number of incident photons to photoelectrons[1], hence digitising the output as a number of counts with an analog-to-digital converter (ADC). The ADC digitises the analogue pulse from the PMTs by integrating over the height of the pulse over a given time (Konopelko, 2005).

---

[1]Equivalent conversion of one photon to an electron.
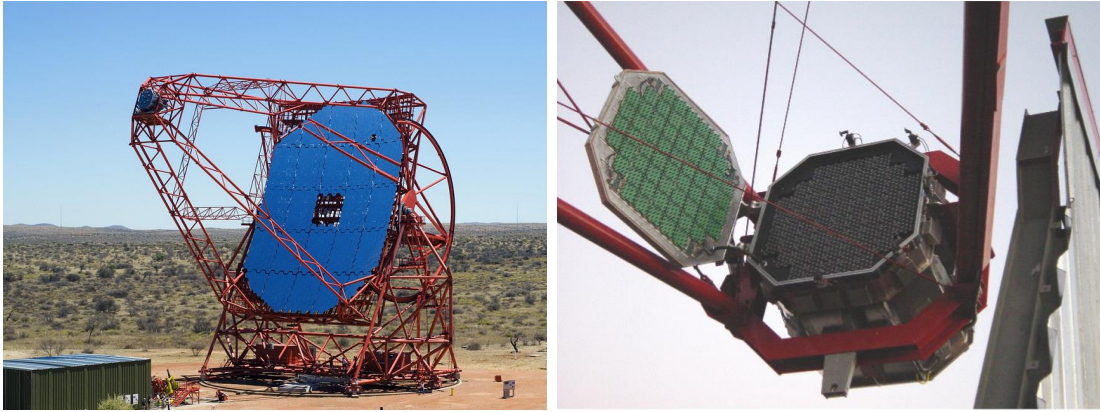
Figure 3.7: IACT: mirror dish with camera located at the focus of these mirrors (left) and the camera containing the PMTs (right). Image credit: H.E.S.S. Collaboration, Frikkie van Greunen, 2012.

Using a multi-telescope array allows for multiple views of a shower (see Figure 3.8, described as a 'stereoscopic' view) which allows for better reconstruction of the energy and direction of the primary particle. It also improves angular resolution and reduces backgrounds, for example, a shower induced by CRs, which is far more complex and isotropic leading to better gamma-hadron separation (Aharonian et al., 1997b). Many IACTs, such as H.E.S.S., utilise this stereoscopic approach, hence requiring a shower to trigger a minimum of two telescopes for the cascade event to be recorded (Mirzoyan et al., 1994). A reconstruction of the initial direction and energy of the primary γ-ray is performed from the information obtained about the intensity and shape of the Cherenkov image in each camera (Hillas, 1985).
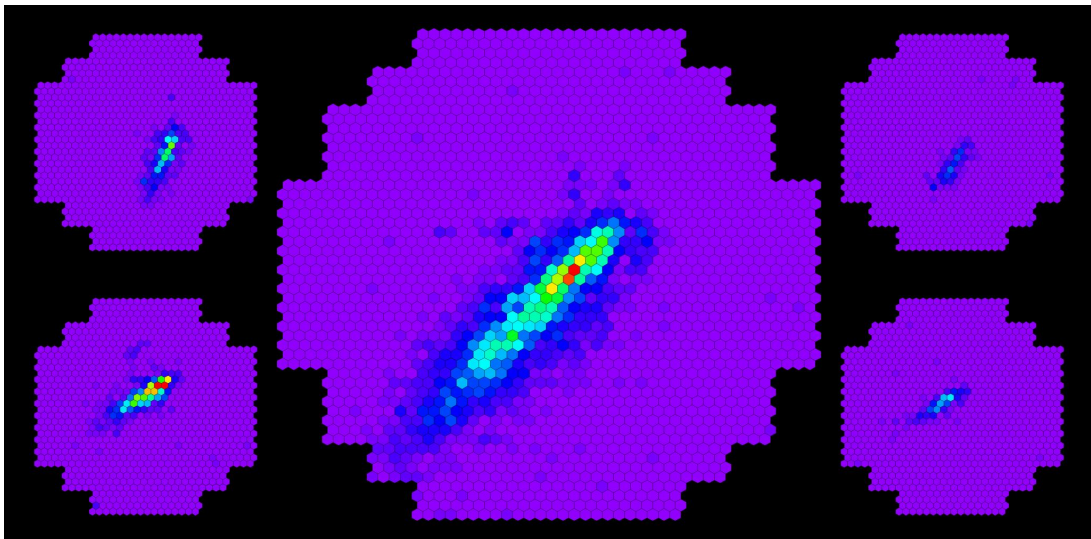
Figure 3.8: Cherenkov light images of an air shower induced by a γ-ray, as captured by photon detectors in five telescopes. The intensity of the image is related to the energy of the γ-ray. Image from Hofmann, 2012b.

Figure 3.9 shows a schematic of a set of Cherenkov images of an air shower. The Cherenkov images are parametrised by an ellipse, which is described by the 'Hillas

parameters' (Hillas, 1985), namely the width and length which are determined by taking the second moment along the minor and major axes of the shower ellipse, respectively. The arrival direction and impact distance of the air shower can be reconstructed geometrically. The source position in this model is determined by the angular separation, θ, from the reconstructed source position. The energy of the initial γ-ray is estimated from the reconstructed shower images (Hillas, 1985).
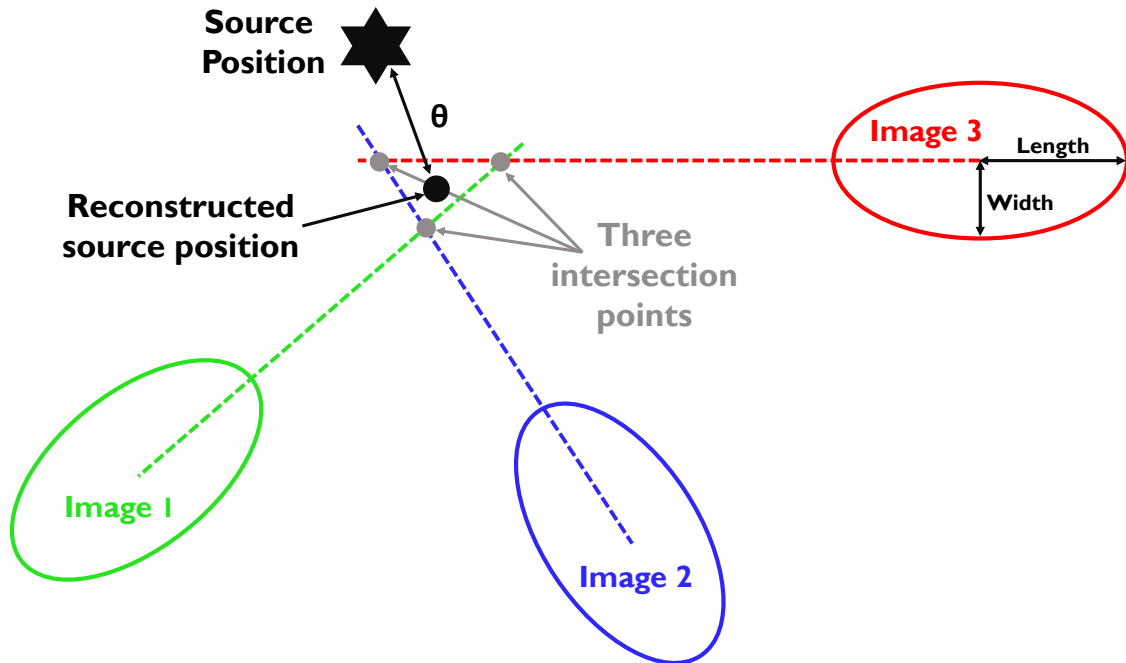
Figure 3.9: Sketch of the geometric direction reconstruction from three Cherenkov images. The shower images in the camera are illustrated by an ellipse. The major axis of each ellipse is used to determine the reconstructed arrival direction. The parameter θ is the angular offset between the reconstructed event direction on the sky and the true source position on the sky. Image adapted from Hofmann et al., 1999.

3.1.4 *Fermi* Gamma-ray Space Telescope

The *Fermi* gamma-ray space telescope is an all-sky high-energy γ-ray telescope in low Earth orbit (at an altitude of 550 km). Its main instrument is the Large Area Telescope (hereafter *Fermi*-LAT), which covers an energy range from below 20 MeV to above 300 GeV (Atwood et al., 2009). Its secondary instrument is the Gamma-ray Burst Monitor (GBM), which aims to detect bursts with a photon sensitivity as low as 8 keV. The energy range of *Fermi*-LAT overlapping with the H.E.S.S. energy coverage means the two complement each other well. *Fermi*-LAT has a large field of view, such that it can survey 2.4 steradians at 1 GeV, with a resolution of 1 arcminute (Atwood et al., 2009). This large coverage is one advantage of space-based γ-ray telescopes, however, it is not possible for *Fermi*-LAT to detect very high energy γ-rays due to their low flux, and the small collection area of the telescope.

Fermi-LAT comprises of four subsystems that are used to detect γ-rays, whilst rejecting the background CRs (as described in Atwood et al., 2009, and summarised here). As a γ-ray enters the detector it passes through the 'Anticoincidence Detector (ACD)', converting the γ-ray into an electron-positron pair through pair production. The 'Tracker' measures the path of the electron-positron pair which is produced from the primary γ-ray (see Figure 3.10) using silicon strips. From here the arrival direction of the γ-ray is determined. The energy of the particles is measured by the 'Calorimeter', which is also used to reject CRs due to their distinctly different energy deposition pattern compared to γ-rays. The ACD produces a signal only when hit by charged particles i.e. CRs, sending a message to the 'Data Acquisition System (DAQ)' to reject that signal. The ACD therefore rejects any signals produced by CRs, with an efficiency of 99.97% (Atwood et al., 2009).
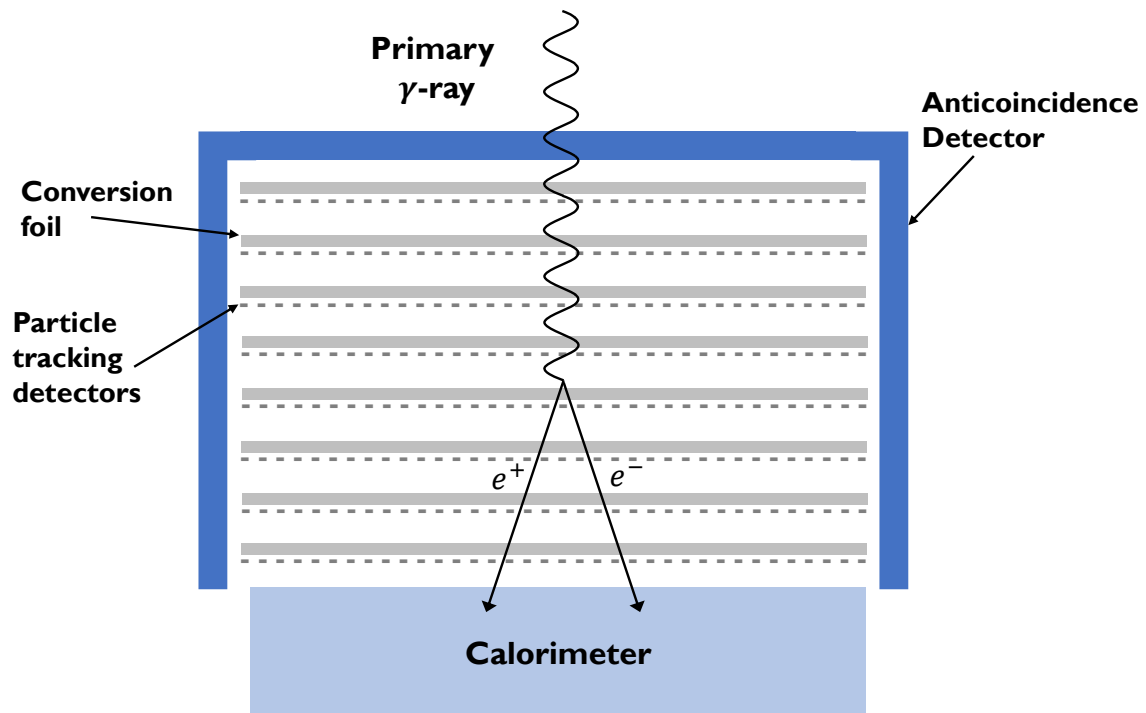
Figure 3.10: Simplified 2D schematic of the *Fermi*-LAT detector showing the conversion from an electron-positron pair to γ-ray. Image adapted from Atwood et al., 2009.

Fermi was launched in 2008, initially named the Gamma-ray Large Area Space Telescope (GLAST), until NASA renamed it to *Fermi*, to honour Enrico Fermi, who introduced the theory on the acceleration of charged particles (see Section 2.2.2). Since then, it has provided many source catalogs available at `https://fermi.gsfc.nasa.gov/ssc/data/access/`. The catalogs utilised throughout this thesis include the Extended Sources in the Galactic Plane (FGES) catalog (Ackermann et al., 2017), and the Third Catalog of Hard *Fermi*-LAT Sources (3FHL, Ajello et al., 2017). The FGES includes 6 years of the most recent *Fermi*-LAT data covering an energy range from 10 GeV to 2 TeV for low Galactic latitude sources ($\pm 7°$). It is the first catalog of extended sources, with spectral and morphology characteristics described for 46 sources. The 3FHL uses the first 7 years of *Fermi*-LAT data in the same energy range as the FGES catalog and contains 1556 objects. The lower

limit of 10 GeV for both catalogs allows for a narrow PSF of less than 0.2°. The 3FHL contains twice as many sources above 10 GeV than the previous 2FHL which detected sources above 50 GeV (Ajello et al., 2017).

The region surrounding the source of interest in this thesis HESS J1804−216 is shown in the *Fermi*-LAT sky map in Figure 3.11. The GeV γ-ray source of interest here is FGES J1804.8−2144 (also designated 3FHL J1804.7−2144e). This source has a disk radius of 0.38° with its centroid coinciding with HESS J1804−216 (Ackermann et al., 2017).
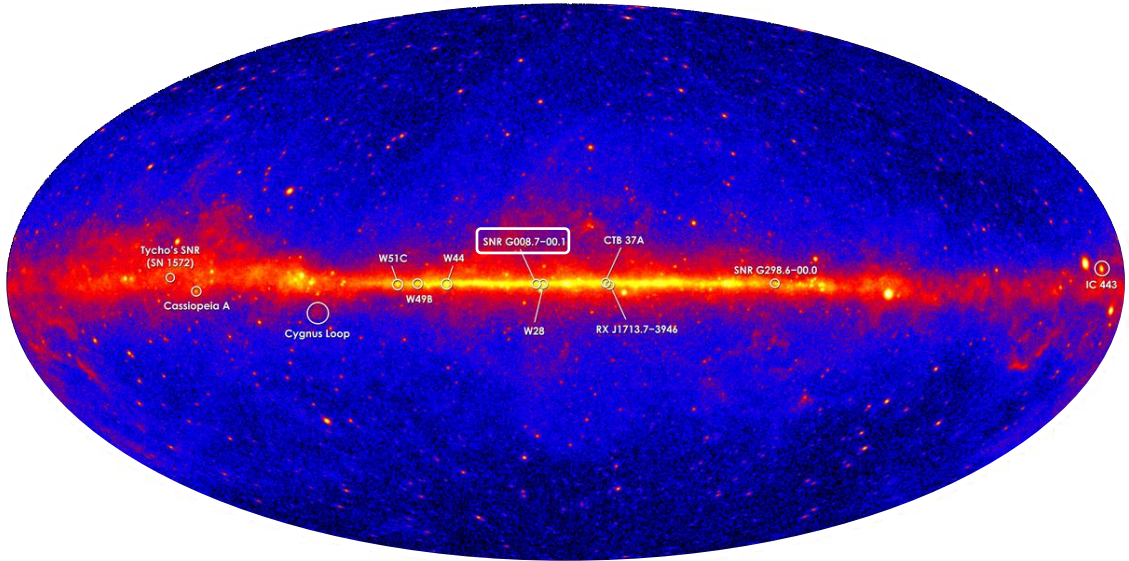
Figure 3.11: *Fermi*-LAT 5 year image of γ-rays above 1 GeV. The white circle in the centre of the image indicates SNR G8.7−0.1 which is close by to HESS J1804−216. Image adapted from NASA/DOE/Fermi LAT Collaboration, 2013.

3.1.5 High Energy Stereoscopic System

Ground-based telescopes have been extremely useful in detecting TeV γ-rays. H.E.S.S. is one of the many telescope arrays in operation, located in the Khomas Highlands of Namibia, at an altitude of ∼1.8 km. Whilst the name is an acronym it was also chosen to honour Victor Hess, who discovered cosmic radiation in 1912 and later in 1936 was awarded the Nobel Prize for the discovery. H.E.S.S. consists of an array of five telescopes (as shown by Figure 3.12); four identical telescopes (Phase I) with a 12 m mirror diameter and one larger telescope (Phase II) in the centre of the array with a 28 m mirror diameter. H.E.S.S. is sensitive to γ-rays of energy tens of GeV to ∼100 TeV. The five telescopes work in conjunction with one another to detect Cherenkov light that originates from EAS. The original survey covered the inner Galactic Plane from ±3° latitude (*b*) and ±30° longitude (*l*) conducted in 2005. However, the current range has been extended to $b = \pm 3.5°$ and $l = 250°$ to 65°.
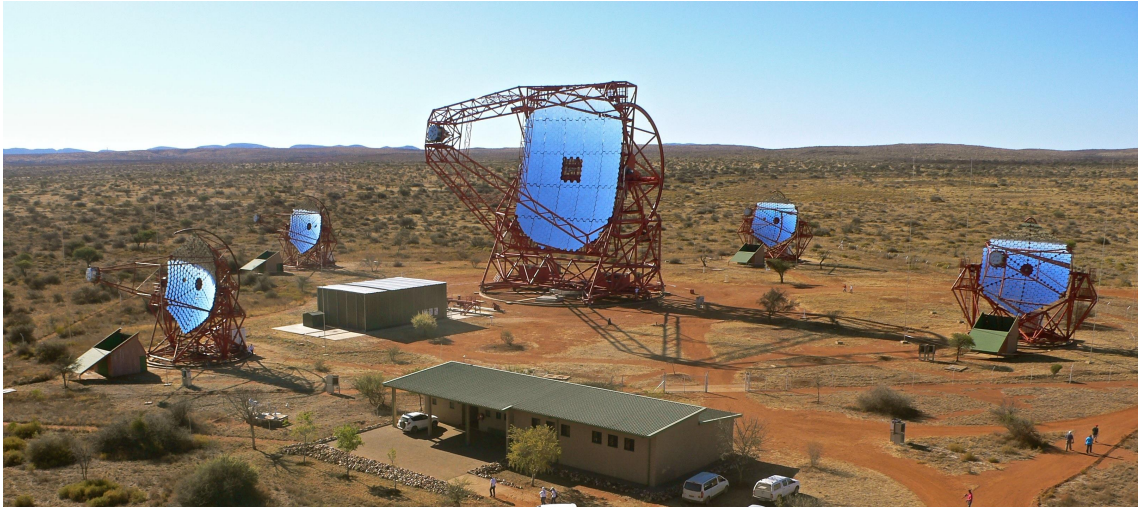
Figure 3.12: H.E.S.S. array of telescopes; four smaller telescopes and one larger telescope located in the centre of the array. Image credit: H.E.S.S. Collaboration, Clementina Medina, 2012.

The Phase I telescopes (CT1-4) are set on an alt-azimuth mount so that they can view all points in the sky. This is composed of a base frame to adjust the elevation and a dish, which are both driven by a computer to track any object in the sky. Each telescope is made up of 382 spherical mirrors which are positioned to create a hexagonal shape. An energy threshold of $\sim 100\,\mathrm{GeV}$ is obtained for Phase I, along with an angular resolution of $< 0.1°$ for individual γ-rays (Bernlöhr et al., 2003). To detect 5% of the Crab Nebula flux at a significance of 5σ above the CR background, it takes only one hour of observations.

Phase II is a single dish (CT5) positioned at the centre of the array, with 875 mirrors, which also adopts an alt-azimuth mounted dish. This telescope has a total mirror area of $\sim 600\,\mathrm{m}^2$, which has an equivalent area to two tennis courts. The size of the telescope allows for greater energy coverage, sensitivity, and angular resolution. Phase II has a lower energy threshold allowing coverage over a wider energy range in addition to improved sensitivity above the $100\,\mathrm{GeV}$ of Phase I (Cornils et al., 2005).

H.E.S.S. has been used to survey and detect Galactic TeV γ-ray emitters to create the H.E.S.S. Galactic Plane Survey (HGPS, H.E.S.S. Collaboration et al., 2018). This incorporates data from January 2004 to January 2013. It was found that TeV γ-ray sources are often also the sites of CR accelerators. The population of these sources are dominated by objects within their final stages of stellar evolution. The most common being supernova remnants and pulsar wind nebulae powered by pulsars (H.E.S.S. Collaboration et al., 2018). A large portion of the sources discovered, however, are still unidentified (shown in Figure 2.3), meaning there has been no confirmation of the counterpart which powers the source. The Crab Nebula is a large TeV γ-ray source, which has been detected with different instruments including H.E.S.S.. Due to its large flux and stable emission, it has become a reference for various γ-ray detection methods.

The source of interest in this thesis is HESS J1804$-$216. Like many of the detected H.E.S.S. sources, HESS J1804$-$216 is an unidentified source located along the Galac-

tic plane (Aharonian et al., 2006c). A detailed analysis of the interstellar medium (ISM) towards HESS J1804−216, as well as the modelling of the γ-ray emission from HESS J1804−216 is presented here, in order to help find the origin of the TeV γ-rays from HESS J1804−216. HESS J1804−216 is circled in green in Figure 3.13, which shows the statistical significance for the HGPS, which is given by the standard deviation above the CR background.
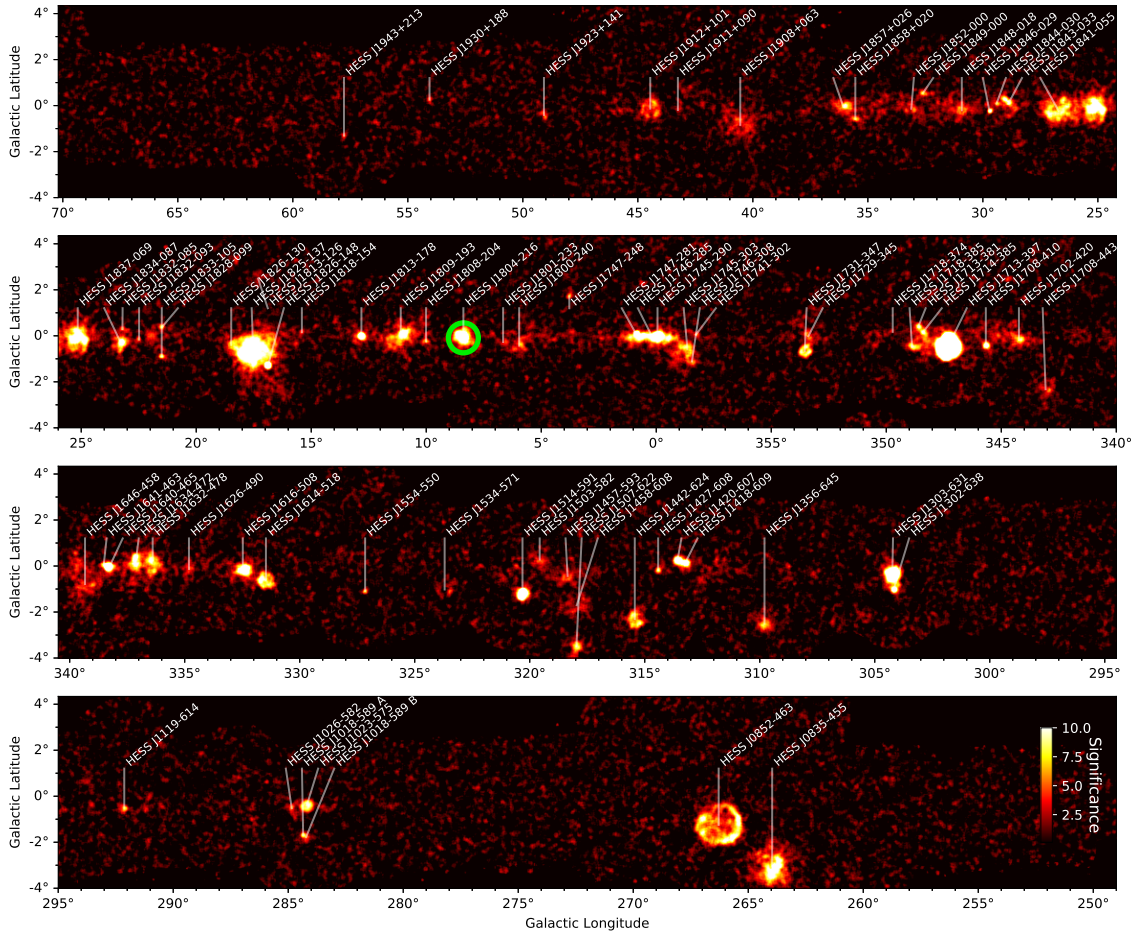
Figure 3.13: Significance map of sources from the H.E.S.S. Galactic Plane Survey. The green circle indicates the source of focus for this thesis, HESS J1804−216. Image adapted from H.E.S.S. Collaboration et al., 2018.

3.1.6 Cherenkov Telescope Array

Future γ-ray observations will be taken by the next-generation ground-based observatory, the Cherenkov Telescope Array (CTA). CTA will consist of over 100 IACTs located both in the Southern (Chile) and Northern (La Palma) Hemisphere to allow for full sky coverage (locations shown in Figure 3.1, CTA Consortium et al., 2018). The array will consist of three different sized telescopes to allow for large energy coverage; small-sized telescopes (SSTs), medium-sized telescopes (MSTs), and large-sized telescopes (LSTs). The current official configuration known as the Alpha configuration will consist of 4 LSTs and 9 MSTs at CTA-North and 14 MSTs and 37 SSTs at CTA-South (CTA Collaboration, 2021). Figure 3.14 shows a rendered

image of the north and south sites. The SSTs are for detecting the highest energy γ-rays (few TeV to 300 TeV), the MSTs for the mid-range energy γ-rays (100 GeV to 10 TeV) and the LSTs will detect the lowest energy γ-rays ($\sim$20 GeV to 200 GeV).
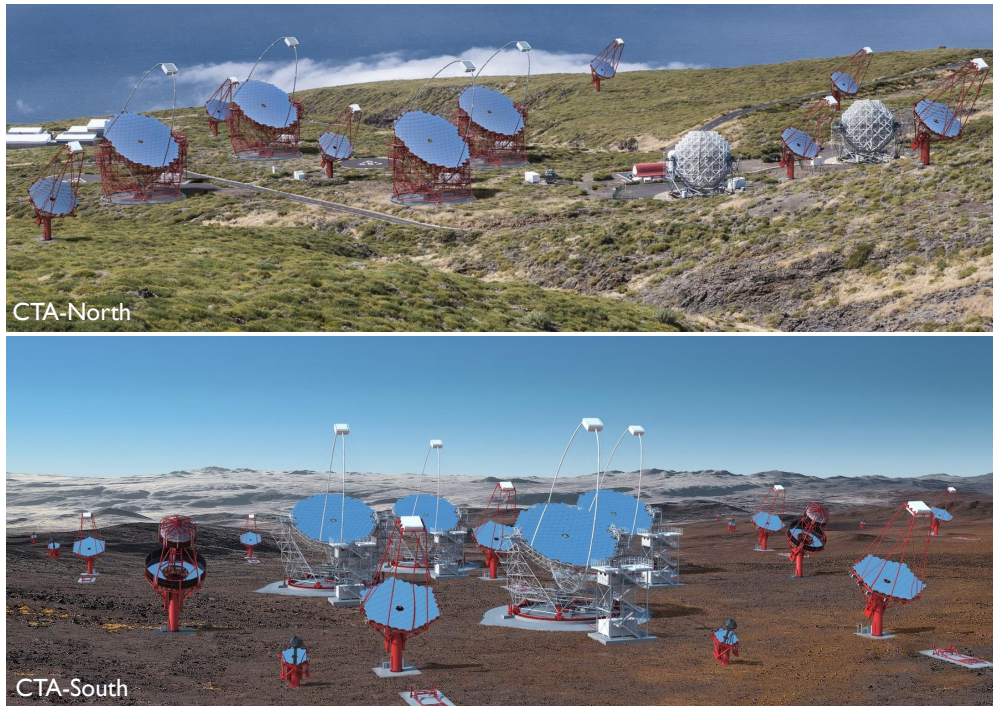
Figure 3.14: A rendered image of the CTA-North site (top, image credit: IAC, Gabriel Pérez Diaz, 2017) and CTA-South site (bottom, image credit: IAC, Gabriel Pérez Diaz and CTAO, Marc-André Besel, 2015).

The LSTs have an alt-azimuth mount, with a 23 m diameter parabolic mirror. It has a very large surface area of 400 m^2, with a height of 45 m. Despite its large design, it will be able to move quickly taking $\sim$20 seconds to re-position, which is a critical component in studying Galactic transients, high redshift active galactic nuclei, and γ-ray bursts (CTA Consortium et al., 2018). The first CTA LST telescope was completed in 2018 at the North Site, in the Canary Islands. The MST will be a modified Davies-Cotton telescope on a polar mount, with a mirror of 12 m diameter. The SST configuration is a dual-mirror Schwarzschild-Couder telescope, consisting of a 4.3 m diameter primary mirror with hexagonal-shaped mirror facets and a secondary mirror of 1.8 m diameter (CTA Collaboration, 2016).

CTA will achieve much better efficiency and sensitivity than the existing ground-based γ-ray instruments, providing higher angular resolution, and energy and directional analysis, see Figure 3.15. The higher sensitivity and angular resolution of CTA will provide a more detailed look into the many unidentified γ-ray sources. See CTA Consortium et al., 2018 for further information on the science goals for CTA.
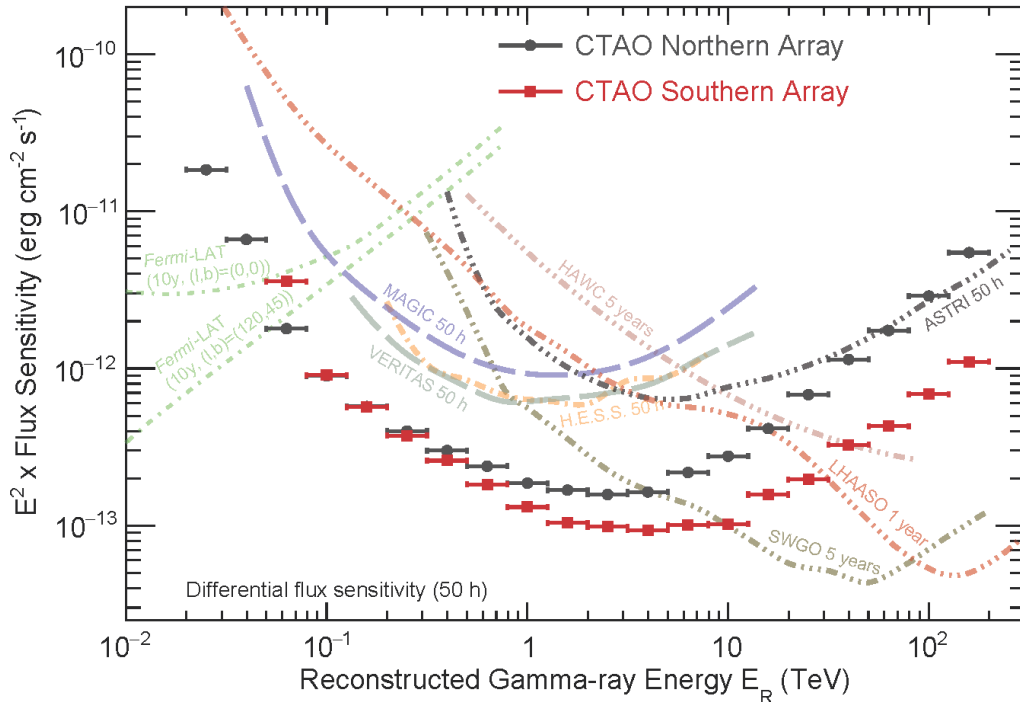
Figure 3.15: The CTA differential flux sensitivity for point-like sources, as compared to other current γ-ray instruments. The black and red curves show the performance for an observation time of 50 hours for CTA-North and CTA-South, respectively. These curves are a factor of five to ten better than other arrays depending on the energy range. Image from CTA Collaboration, 2021.

3.2 Radio Spectral Line Astronomy

In 1932 Karl Jansky first discovered radio waves through the use of a rotating antenna. These were recorded as peaks which had a specific period. Since this, the radio band of the electromagnetic spectrum has been studied closely. The detection of radio emission towards different objects in the Milky Way galaxy has allowed us to learn more about the important processes occurring near or in these objects. The spectral line emission from various atoms and molecules in the ISM are typically within the millimeter band of the electromagnetic spectrum. This section discusses the different radio telescopes used to obtain data from the ISM.

3.2.1 Mopra

Located near Coonabarabran in New South Wales, Australia, is the Mopra Telescope (see Figure 3.16, Ladd et al., 2005). Mopra is a radio millimetre band telescope primarily used to survey the southern Galactic plane for carbon monoxide (CO). It surveys the four CO isotopologue lines simultaneously (^{12}CO, ^{13}CO, C^{17}O & C^{18}O, Braiding et al., 2015). It was operated by the CSIRO (Commonwealth Scientific and Industrial Research Organisation) and is part of the Australia Telescope National Facility (ATNF). From 2013 to 2019 it was operated by external groups. The University of Adelaide and University of New South Wales are among several institutes

which have contributed to both funding and operation, with interest in creating the Mopra Southern Galactic Plane CO Survey, which has involved multiple data releases (DR0, DR1, DR2, and DR3, shown in Burton et al., 2013; Braiding et al., 2015; Rebolledo et al., 2016; Braiding et al., 2018, respectively).
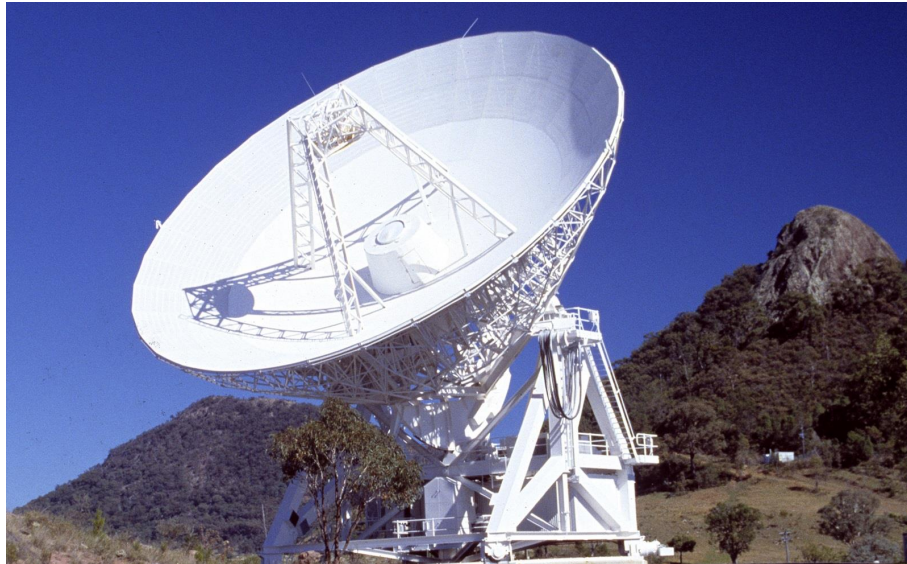
Figure 3.16: The Mopra radio telescope. Image from CSIRO, 2021a.

Mopra consists of a single dish with a 22 m diameter surface, with three different wavelength receivers. The 3 mm receiver covers the frequency range 76-117 GHz, the 7 mm receiver covering a frequency range of 30-50 GHz and a 12 mm band receiver covering a frequency range 16-27 GHz. MOPS (Mopra spectrometer) is a backend system which produces two 8 GHz intermediate frequencies (IFs) for each bandwidth channel (Urquhart et al., 2010). MOPS operates in two different configurations: 'zoom' and 'wideband'. The wideband mode consists of four overlapping sub-bands, which are 2.2 GHz wide with a total of 8096 channels per polarisation. These four sub-bands are then split into a further four zoom bands (or 'windows') to produce 16 bands in the zoom mode. In this mode, the windows are 137.5 MHz in width with 4096 channels per polarisation. Table 3.1 shows the characteristics of the Mopra telescope for each wavelength receiver.

Table 3.1: Characteristics of the Mopra telescope. The three beams with their central frequency and full-width-half-maximum (FWHM). The bandwidth and spectral resolution for both the wideband and zoom modes are also shown. Values taken from Ladd et al., 2005 and Urquhart et al., 2010.

Band	Central frequency	FWHM	Bandwidth (km/s)		Spectral Resolution (km/s)	
	(GHz)	(")	Wideband	Zoom	Wideband	Zoom
3 mm	90	36	30378	505	0.915	0.11
7 mm	42	70	56025	932	1.69	0.21
12 mm	24	120	112050	1826	3.38	0.41

3.2.2 Parkes and ATCA

The Parkes telescope is located in New South Wales, Australia just outside the town of Parkes (hence its name). Parkes (more colloquially named 'The Dish') is a radio telescope with a 64 m parabolic dish, run by the CSIRO and part of the ATNF (Staveley-Smith et al., 1996). Parkes is typically used for cm wavelengths, including surveying the sky for HI at 21 cm.

The Australia Telescope Compact Array (ATCA) is also a well-known array of radio telescopes, located in Narrabri, New South Wales, Australia. ATCA consists of six 22 m dishes, which all work together along with the use of interferometry to produce radio images in fine detail (Frater et al., 1992).

Figure 3.17: Five of the ATCA radio telescopes (left, image credit: CSIRO, David Smyth) and the Parkes radio telescope (right, image from CSIRO, 2021b).

With the use of ATCA and Parkes (see Figure 3.17), the Southern Galactic Plane Survey (SGPS) mapped the atomic hydrogen (HI) emission along the Galactic plane, for latitudes of $\pm 1.5°$ and longitudes covering 253° to 358° (SGPS I) as well as 5° to 20° (SGPS II, McClure-Griffiths et al., 2005). The data has an angular resolution of a few arcminutes with an RMS sensitivity of 1.6 K.

4 Tracing the Interstellar Medium

The good thing about science is that it's true whether or not you believe in it.

— Neil deGrasse Tyson, *American Astrophysicist*

It is vital to have a detailed understanding of the interstellar medium (ISM) surrounding a TeV γ-ray source in order to constrain its production mechanism. The radio emission from the ISM spread throughout the Galaxy is detected with various radio telescopes, such as those discussed in Section 3.2. Atomic and molecular gas can be probed by spectral line emission in order to learn more about the physical characteristics of the gas, such as density, mass, and energy, hence furthering our knowledge about different gas components towards γ-ray sources.

This chapter outlines the fundamentals of radiation transfer theory and the basics of molecular line emission. The concepts of radio astronomy and radiative theory are discussed in detail in the following books Wilson et al., 2010, Rybicki and Lightman, 1986 and Townes and Schwalow, 1955. The spectral lines used throughout this thesis are discussed in Section 4.6. These include atomic hydrogen (HI) from the SGPS survey and molecular hydrogen (H_2), detected through carbon monoxide (CO) from Mopra CO Survey.

4.1 Fundamentals of Radiation Theory

As light travels from its radiation source to Earth it can be absorbed, emitted, or scattered. In order to understand astrophysical environments and the physical properties of gas clouds, it is crucial to understand the aforementioned processes. This section outlines the concept of thermal radiation and radiative transfer.

4.1.1 Intensity, Flux and Luminosity

The specific intensity (or brightness) from direction $\hat{\Omega}$, in the frequency range from ν to $(\nu + d\nu)$ is given by:

$$I_\nu(\hat{\Omega}) = \frac{dE}{dA\,dt\,d\nu\,d\Omega} \qquad \left[\mathrm{W\,m^{-2}\,Hz^{-1}\,sr^{-1}}\right], \qquad (4.1)$$

where dE is the energy received in an area of dA over a time interval of dt from some solid angle $d\Omega$. This is depicted in Figure 4.1. The specific intensity, I_ν, gives the power emitted by some astrophysical source over some time, per area, unit frequency, and solid angle.
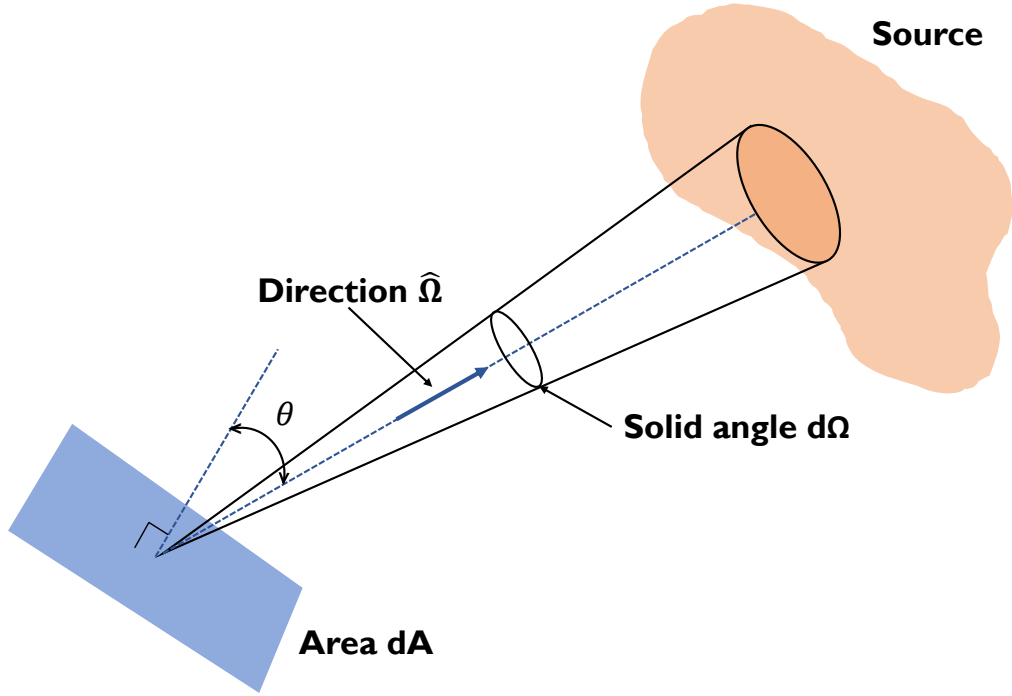
Figure 4.1: Diagram showing the radiation produced by some source, located some distance from a detector of area dA. The specific intensity, flux and luminosity of the source are given by Equations 4.1, 4.4 and 4.5 respectively. Image adapted from Rybicki and Lightman, 1986.

The specific flux, F_ν, is obtained by integrating the specific intensity, I_ν, with respect to the solid angle, $d\Omega$ (Equation 4.2). This assumes radiation is coming from some astrophysical source with an angular diameter of $d\Omega$.

$$F_\nu = \int I_\nu(\hat{\Omega}) \cos\theta \, d\Omega \tag{4.2}$$

The net flux, assuming the telescope is pointed directly towards the source $(\cos\theta \sim 1)$, is therefore:

$$F_\nu = \int I_\nu(\hat{\Omega}) \, d\Omega \qquad [\text{W m}^{-2}\,\text{Hz}^{-1}] . \tag{4.3}$$

This is simplified to Equation 4.4 for a source which has uniform intensity and subtends a small solid angle $\Delta\Omega$.

$$F_\nu = I_\nu \Delta\Omega \qquad [\text{W m}^{-2}\,\text{Hz}^{-1}] \tag{4.4}$$

The specific luminosity, L_ν, is the total radiative energy from a source, between the frequency range from ν to $(\nu + d\nu)$. The radiative energy is spread across a sphere with surface area $4\pi d^2$ where the distance is given by d. The specific luminosity for an isotropically emitting source is given by:

$$L_\nu = 4\pi d^2 F_\nu \qquad [\text{W Hz}^{-1}]. \tag{4.5}$$

By integrating I_ν, F_ν and L_ν with respect to frequency the bolometric intensity, flux and luminosity are obtained.

Assuming the flux is isotropic, this allows us to define the well known flux-luminosity relationship for a source located at a distance d from Earth (or the detector):

$$F = \frac{L}{4\pi d^2} \qquad [\text{erg s}^{-1}]. \tag{4.6}$$

4.1.2   Radiative Transfer Fundamentals

As light travels through interstellar space towards Earth it can be absorbed and emitted by the gas in the ISM, which allows us to examine the characteristics of molecular clouds. Their spectral lines can be analysed to understand the physical properties of the gas.

Radiation from some astrophysical source enters a cloud with an initial intensity of I_ν, as shown by Figure 4.2. The gas cloud can be approximated by a cylinder with length ds and cross-sectional area dA and volume $dV = dA\,ds$. The volume contains a number of absorbing particles with a number density n and absorption cross-section σ_ν. The number of absorbers is then $N = n\,dV = n\,dA\,ds$, giving an absorbing area of $N\,\sigma_\nu = n\,ds\,dA\,\sigma_\nu$. The radiation after travelling through the volume is described by $I_\nu + dI_\nu$, as shown by Figure 4.2.
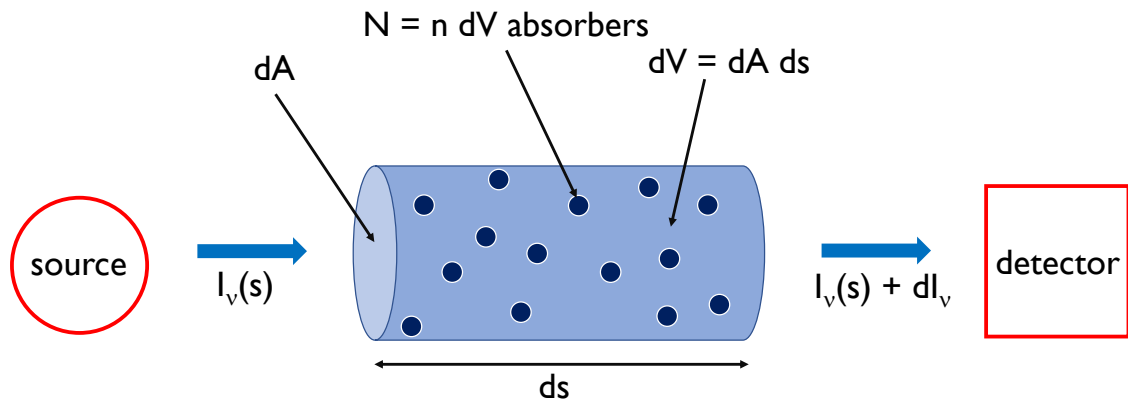
Figure 4.2: Diagram of radiation of frequency ν being absorbed by a gas cloud of length ds in the ISM. The particles in this gas column both emit and absorb the radiation, which causes a change in intensity of dI_ν. Image adapted from Wilson et al., 2010.

The equation of radiative transfer through the ISM is described by the absorption and emission coefficients, $\alpha_\nu(s)$ and $j_\nu(s)$ respectively.

$$\frac{dI_\nu}{ds} = -\alpha_\nu(s)I_\nu(s) + j_\nu(s)\,, \tag{4.7}$$

where $\alpha_\nu(s)$ (m^{-1}) is the number of absorption interactions and $j_\nu(s)$ $(\mathrm{W\,m^{-3}\,Hz^{-1}})$ is the amount of power emitted by an infinitesimal volume. The absorption coefficient for a medium with number density, n, is $\alpha_\nu = n\sigma_\nu$ for a constant absorption cross section σ_ν. The absorption mean free path is given by the inverse of the absorption coefficient, $l_\nu = \alpha_\nu^{-1} = (n\sigma_\nu)^{-1}$. This is the distance photons will travel before $\sim63\%$ $(1/e)$ are absorbed.

The absorption coefficient, however, is not directly measurable, instead the optical depth, τ_ν, defined by $d\tau_\nu = \alpha_\nu ds$ is utilised. By dividing Equation 4.7 by the absorption coefficient, the equation of radiative transfer is obtained in terms of the optical depth:

$$\frac{dI_\nu}{d\tau_\nu} = -I_\nu(\tau_\nu) + S_\nu(\tau_\nu)\,, \tag{4.8}$$

where the source function, $S_\nu(\tau_\nu) = j_\nu(\tau_\nu)/\alpha_\nu(\tau_\nu)$, describes the ratio of emitted photons to absorbed photons by the medium.

Equation 4.8 is a First Order Linear Differential Equation with solution:

$$I_\nu(\tau_\nu) = I_\nu(0)e^{-\tau_\nu} + e^{-\tau_\nu}\int_0^{\tau_\nu} e^{-\tau_\nu'}S_\nu(\tau_\nu')d\tau_\nu'\,, \tag{4.9}$$

where the first term represents the attenuation of the background intensity as it passes through the medium. The second term represents the radiation originating from the medium. If the source function, S_ν, is constant throughout the source then Equation 4.9 becomes:

$$I_\nu(\tau_\nu) = S_\nu + e^{-\tau_\nu}[I_\nu(0) - S_\nu]\,. \tag{4.10}$$

For an optically thick scenario $(\tau_\nu \gg 1)$, the medium is opaque and the observer only sees photons which are emitted from the outside regions of the medium:

$$\begin{aligned} e^{-\tau_\nu} &\to 0, \\ \therefore I_\nu(\tau_\nu) &\to S_\nu\,. \end{aligned} \tag{4.11}$$

For an optically thin scenario $(\tau_\nu \ll 1)$, the observer sees the radiation from background sources:

$$\begin{aligned} e^{-\tau_\nu} &\sim 1 - \tau_\nu + ...,\\ I_\nu(\tau_\nu) &\sim S_\nu + (1 - \tau_\nu)[I_\nu(0) - S_\nu],\\ \therefore I_\nu(\tau_\nu) &\sim (1 - \tau_\nu)I_\nu(0) = \tau_\nu S_\nu\,. \end{aligned} \tag{4.12}$$

Equation 4.10 can be expressed in term of the brightness temperature (as defined in Equation 4.19):

$$T_{\mathrm{b}}(\nu) = T_{\mathrm{s}} + e^{-\tau_\nu}[T_{\mathrm{bg}}(\nu - T_{\mathrm{s}}], \tag{4.13}$$

where T_{s} is the brightness temperature of the source and T_{bg} is the brightness temperature of the background. The common technique employed for radio astronomy is to point the telescope at both the source position (called the 'on-region') and a background region which is expected to have no signal. The brightness temperature of the background region is subtracted from the brightness temperature of the on-source position, to obtain the source signal above any background noise. Using this information, in addition to Equation 4.13, leads to the detection equation:

$$\begin{aligned} T_{\mathrm{b}}(\nu) &= T_{\mathrm{s}} + e^{-\tau_\nu}[T_{\mathrm{bg}}(\nu - T_{\mathrm{s}}] - T_{\mathrm{bg}} \\ &= (1 - e^{-\tau_\nu})(T_{\mathrm{s}} - T_{\mathrm{bg}}) \,. \end{aligned} \tag{4.14}$$

4.1.3   Thermal Radiation and Brightness Temperature

In radio astronomy, brightness temperature is a useful measure of the received intensity from a source. From our knowledge of black-body radiation using Planck's law, it is possible to derive an expression for brightness temperature (see Equation 4.19). Brightness temperature can be defined as the temperature required by an equivalent black body to match the same surface brightness.

Thermal radiation is the radiation produced by the random motion of particles. The ideal case is a black body, which absorbs all radiation incident upon it. At thermal equilibrium, the intensity of the thermal radiation for a black body is given by Planck's law:

$$B_\nu = \frac{2h\nu^3/c^2}{\exp(h\nu/kT) - 1} \,, \tag{4.15}$$

where $h = 6.626 \times 10^{-24}\,\mathrm{J\,s}$ is Planck's constant, ν is the frequency of the radiation, c is the speed of light, $k = 1.38 \times 10^{-23}\,\mathrm{J\,K^{-1}}$ is the Boltzmann constant and T is the temperature of the body. The energy flux radiated from a black body is proportional to the fourth power of the temperature of that body, which is given by the Stefan-Boltzmann law:

$$F = \sigma T^4 \,, \tag{4.16}$$

where $\sigma = 5.67 \times 10^{-8}\,\mathrm{W\,m^{-2}\,K^{-4}}$ is the Stefan-Boltzmann constant. In a region of

thermodynamic equilibrium Kirchoff's law is applicable:

$$B_\nu(T) = \frac{j_\nu(T)}{\alpha_\nu(T)}, \tag{4.17}$$

where $B_\nu(T)$ is the specific intensity of black-body radiation, $j_\nu(T)$ is the emission coefficient and $\alpha_\nu(T)$ is the absorption coefficient. In the low frequency (radio and microwave) band, Planck's law (Equation 4.15) is approximated by the Rayleigh-Jeans Law, Equation 4.18, where $h\nu << kT$. This is done using a Taylor series expansion of the exponential term in Equation 4.15.

$$B_\nu(T_{\rm b}) = I_\nu = \frac{2\nu^2}{c^2}kT \tag{4.18}$$

This can be rearranged for T, to give an expression for the brightness temperature, $T_{\rm b}$ (Equation 4.19).

$$T_{\rm b} = \frac{c^2}{2\nu^2 k}I_\nu, \tag{4.19}$$

where $T_{\rm b}$ is the brightness temperature, c is the speed of light, ν is the frequency and $k = 1.38 \times 10^{-23}\,{\rm J\,K^{-1}}$ is the Boltzmann constant.

4.2   Source and Antenna Temperature

Single dish radio telescopes record the antenna temperature $T_{\rm A}^*$ in a given region of the sky, which presents the power detected by the telescope in terms of the brightness temperature. The typical observing mode for such telescopes involve pointing the telescope in a region in which signal is expected, called the 'on-region'. The background is then measured in another region without a source, called the 'off-region'. When observing the on-region, the telescope records $T_{\rm A}^*$ in terms of the source temperature, $T_{\rm src}$, and the background temperature, $T_{\rm bg}$, usually the cosmic microwave background (CMB). The total recorded signal by the telescope also incorporates the instrument electronics which have brightness temperature $T_{\rm noise}$ and the absorption of photons by the atmosphere which has brightness temperature $T_{\rm atmos}$. When observing the off-region there should be no source signal, hence the antenna temperature $T_{\rm A}^* = 0$. Figure 4.3 shows a schematic of this situation.

During the on and off observations the power received by the telescope is given by:

$$\begin{aligned} P_{\rm ON} &= C[e^{-\tau_\nu}(T_{\rm A}^* + T_{\rm bg}) + T_{\rm atmos}(1 - e^{-\tau_\nu}) + T_{\rm noise}] \\ P_{\rm OFF} &= C[e^{-\tau_\nu}T_{\rm bg} + T_{\rm atmos}(1 - e^{-\tau_\nu}) + T_{\rm noise}], \end{aligned} \tag{4.20}$$

where C is the constant used to convert from brightness temperature to power received and τ_ν is the optical depth of the atmosphere. By subtracting $P_{\rm ON}$ from $P_{\rm OFF}$ and rearranging, the antenna temperature is found:
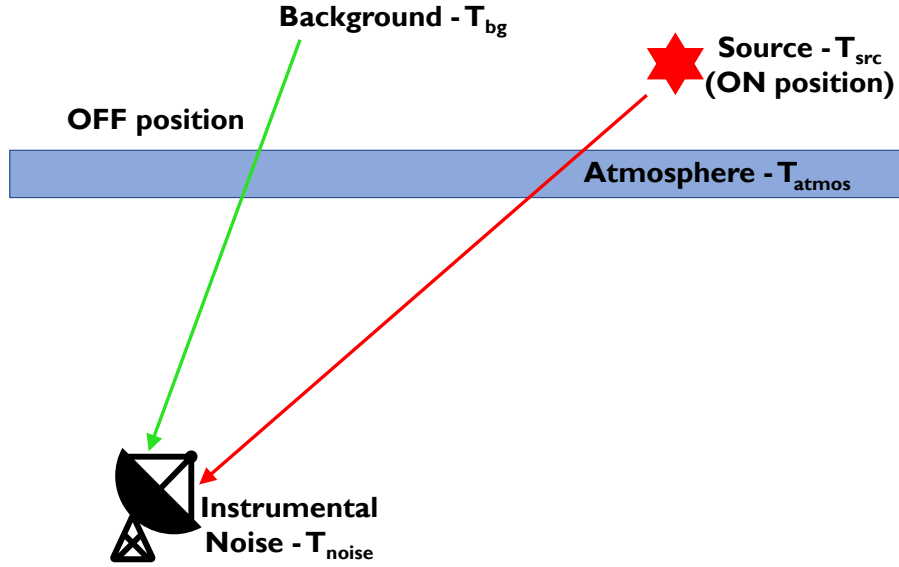
Figure 4.3: Graphical representation of the radiation source contributing to the total signal received by the telescope. The total measured power is a combination of: the CMB (T_{bg}), the desired source (T_{src}), the atmosphere (T_{atmos}) and the electronic noise from the receiver (T_{noise}). Image adapted from Nicholas, 2011.

$$T_{\mathrm{A}}^* = \frac{P_{\mathrm{ON}} - P_{\mathrm{OFF}}}{C} e^{-\tau_\nu} \ . \tag{4.21}$$

In radio astronomy a common measure is the system temperature, T_{sys}, which accounts for the noise from the background radiation, telescope electronics and atmosphere:

$$
\begin{aligned}
T_{\mathrm{sys}} &= \frac{P_{\mathrm{OFF}}}{C} e^{\tau_\nu} \\
&= T_{\mathrm{bg}} + T_{\mathrm{atmos}}(e^{\tau_\nu} - 1) + e^{\tau_\nu} T_{\mathrm{noise}} \ .
\end{aligned}
\tag{4.22}
$$

The system temperature and antenna temperature are therefore related through:

$$T_{\mathrm{A}}^* = \frac{P_{\mathrm{ON}} - P_{\mathrm{OFF}}}{P_{\mathrm{OFF}}} T_{\mathrm{sys}} \ . \tag{4.23}$$

For a radio telescope, the antenna response consists of a main beam, described as a central core with a Gaussian shape, along with a number of smaller peaks known as side lobes. The true antenna temperature of the source, $T_{\mathrm{A}}^{*\prime}$, is given by calibrating the antenna temperature for the main beam efficiency, η_{mb}, of the telescope:

$$T_{\mathrm{A}}^{*\prime} = \frac{T_{\mathrm{A}}^*}{\eta_{\mathrm{mb}}} \ . \tag{4.24}$$

In the case where the angular diameter of the source is much greater than the diameter of the antenna beam ($\theta_\mathrm{s} \gg \theta_\mathrm{FWHM}$), a large fraction of the total power is transferred to the side lobes. To account for this, the extended beam coefficient, η_xb, is introduced to obtain the true antenna temperature:

$$T_\mathrm{A}^{*\prime} = \frac{T_\mathrm{A}^*}{\eta_\mathrm{xb}} \,. \tag{4.25}$$

The source temperature, T_src (Equation 4.26), is related to the true antenna temperature, $T_\mathrm{A}^{*\prime}$, assuming the source solid angle, $\Delta\Omega_\mathrm{s}$, is small compared to the beam solid angle, $\Delta\Omega_\mathrm{b}$.

$$T_\mathrm{src} = T_\mathrm{A}^{*\prime} \left(\frac{\Delta\Omega_\mathrm{b}}{\Delta\Omega_\mathrm{s}} \right) \tag{4.26}$$

Assuming the main beam pattern is approximated by a Gaussian function, the beam solid angle is given by Equation 4.27.

$$\begin{aligned}
\Delta\Omega_\mathrm{b} &= \int_0^{2\pi} \int_0^\infty \exp\left(-\frac{4\theta^2}{\theta_\mathrm{FWHM}^2} \ln 2 \right) \theta\, d\theta\, d\phi \\
&= \frac{\pi \theta_\mathrm{FWHM}^2}{4 \ln 2}
\end{aligned} \tag{4.27}$$

Whilst the solid angle of the source is approximated by a disk, $\Delta\Omega_\mathrm{s} = \pi\theta_\mathrm{s}^2/4$. Taking the ratio of $\Delta\Omega_\mathrm{b}$ to $\Delta\Omega_\mathrm{s}$ gives the beam dilution factor:

$$f = \frac{\Delta\Omega_\mathrm{b}}{\Delta\Omega_\mathrm{s}} = \frac{\theta_\mathrm{FWHM}^2}{\theta_\mathrm{s}^2 \ln 2} \,. \tag{4.28}$$

By introducing an additional correction factor K, the source temperature can be recovered from the true antenna temperature:

$$T_\mathrm{src} = T_\mathrm{A}^{*\prime} f K \,, \tag{4.29}$$

where

$$K = \frac{f^{-1}}{1 - e^{-f^{-1}}} \,. \tag{4.30}$$

For the Mopra radio telescope the correction factors f and K for the 7 mm and 12 mm receivers can be found in Table 3 of Urquhart et al., 2010. This table also contains the beam efficiencies, η_mb and η_xb, for various frequencies. For the 3 mm receiver the beam efficiencies are outlined in Ladd et al., 2005. The values of beam efficiency used in Chapter 5 are shown in Table 4.1.

Table 4.1: Beam efficiency values for molecular lines used throughout this thesis. For a full list see Urquhart et al., 2010 and Ladd et al., 2005.

Receiver	Frequency (GHz)	Line	η_{xb}
3 mm	115	CO(1-0)	0.55
7 mm	49	CS(1-0)	0.56
7 mm	45	HC_3N(5-4)	0.67
7 mm	43	SiO(1-0, v=0)	0.69
12 mm	23	NH_3(1,1)	0.6

4.3   Molecular Line Emission

Gas clouds contain a variety of molecules which store internal energy in three ways; translational, rotational, and vibrational modes. The population of each of these energy levels depends on the interaction undergone with particles external to the cloud. Radiative processes can lead to transitions between the energy levels, resulting in emission and/or absorption of photons with characteristic spectral lines. For a photon that transitions from an energy state j to another state k, the frequency of the photon absorbed/emitted in this process is given by:

$$\nu_{jk} = \frac{|E_j - E_k|}{h} , \tag{4.31}$$

where $h = 6.626 \times 10^{-24}$ J s is Planck's constant. This process is known as line emission. The different characteristics of these spectral lines, which allow us to gain knowledge on the population of particles, are discussed throughout this section.

4.3.1   Energy Levels

The total energy of a molecule is given by the sum of the translational, rotational, electronic, and vibrational energies:

$$E_{\text{total}} = E_{\text{trans}} + E_{\text{rot}} + E_{\text{elec}} + E_{\text{vib}} . \tag{4.32}$$

Rotational line emission is of interest here, as these emissions typically occur in the radio to microwave band. The rotational energy can be described using quantum mechanics under the assumption of a harmonic oscillator. Consider a single molecule in 3D with perpendicular axes x, y and z, with angular momentum J_x, J_y and J_z respectively. The total rotational energy of the particle is related to the moment of inertia, I_i, for each axis, as shown in Equation 4.33.

$$E_{\text{rot}} = \frac{J_x^2}{2I_x} + \frac{J_y^2}{2I_y} + \frac{J_z^2}{2I_z} \tag{4.33}$$

The moment of inertia is given by:

$$I_i = \sum m_i r_i \,, \tag{4.34}$$

where m_i is the mass of the atom and r_i is the distance from the rotational axis.

Molecules can be categorised into four different 'rotor' groups, based on their moments of inertia, as summarised in Table 4.2.

Table 4.2: Rotor types along with the conditions which must be met for their moment of inertia, along with examples of molecular rotors.

Rotor type	Moment of Inertia	Example Molecules
Linear rotor	$I_x = 0, I_y = I_z$	CO, CS, OH, SiO
Spherical rotor	$I_x = I_y = I_z$	CH_4, SiH_4
Symmetric rotor	$I_x = I_y \neq I_z$	NH_3, CH_3CN
Asymmetric rotor	$I_x \neq I_y \neq I_z$	H_2O, CH_3OH

Linear rotor

One of the most common rotor types in the ISM is a linear rotor molecule. A linear rotor has one component equal to zero ($I_x = 0$), whilst the other two principal components are non-zero identical perpendicular axes ($I_y = I_z \equiv I_\perp$). The rotational energy of the molecule is:

$$E_{\text{rot}} = \frac{J_\perp^2}{2I_\perp} \,, \tag{4.35}$$

where $J_\perp$ is the angular momentum perpendicular to the rotation axis and $I_\perp$ is the moment of inertia (as defined in Equation 4.34). The angular momentum can be expressed in terms of the quantum number, J, leading to the following equation for rotational energy:

$$E_{\text{rot}} = \frac{J(J+1)\hbar^2}{2I_\perp} \,. \tag{4.36}$$

For a linear rotor the frequency of a photon which is emitted or absorbed by the molecule is $\nu = \Delta E_{\text{rot}}/2\pi\hbar$, where ΔE is the energy difference between two rotational energy levels and $\hbar = h/2\pi$. The absorption/emission transitions are restricted to an angular momentum of $\Delta J = \pm 1$, due to photons having a spin of 1. The frequency of the photon is then:

$$\nu = \frac{\hbar}{2\pi I}(J_L + 1)\,, \tag{4.37}$$

where J_L is the angular momentum quantum number of the lower energy state. An example of a linear rotor molecule which is detected throughout the ISM through radio telescopes is CO (discussed further in Section 4.6).

4.3.2   Einstein Coefficients

The Einstein Coefficients can be used to describe the rate of emission and absorption of photons in a medium, due to the change in energy state. There are three mechanisms of importance, shown in Figure 4.4, which are discussed below.
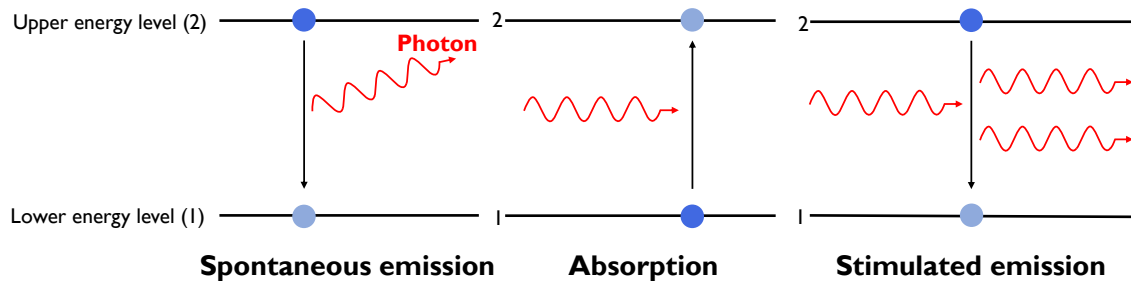
Figure 4.4: Mechanisms associated with line emission, resulting in a change in the energy state of the molecule. The frequency of the photon is ν_{21} with corresponding energy $h\nu_{21}$ equal to the difference in the energy states 2 and 1. Image adapted from Rybicki and Lightman, 1986.

Spontaneous emission
Spontaneous emission is the process in which a single photon is emitted when a molecule spontaneously decays from a higher excited energy state, 2, to a lower energy state, 1, as shown in the left panel of Figure 4.4. The rate at which this transition occurs per unit time is given by the Einstein coefficient in Equation 4.38.

$$A_{21} = \frac{16\pi^3\nu_{21}^3}{3\epsilon_0 hc^3}\,|\mu_{21}^2|\qquad [\mathrm{s}^{-1}]\,, \tag{4.38}$$

where $\nu_{21} = (E_2 - E_1)/h$ is the central frequency for the transition and μ_{21} is the electric dipole moment of the molecule for the transition.

Absorption
Absorption occurs when a single photon is spontaneously absorbed causing a transition from the lower energy state, 1, to a higher energy state, 2, as shown by the middle panel of Figure 4.4. The rate of transition for this process is given by the Einstein coefficient for absorption, denoted B_{12} (units of $\mathrm{W}^{-1}\,\mathrm{cm}^2\,\mathrm{Hz}\,\mathrm{sr}\,\mathrm{s}^{-1}$), which

is proportional to the specific intensity of the photons, I_ν. The rate of absorption is $B_{12}I_\nu$.

Stimulated emission

For the absorption process described above, the reverse transition is expected at the same rate. This process is known as stimulated emission (or negative absorption) in which a molecule in the higher energy state, 2, interacts with a photon with frequency ν_{21}, causing a transition to the lower energy state, 1. Resulting in the emission of two photons of the same frequency, ν_{21}, as shown by the right panel in Figure 4.4. Similar to absorption, stimulated emission depends on the specific intensity of the photons, I_ν, and the Einstein coefficient B_{21} (units of $\mathrm{W}^{-1}\,\mathrm{cm}^2\,\mathrm{Hz}\,\mathrm{sr}\,\mathrm{s}^{-1}$).

Local Thermodynamic Equilibrium

The Einstein coefficients for spontaneous (B_{12}) and stimulated emission (B_{21}), and absorption (A_{21}) are related assuming the system is in local thermodynamic equilibrium (LTE). LTE assumes that the population of particles is in thermodynamic equilibrium and that the distribution of the energy levels follows the Boltzmann distribution:

$$n_i = g_i \exp\left(-\frac{E_i}{kT}\right), \tag{4.39}$$

where i is the energy state, n_i is the population density, g_i is the degeneracy of the state, E_i is the energy, k is the Boltzmann constant and T is the temperature.

Consider a system where a molecule has two energy states. The lower energy state E_1 has a population density n_1 and the higher energy state E_2 has a population density n_2. The ratio of the number density of the two states is:

$$\frac{n_2}{n_1} = \frac{g_2}{g_1} \exp\left(-\frac{E_2 - E_1}{kT_\mathrm{x}}\right) = \frac{g_2}{g_1} \exp\left(-\frac{h\nu_{21}}{kT_\mathrm{x}}\right), \tag{4.40}$$

where g_2 and g_1 are the degeneracies of each state and T_x is the kinetic/excitation temperature of the transition. In LTE the rate at which particles transition to the upper energy state must be equal to the rate at which particles transition to the lower energy state. Giving the following relation between the transition rates:

$$n_2 A_{21} + n_2 B_{21} B_\nu(T) = n_1 B_{12} B_\nu(T). \tag{4.41}$$

Rearranging Equation 4.41 for the specific intensity gives:

$$B_\nu(T) = \frac{n_2 A_{21}}{n_1 B_{12} - n_2 B_{21}}$$
$$= \frac{A_{21}}{\frac{n_1}{n_2} B_{12} - B_{21}}. \tag{4.42}$$

The specific intensity here is for thermal radiation as given by Planck's law in
Equation 4.15. Combining these two equations along with Equation 4.40 gives the
following relationship:

$$\frac{2h\nu^3/c^2}{\exp(h\nu/kT) - 1} = \frac{A_{21}}{\frac{g_1}{g_2}\exp(h\nu/kT)B_{12} - B_{21}}$$
$$= \frac{A_{21}/B_{21}}{\frac{g_1 B_{12}}{g_2 B_{21}}\exp(h\nu/kT) - 1}. \tag{4.43}$$

The above is only true if A and B Einstein coefficients obey the following relation-
ships:

$$g_2 B_{21} = g_1 B_{12}$$
$$A_{21} = \frac{2h\nu^2}{c^2} B_{21}. \tag{4.44}$$

The Einstein coefficients can be used to redefined the expressions for the absorption,
α_ν, and emission, j_ν, coefficients, discussed in Section 4.1.2.

$$j_\nu = \frac{h\nu_{21}}{4\pi} n_1 A_{12}\phi(\nu) \tag{4.45}$$

$$\alpha_\nu = \frac{h\nu_{21}}{4\pi}(n_1 B_{12} - n_2 B_{21})\phi(\nu), \tag{4.46}$$

where $h\nu_{21}$ is the photon energy, A_{12}, B_{12}, B_{21} are the emission/absorption rates and
$\phi(\nu)$ is the normalised shape function. This function characterises the spectral line
emission from thermal motions caused by Doppler effects, as a function of frequency,
ν (see Section 4.5.1).

4.3.3   Critical Density

In addition to the radiative processes already discussed, molecules are also excited/de-
excited to different energy states through collisions. To study the critical density a

simple two-level system is considered, in which the Einstein coefficients C_{12} and C_{21} describe the collisional excitation rate and de-excitation rate, respectively. The critical density, n_c, for any molecular transition is the density when the rate of collisions (excitation) and rate of de-excitation (radiative) are equal:

$$n_c = \frac{A_{21}}{C_{12}} \approx \frac{A_{21}}{< \sigma v >} \qquad [\text{cm}^{-3}], \qquad (4.47)$$

where A_{21} is the spontaneous emission rate, σ is the collisional cross-section and $v = \sqrt{3kT/m}$ is the average thermal velocity of the molecule.

Different molecules have different critical densities, as shown in Table 4.3, which are used to determine different properties of molecular gas in the ISM (discussed further in Section 4.6).

Table 4.3: Critical density, n_c, values given the Einstein coefficients, A_{21}, for various molecular transitions in the ISM. Values taken from Wilson et al., 2010.

Molecule	Transition	A_{21} (s^{-1})	Critical density (cm^{-3})
CO	$J = 1 - 0$	7.4×10^{-8}	$\sim 5.0 \times 10^2$
CS	$J = 1 - 0$	1.8×10^{-6}	$\sim 1.8 \times 10^4$
SiO	$J = 1 - 0, v = 0$	3.0×10^{-6}	$\sim 6.0 \times 10^4$
NH$_3$	$J, K = 1, 1$	1.7×10^{-7}	$\sim 1.0 \times 10^3$

If the density of the ISM is larger than the critical density, n_c, then a population inversion occurs in which collisional excitations occur at a higher rate than radiative de-excitation. This behaviour allows detection of the line emission above the background signal. For example, CO has a relatively low critical density in addition to a low excitation temperature, making it easier to detect the diffuse CO gas in the ISM.

4.4   Physical Parameters of the ISM

As light travels through interstellar space towards Earth it can be absorbed and emitted by the gas in the ISM, which allows us to examine the characteristics of molecular clouds. Their spectral lines can be analysed to understand the physical properties of the gas, including column density, optical depth, mass, and density. The following section discusses various methods and analysis techniques for obtaining the physical properties of gas data.

4.4.1   Optical Depth

It is necessary to have an understanding of optical depth when considering different gases in the ISM. The optical depth of interstellar gas varies throughout our galaxy, hence it can provide useful information about the structure of various astrophysical environments. Optical depth is a measure of the amount of radiation that a particle has absorbed over a given distance. It is a unitless parameter, which is dependent on both the absorption coefficient, α_ν and the path length, ds. The optical depth, τ_ν, is defined as:

$$\tau_\nu = \int \alpha_\nu ds \tag{4.48}$$

The optical depth varies throughout interstellar space depending on the absorptivity of the environment. The optical depth is defined such that for $\tau_\nu \ll 1$ the gas is optically thin, whilst for $\tau_\nu \gg 1$ the gas is optically thick. If $\tau_\nu = 1$, we do not expect to see any deeper into the cloud. Due to this, it is possible to see much further into a diffuse medium as opposed to a dense medium.

4.4.2   Column Density

The column density of the ISM is an important parameter used to estimate the amount of gas along the line of sight in the ISM, typically given in units of atoms per square centimetre. Previously, in Equation 4.46 the absorption coefficient was defined in terms of the Einstein coefficients. Combining this equation along with the relationships in Equation 4.44, gives the following:

$$\alpha_\nu = \frac{c^2}{8\pi\nu_{21}^2} A_{21} \left(n_1 \frac{g_2}{g_1} - n_2 \right) \phi(\nu) \,. \tag{4.49}$$

For a thermally excited spectral line, the Boltzmann relation (Equation 4.40) is assumed, giving the following equation for the absorption coefficient:

$$\alpha_\nu = \frac{c^2}{8\pi\nu_{21}^2} A_{21} n_2 \left(\exp\left(\frac{h\nu_{21}}{kT} \right) - 1 \right) \phi(\nu) \,. \tag{4.50}$$

For the upper energy state, 2, the column density is defined as $N_2 = \int n_2 \, ds$, where ds is a distance element along the line of sight. The optical depth is found by integrating the absorption coefficient along the line of sight and expressing this in terms of the column density, N_2 (Equation 4.51).

$$
\begin{aligned}
\tau_\nu &= \int \alpha_\nu \, ds \\
&= \int \frac{c^2}{8\pi\nu_{21}^2} A_{21} \left(\exp\left(\frac{h\nu_{21}}{kT}\right) - 1 \right) n_2 \, ds \\
&= \frac{c^2}{8\pi\nu_{21}^2} A_{21} N_2 \left(\exp\left(\frac{h\nu_{21}}{kT}\right) - 1 \right)
\end{aligned}
\tag{4.51}
$$

Consider a case in which no background radiation is present (i.e. $T_{\mathrm{bg}} = 0$), multiplying Equation 4.14 by τ_ν/τ_ν gives:

$$
T_{\mathrm{b}}(\nu) = T_{\mathrm{s}} \left(\frac{1 - e^{-\tau_\nu}}{\tau_\nu} \right) \tau_\nu \, .
\tag{4.52}
$$

Assuming the source is thermally excited, T_{s} can be approximated by Equation 4.53.

$$
T_{\mathrm{s}} = \frac{h\nu_{21}}{k} \left[\exp\left(\frac{h\nu_{21}}{kT}\right) - 1 \right]^{-1}
\tag{4.53}
$$

By combining Equation 4.52 and Equation 4.53 the column density is related to the antenna temperature, T_{A}^*, through:

$$
T_{\mathrm{b}}(\nu) \equiv T_{\mathrm{A}}^* = \frac{hc^2}{8\pi\nu_{21}k} A_{21} N_2 \left(\frac{1 - e^{-\tau_\nu}}{\tau_\nu} \right) \phi(\nu) \, .
\tag{4.54}
$$

The integral of the antenna temperature over all frequencies, assuming a constant optical depth over the frequency range, is:

$$
\int_{-\infty}^{\infty} T_{\mathrm{A}}^* d\nu = \frac{hc^2}{8\pi\nu_{21}k} A_{21} N_2 \left(\frac{1 - e^{-\tau_\nu}}{\tau_\nu} \right) \int_{-\infty}^{\infty} \phi(\nu) d\nu \, .
\tag{4.55}
$$

The antenna temperature can be expressed in terms of the Doppler-shifted velocity, v (discussed later in Section 4.5.1):

$$
\int_{-\infty}^{\infty} T_{\mathrm{A}}^* d\nu = \frac{\nu}{c} \int_{-\infty}^{\infty} T_{\mathrm{A}}^* dv \, .
\tag{4.56}
$$

Whilst the integral of the normalised shape function is $\int_{-\infty}^{\infty} \phi(\nu) d\nu = 1$. Applying both of these to Equation 4.55 and rearranging gives an expression for the column density:

$$
N_2 = \frac{8\pi\nu_{21}^2 k}{A_{21} hc^3} \frac{\tau_\nu}{1 - e^{-\tau_\nu}} \int_{-\infty}^{\infty} T_{\mathrm{A}}^* dv \, .
\tag{4.57}
$$

This equation is suitable for calculating the column density provided we assume the medium is optically thin, meaning $\frac{\tau_\nu}{1 - e^{-\tau_\nu}} \sim 1$ (from the Taylor expansion of $\exp(-\tau_\nu)$).

A common way to estimate the column density for a specific spectral line is to use the X-factor approximation given by:

$$N = X \int T_{\mathrm{B}} \, dv \,, \tag{4.58}$$

where T_{B} is the brightness temperature, dv is the integration over the velocity of the cloud and X is the X-factor for the given molecule (see Section 4.6 for further information).

4.5   Estimating Distances in the Milky Way

The distances to different sources of interest are not easily resolved in astronomy. However, from the Doppler shifting of spectral lines, it is possible to estimate the distance to different objects within our galaxy. This is done using the Galactic rotation curve (Brand and Blitz, 1993), as discussed in this section.

4.5.1   Doppler Effect

Molecular clouds exhibit motion within the galaxy. Various types of particle motion are present within these clouds. Turbulent movement inside the cloud is caused by the randomized motions of individual particles as they are scattered off the magnetic irregularities contained within the cloud itself. Bulk motion is also present from gas 'clumps' as they move around the Galactic Centre (GC). Clouds also have intrinsic motion around the galaxy. Each of these combined causes the gas to have motion relative to the Earth. Bulk movement causes the spectral lines to systematically shift, whilst thermal motion of the particles leads to the broadening of spectral lines with respect to a stationary observer at Earth, commonly know as Doppler (thermal) broadening. Therefore, the observed frequency of clouds, ν_{obs}, are Doppler shifted from their original frequency, ν_0, shown by Equation 4.59.

$$\nu_{\mathrm{obs}} = \frac{v + v_{\mathrm{obs}}}{v + v_{\mathrm{src}}} \nu_0 \,, \tag{4.59}$$

where v_{src} is the velocity of the source, v_{obs} is the velocity of the observer and v is the velocity of the emitted wave, often taken to be the speed of light, c. Broadening can also occur from the interaction between atoms and molecules leading to a difference in the energy level spacings and therefore a broader range of frequencies. This is commonly known as 'pressure' broadening.

The observed frequency of spectral lines (both emission and absorption) may deviate from their rest frequencies due to the motion of the particles. This frequency shift can be expressed in terms of a Doppler-shifted velocity, with respect to some rest frame. The local standard of rest (LSR) is defined by a point coincident with the Suns position in its circular orbit around the GC. The LSR is commonly adopted as the reference frame when interpreting such velocities:

$$v_{\text{LSR}} = \frac{c(\nu_0 - \nu)}{\nu_0} \,, \tag{4.60}$$

where v_{LSR}, is the Doppler-shifted velocity, typically obtained using the Galactic Rotation Curve (GRC, discussed further in Section 4.5.2), ν is the frequency and c is the speed of light.

The thermal motion of particles results in Doppler-shifted velocities, which can be described by a Gaussian line profile dependent on frequency, as shown by Equation 4.61.

$$\phi(\nu) = \sqrt{\frac{mc^2}{2\pi kT\nu_0^2}} \exp\left(-\frac{(\nu - \nu_0)^2 mc^2}{2kT\nu_0^2}\right) \,, \tag{4.61}$$

where m is the mass of the molecule, $k = 1.38 \times 10^{-23}\,\text{J}\,\text{K}^{-1}$ is the Boltzmann constant and T is the temperature.

For a line shape function that is normalised, $\phi(\nu)d\nu = 1$, the line width for thermal Doppler broadening is given by:

$$\Delta\nu \sim \nu_0\sqrt{kT/mc^2} \,, \tag{4.62}$$

where $\Delta\nu = \nu - \nu_0$.

The Doppler-shifted velocity with respect to the LSR, v_{LSR}, is redefined to include the Doppler-shifted velocity, v_0:

$$\begin{aligned} v_{\text{LSR}} &= \frac{c(\nu_0 - \nu)}{\nu_0} + v_0 \\ \therefore \nu &= \nu_0 - \frac{(v_{\text{LSR}} - v_0)\nu_0}{c} \,. \end{aligned} \tag{4.63}$$

The line profile in Equation 4.61 is then adjusted to be expressed in terms of the Doppler-shifted velocity:

$$\phi(v_{\text{LSR}}) = \sqrt{\frac{mc^2}{2\pi kT\nu_0^2}} \exp\left(-\frac{m(v_{\text{LSR}} - v_0)^2}{2kT}\right) \,. \tag{4.64}$$

Typically, the spectral line emission profiles can be described in velocity-space only with a Gaussian function given by:

$$\phi(v_{\text{LSR}}) = A \exp -\frac{4(v_{\text{LSR}} - v_0)^2}{\Delta v_{\text{FWHM}}^2} \ln 2 \,, \tag{4.65}$$

where A is the emission line amplitude, and Δv_{FWHM} is the full width half maximum, which is given by Equation 4.66 provided the broadening of the line is due only to thermal motions.

$$\Delta v_{\text{FWHM}} = \sqrt{\frac{8kT \ln 2}{m}} \,, \tag{4.66}$$

where m is the mass of the molecule.

4.5.2 Galactic Rotation Curve

Objects within the galaxy are rotating around the Galactic Centre (GC), see Figure 4.5). The Galactic rotation curve is a model which gives the average Doppler-shifted velocity of an object in the galaxy with respect to the GC as a function of distance. The velocity given to particular objects depends on the motion of the observer, as well as motions described in Section 4.5.1. In the case of Earth, the rotation and orbit must be considered in addition to the motion of the Sun around our galaxy. The local standard of rest (LSR) is commonly adopted as the reference frame when interpreting such velocities. It is noted that the velocity field includes non-circular motions so it is the radial velocity (v_{LSR}) which is of importance. Hence, the kinematic distance to an object can be found by knowing the position and radial velocity of the given object, from Equation 4.67 (Brand and Blitz, 1993).

$$v_{\text{LSR}} = \left[\frac{\Theta R_0}{R} - \Theta_0 \right] \sin l \cos b \,, \tag{4.67}$$

where R is the galactocentric distance to the object[2] and Θ is the circular rotation velocity of the object. R_0 is the galactocentric distance from the sun and Θ_0 is the circular rotation velocity at the position of the Sun, commonly given values $8.5\,\text{kpc}$ and $220\,\text{km\,s}^{-1}$ respectively (Kerr and Lynden-Bell, 1986). The Galactic coordinates are given by l (Galactic longitude) and b (Galactic latitude).

Brand and Blitz, 1993 provide the following relationship between R and Θ:

$$\frac{\Theta}{\Theta_0} = a_1 \left(\frac{R}{R_0} \right)^{a_2} + a_3 \,, \tag{4.68}$$

---

[2]The galactocentric distance is the distance of an object from the centre of the Milky Way galaxy
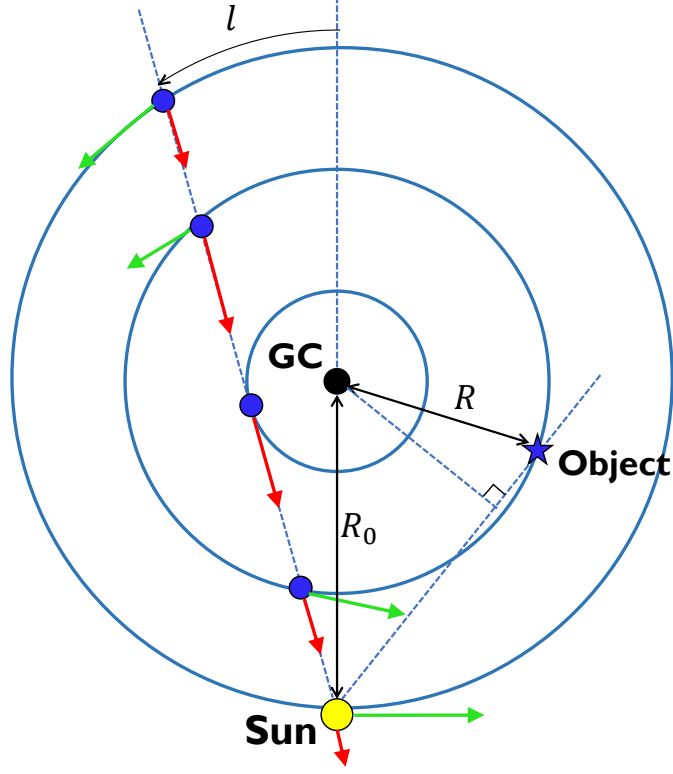
Figure 4.5: Matter rotating about the GC with velocity Θ_0. The Galactic Longitude, l, is the angle between the line which connects the centre of the galaxy with the Sun and the line which connects the Sun with the object. The red arrows are the velocity projected along the line of sight of the Sun and green arrows show the tangential velocity. Image adapted from (Sofue, 2013).

where $a_1 = 1.00767$, $a_2 = 0.0394$ and $a_3 = 0.00712$ are observationally derived, and the galactocentric distance, R, is found through trigonometry:

$$R = \sqrt{d^2 \cos^2 b + R_0^2 - 2R_0 d \cos b \cos l}\,. \tag{4.69}$$

The distance to some object in the Galaxy, d, is found by solving Equations 4.67 and 4.68 numerically. For objects which are closer to the Galactic Centre than the Sun ($R < R_0$), degeneracy occurs, resulting in two solutions called the 'near' and 'far' distances. The Galactic model along the line of sight for HESS J1804−216 is shown by Figure 4.6. Other models for the rotation curve are also used throughout literature in which the equations follow a different form. For example Reid et al., 2014 use a polynomial to describe the relationship between R and Θ, however, Persic et al., 1996 describe a 'universal' rotation curve. Russeil et al., 2017 discuss and test various rotation curve models for our Galaxy.
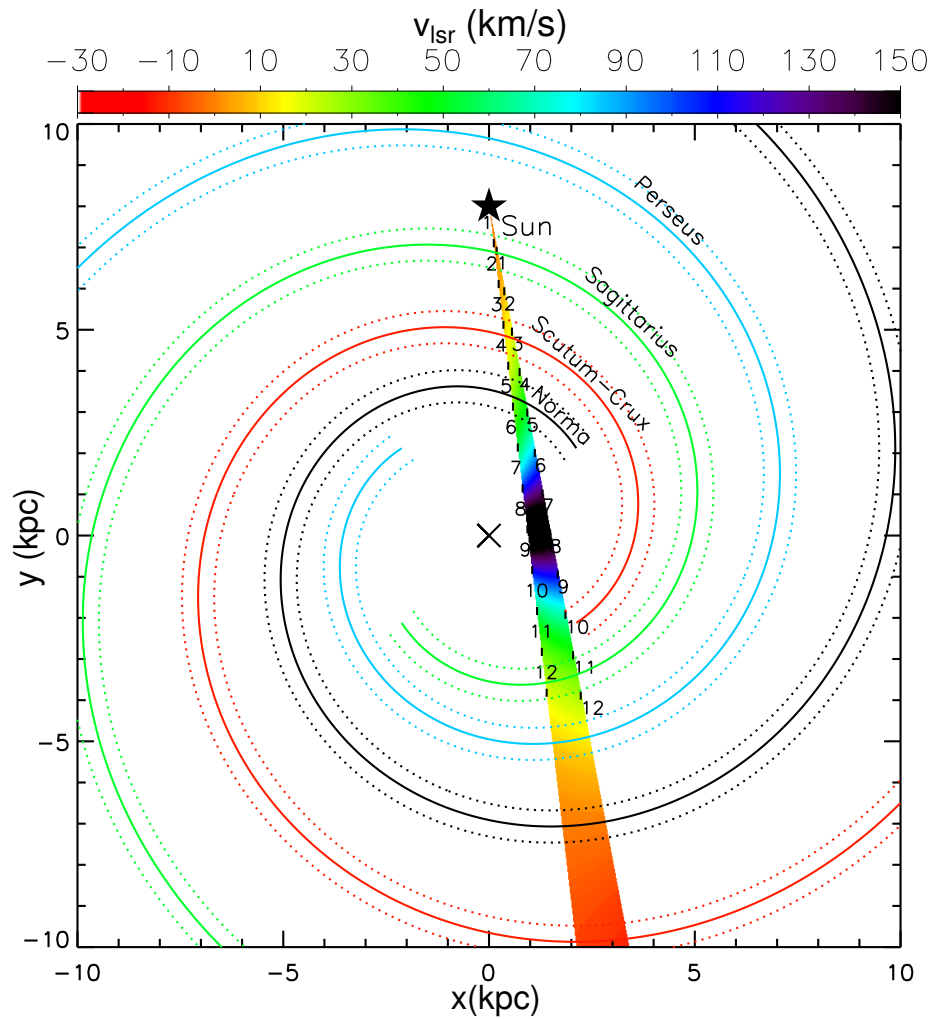
Figure 4.6: Model of the Galaxy along the line of sight of HESS J1804−216. Parameters used in this model are from Vallée, 2014 for each spiral arm shown by the solid coloured lines, Perseus (light blue), Sagittarius (light green), Scutum-Crux (red) and Norma (black). The dashed lines for each spiral arm show their extent. The coloured wedge shows the expected line of sight for HESS J1804−216 from the Sun for the radial velocities (v_{LSR}) using the Galactic rotation model from Brand and Blitz, 1993. The numbers along this wedge show the distance to the source in kilo-parsecs (kpc). The spatial coordinates along the axes are given in kpc also. Image courtesy of Nigel Maxted.

4.6 Gas Tracers

An interstellar gas cloud commonly has a dense core, surrounded by thinner layers of gas (see Figure 4.7). The inner layers are composed of molecular hydrogen (H_2) and carbon monoxide (CO), whilst the outer layers contain atomic hydrogen (HI). CO is not often found on the outer layers of a gas cloud as the ultra-violet (UV) radiation from stars breaks the CO up into its constituents; carbon (CI) and oxygen (OI). The following section describes some of the most abundant gas tracers, which have been used within the project.
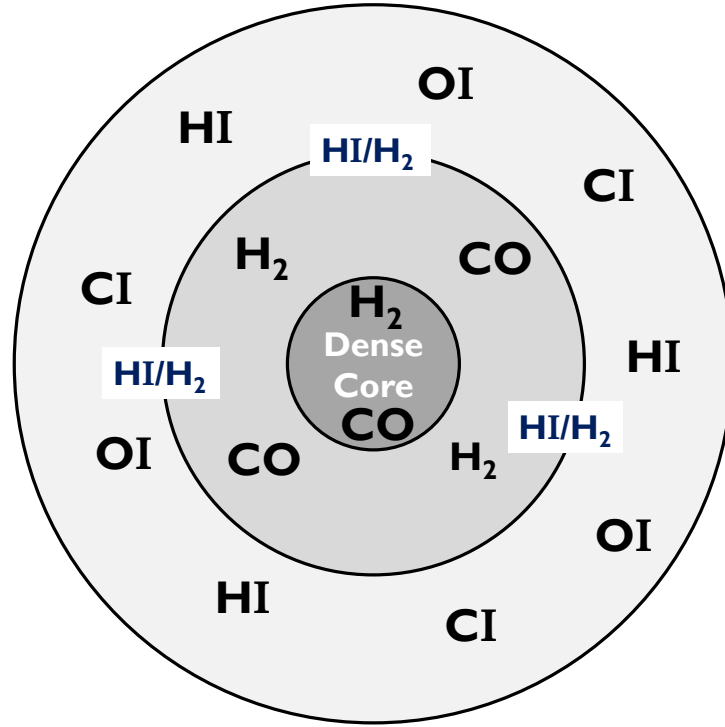
Figure 4.7: Schematic of an interstellar gas cloud profile. The dense core indicated by the dark grey region and surrounding first layer (indicated by grey region) consisting of primarily H_2 and CO. The boundary between the first and outer layer consists of both HI and H_2. The outer layer indicated by the light grey region consists of predominately HI, OI, and CI. Observations made in this thesis will measure the HI and CO components in this diagram.

The mass of a region of gas can be calculated through:

$$M = \mu m_{\mathrm{H}} N A \,, \tag{4.70}$$

where μ is the weighting factor, m_{H} is the mass of hydrogen atom, N is the column density of the region and A is the cross-sectional area of the region. Assuming that the gas consists of mostly molecular hydrogen with $\sim 10\%$ helium atoms and the other components of the gas are negligible, $\mu = 2$.

4.6.1   Atomic Hydrogen

The most abundant molecule in the Universe is hydrogen. Hydrogen can easily exist in its atomic form (HI) consisting of only one proton and one electron at low densities, typically found in space. HI produces a characteristic 21 cm hyperfine spectral line in both emission and absorption, making it possible to trace atomic hydrogen. The 21 cm hyperfine spectral line is the radiation emitted from the interaction of the spin state of the electron and proton (shown in Figure 4.8). The average temperature of the CMB and hence the universe is approximately 2.7 K, making it unlikely for HI to be ionised, as temperatures above 1000 K are required. The primary form

of emission is therefore from interactions of the spin states of both the electron and proton (Furlanetto, 2016). The 21 cm transition corresponds to a frequency emitted of $f = 1.42 \times 10^9$ Hz.
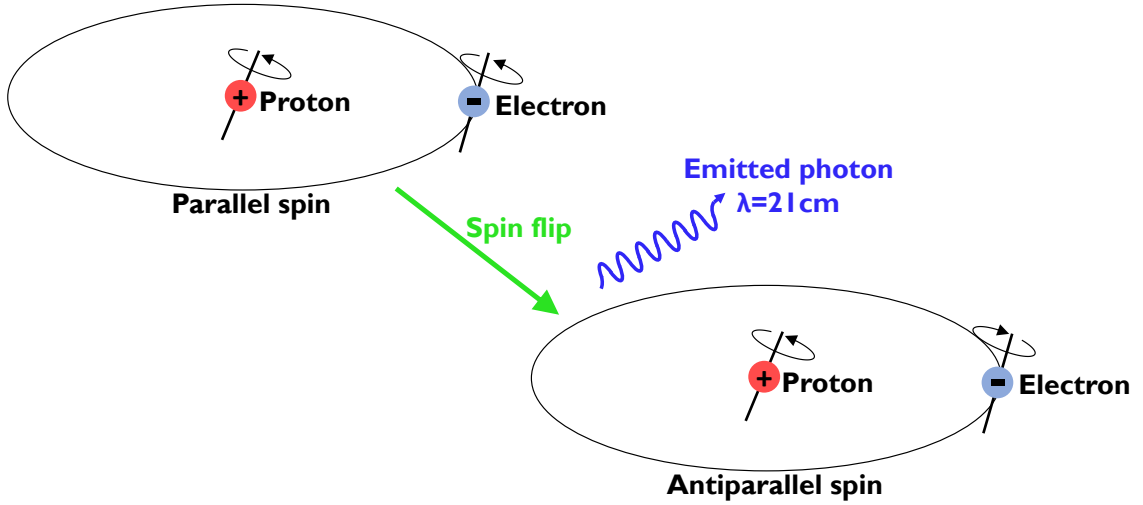
Figure 4.8: Diagram of the electromagnetic radiation emitted, with wavelength of 21 cm, when a hydrogen atom changes energy state leading to the HI spectral line.

The density of the medium varies as the temperature changes. A diffuse warm medium has a density of $10^{-2}\,\mathrm{cm}^{-3}$ whilst a cold neutral medium has a density $10^2\,\mathrm{cm}^{-3}$. To calculate the column density corresponding to a specific region, the X-factor is used (Dickey and Lockman, 1990):

$$N_{\mathrm{H}} = X_{\mathrm{HI}} \int T_{\mathrm{b}} dv \,, \tag{4.71}$$

where $\int T_{\mathrm{b}}\, dv$ is the integrated velocity (K km /s) and the X-factor for HI assuming an optically thin medium is:

$$X_{\mathrm{HI}} = 1.823 \times 10^{18}\,\mathrm{cm}^{-2}\mathrm{K}^{-1}\mathrm{km}^{-1}\mathrm{s} \,. \tag{4.72}$$

If the medium is not optically thin this value will be an underestimate of the X-factor (Fukui et al., 2015). The X-factor is empirically derived and depends on the conditions of the ISM (i.e. Strong et al., 2004; Fukui and Kawamura, 2010; Bolatto et al., 2013). It encompasses the physical parameters of the gas cloud and its environment. The X-factor depends on the cloud density. It has a latitude dependence, meaning X_{HI} varies throughout the galaxy. The HI data used in this thesis was taken from the SGPS, available at the CSIRO website[3]. This data provided full coverage of the source of interest.

---

[3]CSIRO: http://www.atnf.csiro.au/research/HI/sgps/fits_files.html

4.6.2   Carbon Monoxide

Molecular hydrogen (H_2) can be difficult to detect as it does not emit in the radio range. H_2 also has a very high excitation temperature to reach the first rotational excited state ($> 300\,$K, Habart et al., 2005). Vibrational excitation temperatures are even higher than this. CO makes for an ideal tracer of H_2 as it is the next most abundant molecule, and emits/absorbs electromagnetic radiation in the millimetre (radio) range. It is a linear rotor (see Section 4.3.1) with a weak dipole moment, $\sim 0.1\,$Debye, therefore spontaneous de-excitation is small. CO also has a low excitation temperature of $\sim$10-20 K, in addition to a relatively low critical density (see Section 4.3.3) of 10-1000 particles/cm^3, allowing it to be excited in molecular clouds of lower temperatures. CO is commonly detected in the J=1$\rightarrow$0 transition (i.e. CO(1-0)), where J represents the rotational level. This is the rotational transition that occurs between the first excited state and the ground state (see Heyer and Dame, 2015 for a review).

The standard method in determining the column density of H_2 from CO is adopted, in which the brightness temperature is converted to column density with the use of the X-factor (see Equation 4.73).

$$X_{\mathrm{CO}} = \frac{N(\mathrm{H_2})}{W_{\mathrm{CO}}} \, . \tag{4.73}$$

Here, $N(\mathrm{H_2})$ is the column density of H_2, W_{CO} is the integrated intensity of J=1$\rightarrow$0 transition of either ^{12}CO or ^{13}CO and X_{CO} is a scaling factor. Bolatto et al., 2013 provide an overview of the various methods used to obtain the X-factor for CO. In this thesis we adopt the X-factor as determined by Dame et al., 2001 and Simon et al., 2001 for ^{12}CO and ^{13}CO respectively:

$$\begin{aligned} X_{^{12}\mathrm{CO}} &= 1.8 \times 10^{20}\,\mathrm{cm^{-2}\,K^{-1}\,km^{-1}\,s} \\ X_{^{13}\mathrm{CO}} &= 4.92 \times 10^{20}\,\mathrm{cm^{-2}\,K^{-1}\,km^{-1}\,s} \, . \end{aligned} \tag{4.74}$$

^{12}CO(1-0) is the standard molecule used to traced diffuse H_2 gas. ^{13}CO(1-0) on the other hand is far less dense and most often optically thin. The ^{13}CO therefore provides a deeper look into the inside of a molecular cloud. As CO emission is a suitable tracer for H_2, it can be used to estimate both the mass of a molecular cloud (given by Equation 4.70) and the column density of the molecular hydrogen, within a specific region of cloud.

4.6.3   Carbon Monosulfide

Carbon monosulfide (CS) is a diatomic molecule found in molecular clouds in the ISM. It has a high electric dipole moment of $\mu = 1.9\,$Debye. CS is far less abundant (Penzias et al., 1971) than hydrogen and has a much higher critical density, on the

order of $10^4\,\mathrm{cm}^{-3}$ (see Table 4.3). The abundance ratio between CS and molecular hydrogen is taken from Frerking et al., 1980 to be $\sim 10^{-9}$. Due to these factors, CS is known to be a good tracer of dense molecular gas, especially in cases where the CO is optically thick. The abundance ratio can also be used to convert the CS column density to the $\mathrm{H_2}$ column density, $N_{\mathrm{H_2}} = N_{\mathrm{CS}}/10^{-9}$. In cases where the ISM is particularly dense $(> 10^5\,\mathrm{cm}^{-3})$ or at temperatures as low as $\sim 10\,\mathrm{K}$ it is possible for CS to 'freeze out' onto dust grains, hence lowering the abundance of CS (Tafalla et al., 2004).

CS has multiple observable transitions including J=3-2, J=2-1, and J=1-0. The focus for the work shown in this thesis is CS(J=1-0) which has a line frequency of $\sim 49\,\mathrm{GHz}$ meaning it is observable by the Mopra 7 mm receiver. The CS(J=1-0) line provides a look into the dense cores of clouds, allowing further information on the internal dynamics and physical conditions of these clouds to be explored.

4.6.4   Silicon Monoxide

Similar to CS, silicon monoxide (SiO) is a linear rotor, with a high electric dipole moment of $\mu = 3.09\,\mathrm{Debye}$ and critical density of $\sim 10^4\,\mathrm{cm}^{-3}$. SiO is therefore also a tracer of dense gas $(n > 10^4\,\mathrm{cm}^{-3})$, and detectable via observing with a 7 mm receiver.

The SiO molecule originates in the compressed gas behind the shock produced by molecular clouds (Martin-Pintado et al., 1992). These are typically C-type shocks (continuous shocks), which are found in star-forming regions or SNRs when they interact with the surrounding ISM (Gusdorf et al., 2008). Therefore, SiO can be a useful signpost of disrupted or shocked molecular clouds, where the SiO abundance is higher (e.g. Martin-Pintado et al., 1992).

SiO is rarer than other dense gas tracers such as CS, as silicon is depleted in large fractions onto dust grains. Silicates are, however, expected to be released, when dust particles are bombarded by molecules, such as CO, in shocks of sufficiently high speeds $(v_\mathrm{s} \sim 25\,\mathrm{km\,s}^{-1})$. The released Si particles are eroded by oxygen atoms which eventually leads to the formation of SiO (Gusdorf et al., 2008). This process occurs in dense clouds and can be described with the following reaction chain (Herbst et al., 1989):

$$\mathrm{Si} + \mathrm{O_2} \rightarrow \mathrm{SiO} + \mathrm{O}\,. \tag{4.75}$$

4.6.5   Ammonia

Ammonia (NH$_3$) is a polyatomic molecule with a pyramidal symmetric top in which three hydrogen atoms form the base of the pyramid and one nitrogen atom at the apex of the molecule. The abundance ratio of NH$_3$ to H$_2$ is typically between 10^{-5} and 10^{-7}, so NH$_3$ is far less abundant than H$_2$ (Ho and Townes, 1983). The

rotational transition of the ammonia molecule is denoted NH_3(J,K), for different quantum numbers J and K. There are two species of NH_3, the ortho-NH_3 and para-NH_3. Ortho-NH_3 occurs when all three hydrogen nuclei spins are aligned and K is a multiple of 3 (K= $3n$). Para-NH_3 occurs when the three hydrogen nuclei spins are not aligned (i.e. one spin is anti-parallel to the other two) and K is not a multiple of 3 (K$\neq$ $3n$).

Similar to SiO and CS, NH_3 also traces high density gas ($10^4\,cm^{-3}$) in dense cores and star-forming regions (i.e. young stars, Ho and Townes, 1983). NH_3 typically indicates cold ($< 30\,K$) dense clouds or for temperatures between $30\,K$ and $100\,K$ it can indicate the presence of compact H_{II} regions and maser sources. The NH_3 molecule can also display maser action, however, the pumping mechanism for the maser emission is unclear for most NH_3 masers, as discussed in Walsh et al., 2007. NH_3 masers are typically found with other collisional masers such as H_2O. These NH_3 masers have been detected towards various sources, such as W51 and W33 (Walsh et al., 2011; Wilson and Schilke, 1993).

The NH_3(1,1), NH_3(2,2) and NH_3(3,3) inversion transitions are detected between 23-25 GHz, which are observable with the 12 mm receiver on the Mopra radio telescope (Walsh et al., 2011). These inversion transitions have a unique spectra containing the main emission line surrounded by the weaker hyperfine components, called the satellite lines (see Fig. 2 in Ho and Townes, 1983).

4.6.6   Hydroxyl

The hydroxyl (OH) radical is detected at radio wavelengths in the ISM and can be important in tracing shocked gas. OH contains one oxygen atom and one hydrogen atom bound together covalently. OH molecules populate the four hyperfine levels of the ground state; 1612 MHz, 1665 MHz, 1667 MHz and 1720 MHz, all of which are observable in the radio range for both emission and absorption. The 1665 MHz and 1667 MHz lines are the strongest of the four and are often referred to as the main lines, whereas 1612 MHz and 1720 MHz are weaker and known as satellite lines (see Figure 4.9). The 1720 MHz satellite line requires temperatures between 25 K and 200 K, a density of $\sim 10^5\,cm^{-3}$ and an OH column density of $10^{16}-10^{17}\,cm^{-2}$ (Lockett et al., 1999). Due to the large critical density, the emission is often characteristic of warm, dense material. Dawson et al., 2014 provide a survey (SPLASH) of OH in each of the four ground state transitions. See Dawson et al., 2014 and references therein for further information.

Hydroxyl maser
There are various sources of astrophysical masers in our universe. A maser (Microwave Amplification by Stimulated Emission of Radiation) is the natural form of the man-made laser in the microwave range, which produces stimulated electromagnetic emission from excited atoms. Astrophysical masers are slightly different to those created in a laboratory, as they lack resonance, meaning the emission from an astrophysical maser is produced via one pass through the gain medium. Masers

can provide information on the temperature and velocity structure of astrophysical regions. There are many different species which have been observed, however, the species of interest in this case is the 1720 MHz OH maser. This particular species is believed to be a strong tracer in the study of the relationship between SNR shocks and molecular clouds (Frail and G. F. Mitchell, 1998).

Within a 1720 MHz region of low temperature the molecules populate the lowest rotational energy state (J=3/2). The molecules can also be excited to the higher rotational levels, in which they emit radiation to then fall back to the ground state. The 1720 MHz transition is inverted when the final decay is from the first excited state with J=5/2, which is simply due to the structure of OH (Lockett et al., 1999). The OH J=3/2 state is split in two by the Lambda doubling effect. This effect is when the rotation of the nuclei and motion of an unpaired electron interact with one another, often resulting in a slight change in energy. These 'Lambda-doubled' levels can then split into sublevels via hyperfine splitting, creating the four hyperfine levels of the ground state (see Figure 4.9, Lockett et al., 1999).
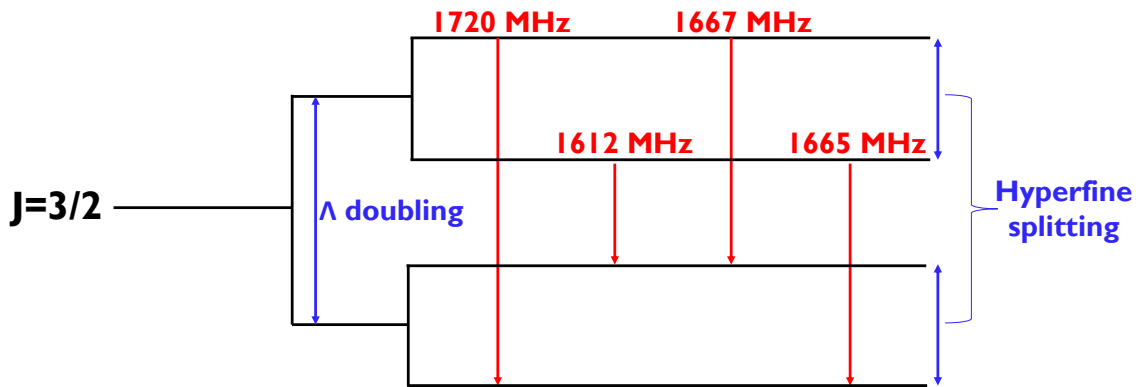
Figure 4.9: Ground state energy level of OH, including transitions of the hyperfine sublevels. Image adapted from Lockett et al., 1999.

The 1720 MHz OH maser is excited by collisionally pumped gas. The common type of pumped environment is that of a C-type shock (continuous shock), which is most often the result of a supernova explosion. The OH maser has been an extremely effective way for investigating the correlation between SNRs and molecular clouds (Lockett et al., 1999). It is believed that the 1720 MHz OH maser originates in the post-shock environment, in which the SNR shock interacts with dense molecular clouds surrounding the SNR. This theory is supported by various observations, and should be noted that these conditions do not occur within other ground state masers. Many 1720 MHz OH masers have been seen towards other TeV γ-ray SNRs, such as W44, which provides evidence of interaction between molecular gas and this SNR (Frail and G. F. Mitchell, 1998).

5   Paper 1: Interstellar Gas towards HESS J1804−216

The following paper entitled 'Arc-minute-scale studies of the interstellar gas towards HESS J1804−216: Still an unidentified TeV γ-ray source' was published in the peer-reviewed journal Publications of the Astronomical Society of Australia (PASA). In this paper we present a detailed study of the interstellar gas towards the γ-ray source HESS J1804−216. Several origin scenarios for the TeV γ-ray emission from HESS J1804−216 are identified and studied. This paper also models the energy spectra of CR protons in the hadronic scenario for two different SNRs.

Statement of Authorship

Title of Paper	Arcminute-scale studies of the interstellar gas towards HESS J1804−216: Still an unidentified TeV γ -ray source
Publication Status	☒ Published ☐ Accepted for Publication ☐ Submitted for Publication ☐ Unpublished and Unsubmitted work written in manuscript style
Publication Details	K. Feijen et al. 2020, PASA, 37, e056 Author list: K. Feijen, G. Rowell, S. Einecke, C. Braiding, M. G. Burton, N. Maxted, F. Voisin, G. F. Wong

Principal Author

Name of Principal Author	Kirsty Feijen
Contribution to the Paper	Spectral line analysis, interstellar medium and high energy interpretation, modelling of SEDs, writing the paper
Overall percentage (%)	68%
Certification:	This paper reports on original research I conducted during the period of my Higher Degree by Research candidature and is not subject to any obligations or contractual agreements with a third party that would constrain its inclusion in this thesis. I am the primary author of this paper.
Signature		Date	24-12-20

Co-Author Contributions

By signing the Statement of Authorship, each author certifies that:

i.   the candidate's stated contribution to the publication is accurate (as detailed above);

ii.   permission is granted for the candidate in include the publication in the thesis; and

iii. the sum of all co-author contributions is equal to 100% less the candidate's stated contribution.

Name of Co-Author	Gavin Rowell
Contribution to the Paper	Interstellar medium analysis and high energy interpretation, general paper review (12%)
Signature		Date	5/2/21

Name of Co-Author	Sabrina Einecke
Contribution to the Paper	High energy interpretation, SED modelling, general paper review (10%)
Signature		Date	5/2/21

Name of Co-Author	Catherine Braiding		
Contribution to the Paper	Mopra observation, data reduction and cleaning (2%)		
Signature		Date	1/7/2020

Name of Co-Author	Michael Burton		
Contribution to the Paper	Mopra observation, data reduction and cleaning (2%)		
Signature		Date	24/04/20

Name of Co-Author	Nigel Maxted		
Contribution to the Paper	ISM interpretation (2%)		
Signature		Date	26/04/2020

Name of Co-Author	Fabien Voisin		
Contribution to the Paper	Mopra observation, ISM interpretation (2%)		
Signature		Date	22/06/2020

Name of Co-Author	Graeme Wong		
Contribution to the Paper	Mopra observation, data reduction and cleaning (2%)		
Signature		Date	24/04/2020

CrossMark

CAMBRIDGE
UNIVERSITY PRESS

Research Paper

Arcminute-scale studies of the interstellar gas towards HESS J1804−216: Still an unidentified TeV γ-ray source

Kirsty Feijen[1,*] , Gavin Rowell[1], Sabrina Einecke[1], Catherine Braiding[2], Michael G. Burton[2,3], Nigel Maxted[4,5], Fabien Voisin[1] and Graeme F. Wong[5,6,7]

[1]School of Physical Sciences, University of Adelaide, Adelaide, SA 5005, Australia, [2]School of Physics, University of New South Wales, Sydney, NSW 2052, Australia, [3]Armagh Observatory and Planetarium, College Hill, Armagh BT61 9DG, UK, [4]School of Science, The University of New South Wales, Australian Defence Force Academy, Canberra, 2600, Australia, [5]Western Sydney University, Locked Bag 1797, Penrith South DC, NSW 2751, Australia, [6]Pawsey Supercomputing Centre, 26 Dick Perry Ave, Kensington 6151, WA, Australia and [7]School of Physics, The University of New South Wales, Sydney 2052, Australia

Abstract

The Galactic TeV γ-ray source HESS J1804−216 is currently an unidentified source. In an attempt to unveil its origin, we present here the most detailed study of interstellar gas using data from the Mopra Southern Galactic Plane CO Survey, 7- and 12-mm wavelength Mopra surveys and Southern Galactic Plane Survey of HI. Several components of atomic and molecular gas are found to overlap HESS J1804−216 at various velocities along the line of sight. The CS(1-0) emission clumps confirm the presence of dense gas. Both correlation and anti-correlation between the gas and TeV γ-ray emission have been identified in various gas tracers, enabling several origin scenarios for the TeV γ-ray emission from HESS J1804−216. For a hadronic scenario, SNR G8.7−0.1 and the progenitor supernova remnant (SNR) of PSR J1803−2137 require cosmic ray (CR) enhancement factors of ∼50 times the solar neighbour CR flux value to produce the TeV γ-ray emission. Assuming an isotropic diffusion model, CRs from both these SNRs require a slow diffusion coefficient, as found for other TeV SNRs associated with adjacent ISM gas. The morphology of gas located at 3.8 kpc (the dispersion measure distance to PSR J1803−2137) tends to anti-correlate with features of the TeV emission from HESS J1804−216, making the leptonic scenario possible. Both pure hadronic and pure leptonic scenarios thus remain plausible.

Keywords: ISM: clouds – ISM: cosmic rays – ISM: individual objects (HESS J1804–216) – gamma rays: ISM – molecular data

(Received 24 April 2020; revised 4 August 2020; accepted 16 November 2020)

1. Introduction

HESS J1804−216 is one of the brightest unidentified γ-ray sources, discovered by the High Energy Stereoscopic System (H.E.S.S.) in 2004 as part of the first H.E.S.S. Galactic Plane Survey (Aharonian et al. 2005). HESS J1804−216 features extended emission with a radius of ∼22 arcmin, a photon flux of almost 25% of the Crab Nebula above 200 GeV (Aharonian et al. 2006), and a TeV luminosity of $5 \times 10^{33} (d/kpc)^2$ erg s^{-1} and is one of the softest galactic sources with a photon index of $\Gamma = 2.69 \pm 0.04$ (H.E.S.S. Collaboration et al. 2018a).

High-Altitude Water Cherenkov observatory (HAWC) detected emission at ∼4σ towards the north of HESS J1804−216; however, no source has been identified.

The GeV γ-ray source, FGES J1804.8−2144, (Ackermann et al. 2017) is a disc of radius ∼23 arcmin, coincident with the TeV emission from HESS J1804−216 (see Figure 1).

HESS J1804−216 has several possible counterparts found within ∼1° of its centroid, but none of these have been unambiguously associated with the TeV source. Two prominent candidates

for the acceleration of cosmic rays (CRs) are supernova remnants (SNRs) and pulsar wind nebulae (PWNe). Here, the potential counterparts are SNR G8.7−0.1, SNR 8.3−0.1 (also referred to as SNR G8.3−0.0 in other literature, see Hewitt & Yusef-Zadeh 2009), PSR J1803−2137, PSR J1803−2149, and PSR J1806−2125. The location of each counterpart with respect to HESS J1804−216 is shown in Figure 1. The γ-ray contours used here were obtained from Aharonian et al. (2006).

SNR 8.3−0.1 has radio shell-like morphology with a radius of 0.04° (Kilpatrick, Bieging, & Rieke 2016; Acero et al. 2016). Kilpatrick et al. (2016) find a systematic velocity of +2.6 km s^{-1}, placing it at a kinematic distance of 16.4 kpc, hence it is in the background. SNR 8.3−0.1 would have an unusually high TeV luminosity (H.E.S.S. Collaboration et al. 2018a) at 16.4 kpc of 1.34×10^{36} erg s^{-1}, making it unlikely to be powering HESS J1804−216.

SNR G8.7−0.1 has a large radius of 26 arcmin as determined by radio observations (Fang & Zhang 2008). It has been associated with a number of young HII regions, forming the W30 complex, a large star-forming region with a ∼1° region of radio continuum emission (Kassim & Weiler 1990). SNR G8.7−0.1 is a mature SNR with an age of 15 kyr (Odegard 1986). A distance of 4.5 kpc is adopted here, which is found through X-ray observations and the column density of neutral hydrogen (Hewitt & Yusef-Zadeh 2009). Ajello et al. (2012) modelled the GeV to TeV emission assuming CRs are accelerated by this SNR.

Table 1. Pulsar characteristics, including spin period (P), period derivative ($\dot{P}$), characteristic age (τ_c), spin-down power ($\dot{E}$), distance, and TeV luminosity at that distance.

Pulsar name	P (ms)	$\dot{P}$ (10^{-14})	τ_c (kyr)	$\dot{E}$ (10^{35} erg s^{-1})	Distance (kpc)	TeV luminosity (10^{34} erg s^{-1})
J1803−2137[a]	133.6	13.41	15.8	22.2	3.8	7.2
J1803−2149[b]	106.3	1.95	86.4	6.41	1.3	0.8
J1806−2125[c]	481.8	11.73	65.0	0.41	10	50

[a]From Brisken et al. (2006).
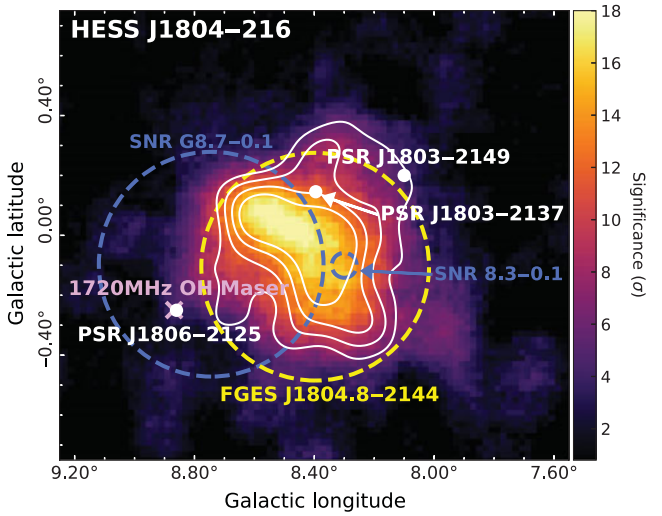[b]From Abdo et al. (2013).
[c]From Morris et al. (2002).

Figure 1. TeV γ-ray significance map of HESS J1804−216, along with potential counterparts. SNR G8.7−0.1 and SNR 8.3−0.1 are indicated by the blue dashed circles, PSR J1803−2137, PSR J1803−2149, and PSR J1806−2125 are indicated by the white dots and the 1720-MHz OH is indicated by a purple cross. FGES J1804.8−2144 is shown by the yellow dashed circle. The TeV γ-ray emission for 5-10σ is shown by the solid white contours. Image adapted from H.E.S.S. Collaboration et al. (2018a).

A 1720-MHz OH is located along the southern edge of SNR G8.7−0.1 (Hewitt & Yusef-Zadeh 2009). It is currently categorised as an SNR-type maser, as no compact radio source has been found within 5 arcmin and it is believed to originate in a post-shock environment (Fernandez et al. 2013). It is located at a velocity (v_{lsr}) of 36 km s^{-1} corresponding to a distance of ∼4.55 kpc, similar to the distance to SNR G8.7−0.1. The coexistence of molecular clouds with SNR G8.7−0.1 and the location of the OH maser suggest that the SNR is interacting with nearby molecular clouds (Hewitt & Yusef-Zadeh 2009).

The characteristics of the pulsars are summarised in Table 1. PSR J1803−2137 was found by high-frequency radio observations by Clifton & Lyne (1986). A dispersion measure distance of 3.8 kpc is used here (Kargaltsev, Pavlov, & Garmire 2007a). *Chandra* detected a faint and small (∼7 arcsec × 4 arcsec) synchrotron nebula around PSR J1803−2137, with the inner PWN positioned perpendicular to the direction of proper motion of the pulsar (Kargaltsev et al. 2007a).

PSR J1803−2137 is located towards the north-eastern edge of SNR G8.7−0.1, but their association is highly unlikely according to a proper motion study of the pulsar (Brisken et al. 2006). This study showed that for the pulsar to be born at the centre of SNR G8.7−0.1, a transverse velocity of ∼1700 km s^{-1} is required. Therefore, PSR J1803−2137 was born outside the central

region of SNR G8.7−0.1 (see Figure A1). The pulsar is most likely moving towards this area, rather than away from it, ruling out their connection (Brisken et al. 2006).

PSR J1806−2125 is a γ-ray-quiet radio pulsar discovered with the Parkes radio telescope (Morris et al. 2002), and is located at a distance of ∼10 kpc. Comparing the inferred γ-ray luminosity at 10 kpc to the spin-down power, we obtain a TeV γ-ray efficiency ($\eta_\gamma = L_\gamma/\dot{E}$) of more than 100%, excluding it as a plausible counterpart.

PSR J1803−2149 is a radio-quiet γ-ray pulsar located at a distance of 1.3 kpc (Pletsch et al. 2012). This distance is obtained by inverting the γ-ray luminosity equation (see Saz Parkinson et al. 2010) and is discussed further in Section 5.1.

Multiple studies (Higashi et al. 2008; Kargaltsev, Pavlov, & Garmire 2007b; Lin, Webb, & Barret 2013) have found a lack of X-ray emission towards HESS J1804−216, particularly towards SNR G8.7−0.1 and PSR J1803−2137. As mentioned previously, there is a faint and small X-ray nebula towards PSR J1803−2137. No SNR shell has been detected within the field of view of the *Chandra* imaging (Kargaltsev et al. 2007b). Investigation of this region by *XMM-Newton* (Lin et al. 2013) showed that the detected X-ray sources (both extended and point-like) are unlikely to be associated with HESS J1804−216 due to them being located far away from the TeV peak.

Our detailed arcminute-scale ISM study here follows on from earlier work by de Wilt et al. (2017) who revealed dense clumpy gas using the ammonia inversion line tracer. By studying the distribution and density of the ISM towards HESS J1804−216 on arcminute scales, we can investigate morphological differences between hadronic and leptonic scenarios for the γ-ray production. We will utilise data from the Mopra radio telescope and Southern Galactic Plane Survey (SGPS) in order to carry out such an investigation and look at an isotropic CR diffusion model for further insight into the likelihood of a hadronic interpretation.

2. ISM observations

In this work, we utilised the publicly available SGPS[a] of atomic hydrogen (HI) and 3, 7, and 12 mm (frequency ranges 76–117, 30–50, and 16–27 GHz, respectively) data taken with the Mopra radio telescope towards the HESS J1804−216 region.

The Australia Telescope Compact Array (ATCA) and Parkes telescope together mapped the HI emission along the Galactic Plane to form the SGPS. The survey is for latitudes of $b = \pm 1.5°$ and longitudes covering $l = 253°$ – $358°$ (SGPS I) as well as $l = 5°$ – $20°$ (SGPS II, McClure-Griffiths et al. 2005).

Mopra is a single dish with a 22-m diameter surface. The 3-mm data were taken from the Mopra SGPS, which is designed to map the fourth quadrant in the CO isotopologues (e.g. Braiding et al. 2018[b]). The Mopra spectrometer (MOPS) was used in wide-band mode at 8 GHz in Fast-On-The-Fly (FOTF) mapping to detect the four isotopologue lines (^{12}CO, ^{13}CO, C^{17}O, and C^{18}O). FOTF mapping is conducted by scanning across 1 square degree segments. To reduce artefacts in the data, each segment contains a longitudinal and latitudinal scan. The target region covering HESS J1804−216 is $b = \pm 0.5°$ and $l = 7.0$ – $9.0°$ for the two CO isotopologue lines of interest: ^{12}CO and ^{13}CO.

[a]Data can be found at https://www.atnf.csiro.au/research/HI/sgps/fits_files.html
[b]Published Mopra data can be found at https://dataverse.harvard.edu/dataverse/harvard/

The 7-mm studies towards HESS J1804−216 were taken in 2011 and 2012. The 7-mm coverage is for a 49×52 arcmin region centred on $l = 8.45°$ and $b = -0.07°$. MOPS was used in 'zoom' mode for these observations. This provides 16 different subbands each with 4096 channels and a bandwidth of 137.5 MHz (Urquhart et al. 2010). Table F.1 lists the various spectral lines at 7 mm.

The 12-mm receiver on the Mopra telescope was used to carry out the H_2O SGPS (Walsh et al. 2011, HOPS). This survey also detected other molecules such as the different inversion transitions of ammonia (NH_3). HOPS utilised On-The-Fly (OTF) mode with the Mopra wide-bandwidth spectrometer. HOPS mapped the region surrounding HESS J1804−216; $b = \pm 0.5°$ and $l = 7.0° - 9.0°$.

The Mopra 3-, 7-, and 12-mm data must be corrected to account for the extended beam efficiency of Mopra before any data analysis can be performed. The main beam brightness temperature is obtained by dividing the antenna temperature by the extended beam efficiency (η_{XB}). At 3 mm (115 GHz), for the CO(1-0) lines (^{12}CO and ^{13}CO), a value of $\eta_{XB} = 0.55$ (Ladd et al. 2005) is used. Following Urquhart et al. (2010), the 7-mm data are corrected to account for the beam efficiency of each frequency from Table F.1. At 12 mm for the NH_3(1,1) (24 GHz) line, the main beam efficiency of $\eta_{mb} = 0.6$ is used (Walsh et al. 2011).

The Mopra data were processed using the Australia Telescope National Facility (ATNF) analysis software, LIVE-DATA, GRIDZILLA, and MIRIAD[c]. Custom IDL scripts were written to add further corrections and adjustments to the data (see Braiding et al. 2018). LIVEDATA was used first to calibrate each map by the given OFF position and apply a baseline subtraction to the spectra. Next, GRIDZILLA was used to regrid and combine the data from each scan to create three-dimensional cubes (one for each molecular line in Table F.1) of Galactic longitude, Galactic latitude, and velocity along the line of sight (v_{lsr}). The produced FITS file is processed with both MIRIAD and IDL.

3. Spectral line analysis

IDL and MIRIAD were used to create integrated intensity maps. Different parameters, such as the mass and density, are calculated using these integrated intensity maps for each line described within this section. These parameters are examined to calculate important characteristics of each gas component towards HESS J1804−216 (as shown in Sections 5.1 and 5.2).

The mass of each gas region can be calculated, assuming that the gas consists of mostly molecular hydrogen with other constituents of the gas being negligible. The mass relationship is then given by:

$$M = 2m_H N_{H_2} A, \qquad (1)$$

where m_H is the mass of a hydrogen atom, N_{H_2} is the mean column density as obtained from each region, and A is the cross-sectional area of the region. The number density of the gas, n, is estimated using the area, A, column density, N_{H_2}, and volume, V of the gas region, $n = N_{H_2} A/V$. For simplicity, we assume a spherical volume for the clouds.

3.1. Carbon monoxide

The focus for the 3-mm study is the $J = 1$-0 transition of the ^{12}CO and ^{13}CO lines. ^{12}CO(1-0) is the standard molecule used to

trace diffuse H_2 gas, as it is abundant and has a critical density of $\sim 10^3$ cm^{-3} (Bolatto, Wolfire, & Leroy 2013). The CO brightness temperature is converted to column density with the use of an X-factor according to Equation (2):

$$N_{H_2} = W_{CO} X_{CO} \quad \text{cm}^{-2}. \qquad (2)$$

Here, N_{H_2} is the column density of H_2, W_{CO} is the integrated intensity of the J = 1-0 transition of either ^{12}CO or ^{13}CO, and X_{CO} is a scaling factor with values presented in Equation (3), from Dame, Hartmann, & Thaddeus (2001) and Simon et al. (2001) for ^{12}CO and ^{13}CO, respectively:

$$X_{^{12}CO} = 1.8 \times 10^{20} \text{ cm}^{-2} \text{ (K km/s)}^{-1},$$

$$X_{^{13}CO} = 4.92 \times 10^{20} \text{ cm}^{-2} \text{ (K km/s)}^{-1}. \qquad (3)$$

Since the ^{13}CO(1-0) line is generally optically thin, as ^{13}CO is 50 times less abundant than ^{12}CO (Burton et al. 2013), the ^{13}CO(1-0) line tends to follow denser regions of gas. The ^{13}CO data will provide indication of the dense molecular gas components towards HESS J1804−216.

3.2. Atomic hydrogen

The atomic form of hydrogen is detected through the 21-cm line. The column density corresponding to a specific region is calculated through the relationship $N_{HI} = W_{HI} X_{HI}$. Here, the X-factor is from Dickey & Lockman (1990) (assuming the line is optically thin), as given by Equation (4):

$$X_{HI} = 1.823 \times 10^{18} \text{ cm}^{-2} \text{ (K km/s)}^{-1}. \qquad (4)$$

3.3. Dense gas tracers

As ^{12}CO is one of the most abundant molecules in the universe, it quickly becomes optically thick towards dense gas clumps. Tracers of dense gas ($n > 10^4$ cm^{-3}) are required to understand the internal dynamics and physical conditions of dense cloud cores. The following paragraphs outline the properties of various molecules used to trace the dense molecular clouds. These have a higher critical density and typically a much lower abundance compared to ^{12}CO.

Carbon monosulfide

Carbon monosulfide (CS) is far less abundant (Penzias et al. 1971) than the other molecules previously mentioned and has a much higher critical density, on the order 10^4 cm^{-3}. The average abundance ratio between CS and molecular hydrogen is taken from Frerking et al. (1980) for quiescent gas to be $\sim 10^{-9}$. CS is known to be a good tracer of dense molecular gas, especially in cases where the CO is optically thick. The focus here is CS(J = 1-0) which is observable with the Mopra 7-mm receiver.

Silicon monoxide

Similar to CS, silicon monoxide (SiO) is a tracer of dense gas and detectable via observing with a 7-mm receiver. The SiO molecule originates in the compressed gas behind a shock moving through the ISM (Martin-Pintado, Bachiller, & Fuente 1992). Such a shock can be found in star formation regions and in SNRs as they interact with the ISM (Gusdorf et al. 2008). SiO can be a useful signpost of disruption in molecular clouds, where the SiO abundance is higher. Nicholas et al. (2012) detected clumps of SiO(1-0) towards various TeV sources, including the W28 SNR.

W28 shows a cluster of 1720-MHz OH masers around the SiO emission, providing evidence of disrupted molecular clouds.

Methanol

Methanol (CH$_3$OH) emission is a marker for star formation outflows and is an abundant organic molecule in the ISM (Qasim et al. 2018). The CH$_3$OH line is often seen as a Class I maser. The detection of CH$_3$OH can be indicative of young massive stars and hence star formation regions. CH$_3$OH has also been detected in SNR shocks, where the gas is heated behind the shock front (Voronkov et al. 2010; Nicholas et al. 2012).

Cyanopolyyne

A cyanopolyyne is a long chain of carbon triple bonds (HC$_{2n+1}$N) found in the ISM often representing the beginning stages of high-mass star formation. The cyanopolyyne used here is cyanoacetylene, HC$_3$N. HC$_3$N is typically detected in warm molecular clouds and hot cores. It is present in dense molecular clouds and can be associated with star formation and H II regions (Jackson et al. 2013).

Ammonia

The inversion transition of the ammonia molecule is denoted as NH$_3$(J, K), for different quantum numbers J and K. NH$_3$ traces the higher density ($n \sim 10^4$ cm^{-3}) gas which can be associated with young stars (Ho & Townes 1983; Walsh et al. 2011). It is readily observed in dense molecular clouds and towards various H II regions. One common transition is NH$_3$(1, 1) detected at a line frequency of $\sim$23.69 GHz (Walsh et al. 2011). The spectra of this inversion transition contain the main emission line surrounded by four weaker satellite lines. A study by de Wilt et al. (2017) detected NH$_3$(1, 1) emission towards H$_2$O masers in the vicinity of HESS J1804$-$216.

4. Results

The distribution and morphology of interstellar gas along the line of sight of the TeV γ-ray source HESS J1804$-$216 are investigated in depth within this section. Multiple line emissions are analysed to investigate the characteristics of each ISM gas component along the line of sight. In particular, we are interested in any spatial correlation or anti-correlation between the gas and the TeV γ-ray emission, as mentioned in Section 1.

4.1. Interstellar gas towards HESS J1804$-$216

A circular region with a radius of 0.42° which encompasses the extent of the TeV γ-ray emission from HESS J1804$-$216 (shown by the cyan circle in Figure B.1) is used to obtain spectra of the various molecular lines. The emission spectrum of the Mopra CO(1-0) data (Figure 2) shows large regions of gas which overlap with HESS J1804$-$216 and encompasses the bulk of its emission. Figure C.1 shows a position–velocity (PV) plot of the Mopra ^{12}CO(1-0) data, revealing the structure of the gas in velocity space.

The CO(1-0) spectra show a large portion of the emission corresponds to a velocity range of v$_{lsr}$ ≈ $-$40 to 160 km s^{-1}. There are six main regions of emission along the line of sight as denoted by Table 2 and Figure 2. The galactic rotation curve (GRC) model for HESS J1804$-$216 (Figure D.1) is used to obtain 'near' and 'far' distances, based on the kinematic velocities to different ISM features.

Table 2. Velocity (v_{lsr}) integration intervals, with the corresponding distance measures, towards *HESS J*1804$-$216 based on the components derived from the CO(1-0) spectra in Figure 2.

Component	v_{lsr} (km s^{-1})	Near distance (kpc)	Far distance (kpc)
A	-27 to -10	0.1	17
B	-10 to 8	0.2	16.7
C	8 to 26	3.0	13.8
D	26 to 56	4.9	11.9
E	56 to 105	6.4	10.4
F	105 to 153	7.4	9.5
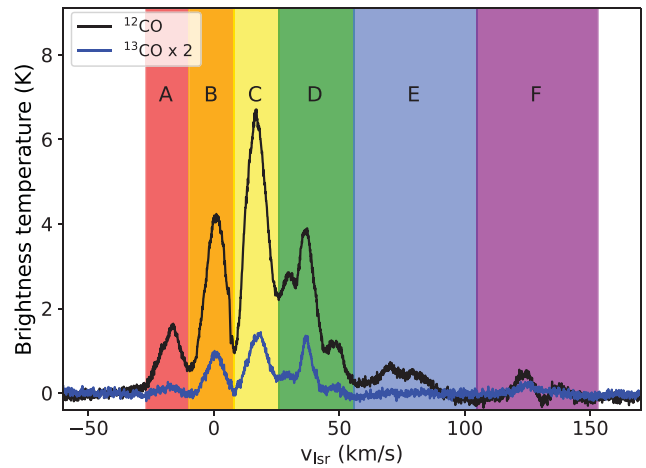
Figure 2. CO(1-0) spectra towards HESS J1804$-$216 with a radius of 0.42° centred on $[l, b] = [8.4, -0.02]$ (see Figure B.1). Solid black lines and blue lines represent the emission spectra for Mopra ^{12}CO(1-0) and ^{13}CO(1-0) (scaled by a factor of 2), respectively. Velocity integration intervals for components A through F are shown by the coloured rectangles.

The spectra for the HI data towards HESS J1804$-$216 exhibit emission and absorption as shown in Figure E.1. Given HI is extremely abundant in the ISM, the data analysis will use the same velocity components as defined above from the CO data (Figure 2).

4.2. Discussion of ISM components

It is important to look at both atomic and molecular hydrogen as they provide a look at the total target material available for CRs. The column density of both ^{12}CO and HI are calculated using the X-factors from Equations (2) and (4), respectively. Maps of total column density for the selected integrated velocity ranges are essential in comparing the γ-ray emission and column density for the hadronic scenario. The total hydrogen column density, N_H, is the sum of $2N_{H_2}$ and N_{HI} from Mopra ^{12}CO (smoothed up to the beam size of the SGPS HI data) and SGPS HI observations, respectively, giving the total proton content for each gas component. Figure F.5 shows the ratio between the column densities of molecular hydrogen and atomic hydrogen. This figure shows that the molecular gas tends to dominate over the atomic gas. The total column density maps for the defined velocity components are shown in Figure 3. This excludes components E and F (shown in Figure F.4) as these have the weakest emission features and are distant.
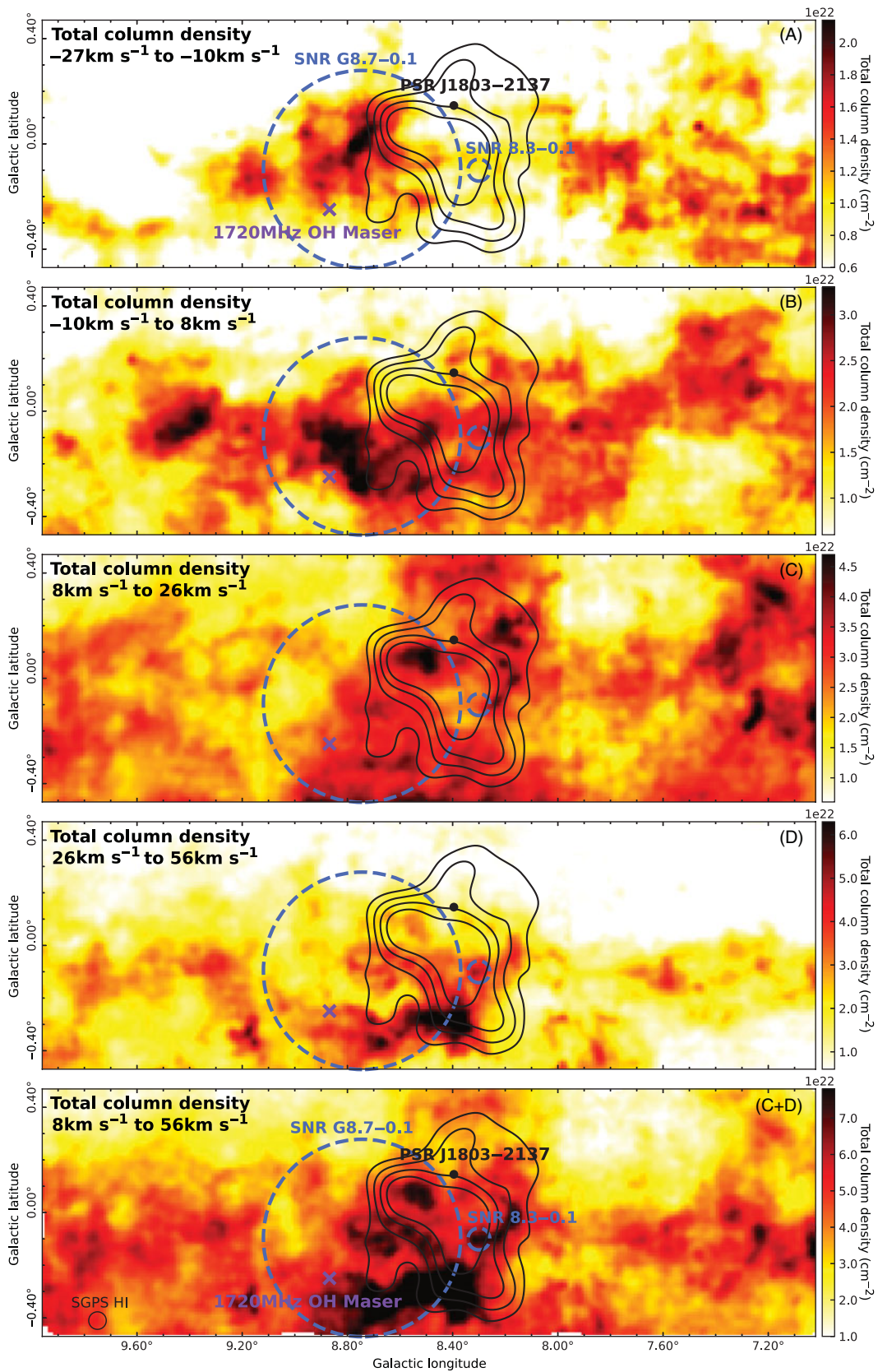
Figure 3. Total column density maps, $2N_{H_2} + N_{HI}$, (cm^{-2}) towards HESS J1804−216, for gas components A, B, C, D, and C+D. The two dashed blue circles indicate SNR G8.7 − 0.1 and SNR 8.3−0.1. The 1720-MHz OH is indicated by the purple cross and PSR J1803−2137 is indicated by the black dot. The TeV γ-ray emission for 5-10σ is shown by the solid black contours.

Figure 3 also shows an extra component which covers the velocity range $v_{lsr} = 8$ to $56 \, \mathrm{km \, s^{-1}}$ encompassing both components C and D, showing features that overlap much of HESS J1804−216. The dense gas structures in components C and D are connected by a lane of gas as shown in the PV plot (Figures C.1). This indicates that some of the gas in these components are physically close to one another. The distances obtained from the galactic rotation model remain uncertain closer to the Galactic Centre (GC). Due to this, it is possible that the velocity/distance differences in component C and D (see Table 2) arise from local motion.

Figures F.1, F.2, and F.3 show mosaics of the integrated intensity maps of the Mopra ^{12}CO(1-0), ^{13}CO(1-0), and SGPS HI data, respectively. The integrated intensity maps for the dense gas tracers are shown in the Appendix by Figures F.7, F.8, F.9, F.11, and F.11. The CS(1-0) and NH$_3$(1, 1) will be discussed here. A number of H II regions seen towards HESS J1804−216 (see Figure B.1) overlap with dense regions of interstellar gas, as discussed here.

4.2.1. Component A

The ^{12}CO(1-0) and ^{13}CO(1-0) emission in component A ($v_{lsr} = -27$ to $-10 \, \mathrm{km \, s^{-1}}$) show little overlap with HESS J1804−216. The emission in this component appears to be localised to the Galactic West of the TeV source.

In HI, there is a gas feature overlapping with the Galactic East edge of SNR G8.7−0.1 which coincides with the central region of HESS J1804−216.

The NH$_3$(1, 1) emission towards component A has no distinct features. The CS(1-0) data show two dense features, one in the Galactic North-East of HESS J1804−216 and the other to the Galactic South-East of the TeV source. The Galactic North-East feature overlaps two H II regions, G008.103+00.340 and G008.138+00.228, shown in Figure B.1.

4.2.2. Component B

In component B ($v_{lsr} = -10$ to $8 \, \mathrm{km \, s^{-1}}$), the ^{12}CO(1-0) emission overlaps most of HESS J1804−216. There is gas filling the inner region of SNR G8.7−0.1, with significant overlap with the Galactic South-West to Galactic West of the TeV source. This emission also extends West beyond both the SNR and TeV source. The ^{13}CO(1-0) emission in this component follows a similar spatial morphology to the ^{12}CO(1-0).

There is no HI overlap with HESS J1804−216 for this component. The HI appears to anti-correlate with the ^{12}CO(1-0) emission.

There is an intense point-like region of NH$_3$(1, 1) emission in the central region of SNR G8.7−0.1, which corresponds to a maser detection in both CH$_3$OH and H$_2$O (see Figure F.11). CS(1-0) emission in this component is quite weak.

4.2.3. Component C

Component C ($v_{lsr} = 8$ to $26 \, \mathrm{km \, s^{-1}}$) shows some morphological matches between the ^{12}CO(1-0) emission and the TeV γ-ray emission. There is, however, a depletion in molecular emission slightly south of the centre of HESS J1804−216 (also seen in the ^{13}CO(1-0) emission) which anti-correlates with the southern TeV peak. Additionally, there is a prominent structure of gas running from Galactic East to Galactic West at the bottom of this panel (to the Galactic South of the TeV source). Towards the Galactic West

of HESS J1804−216, there is a molecular cloud which is positionally coincident with the northern edge of SNR G8.7−0.1, as well as another clump of intense emission to the Galactic East of this. Both of these features are also prominent in the ^{13}CO(1-0) emission.

The HI emission (Figure F.3) appears to anti-correlate with the TeV γ-ray emission in component C, with very little emission detected in this area. Two clumps of HI gas overlap with the TeV source to the Galactic North-West and East of SNR 8.3−0.1. In component C, there is also a dense region of gas to the Galactic North-West, the aforementioned clumps are not consistent with the ^{12}CO(1-0) data.

The intense emission towards the Galactic East of PSR J1803−2137 in the total column density map (Figure 3) is also visible in both the CS(1-0) and NH$_3$(1, 1) (Figures F.7 and F.11). The significant CS(1-0) emission confirms the presence of dense gas in this region. This dense region is consistent with the infrared (IR) bright clouds and the H II regions G008.103+00.340 and G008.138+00.228, as shown by Figure B.1.

4.2.4. Component D

In component D ($v_{lsr} = 26$ to $56 \, \mathrm{km \, s^{-1}}$), there is a distinct dense structure in the Galactic South of HESS J1804−216 present in both the ^{12}CO(1-0) and ^{13}CO(1-0) Mopra data. This dense emission overlaps with both SNR G8.7−0.1 and HESS J1804−216, so this region is likely to be associated with the SNR. This feature is consistent with several H II regions: G008.362-00.303, G008.373-00.352, G008.438-00.331, and G008.666-00.351 (as indicated in Figures F.2 and B.1).

There is an intensity gradient in the CO emission as there is less gas towards the Galactic North of this region. The CO emission towards the Galactic North is weak and sparse. There is also weak emission seen outside HESS J1804−216 towards the Galactic West and Galactic East.

The HI emission shows a clear arm-like structure of emission that flows from the Galactic East to Galactic West through HESS J1804−216, most likely corresponding to the Norma Galactic Arm. This overlaps much of the central region of the source.

The NH$_3$(1, 1) data for component D show two distinct clumps in the Galactic South which coincide with the previously discussed dense features from the molecular gas. These dense regions overlap with IR emission detected by the Spitzer GLIMPSE Survey in Figure B.1. The IR emission is spatially coincident with several H II regions. The clump outside HESS J1804−216 is also traced by the CS(1-0) emission.

4.2.5. Component E

In component E ($v_{lsr} = 56$ to $105 \, \mathrm{km \, s^{-1}}$), the ^{12}CO(1-0) overlaps only a small portion of HESS J1804−216, corresponding to the central region of SNR G8.7−0.1. There is a region of intense emission to the Galactic North, near PSR J1803−2137. The ^{13}CO(1-0) emission has less-defined structure with no apparent overlap with the TeV source.

The HI emission appears to have an arm-like structure which extends from the Galactic East to West of HESS J1804−216, with the denser regions towards the Galactic West.

Both the NH$_3$(1, 1) and CS(1-0) lines have almost no emission. A dense feature in the Galactic South-West of HESS J1804−216 overlaps the small H II region G008.66−0.00351, shown in Figure B.1.

4.2.6. Component F

Both the ^{12}CO(1-0) and ^{13}CO(1-0) emission in component F ($v_{lsr} = 105$ to 153 km s^{-1}) show no overlap with the TeV source. This velocity component has little molecular emission aside from the clouds to the Galactic South of HESS J1804$-$216.

A large HI feature overlaps HESS J1804$-$216, extending further to the Galactic East in this component.

There is no significant NH$_3$(1, 1) emission in component F. In the CS(1-0) data, there is a dense core to the Galactic South-East that has no spatial connection to the TeV γ-ray emission.

5. Discussion

Two different parent particle scenarios will be considered to be producing HESS J1804$-$216, a purely hadronic scenario and a purely leptonic scenario. As SNRs and PWNe are two candidates for accelerating CRs, the TeV γ-ray emission from HESS J1804$-$216 could be the result of either scenario as both of these types are present within the field of view. The characteristics (i.e. mass and total column density) of the interstellar gas can be analysed to further investigate the complex nature of emission and to place a limit on which scenario is powering the TeV source.

5.1. Purely hadronic scenario

The hadronic production of TeV γ-rays involves the interaction of CRs and matter in the ISM. A study by Yamazaki et al. (2006) showed that old SNRs tend to have a large enough hadronic contribution to account for the TeV γ-ray emission. This is seen both at the SNR shock location and at the associated molecular clouds.

CRs from SNR G8.7$-$0.1

Many 1720-MHz OH masers have been seen towards other TeV γ-ray SNRs, such as W28, W44, and IC 443 (Frail, Goss, & Slysh 1994; Claussen et al. 1997), which provides evidence of interaction between the SNR shock and molecular clouds surrounding it (e.g. Nicholas et al. 2012). The presence of the 1720-MHz OH towards SNR G8.7$-$0.1 is consistent with CRs being accelerated by this SNR. Therefore, this section will assume that SNR G8.7$-$0.1 is the accelerator of hadronic CRs.

To test whether a hadronic scenario is initially feasible, the total energy budget of CRs, $W_{p,\text{TeV}}$, is calculated using:

$$W_{p,\text{TeV}} = L_\gamma \tau_{pp}, \qquad (5)$$

where L_γ is the luminosity of the γ-ray source. The TeV γ-ray luminosity varies depending on the distance to each counterpart, $L_\gamma \sim 5 \times 10^{33} (d/\text{kpc})^2$ erg s^{-1}. The cooling time of proton–proton collisions is given by Aharonian & Atoyan (1996):

$$\tau_{pp} = 6 \times 10^7 \, (n/\text{cm}^{-3})^{-1} \text{ yr}, \qquad (6)$$

where n is the number density of the target ambient gas, found in a circular region which encompasses the TeV γ-ray contours of HESS J1804$-$216 above 5σ, with a radius of $0.42°$.

Another relationship can be made between the amount of CRs that are incident upon the gas and the γ-ray flux $F(> E_\gamma)$ above some energy E_γ. The CRs have diffused through the ISM allowing the spectra to steepen from an E^{-2} power law at the accelerator to $E^{-2.6}$ at some distance from the CR source. Therefore, we assume an $E^{-1.6}$ integral power law spectrum from the integration

Table 3. CR enhancement values, k_{CR} (Equation (7)), and total energy budget of CRs, $W_{p,\text{TeV}}$ (Equation (5)), for each velocity component defined in Figure 2. Each of these numbers are calculated from the maximum extent of HESS J1804$-$216 (circle of radius 0.42°). The values for total mass and and column density are obtained from the total column density of hydrogen, using the ^{12}CO and HI data from Mopra and SGPS, respectively. The near distances were derived using the GRC presented in Figure D.1. The magnetic field is calculated using Equation (11).

Component	d	n	N_H	M	k_{CR}	$W_{p,\text{TeV}}$	B
	(kpc)	(cm^{-3})	(10^{21} cm^{-2})	(10^4 M$_\odot$)		(10^{48} erg)	(μG)
A	0.1	2835	8.6	0.01	123	3×10^{-5}	43
B	0.2	4385	18.8	0.05	56	4×10^{-5}	57
C^a	3.8	325	29.4	36	57	0.5	11
D^b	4.5	160	23.7	79	37	1.1	10
C+D	4.4	400	52.9	138	20	0.5	12
E	6.4	25	4.8	27	221	15.8	10
F	7.4	5	1.3	9	842	91.8	10

The values of distance are taken from the kinematic velocity average of each component.
^{a}Component C values are taken specifically for PSR J1803$-$2137.
^{b}Component D values are taken specifically for SNR G8.7$-$0.1.

of $dN_p = E^{-2.6} \, dE_p$, as given by (Aharonian 1991):

$$F(\geq E_\gamma) = 2.85 \times 10^{-13} E_{\text{TeV}}^{-1.6} \left(\frac{M_5}{d_{\text{kpc}}^2} \right) k_{\text{CR}} \quad \text{cm}^{-2} \text{ s}^{-1}. \qquad (7)$$

The photon flux for γ-rays from HESS J1804$-$216 is $F(\geq 200 \text{ GeV}) = 5.32 \times 10^{-11}$ cm^{-2} s^{-1} (Aharonian et al. 2006). The distance to the gas component in kpc is d_{kpc} and M_5 is the mass of the CR target material in units 10^5 M$_\odot$. The CR enhancement factor, k_{CR}, is the ratio of the CR flux at the ISM interaction point compared to that of Earth-like CR flux.

The maps of total column density ($2N_{H_2} + N_{HI}$) in Figure 3 were used to find the mean column density of each velocity component in order to calculate both the number densities and masses of each velocity component. Equations 5 and 7 are used to calculate the total CR energy budget ($W_{p,\text{TeV}}$) and the CR enhancement factor (k_{CR}) for each gas component, respectively (shown in Table 3).

An SNR has a total canonical kinetic energy budget of $\sim 10^{51}$ erg, of this we expect an amount of $\sim 10^{50}$ erg ($\sim 10\%$) to be converted into CRs. From Table 3, the total energy budget for components C, D, and C+D are on the order of $W_{p,\text{TeV}} = 10^{48}$ erg which suits the criteria of being $< 10^{50}$ erg. The values of k_{CR} for these ISM components are on the order of ~ 10, which is acceptable provided we have a young to middle aged (10^3 to 10^5 yrs) impulsive CR accelerator within 10 to 30 pc of the target material (Aharonian & Atoyan 1996).

At a distance of 4.5 kpc, SNR G8.7$-$0.1 is placed at a kinematic velocity of ~ 35 km s^{-1} according to the GRC (outlined in Appendix D). This corresponds to component D as shown in Table 2. The values for total energy budget, $W_{p,\text{TeV}}$, in Table 3 are considered as a lower limit on the total CR energy budget as we are considering γ-rays of energies above 200 GeV corresponding to CR energies of ~ 1.2 TeV (from the relation $E_\gamma \sim 0.17 E_{CR}$, in Kelner, Aharonian, & Bugayov 2006). For SNR G8.7$-$0.1 (component D), we require a CR enhancement factor, k_{CR}, of ~ 37 times that of the Earth-like CR density to produce the observed γ-ray flux towards HESS J1804$-$216 for a hadronic scenario to be plausible.

The total column density map (Figure 3) shows the ISM partially overlapping the TeV γ-ray emission from HESS J1804−216. This cloud shows a good morphological match with component D (see Figure 3), corresponding to the distance of SNR G8.7−0.1. It is, therefore, possible that this cloud is a target for CRs generated by SNR G8.7−0.1.

Following Aharonian & Atoyan (1996), the volume distribution of CRs (cm^{-3} GeV^{-1}) as a function of the injection spectrum, $N_0 E^{-\alpha}$, is given by Equation (8). This assumes a spherically symmetric case for the diffusion equation, in which relativistic particles accelerated by a source, escape and enter the ISM:

$$f(E, R, t) \approx \frac{N_0 E^{-\alpha}}{\pi^{3/2} R_{\text{dif}}^3} \exp\left(-\frac{(\alpha - 1)t}{\tau_{pp}} - \frac{R^2}{R_{\text{dif}}^2}\right), \qquad (8)$$

where the diffusion radius:

$$R_{\text{dif}} \equiv R_{\text{dif}}(E, t) = 2\sqrt{D(E)t \frac{\exp(t\delta/\tau_{pp}) - 1}{t\delta/\tau_{pp}}}, \qquad (9)$$

is the radius given for CR protons of energy E propagating though the ISM during time t. The proton–proton cooling time, τ_{pp}, is given by Equation (6) and $\alpha = 2$. We consider a specific CR accelerator model in which the age of SNR G8.7−0.1 is taken to be 15 kyr and 28 kyr from Finley & Oegelman (1994). The diffusion coefficient, $D(E)$, is determined using Equation (10) from Gabici, Aharonian, & Blasi (2007):

$$D(E) = \chi D_0 \left(\frac{E/\text{GeV}}{B/3\mu\text{G}}\right)^\delta, \qquad (10)$$

where χ is a diffusion suppression factor (typically $\chi < 1$ inside a molecular cloud). The factor χ from Aharonian & Atoyan (1996) takes values of 0.01 and 1 to represent 'slow' and 'fast' diffusion, respectively. A value of $\chi = 0.01$ is usually taken to account for the dense regions of interstellar gas that CRs may diffuse through. Various diffusion suppression factors have been found through different studies on the W28 SNR (Li & Chen 2010; Giuliani et al. 2010; Gabici et al. 2010). Li & Chen (2010) assume $\chi = 0.1$, Giuliani et al. (2010) use $\chi = 0.01$, whilst Gabici et al. (2010) adopt a value of $\chi = 0.06$. It is clear that the diffusion suppression factor is poorly constrained. Here, we adopt a value from $\chi = 0.001$ to 0.1. The index of diffusion coefficient, δ, is typically given a value of 0.3–0.7 (Berezinskii et al. 1990). D_0 and δ are given the galactic values of 3×10^{27} cm^2 s^{-1} and 0.5, respectively, whilst 3 μG is the Galactic disc's average magnetic field. Crutcher et al. (2010) gives a relationship between the magnetic field B and number density n of a given region, shown by Equation (11). They found that the magnetic field is enhanced in dense ($n > 300$ cm^{-3}) molecular clouds:

$$B = \begin{cases} B_0 & \text{for } n < 300 \text{ cm}^{-3} \\ B_0(n/n_0)^{0.65} & \text{for } n > 300 \text{ cm}^{-3} \end{cases}, \qquad (11)$$

where n is the number density in the cloud, n_0 is a constant number density set to 300 cm-3, B is the maximum magnetic field in the cloud, and $B_0 \sim 10\mu$G. The various magnetic field values for each ISM component are shown in Table 3.

The normalisation factor, N_0, is determined assuming the SNR is at an early epoch of evolution (~ 1 yr) meaning R_{dif} is approximated by the size of the SNR (i.e. $R_{\text{dif}} = R$). The CR energy produced by the SNR is $< 10^{50}$ erg. It is taken here to be 2×10^{48} erg to match the observed GeV and TeV CR enhancement factors as shown in Figure 5. We note that N_0 is considered a lower limit, since the k_{CR} constant from Equation (7) assumes all of the
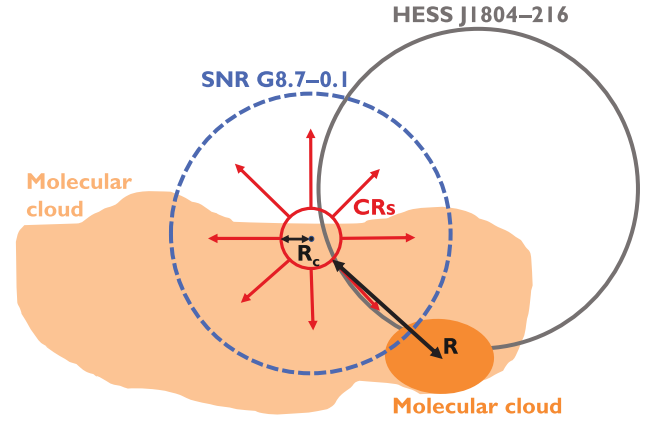
Figure 4. Schematic of CRs escaping SNR G8.7−0.1 before interacting with the molecular clouds in component D to create the TeV γ-ray emission from HESS J1804−216. The red circle shows the release point of CR protons at a radius of $R_c \sim 5$ pc. The black line shows the physical distance between the cloud and the release point of CRs ($R \sim 12$ pc).

cloud mass is impacted by CRs and converted to γ-rays. Energy-dependent diffusion and penetration (e.g. Gabici et al. 2007) inside the dense clouds, highlighted by the ^{13}CO peaks in Figure F.2, could however infer a higher k_{CR} value. In addition, clouds are typically not physically connected, given the typically wide range of distances inferred from the cloud velocities spanning Galactic arms (c.f. Figure C.1).

The initial power law distribution is assumed to be $dN/dE = E^{-2}$ for determining N_0.

The radius of the SNR shock during the Sedov phase (when mass of the swept-up material exceeds the mass of the supernova ejecta) is given by Equation (12) (Reynolds 2008):

$$R_c = 0.31 \left(\frac{E_{51}}{n_0}\right)^{1/5} \left(\frac{\mu_1}{1.4}\right)^{-1/5} t_{\text{yr}}^{2/5} \text{ pc}, \qquad (12)$$

where E_{51} is the ejected supernova kinetic energy in units of 10^{51} erg, n_0 is the number density, μ_1 is the mean mass per particle (taken to be 1.4, from Reynolds 2008), and t_{yr} is the escape time of CR protons. We assume R_c is the radius at which CR protons are released from the accelerator, which can then be used to calculate the distance to the cloud in component D. For SNR G8.7−0.1, we assume $E_{51} = 1$, with a number density of $n_0 = 160$ cm^{-3} for component D. The escape time of CRs (e.g. Gabici, Aharonian, & Casanova 2009) from a SNR shock is

$$t_{\text{esc}} = t_{\text{Sedov}} \left(\frac{E_p}{E_{p,\text{max}}}\right)^{-1/\delta_p}, \qquad (13)$$

where the maximum energy of CR protons is $E_{p,\text{max}} = 500$ TeV, $t_{\text{Sedov}} = 100$ yr, $E_p = 150$ TeV, and $\delta_p = 0.5$ (Casanova et al. 2010). Using Equation (12), the release point of the CRs is taken to be $R_c \sim 5$ pc; therefore, the physical distance to the cloud from this point is $R \sim 12$ pc. Figure 4 shows a schematic of this scenario where CRs are accelerated by SNR G8.7−0.1 and escape before interacting with the nearby cloud structure defined by component D (Figure 3).

The differential flux of CR protons is then given by:

$$J(E, R, t) = (c/4\pi)f(E, R, t) \quad \text{cm}^{-2} \, s^{-1} \, \text{GeV}^{-1} \, \text{sr}^{-1}. \qquad (14)$$

Figure 5 shows the derived energy spectrum of CR protons escaping from SNR G8.7−0.1 from Equation (8). The scenario

Figure 5. Modelled energy spectra of CR protons (Equation (14)) escaping from a potential impulsive accelerator (e.g. SNR G8.7−0.1), with a total energy of 2×10^{48} erg in CRs. The model shows different values for the diffusion suppression factor, χ, and index of the diffusion coefficient, δ. A power law spectrum with an index of $\alpha = 2$ i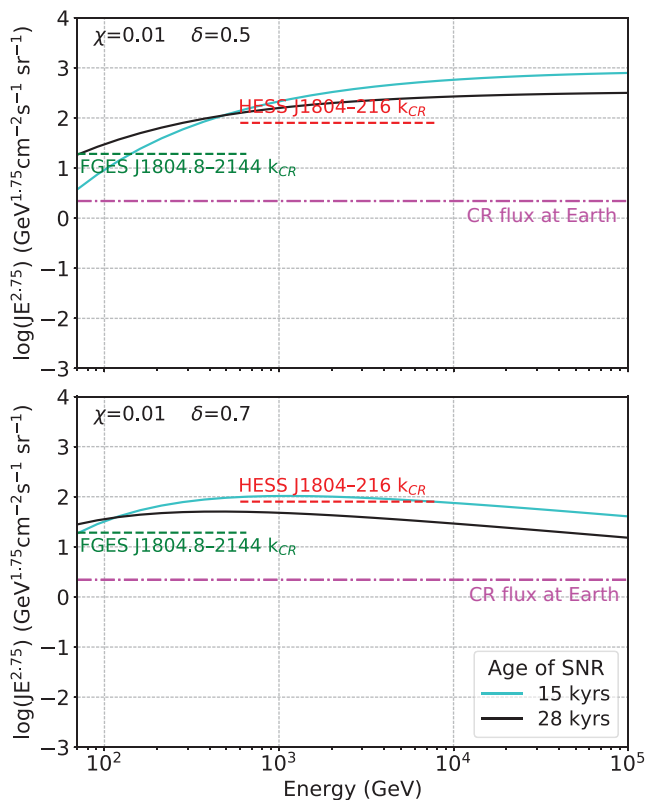s assumed. The number density is taken to be $n = 160$ cm^{-3}. The distance from the accelerator to the cloud is $R \sim 12$ pc and ages of the source are taken to be 15 kyr and 28 kyr for the cyan and black curves, respectively. The magenta dashed line represents the CR flux observed at Earth. The red dashed line represents the calculated CR enhancement factor for HESS J1804−216 ($k_{CR} \approx 37$). The green dashed line represents the calculated CR enhancement factor for FGES J1804.8−2144 ($k_{CR} \approx 9$).

assumes that SNR G8.7−0.1 is an impulsive accelerator meaning the bulk of CRs escape the SNR at $t = 0$, compared to the continuous case in which CRs are continuously injected in the ISM. The CR enhancement factors for component D are shown for TeV energies (from Equation (7) and Table 3) and GeV energies ($k_{CR} \sim 9$ from Equation (G.1)). Here, we show the two cases that broadly match the observed GeV and TeV CR enhancement factors where δ is 0.5 or 0.7 (Equation (9)) and $\chi = 0.01$. The parameters δ and χ were varied, as shown in Appendix G (Figure G.1), until a reasonable match was found. The contribution from the spectrum of CR protons observed at Earth (i.e. in the solar neighbourhood from Dermer 1986), as given by Equation (15), is also shown:

$$J_\odot(E) = 2.2 E^{-2.75} \quad \text{cm}^{-2} \ s^{-1} \ \text{GeV}^{-1} \ \text{sr}^{-1}. \quad (15)$$

The results in Figure 5 show that the older age assumption for SNR G8.7−0.1 (28 kyr) has a lower energy population of CRs, and the higher energy CRs are seen to escape first, as expected. The total CR energy budget of 2×10^{48} erg is consistent with $W_{p,\text{TeV}}$ from Equation (5) (c.f. Table 3) as computed using component D and tends to match the observed CR enhancement factors. It is evident that the pure hadronic scenario requires slow diffusion ($\chi \leq 0.01$) in order to contribute to the γ-ray emission for

HESS J1804−216. Small values of $\chi < 0.05$ are noted in other studies (Li & Chen 2012; Protheroe et al. 2008; Gabici et al. 2010) for various sources including the W28 SNR, W44, and IC443, all with similar ages to SNR G8.7−0.1. Our diffusion index of δ in the range 0.5 to 0.7 is consistent with Ajello et al. (2012) who found a diffusion index of $\delta = 0.6$ from their modelling of the GeV to TeV emission. We note that the GeV emission position now overlaps the TeV position (Ackermann et al. 2017), whereas previously (in Ajello et al. 2012) the GeV emission was located closer to SNR G8.7−0.1.

In Figure 5, both ages tend to match the CR enhancement factors for HESS J1804−216 and FGES J1804.8−2144.

CRs from the progenitor SNR of PSR J1803−2137

PSR J1803−2137 currently has no known SNR associated with it. Here, we discuss the possibility that the undetected progenitor SNR from PSR J1803−2137 is accelerating CRs. Using the hadronic scenario outlined above, we assume the centre of this SNR is located at the birth position of PSR J1803−2137, placing it in gas component C (consistent with PSR J1803−2137). We assume the progenitor SNR is 16-kyr-old, consistent with the age of PSR J1803−2137. A distance of ~ 10 pc is used as the distance from the release point of CRs to the cloud to the Galactic South-West of PSR J1803−2137 in component C. The model in Figure G.2 shows the energy spectrum of CR protons escaping from the progenitor SNR of PSR J1803−2137. The CR enhancement factors for component C are shown for TeV energies ($k_{CR} \sim 57$) and GeV energies ($k_{CR} \sim 14$ from Equation (G.1)). A χ value of 0.01 for $\delta = 0.5$, 0.7 or $\chi = 0.001$ for $\delta = 0.7$ could potentially match the observed values from HESS J1804−216 and FGES J1804.8−2144.

5.2. Purely leptonic scenario

PSR J1803−2137 *powered PWN*

Here, we consider TeV γ-ray emission produced by high-energy (multi-TeV) electrons primarily interacting with soft photon fields via the inverse-Compton process. PSR J1803−2137 is located $\sim 0.2°$ from the centre of HESS J1804−216 (as seen in Figure 1). PSR J1803−2137 is at a distance of 3.8 kpc (see Section 1) which corresponds to a velocity of ~ 25 km s^{-1}, placing this pulsar in gas component C. Due to the extended nature of HESS J1804−216, and the high spin-down luminosity of PSR J1803−2137, it is possible that the TeV emission is produced by high-energy electrons from PSR J1803−2137 as a PWN. A recent study (H.E.S.S. Collaboration et al. 2018b) shows that 14 firmly identified PWNe contribute to the TeV population of H.E.S.S. sources.

The spin-down luminosity of PSR J1803−2137 ($\dot{E} = 2.2 \times 10^{36}$ erg s^{-1}) is compared with the γ-ray luminosity of HESS J1804−216 $L_\gamma = 7.1 \times 10^{34}$ erg s^{-1} at 3.8 kpc to obtain a TeV γ-ray efficiency of $\eta_\gamma = L_\gamma/\dot{E} \sim 3\%$. This is consistent with the typical efficiency of pulsars (potentially) associated with TeV sources according to H.E.S.S. Collaboration et al. (2018b), meaning leptonic γ-ray emission from a PWN is supported from an energetics point of view.

In the scenario of a PWN-driven TeV γ-ray source, the TeV emission is expected to anti-correlate with the surrounding molecular gas. High-energy electrons suffer significant synchrotron radiation losses due to the enhanced magnetic field strength in molecular clouds, leading to anti-correlation between the gas and γ-rays. Assuming the gas in component C is located at the same

Table 4. Cooling times for synchrotron radiation, t_{sync} (Equation (17)), and Bremsstrahlung, t_{brem} (Equation (18)), towards *HESS J*1804−216 for each velocity component defined in Figure 2. The diffusion coefficient, $D(E)$, is calculated using Equation (10) with use of the magnetic field strength, B, within each component. The diffusion time, t_{diff}, for particles to cross the 30 pc distance (from *PSR J*1803−2137 to the nearby cloud in component C), is also shown here.

Component	B	t_{IC}	t_{sync}	t_{brem}	$D(E)$	t_{diff}
	(μG)	(kyr)	(kyr)	(kyr)	(10^{27} cm^2 s^{-1})	(kyr)
A	43	230	1.3	14	5.6	24
B	57	230	0.73	9	4.9	28
C	11	230	21.6	123	11	12
D	10	230	24.0	253	12	12
E	10	230	24.0	1620	12	12
F	10	230	24.0	7120	12	12

distance as PSR J1803−2137, there is indeed some anti-correlation between the total column density in Figure 3 and the TeV emission towards the Galactic South of the TeV peak.

To account for the observed TeV γ-ray emission, electrons must be able to diffuse across the extent of the GeV and TeV sources. Electrons are therefore required to travel a distance of $R \sim 30$ pc from PSR J1803−2137 to the nearby cloud in component C (see Figure 3). The radiative cooling times are calculated based on the assumption that electrons are being accelerated by PSR J1803−2137.

The inverse-Compton cooling time t_{IC} in the Thomson regime is given by:

$$t_{IC} \approx 3 \times 10^8 (U_{rad}/\text{eV/cm}^3)^{-1} (E_e/\text{GeV})^{-1} \text{ yr}, \quad (16)$$

where U_{rad} is 0.26 eV/cm^3 (the energy density of the Cosmic Microwave Background). For any given H.E.S.S. source, we expect 100 GeV γ-rays (the lower limit detectable by H.E.S.S.) as produced by inverse-Compton scattering to correspond to electron of energies of $E_e \sim 6$ TeV ($E_e \sim 20\sqrt{E_\gamma}$ for the Thomson scattering regime).

The synchrotron cooling time t_{sync} is given by:

$$t_{sync} \approx 12 \times 10^6 (B/\mu G)^{-2} (E_e/\text{TeV})^{-1} \text{ yr}, \quad (17)$$

where B is given by Equation (11).

The Bremsstrahlung cooling time t_{brem} is given by:

$$t_{brem} \approx 4 \times 10^7 (n/\text{cm}^3)^{-1} \text{ yr}, \quad (18)$$

where n is the number density for each given component.

The time, t_{diff}, takes for CRs to diffuse across a given distance, R, is given by:

$$t_{diff} = R^2/2D(E), \quad (19)$$

where $D(E)$ is the diffusion coefficient (given by Equation (10) for $\chi = 0.1$) for particles of energy, E.

The cooling time for inverse-Compton scattering (t_{IC}) is estimated to be 230 kyr for all ISM components, as it is independent of the ISM density. The various cooling times for the synchrotron and Bremsstrahlung processes, magnetic field (Equation (11)), diffusion coefficient (Equation (10)), and diffusion times (Equation (19)) for each gas component are displayed in Table 4.

Referring to Table 4, component C has a magnetic field value of $B = 11 \mu$ G and diffusion coefficient of $D(E) = 1.1 \times 10^{28}$ cm^2 s^{-1}, with a corresponding diffusion time of 12 kyr for electrons to cross the TeV source.

As the pulsar's age (16 kyr) is much less than each of the cooling times, the energy losses from each of the cooling effects are negligible at this stage in the pulsar's life. The diffusion time (Equation (19)) for CR electrons of 12 kyr is similar to the age of PSR J1803−2137, suggesting electrons are able to diffuse the required distance of 30 pc in order to contribute to the leptonic TeV emission from HESS J1804−216. Therefore, the leptonic scenario cannot be ruled out and the spatial extent of the emission is limited by diffusion.

PSR J1803−2149 *powered PWN*

The spin-down power 6.41×10^{35} erg s^{-1} for PSR J1803−2149 and TeV luminosity of 8.45×10^{33} erg s^{-1} at 1.3 kpc gives a TeV γ-ray efficiency of 1% for PSR J1803−2149. Therefore, it is possible that PSR J1803−2149 could contribute to the TeV γ-ray emission from HESS J1804−216.

Figure 6 from Abdo et al. (2010) shows the population of pulsars with their given γ-ray luminosity L_γ and spin-down power $\dot{E}$. There is a spread to the data, allowing the authors to place upper ($L_\gamma = \dot{E}$) and lower ($L_\gamma \propto \dot{E}^{1/2}$) bands to this figure. Here, the γ-ray luminosity is given by:

$$L_\gamma \equiv 4\pi d^2 f_\Omega G_{100} \text{ erg s}^{-1}, \quad (20)$$

where f_Ω is the flux correction factor set equal to 1 and $G_{100} = 13.1 \times 10^{-11}$ erg cm^{-2} s^{-1} is the energy flux obtained from Pletsch et al. (2012). Equation (20) can constrain the distance to PSR J1803−2149. The lower and upper limits lead to distances of 1.3 kpc and 6.3 kpc, respectively. As this is within the distances to other counterparts, it is possible that PSR J1803−2149 could be associated with HESS J1804−216. The large angular offset between the TeV peak of HESS J1804−216 and the best-fit position of PSR J1803−2149 of $\sim 0.37°$ indicates that a PWN scenario seems unlikely. More detailed investigation is, however, required to understand if PSR J1803−2149 is a viable counterpart to power the source.

6. Conclusion

In this paper, molecular ISM data from the Mopra radio telescope and HI data from the SGPS were used to study the interstellar gas towards the mysterious unidentified TeV γ-ray source HESS J1804−216. CO(1-0) observations showed different velocity components along the line of sight of HESS J1804−216 which were used to define intriguing features of the interstellar gas along with morphological matches with the TeV γ-ray emission.

The ISM mass and density derived from the total column density maps were used to test the validity of both the purely hadronic and purely leptonic scenarios for the potential CR accelerators towards HESS J1804−216. Components C, D, and C+D were found to contain the bulk of the gas emission towards HESS J1804−216. Component C shows morphological matches between the ^{12}CO and TeV gamma-ray emission. There is also a depletion of gas which anti-correlates with the southern TeV peak. Dense gas emission overlaps both SNR G8.7−0.1 and HESS J1804−216 in component D. The addition of components C and D shows an interesting gas feature which follows the outer most contours of HESS J1804−216 to the south. The southern region of the TeV peak contains a void of gas in this component (C+D).

For the purely hadronic scenario, SNR G8.7−0.1 was assumed to be the accelerator of CRs. Sufficient target material for CRs is

present in component D ($v_{lsr} =$ 26 to 56 km s^{-1}), corresponding to the distance of SNR G8.7−0.1. A total energy budget of $W_{p,\mathrm{TeV}} \sim 1.1 \times 10^{48}$ erg for CRs is required, as calculated from the mass of the total target material. For this scenario, we assume CRs have propagated a distance of $R \sim 12$ pc from the accelerator to the cloud, within the lifetime of the SNR. Modelling of the CR spectra showed that the CR interpretation requires slow diffusion ($\chi \leq 0.01$) in order to match the observed GeV and TeV CR enhancement factors. It is, therefore, possible for SNR G8.7−0.1 to generate the TeV γ-ray emission from HESS J1804−216 for the hadronic scenario. We also consider CRs being produced from the undetected progenitor SNR of PSR J1803−2137 for the hadronic scenario. The derived CR enhancement factors for HESS J1804−216 and FGES J1804.8−2144 are well matched for $\chi = 0.01$ or 0.001.

For the purely leptonic scenario, the TeV emission is produced by highly energetic electrons from PSR J1803−2137 as a PWN. A TeV γ-ray efficiency of $\sim$3% was found, supporting this scenario from an energetics point of view. As the diffusion time for CR electrons of 12 kyr is less than the age of PSR J1803−2137 (16 kyr), the electrons are able to diffuse 30 pc to create a TeV source of this size. Component C (corresponding to the distance of PSR J1803−2137) shows gas structures which anti-correlate with the TeV emission from HESS J1804−216, typical of a PWN-driven TeV source. A PWN from PSR J1803−2137 could, therefore, potentially contributes to the TeV γ-ray emission, so the leptonic scenario cannot be ruled out.

PSR J1803−2149 is also considered for the leptonic scenario. The TeV luminosity at the distance to this pulsar, 1.3 kpc, requires a 1% conversion efficiency of the spin-down power of PSR J1803−2149, a value within the typical efficiencies seen in other firmly identified PWN. However, the large offset between PSR J1803−2149 and the TeV peak of HESS J1804−216 indicates a PWN scenario is unlikely.

HESS J1804−216 still remains unidentified in nature due to the complex environment of the initial detection; however, a middle-aged SNR or PSR provides a valid interpretation. It may also be possible that the TeV emission has contributions from both leptonic and hadronic processes. Future work will focus on modelling the spectral energy distribution in more detail, in particular for the case of high-energy electrons. Future γ-ray observations from the next-generation ground-based observatory, the Cherenkov Telescope Array (CTA), will provide improved angular resolution (few arcminutes) and sensitivity compared to the currently operating telescope arrays. These will provide a more detailed look into many unidentified γ-ray sources, including HESS J1804−216, allowing us to further constrain the nature of HESS J1804−216.

References

Abdo, A. A., et al. 2010, ApJS, 187, 460

Abdo, A. A., et al. 2013, ApJS, 208, 17

Acero, F., et al. 2016, ApJS, 224, 8

Ackermann, M., et al. 2017, ApJ, 843, 139

Ade, P., et al. 2011, A&A 536

Aharonian, F. A. 1991, Ap&SS, 180, 305

Aharonian, F. A., & Atoyan A. M. 1996, A&A, 309, 917

Aharonian, F., et al. 2005, Science, 307, 1938

Aharonian, F., et al. 2006, ApJ, 636, 777

Ajello, M., et al. 2012, ApJ, 744, 80

Anderson, L. D., Bania, T. M., Balser, D. S., Cunningham, V., Wenger, T. V., Johnstone, B. M., & Armentrout, W. P. 2014a, VizieR Online Data Catalog, p. J/ApJS/212/1

Anderson, L. D., Bania, T. M., Balser, D. S., et al. 2014b, APJS, 212, 1

Berezinskii, V. S., Bulanov, S. V., Dogiel, V. A., & Ptuskin, V. S. 1990, Astrophysics of cosmic rays

Bolatto, A. D., Wolfire, M., & Leroy, A. K. 2013, ARA&A, 51, 207

Braiding, C., et al. 2018, PASA, 35, e029

Brand, J., & Blitz, L. 1993, A&A, 275, 67

Brisken, W. F., Carrillo-Barragán, M., Kurtz, S., & Finley, J. P. 2006, ApJ, 652, 554

Burton, M. G., et al. 2013, PASA, 30, e044

Casanova, S., et al. 2010, PASJ, 62, 1127

Claussen, M. J., Frail, D. A., Goss, W. M., & Gaume, R. A. 1997, ApJ, 489, 143

Clifton, T. R., & Lyne, A. G. 1986, Nature, 320, 43

Crutcher, R. M., Wandelt, B., Heiles, C., Falgarone, E., & Troland, T. H. 2010, ApJ, 725, 466

Dame, T. M., Hartmann, D., & Thaddeus, P. 2001, ApJ, 547, 792

Dermer, C. D. 1986, A&A, 157, 223

Dickey, J. M., & Lockman, F. J. 1990, ARA&A, 28, 215

Fang, J., & Zhang, L. 2008, MNRAS, 384, 1119

Fernandez, D., et al. 2013, preprint (arXiv:1305.6396)

Finkbeiner, D. P. 2003, ApJS, 146, 407

Finley, J. P., & Oegelman, H. 1994, ApJ, 434, L25

Frail, D. A., Goss, W. M., & Slysh, V. I. 1994, ApJ, 424, L111

Frerking, M. A., Wilson, R. W., Linke, R. A., & Wannier, P. G. 1980, ApJ, 240, 65

Gabici, S., Aharonian, F. A., & Blasi, P. 2007, Ap&SS, 309, 365

Gabici, S., Aharonian, F. A., & Casanova, S. 2009, MNRAS, 396, 1629

Gabici, S., Casanova, S., Aharonian, F. A., & Rowell, G. 2010, in SF2A-2010: Proceedings of the Annual meeting of the French Society of Astronomy and Astrophysics, ed. S. Boissier, M. Heydari-Malayeri, R. Samadi, & D. Valls-Gabaud, 313 (arXiv:1009.5291)

Giuliani, A., et al. 2010, A&A, 516, L11

Gusdorf, A., Cabrit, S., Flower, D. R., & Pineau Des Forêts, G. 2008, A&A, 482, 809

H.E.S.S. Collaboration, et al. 2018a, A&A, 612, A1

H.E.S.S. Collaboration, et al. 2018b, A&A, 612, A1

Hewitt, J. W., & Yusef-Zadeh, F. 2009, ApJl, 694, L16

Higashi, Y., et al. 2008, ApJ, 683, 957

Ho, P. T. P., & Townes, C. H. 1983, ARA&A, 21, 239

Jackson, J. M., et al. 2013, PASA, 30, e057

Kargaltsev, O., Pavlov, G. G., & Garmire, G. P. 2007a, ApJ, 660, 1413

Kargaltsev, O., Pavlov, G. G., & Garmire, G. P. 2007b, APJ, 670, 643

Kassim, N. E., & Weiler, K. W. 1990, ApJ, 360, 184

Kelner, S. R., Aharonian, F. A., & Bugayov, V. V. 2006, PhRvD, 74, 034018

Kilpatrick, C. D., Bieging, J. H., & Rieke, G. H. 2016, ApJ, 816, 1

Ladd, N., Purcell, C., Wong, T., & Robertson, S. 2005, PASA, 22, 62

Li, H., & Chen, Y. 2010, MNRAS: Letters, 409, L35

Li, H., & Chen, Y. 2012, MNRAS, 421, 935

Li, D., et al. 2018, ApJS, 235, 1

Lin, D., Webb, N. A., & Barret, D. 2013, APJ, 766, 29

Martin-Pintado, J., Bachiller, R., & Fuente, A. 1992, A&A, 254, 315

McClure-Griffiths, N. M., Dickey, J. M., Gaensler, B. M., Green, A. J., Haverkorn, M., & Strasser, S. 2005, ApJS, 158, 178

Morris, D. J., et al. 2002, MNRAS, 335, 275

Nicholas, B. P., Rowell, G., Burton, M. G., Walsh, A. J., Fukui, Y., Kawamura, A., & Maxted, N. I. 2012, MNRAS, 419, 251

Odegard, N. 1986, AJ, 92, 1372

Penzias, A. A., Solomon, P. M., Wilson, R. W., & Jefferts, K. B. 1971, ApJ, 168, L53

Planck Collaboration, et al. 2016, A&A, 594, A10

Pletsch, H. J., et al. 2012, ApJ, 744, 105

Protheroe, R. J., Ott, J., Ekers, R. D., Jones, D. I., & Crocker, R. M. 2008, MNRAS, 390, 683

Qasim, D., Chuang, K.-J., Fedoseev, G., Ioppolo, S., Boogert, A. C. A., & Linnartz, H. 2018, A&A, 612, A83

Reynolds, S. P. 2008, ARA&A, 46, 89

Saz Parkinson, P. M., et al. 2010, ApJ, 725, 571

Simon, R., Jackson, J. M., Clemens, D. P., Bania, T. M., & Heyer, M. H. 2001, ApJ, 551, 747

Sodroski, T. J., Odegard, N., Arendt, R. G., Dwek, E., Weiland, J. L., Hauser, M. G., & Kelsall, T. 1997, ApJ, 480, 173

Urquhart, J. S., et al. 2010, PASA, 27, 321

Vallée, J. P. 2014, AJ, 148, 5

Voronkov, M. A., Caswell, J. L., Ellingsen, S. P., & Sobolev, A. M. 2010, MNRAS, 405, 2471

Walsh, A. J., et al. 2011, MNRAS, 416, 1764

Yamazaki, R., Kohri, K., Bamba, A., Yoshida, T., Tsuribe, T., & Takahara, F. 2006, MNRAS, 371, 1975

de Wilt, P., et al. 2017, MNRAS, 468, 2093

Appendix

A. Pulsar proper motion

The proper motion of PSR J1803−2137 has been studied by Brisken et al. (2006) via radio observations. The proper motion of PSR J1803−2137 has been calculated for the right ascension (RA) and declination (Dec), $\mu_\alpha = (11.6 \pm 1.8) \times 10^{-3}$ arcsec yr^{-1} and $\mu_\delta = (14.8 \pm 2.3) \times 10^{-3}$ arcsec yr^{-1}, respectively. Given an age of ∼16 kyr for PSR J1803−2137, a birth position for the pulsar of RA = $18^h03^m38^s.0$ and Dec = $-21°41'18''.2$ is obtained, placing it on edge of the W30 SNR, SNR G8.7−0.1.

B. HII regions

HII data were used from the WISE (Anderson et al. 2014b) satellite in order to reveal the known HII regions towards HESS J1804−216 (Figure B.1). These regions were chosen such that their radius was larger than 50 arcmins. The online catalogue (Anderson et al. 2014a) provides the velocity (v_{lsr}) of each HII region, which correspond to kinematic distances ranging from 3 to 5 kpc.

C. PV plot

Figure C.1 is a PV plot towards the HESS J1804−216 region. This figure shows distinct Mopra ^{12}CO(1-0) emission in the velocity ranges from $v_{lsr} = 10$ to 25 km s^{-1} and $v_{lsr} = 35$ to 40 km s^{-1} which is consistent with the molecular gas discussed in Section 4.2.

D. Galactic rotation curve

Objects within the galaxy are rotating around the GC. The GRC is a model which gives the average velocity of an object in the galaxy with respect to the GC as a function of distance. The kinematic distance to an object can be found by knowing the position and radial velocity of the given object, from Equation (D.1) (Brand & Blitz 1993):

$$v_{lsr} = \left[\frac{\Theta R_0}{R} - \Theta_0 \right] \sin(l) \cos(b) \qquad (D.1)$$

where R is the galactocentric distance (distance of an object from the centre of the Milky Way galaxy) to the object and Θ is the circular rotation velocity of object. R_0 is the galactocentric distance from the Sun and Θ_0 is the circular rotation velocity at the position of the Sun, commonly given values 8.5 kpc and 220 km s^{-1}, respectively. The galactic coordinates are given by
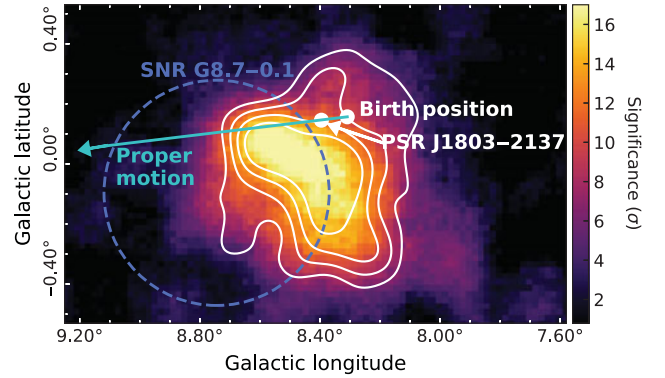
Figure A.1. TeV γ-ray significance image of HESS J1804−216 (H.E.S.S. Collaboration et al. 2018a), showing the proposed proper motion of PSR J1803−2137 (Brisken et al. 2006). The TeV γ-ray emission for 5-10σ is shown by the solid white contours, SNR G8.7−0.1 is shown by the blue dashed circle, and the white dots indicate PSR J1803−2137 and its birth position.
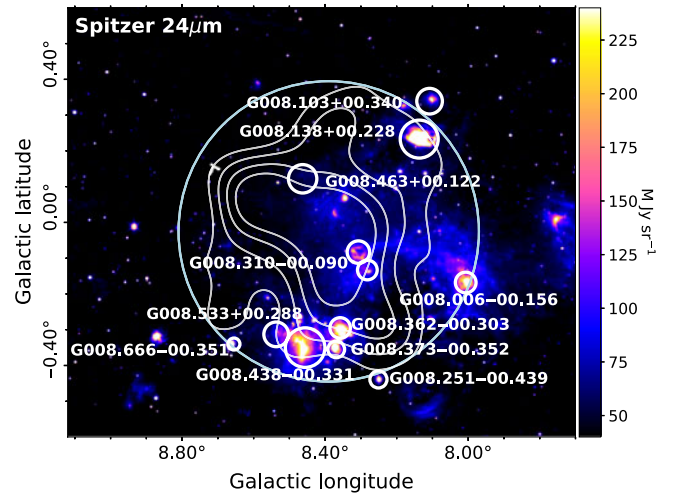
Figure B.1. 24 μm infrared image [M Jy sr^{-1}] towards *HESS J*1804−216 from the Spitzer GLIMPSE Survey. The TeV γ-ray emission for 5-10σ is shown by the solid white contours, with the cyan circle showing the extent of *HESS J*1804−216. HII regions with a radius greater than 50 arcmin are indicated by the white circles from WISE (Anderson et al. 2014b).

l (galactic longitude) and b (galactic latitude). The galactic model along the line of sight for HESS J1804−216 is shown by Figure D.1.

E. HI spectra and absorption

The spectra of the HI data are shown in Figure E.1. Dips tend to occur in the HI spectra which result from either the presence of a background source that leads to absorption or from HI self-absorption. A well-defined HI absorption feature is present at $v_{lsr} + \sim 20$ km s^{-1} which corresponds to a strong emission feature in the ^{12}CO spectra (shown in Figure 2). This strong absorption feature could be due to a continuum source, such as SNR G8.7−0.1. These properties indicate that the gas is most likely to be foreground to SNR G8.7−0.1. This helps to constrain the distance to the SNR, proving that the pre-defined distance of 4.5 kpc (seen in Section 1) is consistent with the gas data analysis shown here.

F. Integrated intensity maps

The ISM is made up of both atomic and molecular gas, primary HI and ^{12}CO emission, respectively. However, there are regions in which these gas tracers become 'invisible', due to a lack of emission. It has been shown that
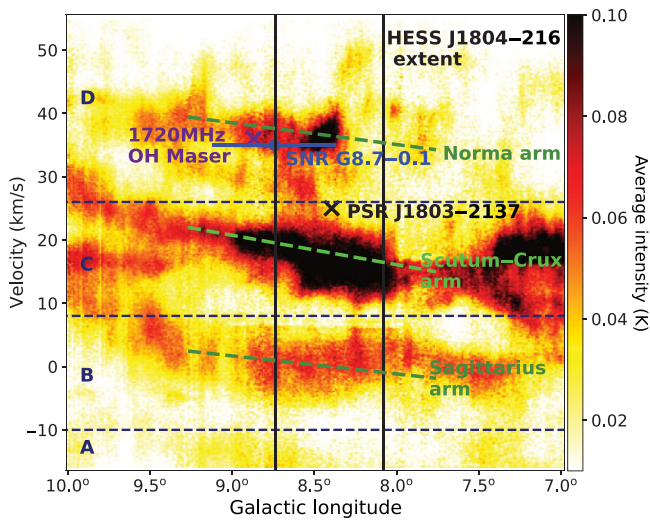
Figure C.1. Position–velocity plot of Mopra ^{12}CO(1-0) emission (K) towards HESS J1804−216. The black vertical lines show the longitudinal extent of HESS J1804−216. The black cross indicates the location of PSR J1803−2137 at its assumed velocity of ∼25 km s^{-1}. The 1720-MHz OH maser is shown by the purple cross at its velocity of 36 km s^{-1}. The centre of SNR G8.7−0.1 is shown by the blue dot, whilst the blue line shows its radial extent. The green dashed lines are estimates of the Galactic spiral arms along the line of sight for HESS J1804−216 (from the model in Vallée 2014).
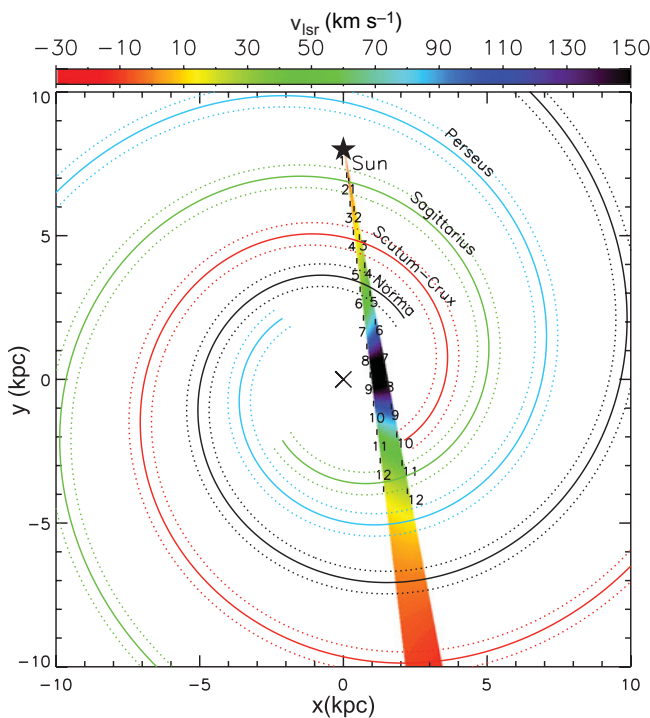
Figure D.1. Model of the galaxy along the line of sight of HESS J1804−216. Parameters used in this model are from Vallée (2014) for each spiral arm shown by the solid coloured lines, Perseus (light blue), Sagittarius (light green), Scutum-Crux (red), and Norma (black). The dashed lines for each spiral arm show their extent. The coloured wedge shows the expected line of sight for HESS J1804−216 from the Sun for the radial velocities (v_{lsr}) using the galactic rotation model from Brand & Blitz (1993). The numbers along this wedge show the distance to the source in kiloparsecs (kpc). The spatial coordinates along the axes are given in kpc also.

Table F.1 Molecular lines with each of their rest line frequencies from the 7-mm receiver of the Mopra telescope.

Molecular line	Line rest frequency (GHz)
^{30}SiO(1-0, v = 0)	42.373365
SiO(1-0, v = 3)	42.519373
SiO(1-0, v = 2)	42.820582
SiO(1-0, v = 1)	43.122079
SiO(1-0, v = 0)	43.423864
CH$_3$OH(I)	44.069476
HC$_7$N(40-39)	45.119064
HC$_5$N(17-16)	45.264750
HC$_3$N(5–4, F = 5-5)	45.488839
^{13}CS(1-0)	46.247580
HC$_5$N(16-15)	47.927275
C^{34}S(1-0)	48.206946
OCS(4-3)	48.651604
CS(1-0)	48.990957
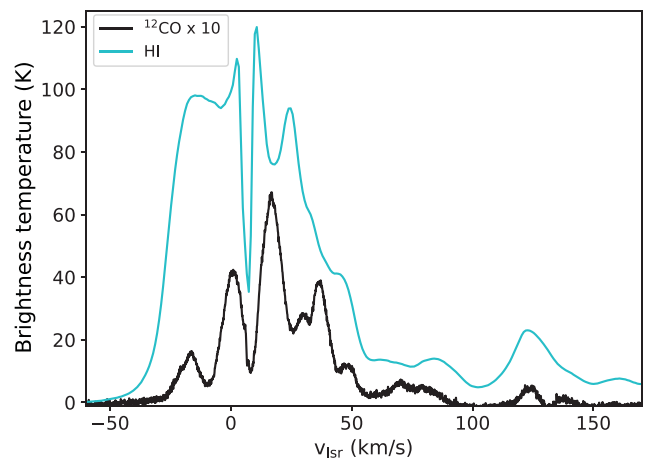
Figure E.1. Emission spectrum towards HESS J1804−216. Solid black lines and cyan lines represent the spectrum for Mopra ^{12}CO(1-0) and SGPS HI, respectively. ^{12}CO is scaled by a factor of 10 for clarity.

there is a component of gas which has not been detected, commonly known as 'dark' gas (Li et al. 2018).

In addition to the common neutral gas tracers (HI and ^{12}CO), a component of ionised gas is present in interstellar clouds. For cases in which clouds are optically thick, the dust opacity that maps from the Planck collaboration (Planck Collaboration et al. 2016) can be used to estimate a hydrogen column density (Ade et al. 2011). The column density derived via this method contains no distance information as the dust opacity map has been summed over the line of sight. The Planck hydrogen column density is, therefore, an upper limit.

To determine the Planck HII column density, the free–free emission map was required (Planck Collaboration et al. 2016). To convert the emission map into a free–free intensity map, the conversion factor is $I_\nu = 46.04$ Jy sr^{-1} at 353 GHz (from Finkbeiner 2003) was applied. Equation (5) from Sodroski et al. (1997) is then used to derive the HII column density. Here, we use an effective electron density (n_{eff}) of 10 cm^{-3} as a lower limit. Similarly to the Planck hydrogen column density, the HII column density is integrated along the whole line of sight. The bottom panel of Figure F.6 shows the ratio

between column density derived from the dust opacity map and column density from free–free emission (H<small>II</small> column density).

The total hydrogen column density traced by the HI and ^{12}CO emission is taken along the entire line of sight ($v_{lsr}+ = 50$ to 150 km s^{-1}) to allow for comparison between it and the Planck data, which has no distance information.

The total hydrogen column density (top panel of Figure F.6) has morphological similarities to the total column density as derived from the dust opacity map, as demonstrated in the middle panel of Figure F.6. In particular, we note the dense region of gas to the Galactic South of the TeV source present in both column density maps. They are also on the same order of magnitude; hence to compare the H<small>II</small> column density with the total hydrogen column density, it is acceptable to use the dust opacity column density. This ratio is presented in the bottom panel of Figure F.6. The ratio values indicate that the total neutral column density is dominating over the component of ionised gas. For this purpose, the total column density used throughout this paper does not take the ionised gas into account.

F.1. Dense gas tracer mosaics

Table F.1 shows the molecular lines that were observed by the 7-mm observing set-up for the MOPS.

The integrated intensity maps for the various dense gas tracers towards HESS J1804−216 are presented in Figure F.7, F.8, F.9, F.10 and F.11.

SiO(1-0, v = 0) emission has been detected towards HESS J1804−216; however, it is quite weak. There are a few dense features in components B, C, and D; however, these show features which have already been seen in the other dense gas tracers (see Section 4.2).

In Figure F.11, we have included the known H$_2$O maser positions from Walsh et al. (2011), at their given velocities.

G. CR spectra model

Equation (7) can be adjusted to calculate the CR enhancement factor from the GeV γ-rays from FGES J1804.8−2144, as shown by Equation (G.1). An integral power law spectrum of $E^{-1.75}$ is assumed, following Aharonian (1991) for GeV energies:

$$F(\geq E_\gamma) = 1.45 \times 10^{-13} E_{\mathrm{TeV}}^{-1.75} \left(\frac{M_5}{d_{\mathrm{kpc}}^2} \right) k_{\mathrm{CR}} \quad \mathrm{cm}^{-2}\ \mathrm{s}^{-1}, \qquad (\mathrm{G}.1)$$

The photon flux for γ-rays from FGES J1804.8−2144 is $F(\geq 10\,\mathrm{GeV}) = 1.56 \times 10^{-9}$ cm^{-2} s^{-1} (Ackermann et al. 2017). This leads to a CR enhancement factor, k_{CR}, of ~ 9 times that of the Earth-like CR density for SNR G8.7−0.1 (component D) at GeV energies.

Using Equation (14), the energy spectrum of CR protons is obtained for a range of diffusion suppression factors, χ's, and indices of the diffusion coefficient, δ's, to test the validity of each value, as shown in Figure G.1.

Values of $\delta = 0.5$ & 0.7 for $\chi = 0.01$ are the most plausible for the hadronic scenario for SNR G8.7−0.1 (see Section 5.1).

Figure G.2 shows the energy spectrum of CR protons escaping from the progenitor SNR of PSR J1803−2137. The total energy budget of CRs in this scenario is taken to be 10^{48} erg which is consistent with $W_{p,\mathrm{TeV}}$ from Equation (5) (see also Table 3) using component C. A CR enhancement factor, k_{CR}, of ~ 57 is obtained for TeV energies (using Equation (7)) and ~ 14 for GeV energies (using Equation (G.1)).
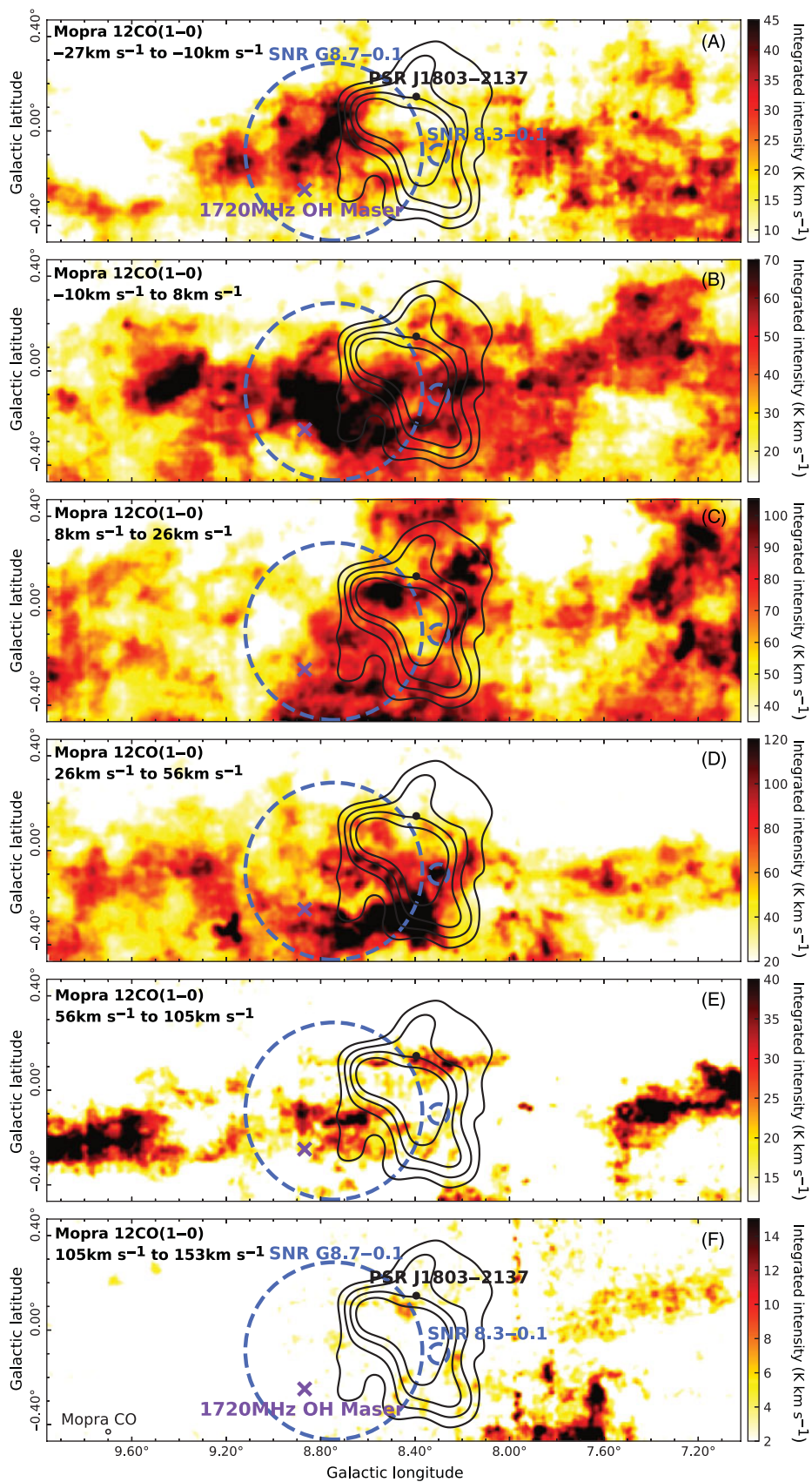
Figure F.1. Mosaic of Mopra ^{12}CO integrated intensity maps (K km s^{-1}) towards HESS J1804−216, for gas components A–F as defined in Figure 2. The two dashed blue circles indicate SNR G8.7−0.1 and SNR 8.3−0.1. The 1720-MHz OH is indicated by the purple cross and PSR J1803−2137 is indicated by the black dot. The TeV γ-ray emission for 5-10σ is shown by the solid black contours.
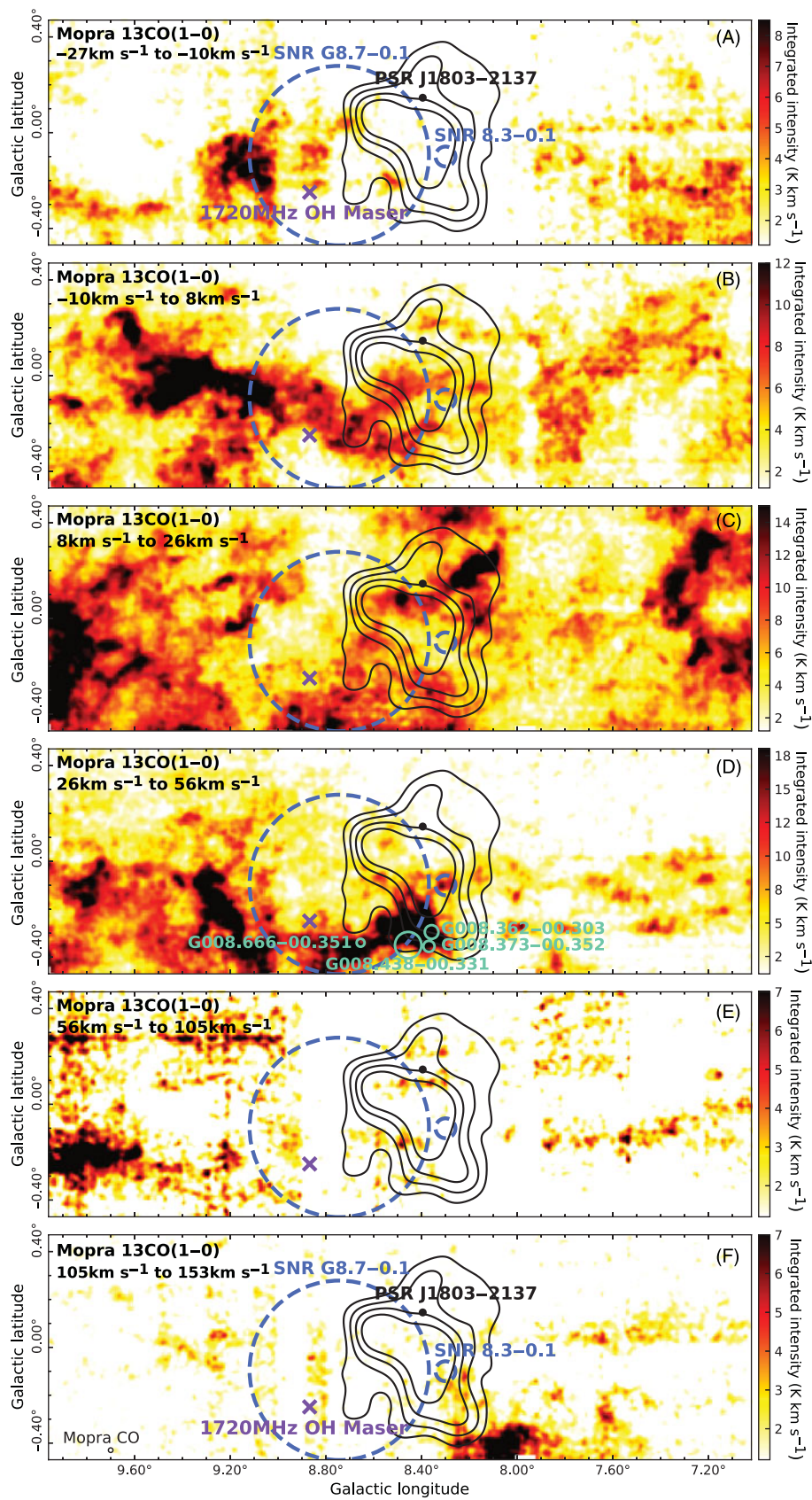
Figure F.2. Mosaic of Mopra ^{13}CO integrated intensity maps (K km s^{-1}) towards HESS J1804−216. The two dashed blue circles indicate SNR G8.7−0.1 and SNR 8.3−0.1. The 1720-MHz OH is indicated by the purple cross and PSR J1803−2137 is indicated by the black dot. The TeV γ-ray emission for 5-10σ is shown by the solid black contours. The aqua circles in component D indicate H$_{II}$ regions.
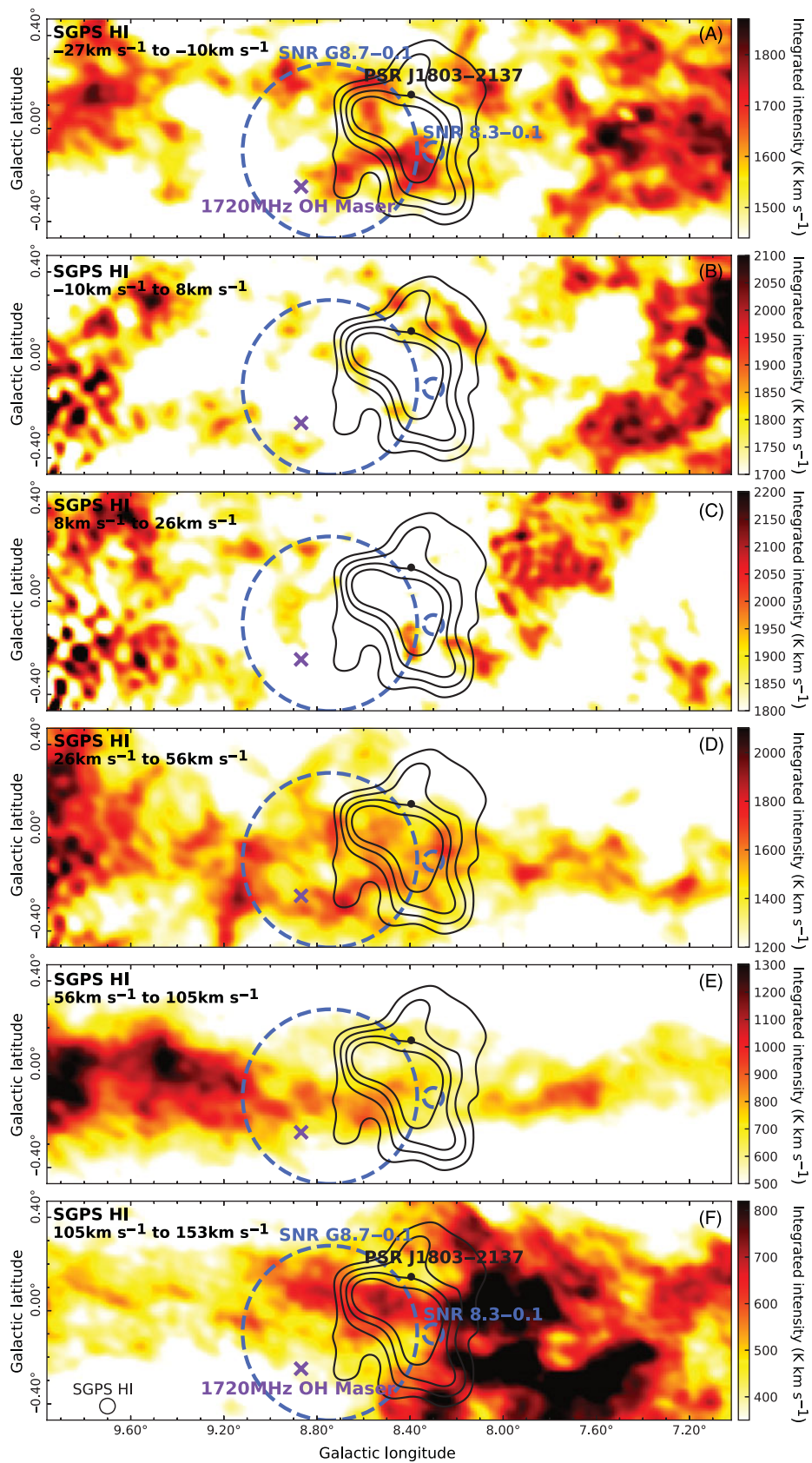
Figure F.3. Mosaic of SGPS HI integrated intensity maps (K km s^{-1}) towards HESS J1804$-$216. The two dashed blue circles indicate SNR G8.7$-$0.1 and SNR 8.3$-$0.1. The 1720-MHz OH is indicated by the purple cross and PSR J1803$-$2137 is indicated by the black dot. The TeV γ-ray emission for 5-10σ is shown by the solid black contours.
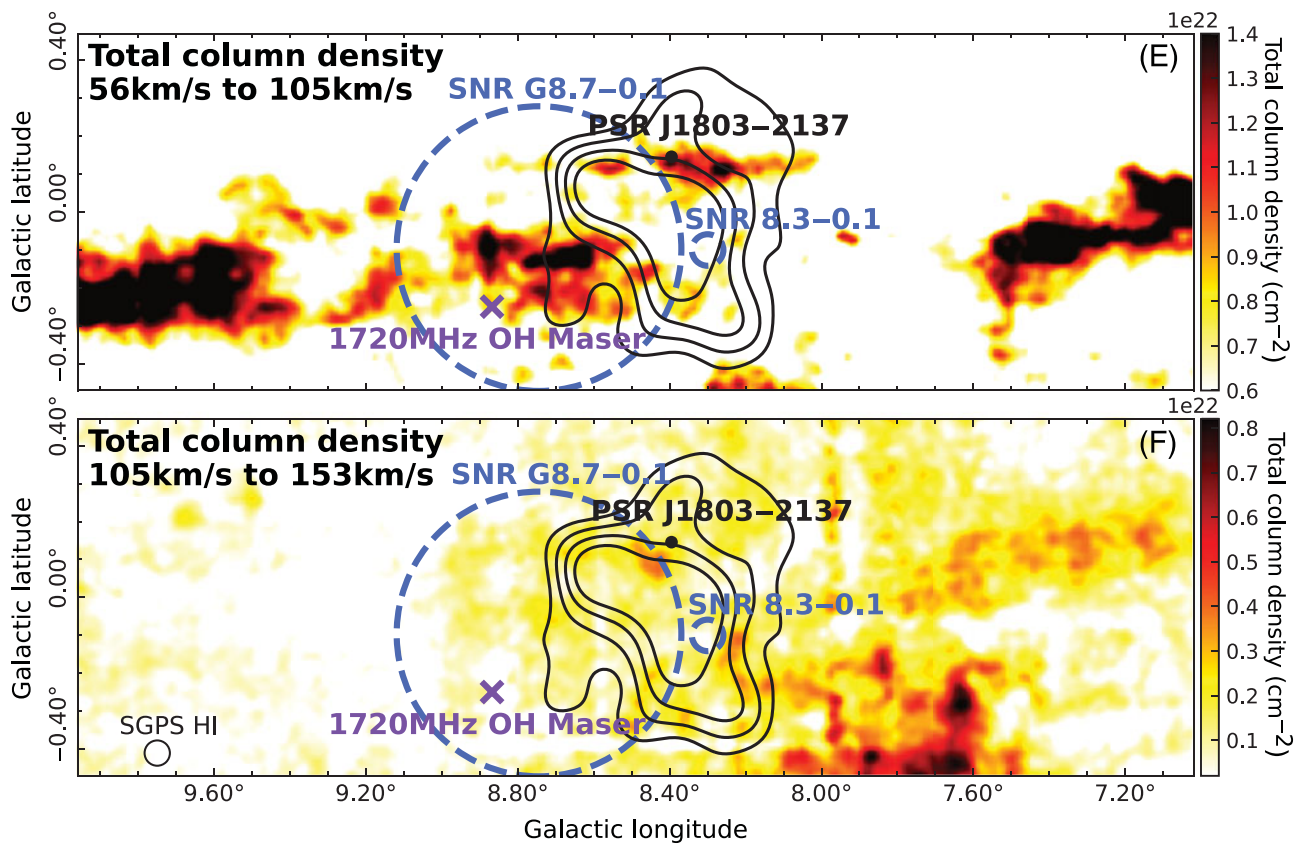
Figure F.4. Total column density maps, $2N_{H_2} + N_{HI}$, (cm^{-2}) towards HESS J1804−216, for gas components E and F. The two dashed blue circles indicate SNR G8.7−0.1 and SNR 8.3−0.1. The 1720-MHz OH is indicated by the purple cross and PSR J1803−2137 is indicated by the black dot. The TeV γ-ray emission for 5-10σ is shown by the solid black contours.
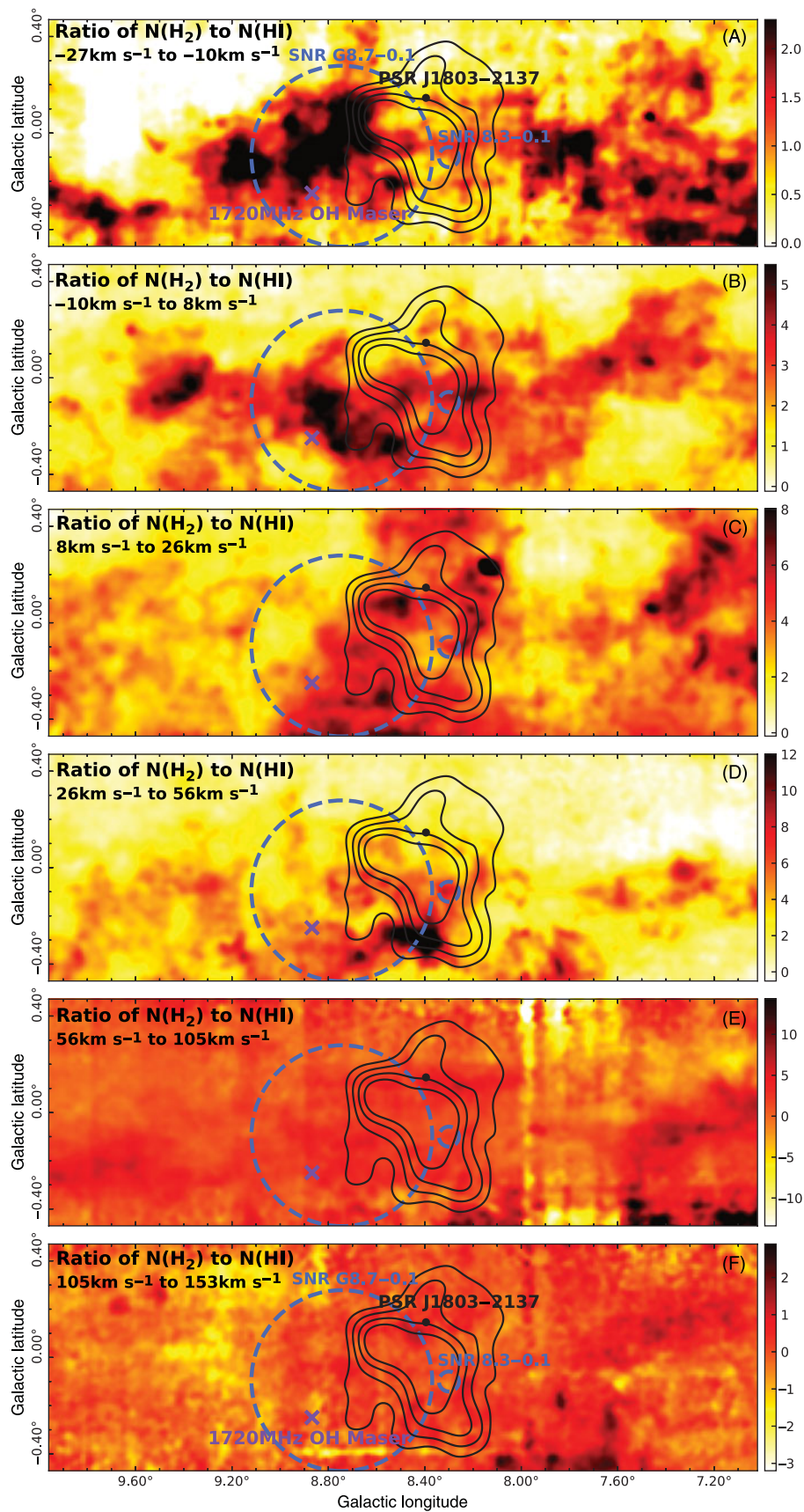
Figure F.5. Ratio of molecular hydrogen (N_{H_2}) and atomic hydrogen (N_{HI}) column densities towards HESS J1804−216, for gas components A–E. The two dashed blue circles indicate SNR G8.7−0.1 and SNR 8.3−0.1. The 1720-MHz OH is indicated by the purple cross and PSR J1803−2137 is indicated by the black dot. The TeV γ-ray emission for 5-10σ is shown by the solid black contours.
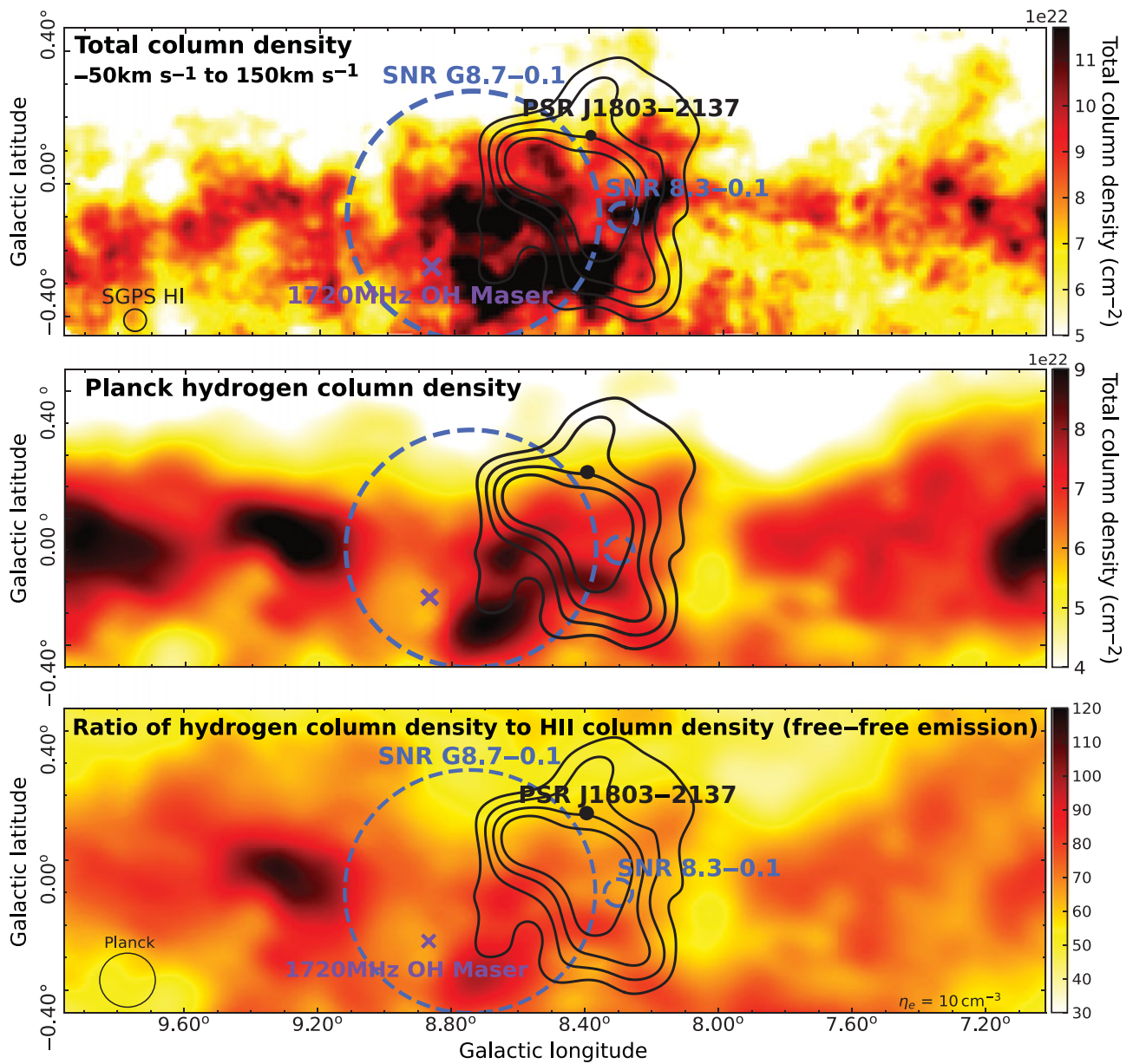
Figure F.6. *Top:* Total column density map (cm^{-2}) from the SGPS HI and Mopra ^{12}CO emission, along the entire line of sight (v_{lsr} = 50 to 150 km s^{-1}) of HESS J1804−216. *Middle*: Planck hydrogen column density. *Bottom*: Ratio of hydrogen column density as derived from Planck dust opacity and H II column density from free–free emission. *All*: The two dashed blue circles indicate SNR G8.7−0.1 and SNR 8.3−0.1. The 1720-MHz OH is indicated by the purple cross and PSR J1803−2137 is indicated by the black dot. The TeV γ-ray emission for 5-10σ is shown by the solid black contours.
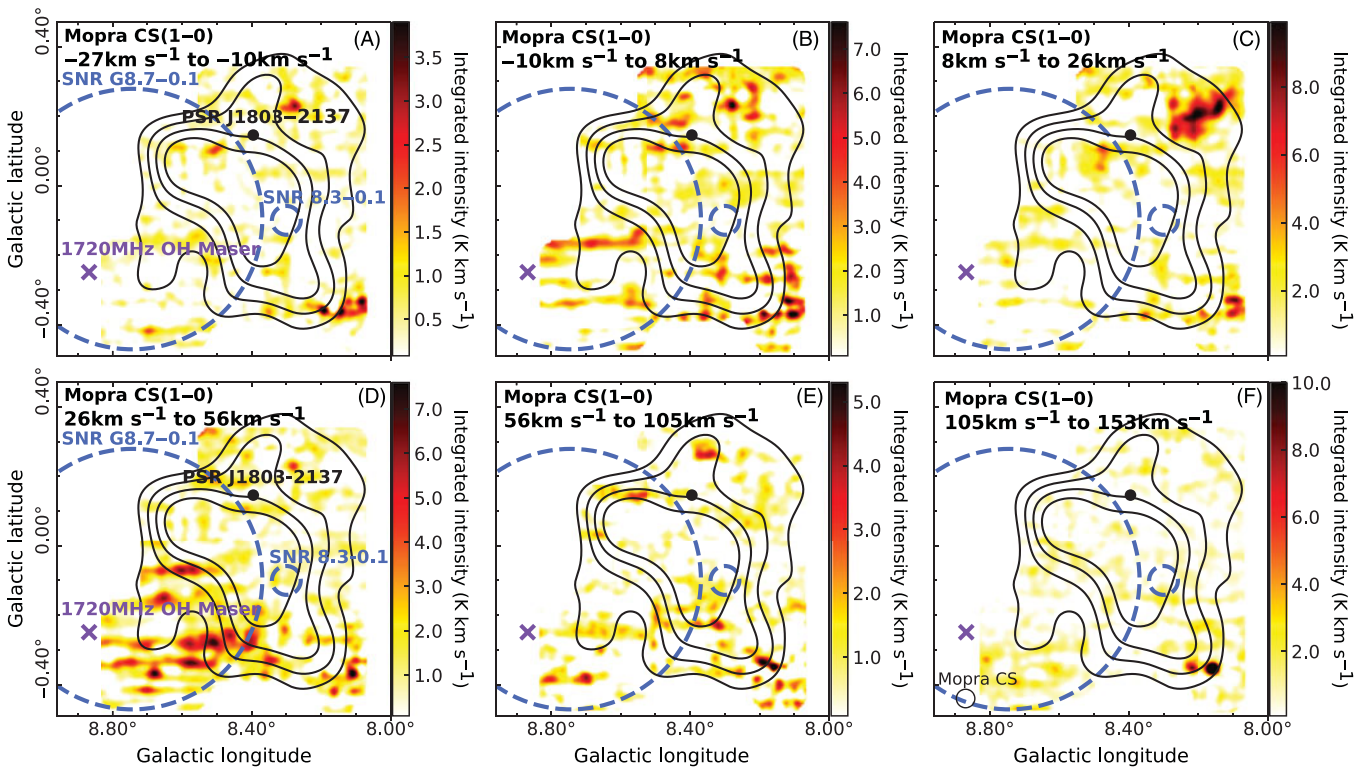
Figure F.7. CS(1-0) integrated intensity maps (K km s^{-1}) towards HESS J1804−216. For components A through F, the T$_{rms}$ is 2.5, 2.7, 2.8, 3.5, 4.3, and 4.2 K, respectively. The two dashed blue circles indicate SNR G8.7−0.1 and SNR 8.3−0.1. The 1720-MHz OH is indicated by the purple cross and PSR J1803−2137 is indicated by the black dot. The TeV γ-ray emission for 5-10σ is shown by the solid black contours.
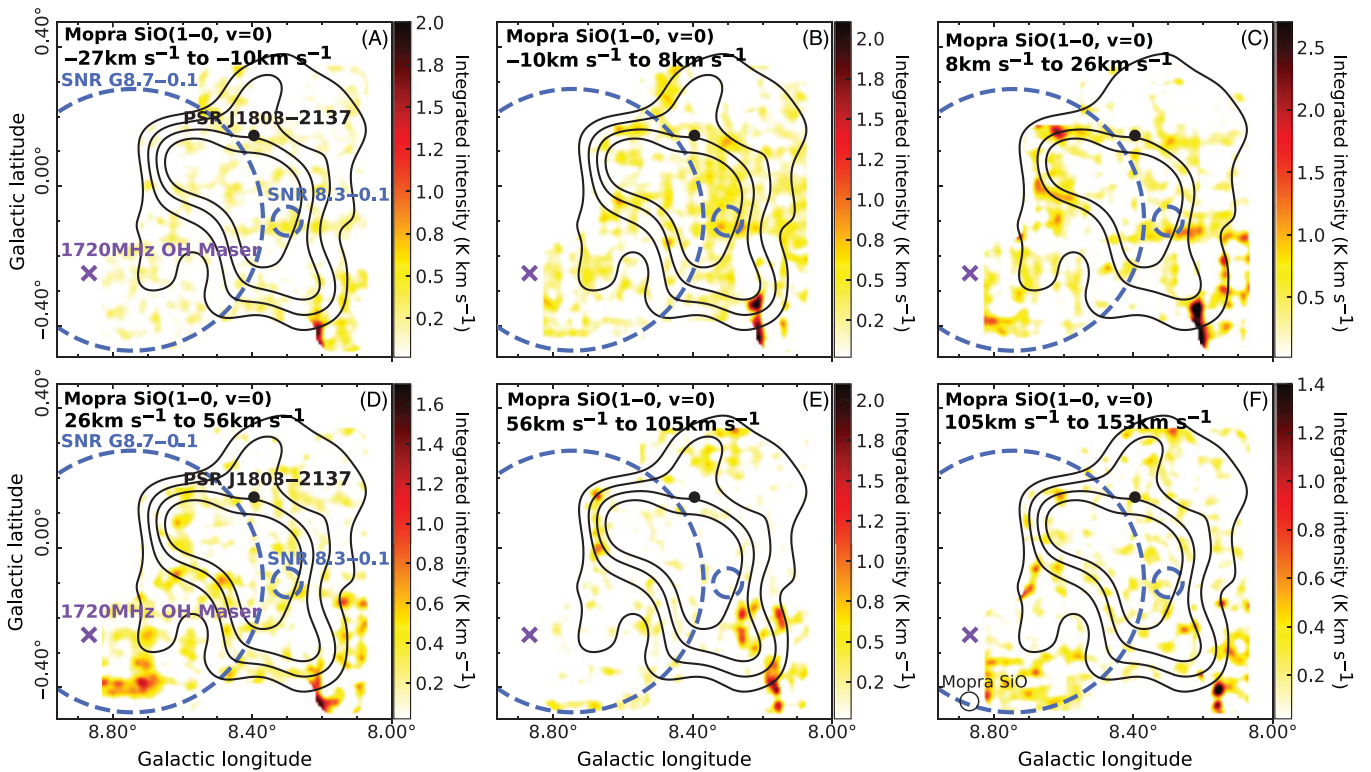
Figure F.8. SiO(1-0, v = 0) integrated intensity maps (K km s^{-1}) towards HESS J1804−216. For components A through F, the T$_{rms}$ is 1.3 K, 1.3 K, 1.4 K, 1.7 K, 2.2 K, and 2.2 K, respectively. The two dashed blue circles indicate SNR G8.7−0.1 and SNR 8.3−0.1. The 1720-MHz OH is indicated by the purple cross and PSR J1803−2137 is indicated by the black dot. The TeV γ-ray emission for 5-10σ is shown by the solid black contours.
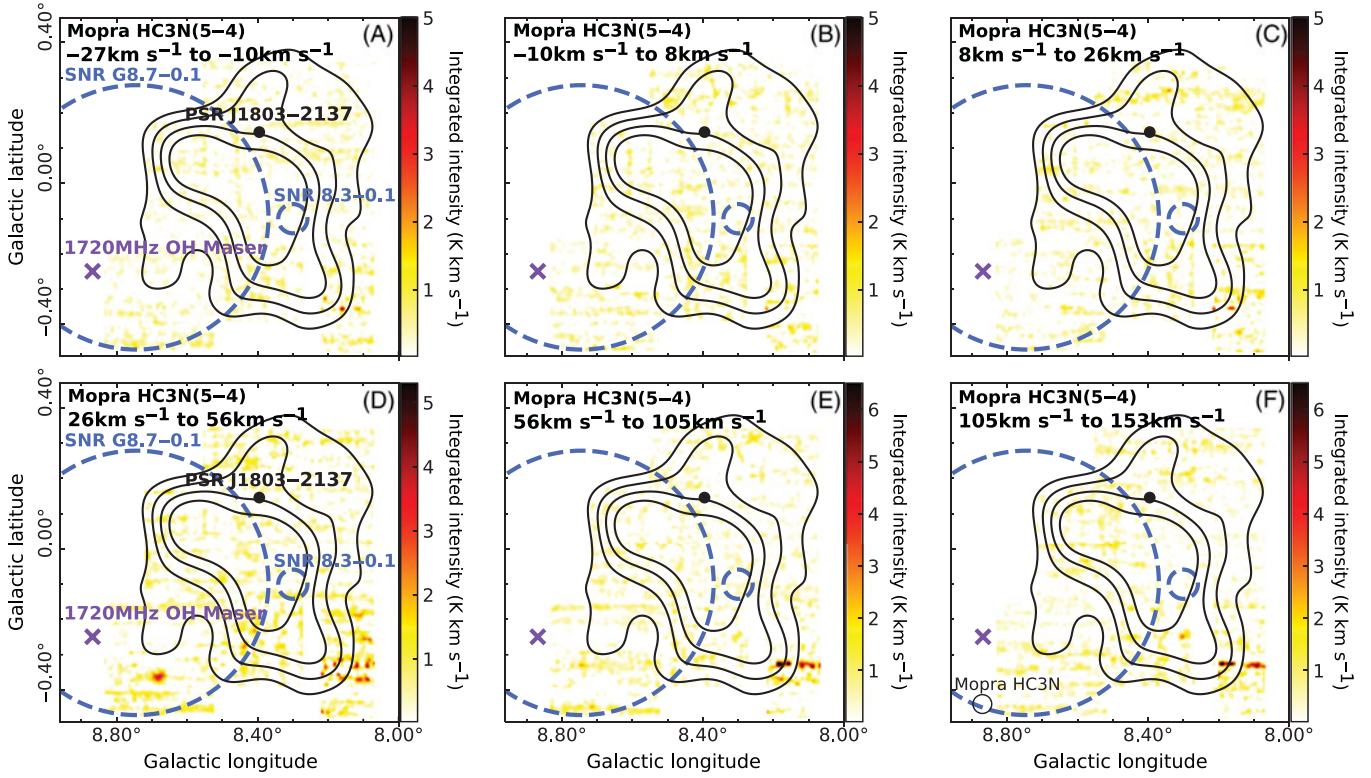
Figure.F.9. HC$_3$N(5-4) integrated intensity maps (K km s^{-1}) towards HESS J1804−216. For components A through F, the T$_{rms}$ is 3.6 K, 3.8 K, 3.8 K, 4.9 K, 6.1 K, and 6.1 K, respectively. The two dashed blue circles indicate SNR G8.7 − 0.1 and SNR 8.3−0.1. The 1720-MHz OH is indicated by the purple cross and PSR J1803−2137 is indicated by the black dot. The TeV γ-ray emission for 5-10σ is shown by the solid black contours.
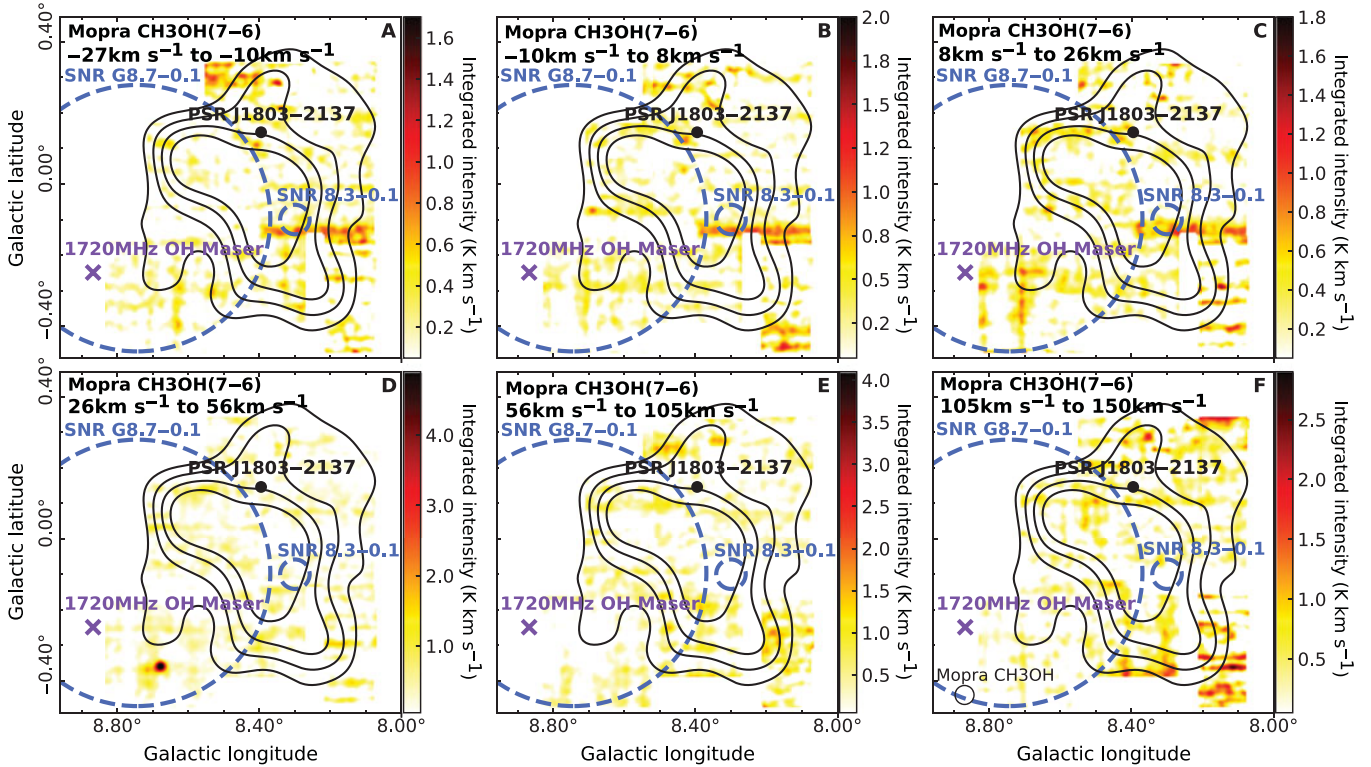
Figure.F.10. CH$_3$OH integrated intensity maps (K km s^{-1}, uncleaned) towards HESS J1804−216. For components A through F, the T$_{rms}$ is 0.8 K, 0.9 K, 0.9 K, 1.1 K, 1.4 K, and 1.4 K, respectively. The two dashed blue circles indicate SNR G8.7−0.1 and SNR 8.3−0.1. The 1720-MHz OH is indicated by the purple cross and PSR J1803−2137 is indicated by the black dot. The TeV γ-ray emission for 5-10σ is shown by the solid black contours.
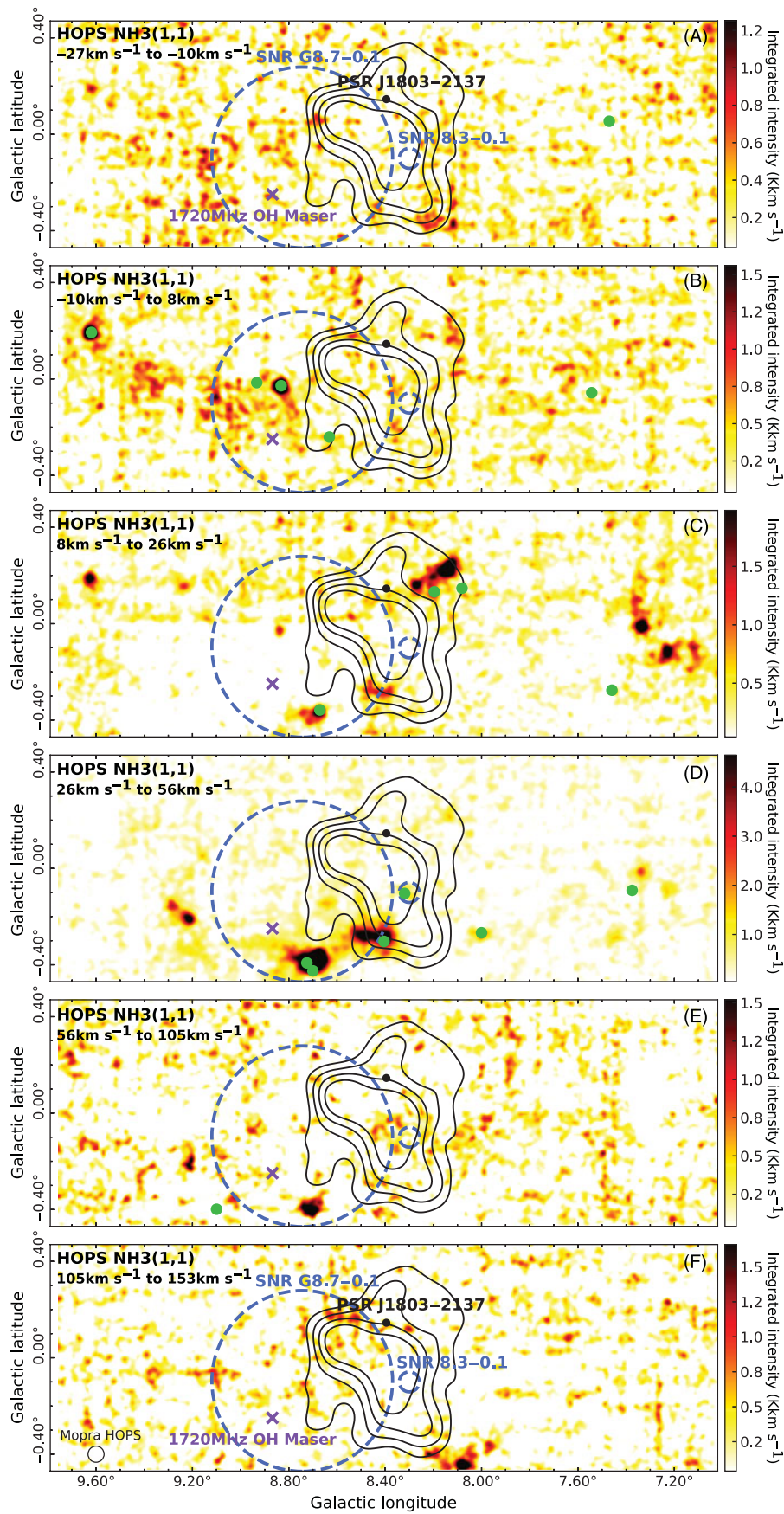
Figure F.11. NH$_3$(1, 1) integrated intensity maps (K km s^{-1}) towards HESS J1804−216 using HOPS data. The two dashed blue circles indicate SNR G8.7−0.1 and SNR 8.3−0.1. The 1720-MHz OH is indicated by the purple cross and PSR J1803−2137 is indicated by the black dot. The TeV γ-ray emission for 5-10σ is shown by the solid black contours. H$_2$O maser positions are shown by the green dots.
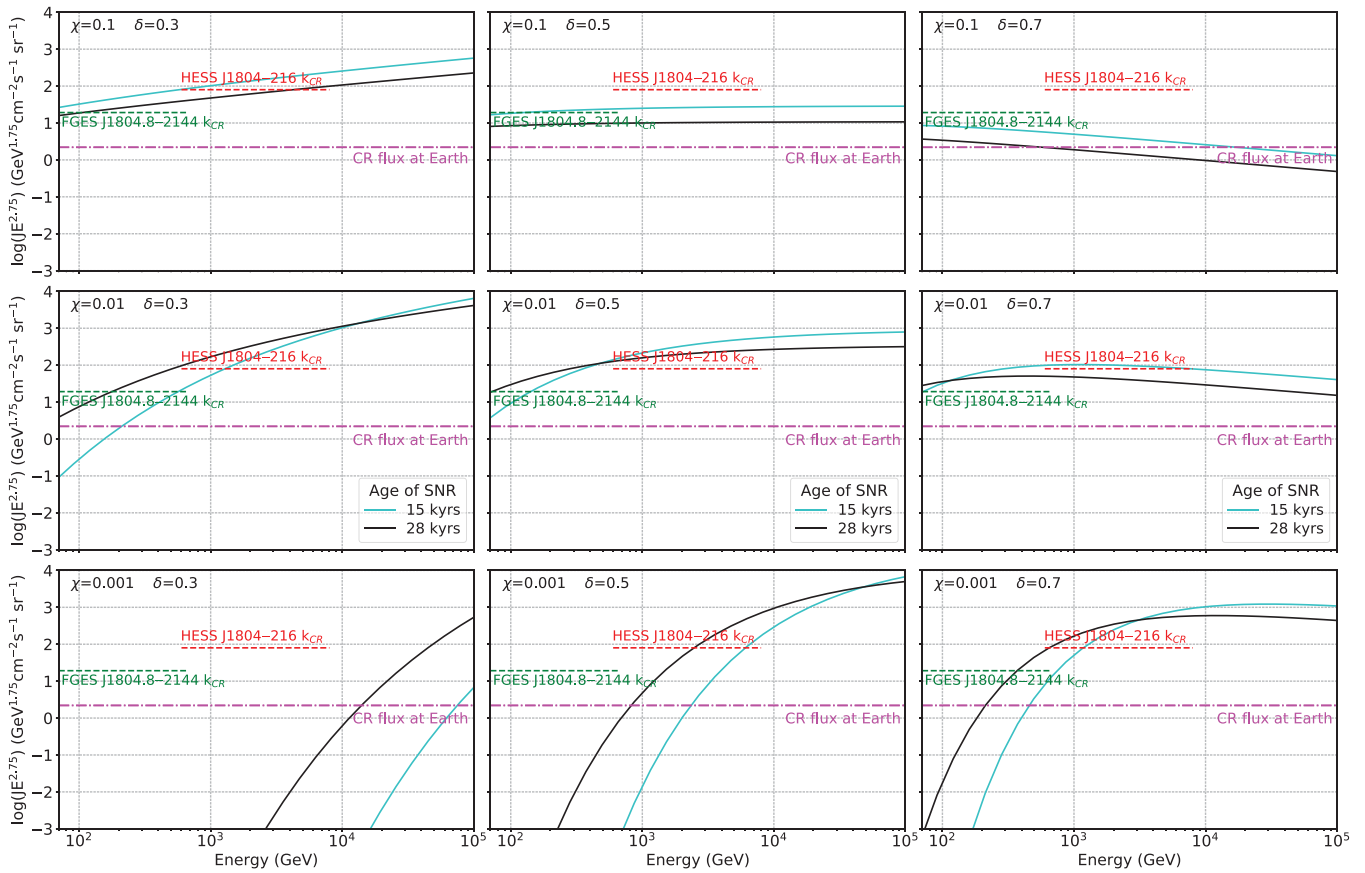
Figure G.1. Modelled energy spectra of CR protons (Equation (14)) escaping from the potential impulsive accelerator SNR G8.7−0.1, with a total energy of 2×10^{48} erg in CRs. Various values of diffusion suppression factor, χ, and index of the diffusion coefficient, δ, are shown here. A power law spectrum with a spectral index of $\alpha = 2$ is assumed. The number density is taken to be $n = 160$ cm^{-3}. The distance from the accelerator to the cloud is $R \sim 12$ pc and age of the source are taken to be 15 kyr and 28 kyr for the cyan and black curves, respectively. The magenta dashed line represents the CR flux observed at Earth. The red represents the calculated CR enhancement factor for HESS J1804−216 ($k_{CR} \approx 37$). The green represents the calculated CR enhancement factor for FGES J1804.8−2144 ($k_{CR} \approx 9$).
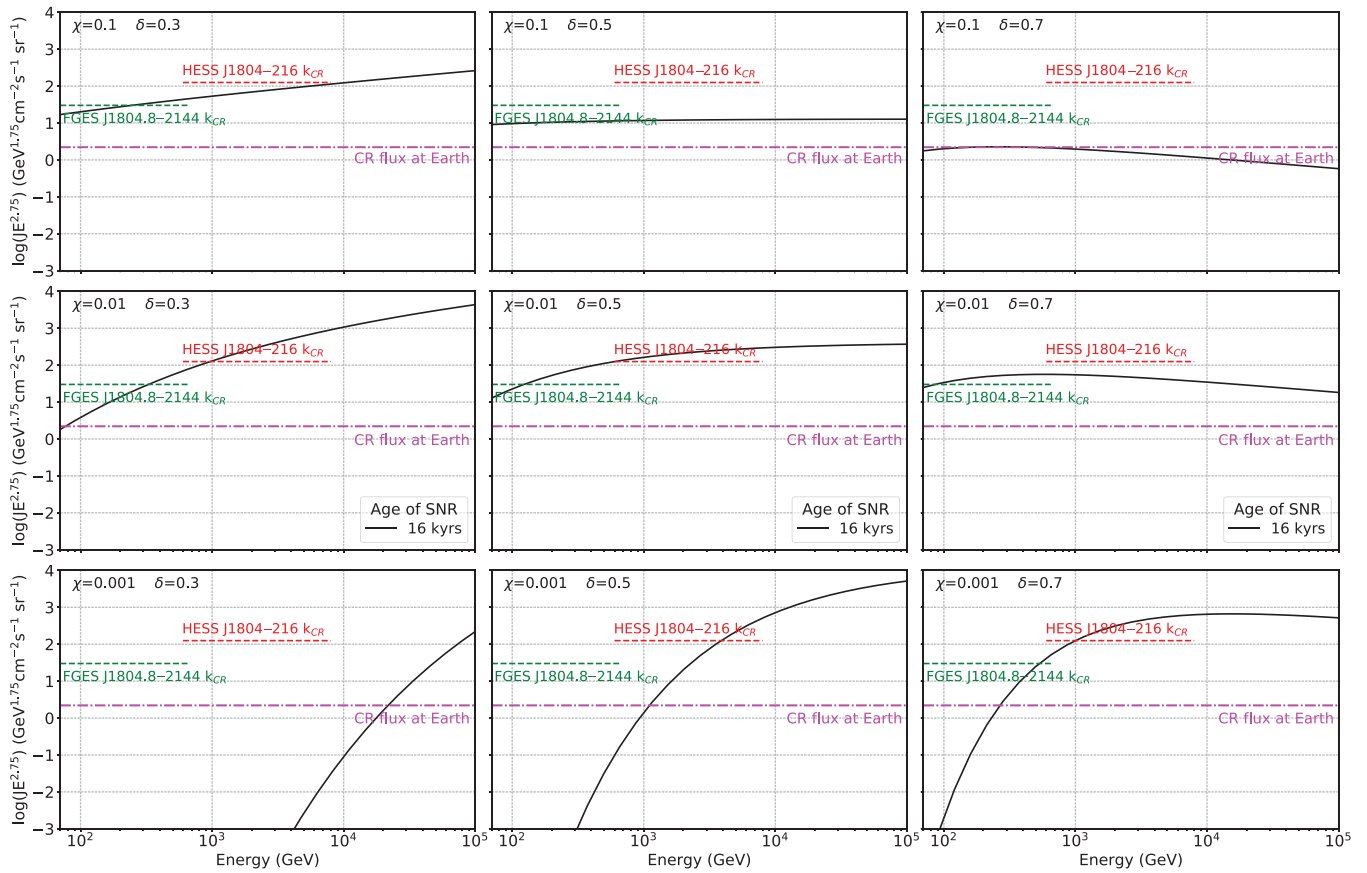
Figure G.2. Modelled energy spectra of CR protons (Equation ([14](#))) escaping from the potential impulsive accelerator (progenitor SNR from PSR J1803−2137), with a total energy of 10^{48} erg in CRs. Various values of diffusion suppression factor, χ, and index of the diffusion coefficient, δ, are shown here. A power law spectrum with a spectral index of $\alpha = 2$ is assumed. The number density is taken to be $n = 325$ cm^{-3}. The distance from the accelerator to the cloud is $R \sim 10$ pc and age of the source is taken to be 16 kyr for the black curves. The magenta dashed line represents the CR flux observed at Earth. The red represents the calculated CR enhancement factor for HESS J1804−216 ($k_{CR} \approx 57$). The green represents the calculated CR enhancement factor for FGES J1804.8−2144 ($k_{CR} \approx 14$).

6   Paper 2: Modelling the Hadronic Scenario for HESS J1804−216

The following paper entitled 'Modelling the Gamma-Ray Morphology of HESS J1804−216 from Two Supernova Remnants in a Hadronic Scenario' has been published in the peer-reviewed journal Monthly Notices of the Royal Astronomical Society (MNRAS). In this contribution, the simulated γ-ray morphology from hadronic interactions is compared to recent observations of HESS J1804−216. The spatial and spectral distributions of cosmic-rays are generated for a range of model parameters, describing, amongst others, the diffusion and the injection spectrum of cosmic rays. Based on these cosmic-ray distributions and measurements of the ISM, the spatial and spectral distributions of γ-rays are created. A comparison between these models and γ-ray observations may reveal the origin and corresponding acceleration processes at place for HESS J1804−216.

Statement of Authorship

Title of Paper	Modelling the Gamma-Ray Morphology of HESS J1804−216 from Two Supernova Remnants in a Hadronic Scenario
Publication Status	☒ Published ☐ Accepted for Publication ☐ Submitted for Publication ☐ Unpublished and Unsubmitted work written in manuscript style
Publication Details	K. Feijen et al. 2022, MNRAS 511, 5915-5926 Author list: K. Feijen, S. Einecke, G. Rowell, C. Braiding, M. G. Burton, G. F. Wong

Principal Author

Name of Principal Author	Kirsty Feijen
Contribution to the Paper	Modelling, programming, high energy interpretation, writing the paper
Overall percentage (%)	59%
Certification:	This paper reports on original research I conducted during the period of my Higher Degree by Research candidature and is not subject to any obligations or contractual agreements with a third party that would constrain its inclusion in this thesis. I am the primary author of this paper.
Signature	Date 3-12-21

Co-Author Contributions

By signing the Statement of Authorship, each author certifies that:

    i.   the candidate's stated contribution to the publication is accurate (as detailed above);

    ii.   permission is granted for the candidate in include the publication in the thesis; and

    iii.   the sum of all co-author contributions is equal to 100% less the candidate's stated contribution.

Name of Co-Author	Sabrina Einecke
Contribution to the Paper	Modelling, programming and high energy interpretation, general paper review (25%)
Signature	Date Nov 30, 2021

Name of Co-Author	Gavin Rowell
Contribution to the Paper	Model ideas and high energy interpretation, general paper review (10%)
Signature	Date 3/12/21

Name of Co-Author	Catherine Braiding		
Contribution to the Paper	Mopra observation, data reduction and cleaning (2%)		
Signature		Date	30/11/21

Name of Co-Author	Michael Burton		
Contribution to the Paper	Mopra observation, data reduction and cleaning (2%)		
Signature		Date	02/11/21

Name of Co-Author	Graeme Wong		
Contribution to the Paper	Mopra observation, data reduction and cleaning (2%)		
Signature		Date	14/11/21

Modelling the gamma-ray morphology of HESSJ1804−216 from two supernova remnants in a hadronic scenario

K. Feijen [1]★ S. Einecke [1]★ G. Rowell,[1] C. Braiding,[2]† M. G. Burton [2,3] and G. F. Wong[4,2]

[1]*School of Physical Sciences, University of Adelaide, Adelaide, SA 5005, Australia*
[2]*School of Physics, The University of New South Wales, Sydney, NSW 2052, Australia*
[3]*Armagh Observatory and Planetarium, College Hill, Armagh BT61 9DG, UK*
[4]*Western Sydney University, Locked Bag 1797, Penrith South DC, NSW 2751, Australia*

ABSTRACT

HESS J1804−216 is one of the brightest yet most mysterious TeV γ-ray sources discovered to date. Previous arc-minute scale studies of the interstellar medium (ISM) surrounding this TeV γ-ray source revealed HESS J1804−216 is likely powered by a mature supernova remnant (SNR) or pulsar, hence its origin remains uncertain. In this paper, we focus on the diffusive escape of cosmic ray protons from potential SNR accelerators. These cosmic rays interact with the ISM to produce TeV γ-rays. We utilize the isotropic diffusion equation solution for particles escaping from a shell, to model the energy-dependent escape and propagation of protons into the ISM. This work is the first attempt at modelling the spatial morphology of γ-rays towards HESS J1804−216, using arc-minute ISM observations from both Mopra and the Southern Galactic Plane Survey. The spectral and spatial distributions of γ-rays for the two nearby potential SNR counterparts, SNR G8.7−0.1 and the progenitor SNR of PSR J1803−2137, are presented here. We vary the diffusion parameters and particle spectrum and use a grid search approach to find the best combination of model parameters. We conclude that moderately slow diffusion is required for both candidates. The most promising candidate to be powering the TeV γ-rays from HESS J1804−216 in a hadronic scenario is the progenitor SNR of PSR J1803−2137.

Key words: cosmic-rays – ISM: individual objects (HESS J1804−216) – Gamma-rays: ISM.

1 INTRODUCTION

The High Energy Stereoscopic System (H.E.S.S.) has a sensitivity to γ-rays of energy 100 GeV to tens of TeV. H.E.S.S. has identified numerous γ-ray sources in the Milky Way (or 'Galactic sources'), however, the exact nature of over 30 per cent of these sources remains unknown (H.E.S.S. Collaboration 2018a). These sources are also possibly the sites of cosmic ray (CR) accelerators, the population of these sources are dominated by objects within their final stages of stellar evolution.

HESS J1804−216 is one of the brightest unidentified TeV γ-ray sources detected, with a soft spectral index of $\Gamma = 2.69$. The GeV γ-ray source, 3FHL J1804.7−2144e, was detected at the same location as the TeV γ-ray source HESS J1804−216 (see Fig. 1).

In a previous paper (Feijen et al. 2020), we studied the interstellar medium (ISM) towards HESS J1804−216 in detail at arc-min scales, to help determine the nature of the γ-ray emission. We investigated multiple plausible CR accelerators and concluded that a mature supernova remnant (SNR G8.7−0.1 or the progenitor SNR of PSR J1803−2137) or a pulsar (PSR J1803−2137) are viable accelerators of CRs to produce the TeV γ-ray emission in the hadronic and

leptonic scenarios, respectively. The hadronic production of γ-rays involves accelerated CR protons interacting with the ISM to produce γ-rays through neutral pion decay (Ackermann et al. 2013). The leptonic scenario primarily involves TeV emission being produced by inverse-Compton upscattering by highly energetic electrons. The TeV emission from HESS J1804−216 could be produced by high-energy electrons from a pulsar wind nebulae (PWNe) powered by PSR J1803−2137 (H.E.S.S. Collaboration 2018b), as supported by the high spin-down luminosity. The modelled energy spectra of CR protons towards both SNR G8.7−0.1 and the progenitor SNR of PSR J1803−2137 matched with GeV and TeV observations, making it plausible for either SNR to generate the GeV and TeV γ-ray emission from HESS J1804−216.

SNRs are a typical candidate in accelerating CR protons at their shock front (Blandford & Ostriker 1980). The hadronic production of γ-rays is investigated in this paper, assuming either SNR G8.7−0.1 or the progenitor SNR of PSR J1803−2137 (shown in Fig. 1) are the plausible CR accelerators. A 1720 MHz OH maser is present at the southern edge of SNR G8.7−0.1 at 36 km s^{-1} indicating the SNR (at a velocity of 35 km s^{-1}) is interacting with the ISM (Hewitt & Yusef-Zadeh 2009).

Models of the γ-ray emission from escaping CRs have previously been presented for different γ-ray sources, such as Casanova et al. (2010) for SNR RX J1713.7−3946 and Mitchell et al. (2021) for multiple SNRs. Casanova et al. (2010) model accelerated CRs escaping SNR RX J1713.7−3946 in the hadronic and leptonic scenarios.

★ Email:kirsty.feijen@adelaide.edu.au (KF); sabrina.einecke@adelaide.edu.au (SE)
† Presently at: Australian Space Agency, Adelaide, Australia

Figure 1. Integrated flux map (cm^{-2} s^{-1}) above 1 TeV adapted from H.E.S.S. Collaboration (2018a). The dashed purple circle indicates SNR G8.7−0.1, the purple cross indicates the 1720 MHz OH maser and the progenitor SNR of PSR J1803−2137 is indicated by the blue dot. The TeV γ-ray emission from H.E.S.S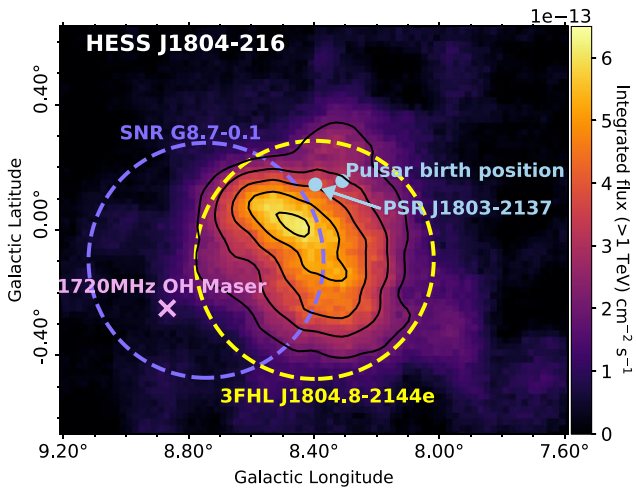. Collaboration (2018a) is shown by the solid black contours (2 × 10^{-13} to 6 × 10^{-13} cm^{-2} s^{-1} levels).

Morphology maps of the γ-ray energy flux at 1 TeV were obtained using the distribution of the ambient gas for different diffusion conditions. Casanova et al. (2010) model the γ-ray morphology by utilizing the LAB survey of HI and the Nanten survey of CO, which provides a detailed look into the distribution of γ-ray emission.

This work expands on our previous paper by predicting the morphology arising from the diffusive energy-dependent escape of CR protons and interaction with the surrounding ISM in the hadronic scenario. We make use of the spherically symmetric case for the isotropic transport equation from Aharonian & Atoyan (1996), assuming CR protons are accelerated by a single source and the energy-dependent diffusion coefficient is constant with position. The γ-ray emission is modelled across all pixels of the gas column density map from the Mopra ^{12}CO(1-0) survey and the Southern Galactic Plane Survey (SGPS) of HI for a wide range of parameters, to find the best combination of model parameters to match the observations. We present a first look at the 2D spatial morphology of γ-rays towards HESS J1804−216. This provides an important framework for understanding the region surrounding γ-ray sources, in particular the diffusive transport of particles from SNRs into the ISM.

2 DATA

The distribution of atomic hydrogen (HI) from the SGPS[1] (McClure-Griffiths et al. 2005) and molecular hydrogen, specifically ^{12}CO(1-0), from the Mopra radio telescope[2] are utilized. The Australia Telescope National Facility (ATNF) analysis software, LIVEDATA, GRIDZILLA, and MIRIAD in addition to custom IDL routines were used to process the data from Mopra (Burton et al. 2013; Braiding et al. 2018). Integrated emission maps were generated from the FITS cubes.

In this work, we use maps of total column density as these provide the distribution of the total target material towards

HESS J1804−216. The total hydrogen column density, N_H, is the sum of N_{HI} and 2N_{H_2}, from SGPS HI observations and Mopra ^{12}CO (regridded to the SGPS HI pixel size of ∼40 arcsec).

The two plausible counterparts of interest are SNR G8.7−0.1 and the progenitor SNR of PSR J1803−2137 which are at distances of 4.5 kpc (Hewitt & Yusef-Zadeh 2009) and 3.8 kpc (Brisken et al. 2006), respectively. SNR G8.7−0.1 has an age of 15–28 kyr (Finley & Oegelman 1994) and the progenitor SNR of PSR J1803−2137 has an age of 16 kyr (Brisken et al. 2006), assumed to be the same age as the pulsar it is attached to.

An 1720 MHz OH maser is indicative of interaction between SNRs and ISM clouds (Hewitt & Yusef-Zadeh 2009). Given the OH maser velocity of 36 km s^{-1}, we expect SNR G8.7−0.1 to be at a similar velocity. With use of the Galactic Rotation Curve (GRC, Brand & Blitz 1993) and the distance to each SNR, the progenitor SNR of PSR J1803−2137 and SNR G8.7−0.1 are placed at a velocity of ∼25 km s^{-1} and ∼35 km s^{-1}, respectively.

The velocity components are determined by taking the velocity of each counterpart as the mid point of our range. If the velocity ranges chosen are too large, additional gas emission which is likely not connected to the source will be included. Due to local motions in the gas and the uncertainty of the GRC model, we estimate that the velocity bands should span 10 km s^{-1}. The position-velocity plots in Figs A1 and A2 show that our defined velocity regions are reasonable as they do not include too much of the gas located in the Galactic arms. Currently, the SGPS HI data (Fig. A2) does not reveal any HI voids making it hard to narrow down these velocity ranges further. Future HI surveys, such as the GASKAP HI survey (Dickey et al. 2013), will have a higher resolution and be more sensitive to voids and bubbles in the HI gas. Fig. 2 shows the total column density maps derived from SGPS HI and Mopra CO for components 1 ($v_{lsr} = 20$ to 30 km s^{-1}) and 2 ($v_{lsr} = 30$ to 40 km s^{-1}).

The TeV γ-ray data used throughout this paper are from H.E.S.S.. Fig. 1 shows the γ-ray flux map above 1 TeV of HESS J1804−216 from the H.E.S.S Galactic Plane Survey (HGPS, H.E.S.S Collaboration 2018a). The HGPS γ-ray flux maps are available as oversampled maps which are obtained by dividing the survey region into a grid of 0.02°, then summing all values within a circular radius of 0.1° for each grid point.

The spectral γ-ray data from Aharonian et al. (2006) is utilized, as this paper focused on the TeV γ-ray sources in the inner part of the Galactic plane, including HESS J1804−216, providing a detailed look at the spectra and morphology of the TeV γ-ray observations. The Aharonian et al. (2006) and H.E.S.S Collaboration (2018a) data show good spectral matches as shown in Fig. C1. The Aharonian et al. (2006) data provides more spectral data points which will allow the spectral shape of our model to be compared with observations. The HESS J1804−216 spectral γ-ray observations from Aharonian et al. (2006) were extracted from a circular region of ∼0.36° radius centred on HESS J1804−216 ($l = 8.4°$, $b = −0.03°$). We also make use of the spectral γ-ray data of 3FHL J1804.7−2144e from Ajello et al. (2017), extracted from a disk region of 0.38° (centred on $l = 8.4°$, $b = −0.09°$).

3 MODELLING

SNRs can be described as impulsive accelerators, in which CRs are accelerated by the SNR shock front, and escape into the ISM. We model the energy-dependent escape and subsequent diffusive transport of these particles using the solution to the isotropic diffusive transport equation (Aharonian & Atoyan 1996). The injection of CRs is assumed to follow a power law, $E_p^{-\alpha}$, with a spectral index of α.
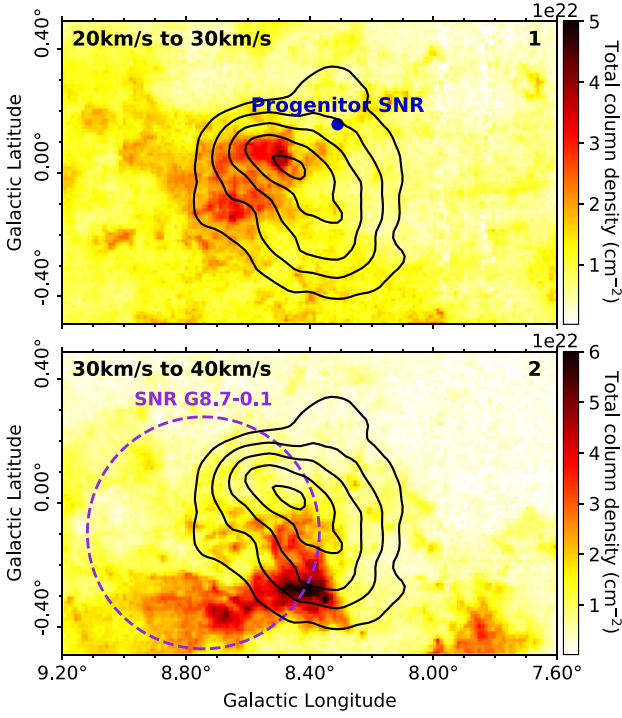
Figure 2. Total column density maps, $N_{\mathrm{HI}} + 2N_{\mathrm{H_2}}$, (cm^{-2}) towards HESS J1804−216, for gas components 1 and 2. The progenitor SNR of PSR J1803−2137 is indicated by the blue dot and the dashed purple circle indicates SNR G8.7−0.1. The TeV γ-ray emission from H.E.S.S Collaboration et al. (2018a) is shown by the solid black contours (2×10^{-13} to 6×10^{-13} cm^{-2} s^{-1} levels).

Protons of different energies escape the accelerator at different times, where the higher energy protons leave the shock earlier than lower energy protons. Particles then diffuse through the ISM and interact to produce γ-rays. Where relevant, we assume either a type Ia or type II supernova explosion occurs with a total kinetic energy of E_{SN}, and an energy budget in CRs of $W_p = \eta E_{\mathrm{SN}}$, where $\eta \leq 0.5$ (Berezhko & Völk 1997, 2000; Ackermann et al. 2013).

3.1 Proton flux

The volume distribution of CRs, escaping from a shell, taking into account the time-dependent escape of protons of energy E_p is given by equation (1).

$$J_{\mathrm{p}}(E_{\mathrm{p}}, R, t) = N_0 E_{\mathrm{p}}^{-\alpha} f_{\mathrm{p}}(E_{\mathrm{p}}, R, t) \ \mathrm{TeV}^{-1} \, \mathrm{cm}^{-3}, \tag{1}$$

where $f_{\mathrm{p}}(E_{\mathrm{p}}, R, t)$ is the probability density function (PDF) of protons, describing the probability of finding a particle of energy E_{p} at some distance from the accelerator, R. The time, t, is the time after the SN explosion. As we are interested in the evolutionary state of the SNR, we will use $t = t_{\mathrm{SNR}}$ in our model. The number density in our model is low ($n_{\mathrm{H}} < 10^2 \, \mathrm{cm}^{-3}$) which leads to a high proton–proton cooling time, $\tau_{\mathrm{pp}} \sim 6 \times 10^7 (n_{\mathrm{H}}/\mathrm{cm}^{-3})^{-1}$ yr. As we consider relatively young accelerators ($\tau_{\mathrm{pp}} \gg t$, where $t < 100$ kyr), we can neglect the cooling term in our model.

We assume the energy budget in CRs is the total energy of particles with energies from $E_{\mathrm{p,min}}$ to $E_{\mathrm{p,max}}$, $W_p = N_0 \int_{E_{\mathrm{p,min}}}^{E_{\mathrm{p,max}}} E \, E^{-\alpha} \mathrm{d}E$. From this definition, we determine the normalization factor, N_0, where the maximum energy is, $E_{\mathrm{p,max}}$ and the minimum energy is $E_{\mathrm{p,min}} = 1$ GeV.

We note that equation (3) from Aharonian & Atoyan (1996) relates to particles released from a point source. Our model instead, describes the time-dependent release of particles from a shell, so a modification (explained shortly) to account for this is adopted. The PDF of CR protons of energy E_{p} is given by:

$$f_{\mathrm{p}}(E_{\mathrm{p}}, R, t) = \begin{cases} f_{\mathrm{bubble}}(E_{\mathrm{p}}, R, t) & E_{\mathrm{p}} < E_{\mathrm{p,esc}}, \ R < R_{\mathrm{esc}} \\ f_{\mathrm{dif}}(E_{\mathrm{p}}, R, t) & E_{\mathrm{p}} > E_{\mathrm{p,esc}}, \ R > R_{\mathrm{esc}} \\ 0 & \mathrm{Otherwise} \end{cases} \tag{2}$$

The radius at which CR protons are released from the accelerator is given by equation (3) (Reynolds 2008).

$$R_{\mathrm{esc}} = 0.31 \left(\frac{E_{\mathrm{SN}}}{10^{51} \mathrm{erg}} \right)^{1/5} \left(\frac{n_0}{\mathrm{cm}^{-3}} \right)^{-1/5} \left(\frac{t_{\mathrm{esc}}}{\mathrm{yr}} \right)^{2/5} \ \mathrm{pc}, \tag{3}$$

where n_0 is the ISM number density the SNR shock wave expands into (Ptuskin & Zirakashvili 2005; Reynolds 2008; Ptuskin, Zirakashvili & Seo 2010). The escape time of CR protons is (Gabici, Aharonian & Casanova 2009):

$$t_{\mathrm{esc}}(E_{\mathrm{p}}) = t_{\mathrm{sedov}} \left(\frac{E_{\mathrm{p}}}{E_{\mathrm{p,max}}} \right)^{-1/\delta_{\mathrm{p}}}, \tag{4}$$

where $E_{\mathrm{p,max}}$ are the most energetic particles present at the start of the Sedov–Taylor phase. The onset of the Sedov–Taylor phase, t_{sedov}, is defined by equation (B1).

The escape energy of protons is defined by rearranging equation (4) and setting $t_{\mathrm{esc}} = t_{\mathrm{SNR}}$:

$$E_{\mathrm{p,esc}} = E_{\mathrm{p,max}} \left(\frac{t_{\mathrm{sedov}}}{t_{\mathrm{SNR}}} \right)^{\delta_{\mathrm{p}}}. \tag{5}$$

Particles at distance less than R_{esc} and with energy less than $E_{\mathrm{p,esc}}$ are trapped inside a sphere, which we call the 'bubble'. We assume that particles are uniformly distributed within this bubble, therefore the CR proton distribution can be described through:

$$f_{\mathrm{bubble}}(E_{\mathrm{p}}, R, t) = \frac{1}{(4/3)\pi R_{\mathrm{esc}}^3}. \tag{6}$$

The PDF for diffused CR protons is given by (Mitchell et al. 2021):

$$f_{\mathrm{dif}}(E_{\mathrm{p}}, R, t) = \frac{f_0}{\pi^{3/2} R_{\mathrm{dif}}^3} \exp\left[-\frac{(R - R_{\mathrm{esc}})^2}{R_{\mathrm{dif}}^2} \right]. \tag{7}$$

We require our equation to be normalized, with a factor:

$$f_0 = \frac{\sqrt{\pi} R_{\mathrm{dif}}^3}{(\sqrt{\pi} R_{\mathrm{dif}}^2 + 2\sqrt{\pi} R_{\mathrm{esc}}^2)|R_{\mathrm{dif}}| + 4 R_{\mathrm{esc}} R_{\mathrm{dif}}^2}. \tag{8}$$

The diffusion radius is

$$R_{\mathrm{dif}} \equiv R_{\mathrm{dif}}(E_{\mathrm{p}}, t) = 2\sqrt{D(E_{\mathrm{p}})t'}, \tag{9}$$

where $t' = t - t_{\mathrm{esc}}(E_{\mathrm{p}})$ represents the time the particles spend in the ISM. The energy-dependent diffusion coefficient from Gabici, Aharonian & Blasi (2007) is used:

$$D(E_{\mathrm{p}}) = \chi D_0 \left(\frac{E_{\mathrm{p}}/\mathrm{GeV}}{B/3\mu\mathrm{G}} \right)^{\delta}, \tag{10}$$

where D_0 takes the Galactic average value of 3×10^{27} cm^2 s^{-1} (Berezinskii et al. 1990), the diffusion suppression factor is χ and the index of diffusion is δ. The magnetic field is taken as a constant value of $B = B_0 = 10 \, \mu\mathrm{G}$ as the average number density of the ISM surrounding HESS J1804−216 is low ($n_{\mathrm{H}} < 300 \, \mathrm{cm}^{-3}$, Crutcher et al. 2010). At low density, the magnetic field does not scale with density, due to diffuse clouds (low density)

being assembled by motions along the magnetic field. The estimates from Zeeman splitting are also neglected at low density, as they are only significant for the dense ISM. This low magnetic field means particles in our model diffuse faster, as the diffusion coefficient increases.

3.2 Gamma-ray flux

The differential γ-ray flux (TeV^{-1} cm^{-2} s^{-1}) for the energy interval $(E_\gamma, E_\gamma + dE_\gamma)$ at position R and time t is computed through (Kelner, Aharonian & Bugayov 2006):

$$\mathcal{F}_\gamma(E_\gamma, R, t) = \frac{N_H A}{4\pi D^2} c \int_{E_\gamma}^{\infty} \sigma_{pp}(E_p) J_p(E_p, R, t) F_\gamma\left(\frac{E_\gamma}{E_p}, E_\gamma\right) \frac{dE_p}{E_p},$$

(11)

where A and N_H are the area, and total hydrogen column density of the region of interest, D is the distance from Earth to the accelerator and c is the speed of light. The inelastic cross-section of proton–proton interactions is σ_{pp} (equation B2) and F_γ is the number of photons per collision given by equation (B3).

4 METHODOLOGY

We calculate the volume distribution of CR protons using equation (1) at every pixel in the total column density map, for a range of proton energies. The predicted 3D γ-ray map is created with the z-axis being γ-ray energy, via equation (11), by combining the proton map with the ISM distribution. The resulting γ-ray 'cube' is used to extract spectra and integrated flux maps. Fig. 3 shows a schematic of the model.

Our model has a range of parameters. Multiple parameters have a similar effect on the model, for example, χ and δ, which both effect the diffusion coefficient, which leads to a redundancy in our model solution. Due to this, we cannot perform a purely quantitative optimization across the entire parameter space. Instead, we perform a systematic grid search over a range of model parameters, in which each combination is modelled, based on typical values from literature, as discussed below and compare these models to γ-ray observations. We calculate metrics to quantify the agreement of GeV–TeV observations with our model. To compare the modelled morphology to the HGPS observations, the oversampling method from H.E.S.S. is applied, as described in Section 2.

The spatial model of γ-rays is largely biased by the bubble component because the accelerators considered here lie within the extension of the γ-ray source. Therefore, we use the spectral model to determine the best matching model. We use the following metric for the spectral optimization:

$$\frac{\chi^2}{m} = \left(\sum_i \frac{(O_i - F_i)^2}{G_i^2}\right) \frac{1}{m},$$

(12)

where O_i is the observed flux, F_i is the model flux, G_i is the uncertainty in the observations, i denotes each data point and m is the number of data points. For testing the spatial agreement, we integrated the γ-ray cube from 1 TeV to 100 TeV to compare to the flux map from H.E.S.S Collaboration (2018a). As a metric for the spatial model we calculate the standard deviation, S (equation 13), of the residuals but exclude the bubble region as we do not model the distribution of particles in detail there.

$$S = \frac{\sum_i (R_i - \mu)^2}{N}$$

(13)
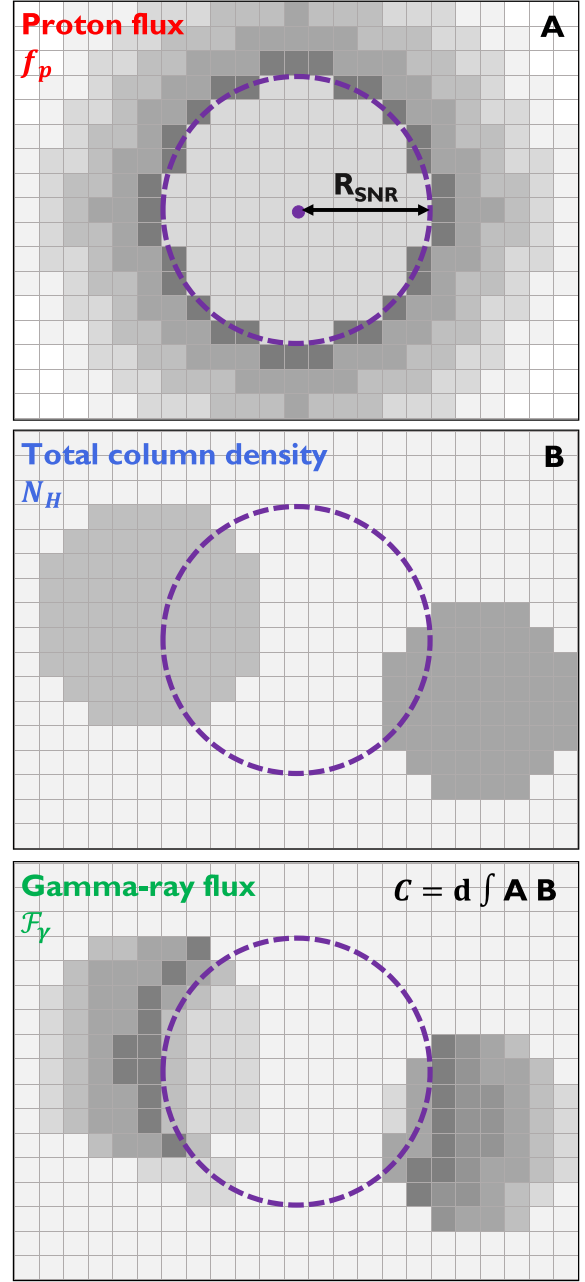
Figure 3. Schematic illustrating our model. Top: example distribution of CR protons (equation 2). Middle: example distribution of the total column density gas. Bottom: example distribution of γ-ray flux (equation 11) by integrating over the top and middle panels with some constant.

Here $R_i = O_i - F_i$ is the residual from the spatial morphology map (residual maps are provided in the supplementary material) for the ith pixel, μ is the mean and N is the number of pixels in the residual map.

Model parameter variation

SNRs are thought to be the main source of CRs for energies below the knee of the CR spectrum (at PeV energies, Lucek & Bell 2000). We define the maximum energy of protons, $E_{p,max}$, at the start of the Sedov phase to be either 1 PeV or 5 PeV (Gabici et al. 2009), for equations (4) and (5) and in the normalization factor, N_0. The energy

Table 1. Model parameters with their discrete values. The spectral index is α, the diffusion suppression factor and the index of diffusion coefficient are given by χ and δ, respectively. The maximum CR proton energy is $E_{p,max}$ and δ_p describes the energy-dependent release of CRs. E_{SN} is the kinetic energy released at the supernova explosion and M_{ej} is the mass of the ejecta.

Parameter	Values
α	1.8, 2.0, 2.2, 2.4
χ	0.001, 0.01, 0.1, 1.0
δ	0.3, 0.4, 0.5, 0.6, 0.7
δ_p	0.2, 1.4, 2.5
$E_{p, max}$	1, 5 PeV
M_{ej} and E_{SN}	$1 M_\odot$ and 10^{51} erg (type Ia)
	$10 M_\odot$, $20 M_\odot$, and 10^{51} erg (type II)
	$10 M_\odot$, $20 M_\odot$, and 10^{52} erg (type II)
n_0*	0.1, 1, 10, 20 cm^{-3}

Note. ∗ For progenitor SNR of PSR J1803−2137

budget, W_p, is a free parameter which is optimized by minimizing the residual between the observations and model spectra. From diffusive shock acceleration theory, we expect a power law with a spectral index of $\alpha \approx 2$ (Malkov & Drury 2001). Therefore, we vary the spectral index from 1.8 to 2.4 in our model.

The factor χ varies from 0.001 to 1, the lower limit ($\chi = 0.001$) is potentially applicable to the dense regions of interstellar gas that the CRs may diffuse through, and the upper limit is taken from various observations (see Feijen et al. 2020, and references therein). Typically, δ varies from 0.3 to 0.7 (Berezinskii et al. 1990) to allow for a range of turbulent spectra to be investigated. Here 0.3 corresponds to Kolmogorov turbulence (indicating slower diffusion), 0.5 indicates Kraichnan turbulence (Strong, Moskalenko & Ptuskin 2007) and 0.7 is consistent with a good fit to the Boron to Carbon ratio measurements.

In equation (4), δ_p describes the energy-dependent release of CRs. The lower limit is taken to be 1/5 which is for a simple stationary particle and the upper limit is taken to be 2.5 (Ptuskin & Zirakashvili 2005; Gabici et al. 2009; Celli et al. 2019). For the Sedov time in equation (B1) we take the typical mass and energy values for different supernovae types. We find for type Ia, where $M_{ej} = 1 M_\odot$ (Ptuskin & Zirakashvili 2005) and $E_{SN} = 10^{51}$ erg, the Sedov time is $t_{sedov} \sim 230$ yr. For yype II, where $M_{ej} = 10 M_\odot$ and $M_{ej} = 20 M_\odot$ (Heger et al. 2003) with $E_{SN} = 10^{51}$ erg, the Sedov time is $t_{sedov} \sim 1600$ yr and $t_{sedov} \sim 2850$ yr, respectively. Type II can also have a higher total kinetic energy (Nomoto et al. 2004) of $E_{SN} = 10^{52}$ erg for $M_{ej} = 10 M_\odot$ and $M_{ej} = 20 M_\odot$, where the Sedov time is $t_{sedov} \sim 500$ yr and $t_{sedov} \sim 900$ yr, respectively.

We expect n_0, from equation (3), to be a small value as it is close to 'SNR birth' before the shock wave has interacted with the gas. If we know the age, t_{SNR}, and radius, R_{SNR}, of the SNR we estimate n_0 by rearranging equation (3):

$$n_0 = \left[\frac{0.31 \text{pc}}{R_{SNR}} \left(\frac{E_{SN}}{10^{51} \text{erg}} \right)^{1/5} \left(\frac{t_{SNR}}{\text{yr}} \right)^{2/5} \right]^5 \text{cm}^{-3}. \quad (14)$$

If R_{SNR} is not known, n_0 takes on values from 0.1 to 20 cm^{-3}. The model parameters discussed are summarized in Table 1.

5 BEST MATCHING MODELS

The following section considers the best matching models for each accelerator, based on the parameter space and minimizing the spectral and spatial criteria (equations 12 and 13, respectively), as described

Figure 4. Best matching spectral and spatial model (G4a) for SNR G8.7−0.1 with an age of 15 kyr. Top: γ-ray spectral model shown in blue. The diffused and bubble spectra are shown by the dashed black curve and dot-dashed red curve, respectively, with HESS J1804−216 observations in dark grey and 3FHL J1804.7−2144e observations in light grey. Bottom: γ-ray flux map above 1 TeV towards HESS J1804−216. The escape radius, R_{esc}, is shown by cyan dashed circle. The TeV γ-ray emission from H.E.S.S. Collaboration (2018a) shown by the solid white contours (2×10^{-13} to 6×10^{-13} cm^{-2} s^{-1} levels). The lower limit of the colorbar is set to 10^{-13} cm^{-2} s^{-1} to exclude any emission below the sensitivity of H.E.S.S.. Model parameters: $\alpha = 2.0$, $\chi = 0.01$, $\delta = 0.6$, $\delta_p = 2.5$, $E_{p, max} = 1$ PeV, type II SN, $E_{p, esc} = 15.8$ TeV. For the spectral model $\chi^2/m = 1.1$.

in Section 4. Specifically, the 5 best matching spectral models are chosen for each accelerator.

5.1 SNR G8.7−0.1

SNR G8.7−0.1 is believed to be contained in component 2 ($v_{lsr} = 30$ to 40 km s^{-1}). We test the various model parameters for both type Ia and type II supernovae for both suggested ages of SNR G8.7−0.1, 15 kyr and 28 kyr, the results shown here are the closest matching spectra to the observations. Tables D1 and D2 show the 5 best matching spectral models with their ranking parameters for the spectral and spatial models, χ^2/m and S respectively.

The 5 best matching models for SNR G8.7−0.1 for each age show a range of χ and δ values. Typically a moderately slow diffusion with $\chi = 0.001$ or 0.01 is seen, which is consistent with other studies in which the diffusion coefficient is suppressed (Gabici et al. 2007; Giuliani et al. 2010; Li & Chen 2010). The index for the energy-dependent release of CRs, δ_p, takes on values of 1.4 or 2.5. A mixture of the $E_{p,max}$ values are present. For SNR G8.7−0.1, we find both a type Ia SN and type II SN, match the γ-ray spectra well for both ages of this accelerator. The escape energy of protons, $E_{p,esc}$, in Figs 4 and
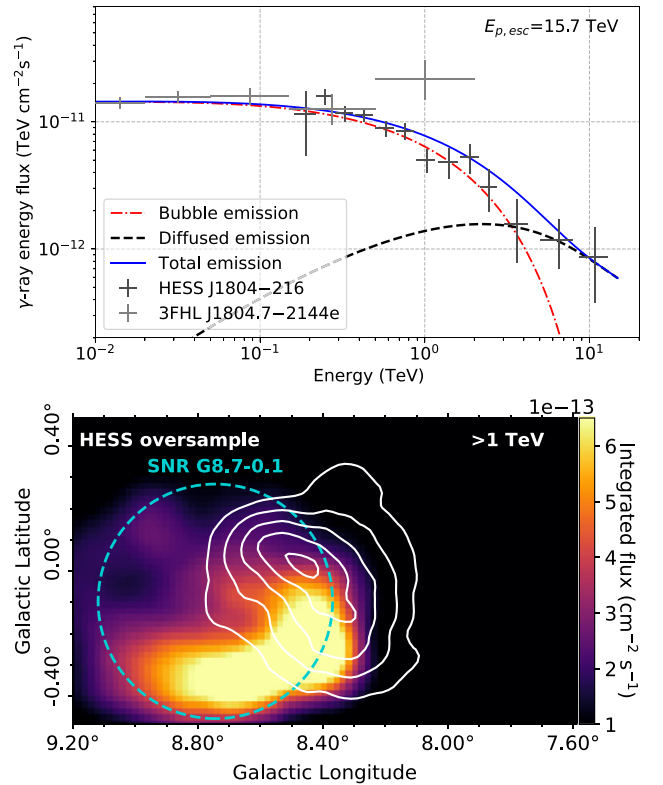
Figure 5. Best matching spectral and spatial model (G2b) for SNR G8.7−0.1 with an age of 28 kyr. Top: γ-ray spectral model shown in blue. The diffused and bubble spectra are shown by the dashed black curve and dot-dashed red curve, respectively, with HESS J1804−216 observations in dark grey and 3FHL J1804.7−2144e observations in light grey. Bottom: γ-ray flux map above 1 TeV towards HESS J1804−216. The escape radius, $R_{\rm esc}$, is shown by cyan dashed circle. The TeV γ-ray emission from H.E.S.S. Collaboration (2018a) shown by the solid white contours (2×10^{-13} to 6×10^{-13} cm^{-2} s^{-1} levels). Model parameters: $\alpha = 1.8$, $\chi = 0.1$, $\delta = 0.4$, $\delta_{\rm p} = 1.4$, $E_{\rm p,max} = 5$ PeV, type Ia SN, $E_{\rm p,esc} = 6.2$ TeV. For the spectral model $\chi^2/m = 0.8$.

Figure 6. Best matching spectral and spatial model (P1) for the progenitor SNR of PSR J1803−2137. Top: γ-ray spectral model shown in blue. The diffused and bubble spectra are shown by the dashed black curve and dot-dashed red curve, respectively, with HESS J1804−216 observations in dark grey and 3FHL J1804.7−2144e observations in light grey. Bottom: γ-ray flux map above 1 TeV towards HESS J1804−216. The progenitor SNR of PSR J1803−2137 is indicated by the cyan dot and the escape radius, $R_{\rm esc}$, is shown by cyan dashed circle. The TeV γ-ray emission from H.E.S.S. Collaboration (2018a) shown by the solid white contours (2×10^{-13} to 6×10^{-13} cm^{-2} s^{-1} levels). Model parameters: $\alpha = 1.8$, $\chi = 0.01$, $\delta = 0.6$, $\delta_{\rm p} = 2.5$, $E_{\rm p,\,max} = 5$ PeV, type II SN, $E_{\rm p,esc} = 3.8$ TeV. For the spectral model $\chi^2/m = 0.9$.

5 are 15.8 TeV and 6.2 TeV respectively. CR protons with energy lower than $E_{\rm p,esc}$ are still confined in the bubble, however higher energy particles have escaped. This is shown by splitting the spectra into its bubble and diffused components as depicted in the top panels of Figs 4 and 5.

For our best matching models, Figs 4 and 5, the spectra tend to match well at low energies. The escape energies for these spectra are quite high, therefore the model spectra are largely dominated by the bubble component. This is seen at higher energies, where the model begins to deviate from the observations, particularly in Fig. 4.

The spatial morphology above 1 TeV cannot explain the γ-ray emission from HESS J1804−216. One contributing factor is the bubble component encompassing a large area of the H.E.S.S. source. The simulated γ-ray emission shows a peak toward the northern edge of HESS J1804−216 and a lack of γ-ray emission towards the western TeV peak of HESS J1804−216. Simulated γ-ray emission is also present at the outer western edge of SNR G8.7−0.1 for both ages, which is not present in the observations from H.E.S.S.. The closest TeV γ-ray source from the HGPS is HESS J1808−204, which is an extended source located at $l = 10.01°$, $b = -0.24°$, which is not close enough to SNR G8.7−0.1 to provide the γ-ray emission at this position.

5.2 Progenitor SNR of PSR J1803−2137

The progenitor SNR is assumed to have an age of 16 kyr, as per the age of PSR J1803−2137, and is placed at the birth position of PSR J1803−2137 as shown in Fig. 1. The progenitor SNR is believed to be in component 1 ($v_{\rm lsr} = 20$ to 30 km s^{-1}). We test a range of combinations of model parameters for a core-collapse supernova, as a pulsar is attached to the system. The 5 best matching spectral models with their ranking parameters for the spectral and spatial models, χ^2/m and S respectively, are shown in Table D3.

Table D3 shows the 5 best matching spectral models typically have a spectral index of $\alpha = 1.8$, with $\chi = 0.001$ or 0.01 and a range of δ. Similarly to SNR G8.7−0.1, this indicates moderately slow diffusion of particles. Both values of the maximum energy, $E_{\rm p,max}$, are present and n_0 takes on all values in the parameter space. The total kinetic energy, $E_{\rm SN}$, is typically the higher value from our parameter space of 10^{52} erg, with the ejecta mass being either $10M_\odot$ or $20M_\odot$. The index for the energy-dependent release of CRs $\delta_{\rm p} = 2.5$, the highest value chosen in our parameter space. The escape energy for the top model is $E_{\rm p,esc} = 3.8$ TeV, therefore some particles are still trapped in the bubble and some have diffused, this can be seen in the spectral components in Fig. 6.

For this accelerator, both the spectral and spatial morphology match the observations well. The modelled integrated γ-ray map peaks towards the northern TeV peak of HESS J1804−216 from H.E.S.S Collaboration (2018a). There is weaker modelled γ-ray emission overlapping the entire γ-ray source and a lack of modelled emission outside the HESS J1804−216 region. No strong γ-ray emission is present outside HESS J1804−216 unlike with SNR G8.7−0.1. However, parts of the morphology do not match well due to the bubble component and the lack of γ-ray emission in the southern and eastern edges of HESS J1804−216.

6 DISCUSSION

In the previous section, we compared the model emission with observational γ-ray emission above 1 TeV. Fig. 17 from Aharonian et al. (2006) shows the morphology of HESS J1804−216 above 0.2 TeV, which is similar to the integrated flux morphology above 1 TeV in Fig. 1 (H.E.S.S Collaboration 2018a). Extensions of both HESS J1804−216 and 3FHL J1804.7−2144e overlap (Fig. 1). To probe the effects of the bubble and diffused components we look at the γ-ray emission in different energy bands: $E_\gamma = 10 - 100$ GeV, $E_\gamma = 0.1 - 1$ TeV, $E_\gamma = 1 - 10$ TeV, and $E_\gamma = 10 - 100$ TeV.

The morphology of the different energy bands for the SNR G8.7−0.1 accelerator show that the bubble component provides stronger γ-ray emission compared to the diffused component (as shown in Figs 7 and 8). At higher energies ($E_\gamma = 1 - 10$ TeV, and $E_\gamma = 10 - 100$ TeV) the model exhibits strong emission towards the southern edge of HESS J1804−216, which does not overlap with the TeV peak. In comparing the four energy bands to morphology of HESS J1804−216, it is clear the morphology is quite different.

Fig. 9 shows the morphology from different energy bands for the best model of the progenitor SNR. The bubble tends to dominate at the two lower energy bands ($E_\gamma = 10 - 100$ GeV and $E_\gamma = 0.1 - 1$ TeV), with strong emission towards the pulsar birth position. The two higher energy bands ($E_\gamma = 1 - 10$ TeV and $E_\gamma = 10 - 100$ TeV) show the γ-ray peak moves away from the pulsar position and closer to the TeV γ-ray peak from HGPS. The emission in these bands becomes diffusion dominated with extended emission outside the bubble.

Overall, the γ-ray emission in the lower energy bands of Figs 7–9 are dominated by the bubble component as the particles have energy less than the escape energy, so are still confined to the bubble region. However, above 1 TeV the diffused component becomes dominant. The morphology of the lower energy band can be compared with the spatial morphology of *Fermi*-LAT observations. However, *Fermi*-LAT has poor resolution (with a PSF of $0.2°$ above 10 GeV), so the spatial map from *Fermi*-LAT observations is described only by a circular region. Therefore, we can only compare the model morphology with the position and extent of 3FHL J1804.7−2144e (seen in Fig. 1). For each accelerator model, the peak of γ-ray emission is offset from the 3FHL catalog position (by up to $0.4°$).

There are a number of known limitations in our model. These arise from:

(i) 2D propagation of CR protons
(ii) 2D arrangement of the ISM
(iii) Uniform distribution of CRs inside bubble
(iv) Simple assumption of ISM inside bubble
(v) Spherical uniformity of the SNR evolution

The main limitation comes from assuming a 2D geometry for the proton model in addition to the accelerators lying within the γ-ray source. This 2D approach to modelling the γ-rays has previously
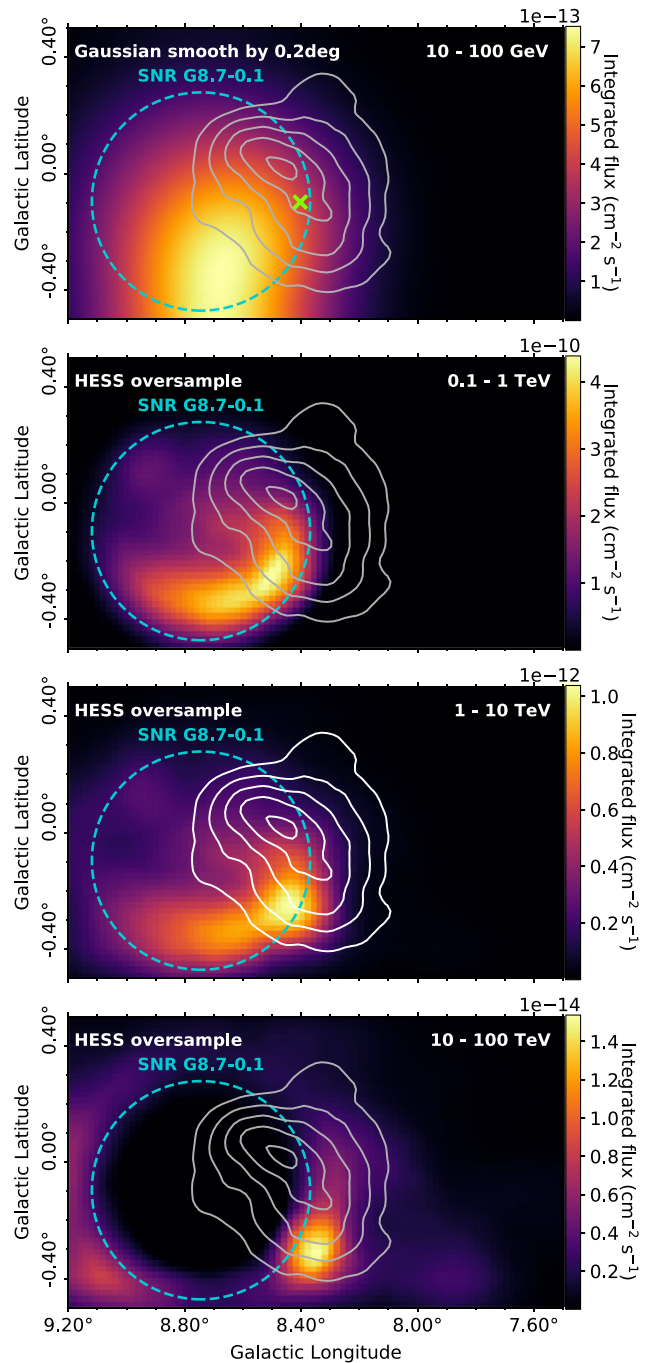
Figure 7. γ-ray flux maps for various energy bands towards HESS J1804−216 for the best matching model (G4a) for SNR G8.7−0.1 with an age of 15 kyr. The escape radius, R_{esc}, is shown by cyan dashed circle. The green cross indicates the centroid of 3FHL J1804.7−2144e. The first energy band ($E_\gamma = 10 - 100$ GeV) corresponds to energies detected by Fermi-LAT so is smoothed using the *Fermi*-LAT PSF of $\sim 0.2°$ above 10 GeV (Ackermann et al. 2017). The other energy bands are oversampled using the H.E.S.S. method described in Section 2. The TeV γ-ray emission above 1 TeV from H.E.S.S. Collaboration (2018a) is shown by the solid white contours in the third panel (2×10^{-13} to 6×10^{-13} cm^{-2} s^{-1} levels) and by grey contours in the other panels as a reference for where the γ-ray emission is expected. Model parameters as described in Fig. 4.
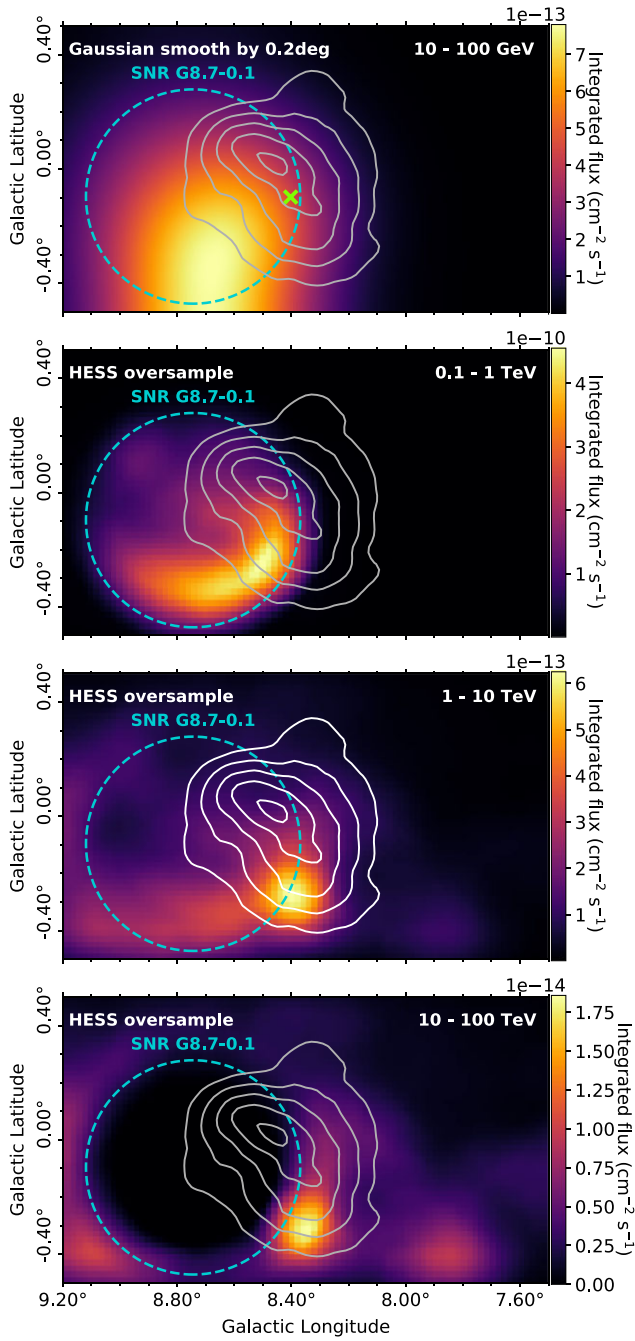
Figure 8. γ-ray flux maps for various energy bands towards HESS J1804$-$216 for the best matching model (G2b) for SNR G8.7$-$0.1 with an age of 28 kyr. The escape radius, R_{esc}, is shown by cyan dashed circle. The green cross indicates the centroid of 3FHL J1804.7$-$2144e. The solid white/grey contours are as described in Fig. 7. Model parameters as described in Fig. 5.

Figure 9. γ-ray flux maps for various energy bands towards HESS J1804$-$216 for the best matching model (P1) for the progenitor SNR of PSR J1803$-$2137. The escape radius, R_{esc}, is shown by cyan dashed circle. The green cross indicates the centroid of 3FHL J1804.7$-$2144e. The solid white/grey contours are as described in Fig. 7. Model parameters as described in Fig. 6.

been implemented e.g. Casanova et al. (2010), in which the accelerator is further away from the γ-ray source. In our model, we have a special case in which both accelerators lie within the extension of the γ-ray source. As we do not model the diffusion inside the bubble component, our results are biased. In our 2D proton model, we do not consider particles diffusing along our line of sight, therefore we are not taking into account the emission foreground/background to the SNR bubble. This makes reconciling the morphology inside the
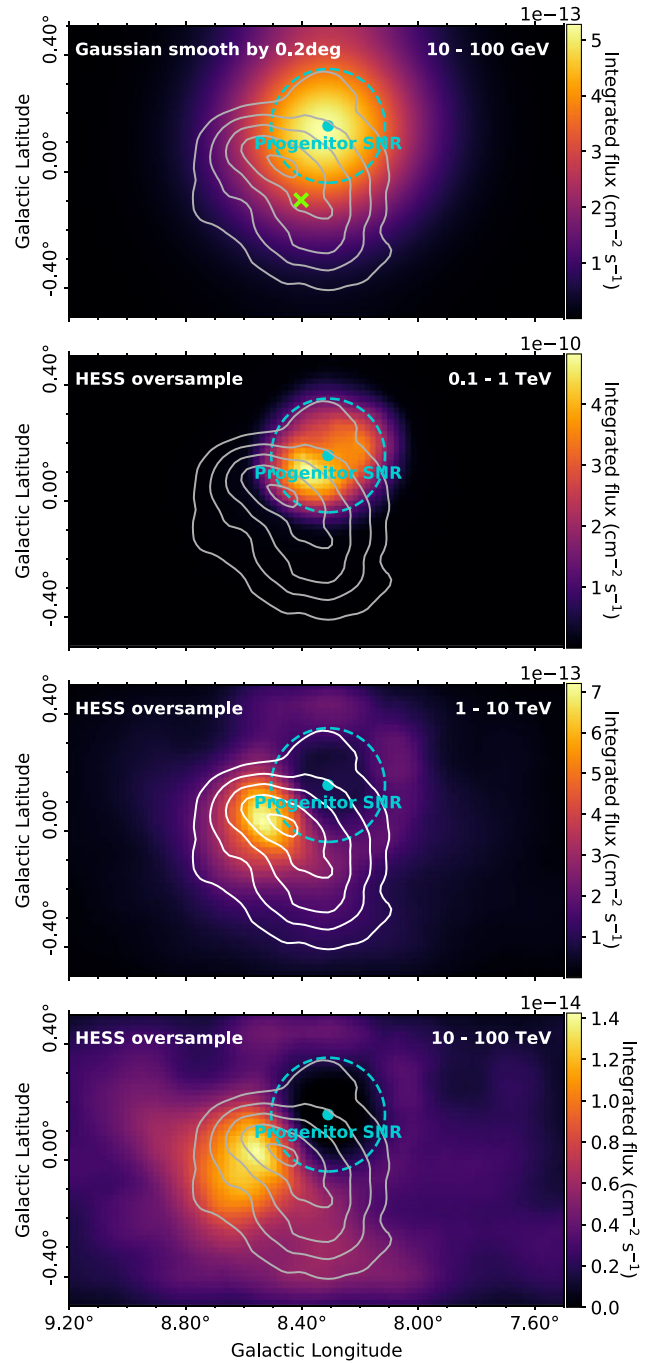
bubble with the observations difficult and is the reason we do not use the spatial criterion (equation 13) to test which model performs best.

Another limitation comes from the assumptions regarding the ISM surrounding HESS J1804$-$216. We assume a 2D model in which the brightness temperature gas cube is integrated over to obtain a total column density map. By using the column density map we assume that all gas we integrated over is interacting with the CRs. Due to

this, we could be including gas that is foreground and/or background to the accelerator, which may not be physically able to interact with the accelerated protons. This effect is more prominent for the bubble component which has radius $R_{esc} \sim 30\,\mathrm{pc}$ compared to the entire column which is integrated over $10\,\mathrm{km\,s^{-1}}$ corresponding to $\sim 800\,\mathrm{pc}$ from the GRC. Our model could therefore be over predicting the bubble component.

One of the largest uncertainties in our model comes from the distribution of CRs and density of the ISM inside the bubble. We assume the CRs are uniformly distributed in the bubble (see e.g. Zirakashvili & Aharonian 2010), however realistically the particle distribution is more complex, with CRs likely accumulating in the shock region (i.e. the expanding SNR shell), as explored by some theoretical studies (Ptuskin & Zirakashvili 2005; Celli et al. 2019; Brose et al. 2020). They suggest the CR distribution can be shell brightened. From diffusive shock acceleration theory, it is possible that the shocked ISM could be ~ 4 times denser than the unshocked gas (Reynolds 2008), according to the expected shock compression factor. Furthermore, it is possible for some of the ISM here to be dissociated by the SNR shock, thereby reducing the density (Fukui et al. 2003; Sano et al. 2020).

For limitation (v) we assume a constant number density for the SNR evolution (n_0, in equation 3), leading to spherical uniformity of the particle escape radius. The escape energy is dependent upon δ_p, which describes the energy dependent release of CRs, which can also effect the evolution of the SNR. A future version of the model would involve tracing the evolution of the shock in closer detail, including the escape radius as it changed with ISM density.

7 CONCLUSIONS

We developed a model to investigate the distribution of γ-rays towards HESS J1804−216 for two SNRs in the hadronic scenario. This is a first attempt to model the morphology of γ-rays towards HESS J1804−216. Gamma-ray spectra and morphology maps of SNR G8.7−0.1 and the progenitor SNR of PSR J1803−2137 were generated for a range of model parameters and compared to observations to gain an understanding of the origin of HESS J1804−216. It was found that the progenitor SNR is the most promising candidate to be creating the TeV γ-rays, however, we are limited by the bubble component. The modelled γ-ray morphology from SNR G8.7−0.1 does not match the γ-ray morphology from observations well, therefore it is either only a minor contributor or does not contribute to the observed γ-ray emission.

The γ-ray observatory CTA (Cherenkov Telescope Array) aims to improve the current measurements from other Imaging Atmospheric Cherenkov Telescope. More detailed features in the morphology may be resolved with CTA, which will provide unprecedented angular resolution and sensitivity. The angular resolution of CTA will reach a few arcmins, comparable to the angular resolution of the Mopra radio telescope, which is utilized for our gas measurements. Here, we compare the best matching model of the progenitor SNR of PSR J1803−2137 (P1) for three different angular resolutions using different oversampling settings for each instrument. The original model (no oversampling, same resolution as the gas maps), the H.E.S.S. over sample (radius=0.1° with a grid size of 0.02°) and the expected CTA oversample (radius=0.03° with a grid size of 0.01°, as per the expected angular resolution from CTA Consortium et al. 2018) maps are shown in Fig. 10.

Fig. 10 shows that the oversampling of CTA (bottom panel) is able to resolve features, comparable to the gas map resolution (middle
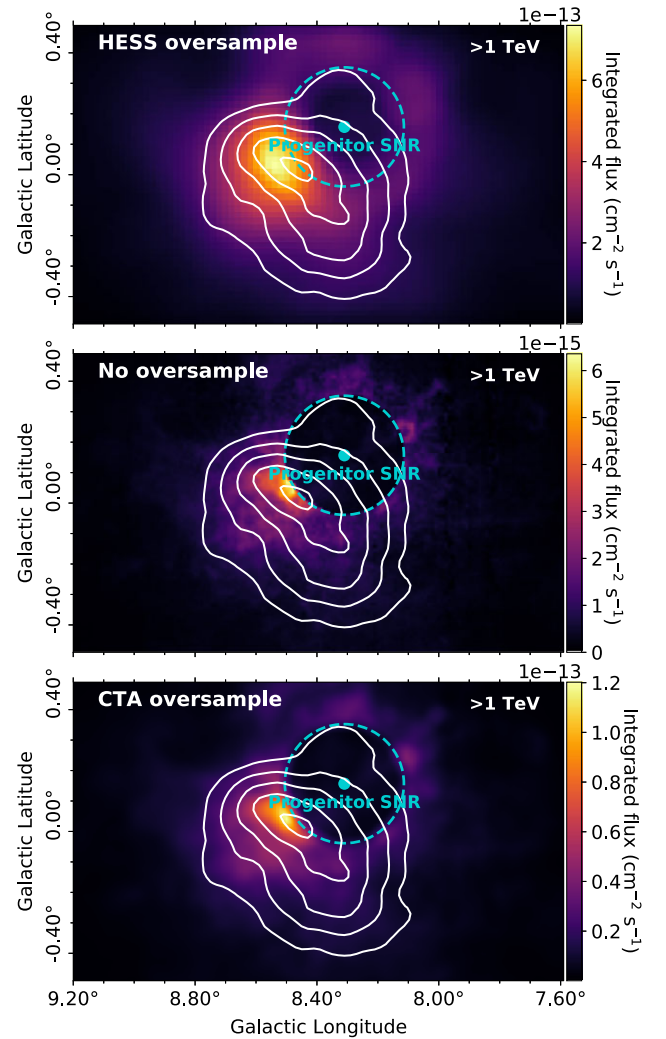
Figure 10. γ-ray flux maps above 1 TeV towards HESS J1804−216 with the progenitor SNR of PSR J1803−2137 as the accelerator (for the top model, P1). The TeV γ-ray emission from H.E.S.S. Collaboration (2018a) shown by the solid white contours (2×10^{-13} to 6×10^{-13} cm^{-2} s^{-1} levels). Top: map oversampled with H.E.S.S. factor of radius=0.1° with grid size of 0.02°. Middle: map not oversampled, with same resolution as gas map. Bottom: map oversampled with CTA factor of radius=0.03° with grid size of 0.01°.

panel with no oversample), meaning the morphology can be further probed with CTA.

Our model provides a good framework for future studies, including insight into what parameters are required. A numerical approach in 3D could be used to more precisely model the particles injected, for each time step. This involves tracing the accelerated particles as they propagate and subsequently interact with the ISM, based on the magnetic field and diffusion parameters of each grid point in the model, hence it is a very computationally expensive approach.

For our model, we currently consider an impulsive injection of particles from the accelerator for the hadronic scenario. Mature aged SNRs may also produce γ-rays leptonically through the inverse-Compton effect (e.g. Araya & Frutos 2012; Devin et al. 2018; Fukui et al. 2021). To finally confirm the accelerator of HESS J1804−216, we need to explore the leptonic scenario, assuming the SNR is accelerating electrons which may contribute to the TeV γ-ray emission as discussed by Ajello et al. (2012), Liu et al. (2019).

TeV emission from a PWNe is a reasonable assumption due to the turn over in the GeV/TeV spectrum, which could be caused by cooling effects of electrons. Along with this, a continuous acceleration scenario should be investigated for both leptonic (typical of PWNe) and hadronic origins. Our model predicts an energy-dependent morphology, largely due to the bubble component, which is not implied by the GeV/TeV observations. Future work will include an energy-dependent morphology study of the H.E.S.S. data, to investigate this further. A dedicated study of the *Fermi*-LAT data could also help to resolve the morphology of γ-rays at lower energies, in addition to the use of CTA in the future. These methods will hopefully help reveal the nature of HESS J1804−216.

ACKNOWLEDGEMENTS

DATA AVAILABILITY

The data underlying this article are available on the MopraGam website at http://www.physics.adelaide.edu.au/astrophysics/Mopra Gam/. Other datasets were derived from sources in the public domain: HGPS at https://www.mpi-hd.mpg.de/hfm/H.E.S.S./hgps/ and SGPS at https://www.atnf.csiro.au/research/HI/sgps/fits_files.html.

REFERENCES

Ackermann M. et al., 2013, Science, 339, 807
Ackermann M. et al., 2017, ApJ, 843, 139
Aharonian F. et al., 2006, ApJ, 636, 777
Aharonian F. A., Atoyan A. M., 1996, A&A, 309, 917
Ajello M. et al., 2012, ApJ, 744, 80
Ajello M. et al., 2017, ApJS, 232, 18
Araya M., Frutos F., 2012, MNRAS, 425, 2810
Berezhko E. G., Völk H. J., 1997, Astropart. Phys., 7, 183
Berezhko E. G., Völk H. J., 2000, A&A, 357, 283
Berezinskii V. S., Bulanov S. V., Dogiel V. A., Ptuskin V. S., 1990, in Ginzburg V.L., ed., Astrophysics of cosmic rays
Blandford R. D., Ostriker J. P., 1980, ApJ, 237, 793
Braiding C. et al., 2018, PASA, 35, e029
Brand J., Blitz L., 1993, A&A, 275, 67
Brisken W. F., Carrillo-Barragán M., Kurtz S., Finley J. P., 2006, ApJ, 652, 554
Brose R., Pohl M., Sushch I., Petruk O., Kuzyo T., 2020, A&A, 634, A59
Burton M. G. et al., 2013, PASA, 30, e044
Casanova S. et al., 2010, PASJ, 62, 1127
Celli S., Morlino G., Gabici S., Aharonian F. A., 2019, MNRAS, 490, 4317
Crutcher R. M., Wandelt B., Heiles C., Falgarone E., Troland T. H., 2010, ApJ, 725, 466
CTA Consortium, Acharya B. S., Agudo I., Al Samarai I., Alfaro R., Alfaro J., 2018, Science with the Cherenkov Telescope Array
Devin J., Acero F., Ballet J., Schmid J., 2018, A&A, 617, A5
Dickey J. M. et al., 2013, PASA, 30, e003
Feijen K., Rowell G., Einecke S., Braiding C., Burton M. G., Maxted N., Voisin F., Wong G. F., 2020, PASA, 37, e056
Finley J. P., Oegelman H., 1994, ApJ, 434, L25
Fukui Y. et al., 2003, PASJ, 55, L61
Fukui Y., Sano H., Yamane Y., Hayakawa T., Inoue T., Tachihara K., Rowell G., Einecke S., 2021, ApJ, 915, 84
Gabici S., Aharonian F. A., Blasi P., 2007, Ap&SS, 309, 365
Gabici S., Aharonian F. A., Casanova S., 2009, MNRAS, 396, 1629
Giuliani A. et al., 2010, A&A, 516, L11
H.E.S.S Collaboration et al., 2018a, A&A, 612, A1
H.E.S.S Collaboration et al., 2018b, A&A, 612, A2
Heger A., Fryer C. L., Woosley S. E., Langer N., Hartmann D. H., 2003, ApJ, 591, 288
Hewitt J. W., Yusef-Zadeh F., 2009, ApJ, 694, L16
Kafexhiu E., Aharonian F., Taylor A. M., Vila G. S., 2014, Phys. Rev. D, 90, 123014
Kelner S. R., Aharonian F. A., Bugayov V. V., 2006, Phys. Rev. D, 74, 034018
Li H., Chen Y., 2010, MNRAS, 409, L35
Liu B., Yang R.-z., Sun X.-n., Aharonian F., Chen Y., 2019, ApJ, 881, 94
Lucek S. G., Bell A. R., 2000, MNRAS, 314, 65
Malkov M. A., Drury L. O., 2001, Rep. Prog. Phys., 64, 429
McClure-Griffiths N. M., Dickey J. M., Gaensler B. M., Green A. J., Haverkorn M., Strasser S., 2005, ApJS, 158, 178
Mitchell A. M. W., Rowell G. P., Celli S., Einecke S., 2021, MNRAS, 503, 3522
Nomoto K. Maeda K., Mazzali P. A., Umeda H., Deng J., Iwamoto K., 2004, Hypernovae and Other Black-Hole-Forming Supernovae. Springer, Netherlands
Ptuskin V. S., Zirakashvili V. N., 2005, A&A, 429, 755
Ptuskin V., Zirakashvili V., Seo E.-S., 2010, ApJ, 718, 31
Reynolds S. P., 2008, ARA&A, 46, 89
Sano H. et al., 2020, ApJ, 904, L24
Strong A. W., Moskalenko I. V., Ptuskin V. S., 2007, Annu. Rev. Nucl. Part. Sci., 57, 285
Vallée J. P., 2014, AJ, 148, 5
Zirakashvili V. N., Aharonian F. A., 2010, ApJ, 708, 965

SUPPORTING INFORMATION

Supplementary data are available at *MNRAS* online.

Figure S1. γ-ray flux map above 0.2 TeV towards HESS J1804–216 for SNR G8.7–0.1 with an age of 15 kyr.
Figure S2. γ-ray flux map above 0.2 TeV towards HESS J1804–216 for SNR G8.7–0.1 with an age of 28 kyr.
Figure S3. γ-ray flux map above 0.2 TeV towards HESS J1804–216 for the progenitor SNR of PSR J1803–2137.
Figure S4. Best matching spectral and spatial model (G4a) for SNR G8.7–0.1 with an age of 15 kyr, showing the residual of the spatial model.
Figure S5. Best matching spectral and spatial model (G2b) for SNR G8.7–0.1 with an age of 28 kyr, showing the residual of the spatial model.
Figure S6. Best matching spectral and spatial model (P1) for PSR J1803–2137 with an age of 16 kyr, showing the residual of the spatial model.

Please note: Oxford University Press is not responsible for the content or functionality of any supporting materials supplied by the authors. Any queries (other than missing material) should be directed to the corresponding author for the article.

APPENDIX A: POSITION-VELOCITY PLOTS

Figs A1 and A2 are position-velocity plots for the ^{12}CO(1-0) and HI data, respectively, towards the HESS J1804−216 region, integrated over latitudes $b = -0.49°$ to $0.49°$. Using this figure, we defined two gas velocity regions, component 1 ($v_{lsr} = 20$ to 30 km s^{-1}) and component 2 ($v_{lsr} = 30$ to 40 km s^{-1}), as shown by the dashed navy lines.
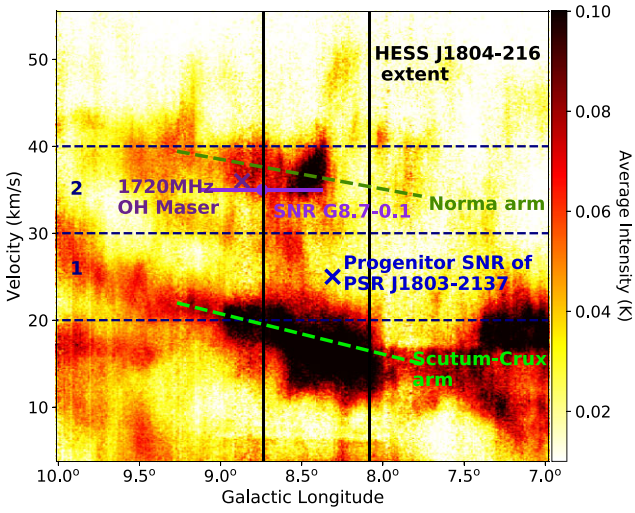
Figure A1. Position-velocity plot of Mopra ^{12}CO(1-0) emission (K) towards HESS J1804−216, integrated over latitudes from −0.49° to 0.49°. The black vertical lines show the longitudinal extent of HESS J1804−216. The blue cross indicates the birth position of PSR J1803−2137 at its assumed velocity of ∼25 km s^{-1}. The 1720 MHz OH maser is shown by the purple cross at its velocity of 36 km s^{-1}. The centre of SNR G8.7−0.1 is shown by the purple dot, whilst the purple line shows its radial extent, at a velocity of 35 km s^{-1}. The green dashed lines are estimates of the Galactic spiral arms along the line of sight for HESS J1804−216 (from the model in Vallée 2014). Components 1 and 2 are indicated by the dashed navy lines.
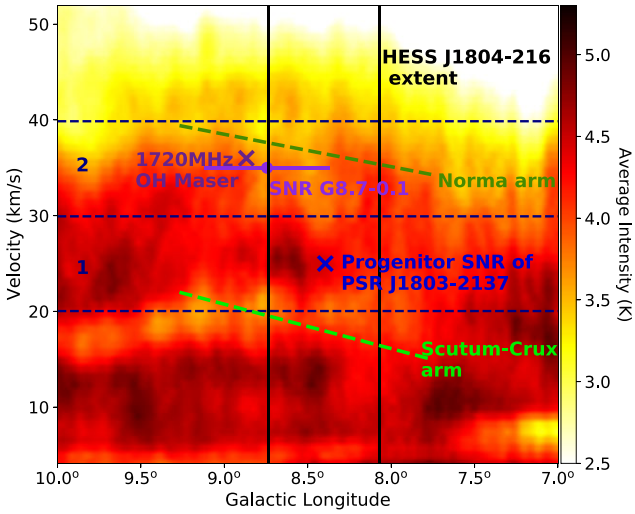
Figure A2. Position-velocity plot of SGPS HI emission (K) towards HESS J1804−216. The annotations are described in Fig. A1.

APPENDIX B: ADDITIONAL MODEL TERMS

The onset of the Sedov–Taylor phase is defined in Celli et al. (2019):

$$t_{\text{sedov}} \sim 1.6 \times 10^3 \left(\frac{E_{\text{SN}}}{10^{51}\text{erg}} \right)^{-1/2} \left(\frac{M_{\text{ej}}}{10M_\odot} \right)^{5/6} \text{yr} \quad \text{(B1)}$$

where E_{SN} is the ejected supernova total kinetic energy and M_{ej} is the mass of the ejecta.

The inelastic cross section of proton–proton collisions is taken from the most recent parametrization by Kafexhiu et al. (2014).

$$\sigma_{\text{pp}}\left(E_{\text{p}}\right) = \left[30.7 - 0.96 \ln\left(\frac{E_{\text{p}}}{E_{\text{p}}^{\text{th}}} \right) + 0.18 \ln\left(\frac{E_{\text{p}}}{E_{\text{p}}^{\text{th}}} \right)^2 \right]$$
$$\times \left[1 - \left(\frac{E_{\text{p}}^{\text{th}}}{E_{\text{p}}} \right)^{1.9} \right]^3 \quad \text{mbarn} \quad \text{(B2)}$$

where E_{p} is the kinetic energy of the proton and $E_{\text{p}}^{\text{th}} = 2m_\pi + m_\pi^2/2m_{\text{p}} \sim 0.2797$ GeV is the threshold kinetic energy.

The total γ-ray spectrum is given by equation (B3), for simplicity $x = E_\gamma/E_{\text{p}}$.

$$F_\gamma\left(x, E_{\text{p}}\right) = B_\gamma \frac{\ln(x)}{x} \left(\frac{1 - x^{\beta_\gamma}}{1 + k_\gamma x^{\beta_\gamma}(1 - x^{\beta_\gamma})} \right)^4 \times$$
$$\left[\frac{1}{\ln(x)} - \frac{4\beta_\gamma x^{\beta_\gamma}}{1 - x^{\beta_\gamma}} - \frac{4k_\gamma \beta_\gamma x^{\beta_\gamma}(1 - 2x^{\beta_\gamma})}{1 + k_\gamma x^{\beta_\gamma}(1 - x^{\beta_\gamma})} \right] \quad \text{(B3)}$$

The additional parameters, B_γ, β_γ, and k_γ, are an approximation from numerical calculation using the best least square fit and dependent on the energy of the CR protons. For the proton energy range from 0.1–10^5 TeV these parameters are defined as:

$$B_\gamma = 1.3 + 0.14L + 0.011L^2$$
$$\beta_\gamma = \left(1.79 + 0.11L + 0.008L^2 \right)^{-1}$$
$$k_\gamma = \left(0.801 + 0.049L + 0.014L^2 \right)^{-1} \quad \text{(B4)}$$

APPENDIX C: HESS J1804−216 SPECTRAL COMPARISON

Fig. C1 shows the spectral comparison between the H.E.S.S. 2006 survey of the inner Galaxy (Aharonian et al. 2006) and the 2018 HGPS data (H.E.S.S Collaboration 2018a) towards HESS J1804−216. These spectra tend to match well. The observations from Aharonian et al. (2006) are between 2004 May and July with 11.7 hours of observation time. The data from H.E.S.S Collaboration (2018a) was collected between 2006 January and 2013
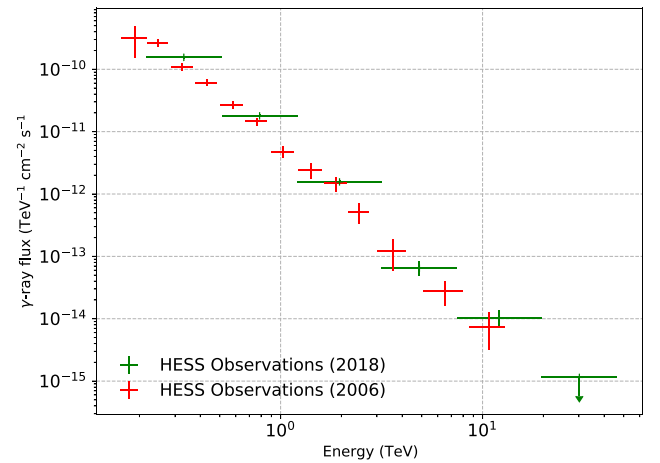
Figure C1. TeV γ-ray spectra towards HESS J1804−216 from Aharonian et al. (2006) in red and H.E.S.S Collaboration (2018a) in green. Aharonian et al. (2006) has more spectral points as this involved a dedicated source analysis on HESS J1804−216.

January with ∼44 hours of observations. Aharonian et al. (2006) provide a dedicated source analysis on HESS J1804−216 with more spectral data points than H.E.S.S Collaboration (2018a) which has a total of six bins (fixed bin number for all sources). The data from Aharonian et al. (2006) is utilized here, as we want to compare the spectral shape of the observations with our model.

APPENDIX D: BEST MATCHING MODELS

The following tables show the model parameters for the best matching spectral models based on their χ^2/m values, shown here in ascending order. Each model is given a name identifier, used within the main text.

Table D1. The 5 best matching spectral models for accelerator SNR G8.7−0.1 for an age of 15 kyr with their model parameters.

Model name	α	χ	δ	δ_p	$E_{p,max}$ (PeV)	SN Type	M_{ej} ($M_\odot$)	E_{SN} (erg)	W_p (10^{49} erg)	$E_{p,esc}$ (TeV)	χ^2/m (Spectral)	S (Spatial, 10^{-13})
G1a	2.0	0.001	0.5	1.4	5.0	Ia	1	10^{51}	7.0	14.8	1.0	2.8
G2a	2.0	0.001	0.4	2.5	5.0	II	10	10^{51}	6.9	18.6	1.1	3.2
G3a	2.0	0.01	0.3	1.4	5.0	Ia	1	10^{51}	7.0	14.8	1.1	3.0
G4a∗	2.0	0.01	0.6	2.5	1.0	II	20	10^{51}	6.2	15.7	1.1	2.7
G5a	2.0	0.001	0.4	2.5	1.0	II	20	10^{51}	6.2	15.7	1.1	2.8

Note.∗ Best spatial model

Table D2. The 5 best matching spectral models for accelerator SNR G8.7−0.1 for an age of 28 kyr with their model parameters.

Model name	α	χ	δ	δ_p	$E_{p,max}$ (PeV)	SN Type	M_{ej} ($M_\odot$)	E_{SN} (erg)	W_p (10^{50} erg)	$E_{p,esc}$ (TeV)	χ^2/m (Spectral)	S (Spatial, 10^{-13})
G1b	1.8	0.01	0.6	1.4	5.0	Ia	1	10^{51}	1.5	6.2	0.6	1.9
G2b∗	1.8	0.1	0.4	1.4	5.0	Ia	1	10^{51}	1.5	6.2	0.8	1.6
G3b	1.8	0.001	0.4	1.4	1.0	II	20	10^{52}	1.0	8.1	1.0	2.3
G4b	2.0	0.001	0.4	1.4	5.0	II	10	10^{52}	0.7	18.1	1.0	3.2
G5b	1.8	0.1	0.4	1.4	1.0	II	20	10^{52}	1.0	8.1	1.0	2.0

Note.∗ Best spatial model

Table D3. The 5 best matching spectral models for accelerator progenitor SNR of PSR J1803−2137 for an age of 16 kyr with their model parameters.

Model name	α	χ	δ	δ_p	n_0 (cm^{-3})	$E_{p,max}$ (PeV)	SN Type	M_{ej} ($M_\odot$)	E_{SN} (erg)	W_p (10^{49} erg)	$E_{p,esc}$ (TeV)	χ^2/m (Spectral)	S (Spatial, 10^{-13})
P1∗	1.8	0.01	0.6	2.5	20	5.0	II	20	10^{52}	3.8	3.8	0.9	1.2
P2	1.8	0.01	0.6	2.5	10	5.0	II	20	10^{52}	4.5	3.8	0.9	1.4
P3	1.8	0.001	0.3	1.4	20	1.0	II	10	10^{52}	2.6	8.0	1.0	2.6
P4	1.8	0.01	0.6	2.5	1	5.0	II	20	10^{52}	8.7	3.8	1.0	2.6
P5	2.0	0.001	0.4	2.5	0.1	1.0	II	20	10^{51}	3.5	13.4	1.0	1.2

Note.∗ Best spatial model

This paper has been typeset from a TEX/LATEX file prepared by the author.

SUPPLEMENTARY MATERIAL

1 GAMMA-RAY FLUX ABOVE 0.2 TEV

Fig. 17 from Aharonian et al. (2006) shows a smoothed excess γ-ray counts maps for energies above 0.2 TeV for HESS J1804−216. Figs. 1 to 3 show the integrated γ-ray flux maps above 0.2 TeV from the model with the contours obtained from Aharonian et al. (2006).

Each of these figures show that the bubble component is dominating over the diffused component. The modelled morphology for both ages for SNR G8.7−0.1 do not match the observations well, with a distinct bright ring feature shown to the southern edge of SNR G8.7−0.1. The γ-ray model for progenitor SNR of PSR J1803−2137 (Fig. 3) shows some overlap with the northern part of the TeV peak, however, there is a lack of emission towards the southern peak.

2 RESIDUALS

Residual maps, equation (1), for the best matching model for each accelerator are shown in Figs. 4 to 6.

$$R_i = O_i - F_i \tag{1}$$

where O_i are the observation data points and F_i are the model data points.

References

Aharonian F., et al., 2006, ApJ, 636, 777
H. E. S. S. Collaboration et al., 2018, A&A, 612, A1

This paper has been typeset from a TeX/LaTeX file prepared by the author.

Figure 2. γ-ray flux map above 0.2 TeV towards HESS J1804−216 for SNR G8.7−0.1 with an age of 28 kyr. The escape radius, $R_{\rm esc}$, is shown by cyan dashed circle. The TeV γ-ray emission from the excess counts map in Aharonian et al. (2006) is shown by the solid white contours (5-10σ levels).

Figure 3. γ-ray flux map above 0.2 TeV towards HESS J1804−216 for the progenitor SNR of PSR J1803−2137. The escape radius, $R_{\rm esc}$, is shown by cyan dashed circle. The TeV γ-ray emission from the excess counts map in Aharonian et al. (2006) is shown by the solid white contours (5-10σ levels).

Figure 1. γ-ray flux map above 0.2 TeV towards HESS J1804−216 for SNR G8.7−0.1 with an age of 15 kyr. The escape radius, $R_{\rm esc}$, is shown by cyan dashed circle. The TeV γ-ray emission from the excess counts map in Aharonian et al. (2006) is shown by the solid white contours (5-10σ levels).

Figure 4. Best matching spectral and spatial model (G4a) for SNR G8.7−0.1 with an age of 15 kyr, showing the residual of the spatial model. The TeV γ-ray emission from H. E. S. S. Collaboration et al. (2018) shown by the solid grey contours (2×10^{-13} to 6×10^{-13} cm^{-2} s^{-1} levels).
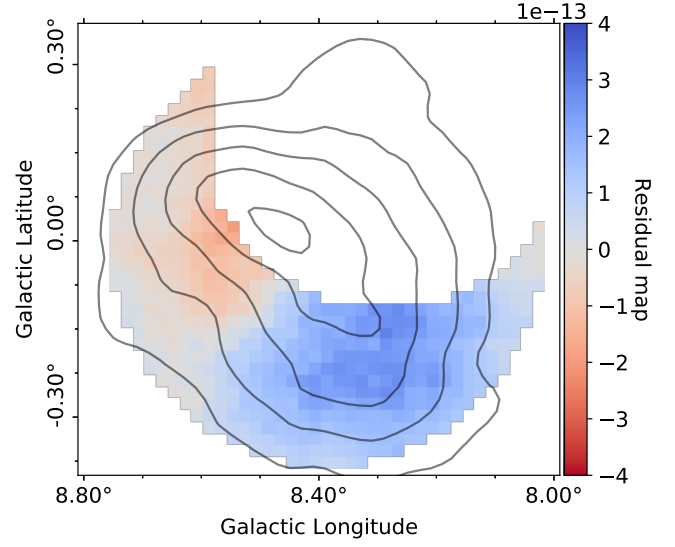
Figure 6. Best matching spectral and spatial model (P1) for PSR J1803−2137 with an age of 16 kyr, showing the residual of the spatial model. The TeV γ-ray emission from H. E. S. S. Collaboration et al. (2018) shown by the solid grey contours (2×10^{-13} to 6×10^{-13} cm^{-2} s^{-1} levels).
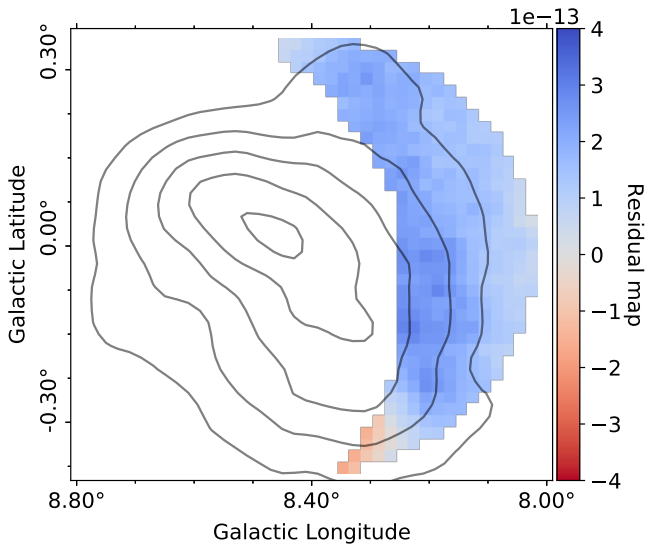
Figure 5. Best matching spectral and spatial model (G2b) for SNR G8.7−0.1 with an age of 28 kyr, showing the residual of the spatial model. The TeV γ-ray emission from H. E. S. S. Collaboration et al. (2018) shown by the solid grey contours (2×10^{-13} to 6×10^{-13} cm^{-2} s^{-1} levels).

7 Modelling Galactic Gamma-Ray Emission

I like to think of ideas as potential energy. They're really wonderful, but nothing will happen until we risk putting them into action.

— Mae Jemison, *American engineer, physicist and NASA astronaut*

The hadronic modelling of supernova remnants (SNRs) with the use of interstellar medium (ISM) gas clouds has been performed previously by multiple authors (Drury et al., 1994; Naito and Takahara, 1994; Ackermann et al., 2013; Jogler and Funk, 2016; A. M. W. Mitchell et al., 2021), to gain an understanding of both the γ-ray spectrum and spatial distribution of γ-rays (i.e. Casanova et al., 2010). A. M. W. Mitchell et al., 2021 present γ-ray energy spectra towards multiple SNRs from hadronic interactions. This study considers interstellar clouds at a specific position with a given mass, density and radius, which act as a target for cosmic-ray (CR) proton collisions. The authors make use of the interstellar cloud catalogue by Rice et al., 2016 along with Green's SNR catalogue (Green, 2019) to pair clouds with nearby SNRs. A. M. W. Mitchell et al., 2021 are able to obtain a realistic description of the γ-ray spectra but do not model the spatial morphology. Casanova et al., 2010 model the morphology of γ-rays in the hadronic and leptonic scenarios assuming SNR RX J1713.7−3946 is the accelerator. They make use of the LAB survey of HI with resolution of 0.6° and the Nanten survey of CO with a resolution of 4′ for their total target material.

This chapter outlines a new framework for modelling both the spatial and spectral distributions of the γ-ray emission originating from SNRs in the hadronic scenario. For this model, we consider both SNR G8.7−0.1 and the progenitor SNR of PSR J1803−2137 as the accelerators of CR protons. Casanova et al., 2010 provide a model for the spectral and spatial morphology of γ-rays towards SNR RX J1713.7−3946, in which the accelerator is at a distance from the γ-ray source. For our case, both of the SNRs considered lie within the extension of the γ-ray source HESS J1804−216, so a different approach must be implemented (outlined in this chapter). This approach allows the γ-rays to be modelled in detail towards HESS J1804−216 using high resolution gas data and a grid search approach over the model parameter space to find the best matching model to the observations.

7.1 Particle Transport in the Interstellar Medium

CR propagation through the Galaxy can be described through the transport equation. The three-dimensional partial differential transport equation for a particular CR species is given by (e.g. Strong et al., 2007):

$$\frac{\partial \psi}{\partial t} = Q(\vec{r}, p, t)$$
$$+ \vec{\nabla} \cdot [D_{xx} \vec{\nabla} \psi - \vec{V} \psi]$$
$$+ \frac{\partial}{\partial p} p^2 D_{pp} \frac{\partial}{\partial p} \frac{\psi}{p^2}$$
$$- \frac{\partial}{\partial p} \left[\dot{p} \psi - \frac{p}{3} (\vec{\nabla} \cdot \vec{V}) \psi \right]$$
$$- \frac{\psi}{\tau_f} - \frac{\psi}{\tau_r}$$

(7.1)

where $\psi \equiv \psi(\vec{r}, p, t)$ is the number density per unit of total particle momentum, p, which can be expressed in terms of the phase-space density, $f(\vec{r}, \vec{p}, t)$, with $\psi(\vec{r}, p, t) dp = 4\pi p^2 f(\vec{r}, \vec{p}, t)$. The source term is $Q(\vec{r}, p, t)$. The source term can be described by the injection of particles from either an impulsive or continuous source. An impulsive source involves particles being injected into the ISM at the same time. The impulsive injection of particles is valid for relatively small accelerator ages $t_{\mathrm{acc}} \leq (10^3\text{-}10^4)$ yr (Aharonian and Atoyan, 1996). A continuous accelerator, as the name suggests, involves particles being continuously ejected into the ISM over the lifetime of the source. The second term describes both diffusive losses and advection, where the spatial diffusion coefficient is $D_{xx} \equiv D_{xx}(\vec{r}, p)$ and the convection velocity is $\vec{V} \equiv \vec{V}(\vec{r})$. The third term describes diffusion reacceleration via second order Fermi acceleration, where the momentum-space diffusion coefficient is $D_{pp} \equiv D_{pp}(\vec{r}, p)$. The fourth term describes radiative losses and adiabatic expansion. The momentum loss rate is given by $\dot{p} \equiv \dot{p}(\vec{r}, p) = dp/dt$. The final term accounts for nuclear fragmentation and radioactive decay of larger nuclei, with timescales of τ_f and τ_r, respectively.

It is possible for this transport equation to be solved either numerically or analytically. In the case of electrons, a numerical solution is vital as the situation is more complex, involving three different radiation mechanisms which compete for the energy (see Section 2.3.2). These solutions are often quite sophisticated and attempt to include all relevant physics to model the propagation in high detail.

The full transport equation (Equation 7.1) is too complex to be solved in general analytically. To solve the equation analytically, various simplifications must be made. Firstly, the geometry must be simplified, for example spherical or cylindrical symmetry. As the formulae are complex, other simplifications that can be made include simplified energy losses, gas distributions, and magnetic fields. As the equation is solved analytically, the computational time is fast with no instabilities. For the purpose of this thesis, the transport equation can be rewritten as the well-known reduced standard diffusion transport equation (neglecting convection and reacceleration, Ginzburg and Syrovatskii, 1964):

$$\frac{\partial f}{\partial t} = \frac{D}{R^2} \frac{\partial}{\partial R} \left(R^2 \frac{\partial f}{\partial R} \right) + \frac{\partial}{\partial E} (Pf) + Q.$$

(7.2)

for the spherically symmetric case. Here, f is the particle distribution function, the continuous energy-loss rate is $P = -dE/dt$, the source function is $Q \equiv Q(E, R, t)$ and $D \equiv D(E)$ is the energy-dependent diffusion coefficient.

For the numerical solution, gas parameters from interstellar gas surveys are utilised, a 3D Galactic magnetic field model including both the regular and random components, including direction, can be used and there is a full consideration of energy losses, i.e. no simplifications for the energy loss equations are used. Using a numerical method means taking advantage of computing power to overcome the limitations of analytical solutions. One numerical solution is to create a grid in space (x, y, z) and energy, E, to trace the propagation of particles at every time step Δt. A template of the ISM which describes both the magnetic field and number density (used for the diffusion coefficient equation) at each grid point is utilised. This gives a detailed description of the diffusion coefficient, D, for each step in space, along with accounting for energy losses (dE/dt) from particle interactions. The energy density for each time step is then calculated. This is incremented over every cell in the grid and time step until the time equals the age of the accelerator. Having a series of time steps allows for a detailed model of the evolution and injection of particles.

The numerical approach provides a way to implement both magnetic field and gas density maps which vary across space. This numerical approach can more precisely model the injected particles over each step taken, however, this also means a large amount of computational memory is required and the computational time is long for high-resolution results. The analytical solution utilised in this thesis, whilst an effective representation of particle acceleration, transport, and interaction, also comes with limitations. Various simplifications were made in order to make the model analytically solvable. A constant diffusion coefficient for each energy is implemented, however, in reality this should vary as a function of position. This comes from using a constant number density and hence magnetic field in the diffusion coefficient when this should vary as a function of position. The use of the analytical approach with simple approximations decreases both the computational time and expense to find a fast solution to the diffusion equation. This solution provides a good overview of the diffusion of particles from a single source distributed across space and time.

7.2   Cosmic-Ray Particle Distribution

One simple analytical solution to Equation 7.2, involves utilising the Green's function technique. For this case, the source function is given by $Q(E, R, t) = N_0 f_{\mathrm{inj}}(E)\delta(R)\delta(t)$ for an arbitrary injection spectrum $f_{\mathrm{inj}}(E)$ (Atoyan et al., 1995), where N_0 is a normalisation factor. The particle distribution is given by $f \equiv f(E, R, t)$. This solution is a simple analytical equation which allows for easy analysis of the diffusion of particles distributed over space and time. For the purpose of this thesis, we are interested in the distribution of CR protons, hence the following sections will discuss these equations in terms of CR protons. In this case, particles are injected into the ISM from a point source with a power law injection spectrum, $f_{\mathrm{inj}}(E_{\mathrm{p}}) = E_{\mathrm{p}}^{-\alpha}$, leading to the solution:

$$f(E_\mathrm{p}, R, t) \approx \frac{N_0 E_\mathrm{p}^{-\alpha}}{\pi^{3/2} R_\mathrm{dif}^3} \exp\left(-\frac{(\alpha-1)t}{\tau_\mathrm{pp}} - \frac{R^2}{R_\mathrm{dif}^2}\right), \tag{7.3}$$

where the diffusion length,

$$R_\mathrm{dif} \equiv R_\mathrm{dif}(E_\mathrm{p}, t) = \sqrt{4D(E_\mathrm{p})t\frac{\exp(t\delta/\tau_\mathrm{pp}) - 1}{t\delta/\tau_\mathrm{pp}}}, \tag{7.4}$$

is the length given for CR protons of energy E_p propagating through the ISM during time t. This is called the 'point origin model'. The energy-dependent diffusion coefficient is taken from Gabici et al., 2007, as given by Equation 7.5.

$$D(E) = \chi D_0 \left(\frac{E_\mathrm{p}/\mathrm{GeV}}{B/3\mu\mathrm{G}}\right)^\delta, \tag{7.5}$$

where χ is the diffusion suppression factor, δ is the index of diffusion and B is the magnetic field (shown by Equation 7.6, Crutcher et al., 2010).

$$B = \begin{cases} B_0 & \text{for } n_\mathrm{H} < 300\,\mathrm{cm}^{-3} \\ B_0 \left(\dfrac{n_\mathrm{H}}{300\,\mathrm{cm}^{-3}}\right)^{0.65} & \text{for } n_\mathrm{H} > 300\,\mathrm{cm}^{-3}. \end{cases} \tag{7.6}$$

The cooling time of proton-proton collisions is given by Aharonian and Atoyan, 1996:

$$\tau_\mathrm{pp} = 6 \times 10^7 \, (n_\mathrm{H}/\mathrm{cm}^{-3})^{-1} \, \mathrm{yr}. \tag{7.7}$$

In the limit $n_\mathrm{H} < 10^2\,\mathrm{cm}^{-3}$ for relatively young accelerators ($t < 100\,\mathrm{kyr}$, Aharonian and Atoyan, 1996) the proton-proton cooling time term can be neglected as $\tau_\mathrm{pp} \gg t$. The diffusion length can then also be simplified to $R_\mathrm{dif} = \sqrt{4D(E_\mathrm{p})t}$.

The equations involved in this thesis (described below) are considered for the source class of SNRs. A specific case is valid in which particles of different energies are released from the accelerator at different times. Equation 7.3 is adapted to account for particles being released from the SNR shell, as this is a more realistic approach. This accounts for particles which have escaped the SNR radius and are diffusing into the ISM, as well as particles which are still trapped within the SNR shell, or 'bubble'. The probability density function (PDF) to describe the energy-dependent release and transport of particles through the ISM is:

$$f(E_\mathrm{p}, R, t) = \begin{cases} f_\mathrm{bubble}(E_\mathrm{p}, R, t) & E_\mathrm{p} < E_\mathrm{p,esc}, R < R_\mathrm{esc} \\ f_\mathrm{dif}(E_\mathrm{p}, R, t) & E_\mathrm{p} > E_\mathrm{p,esc}, R > R_\mathrm{esc} \\ 0 & \text{Otherwise}. \end{cases} \tag{7.8}$$

This model is hereafter called the 'shell origin model'. Assuming the limit $n_{\mathrm{H}} < 10^2\,\mathrm{cm^{-3}}$ applies, the PDF for the diffused emission is:

$$f_{\mathrm{dif}}(E_{\mathrm{p}}, R, t) = \frac{f_0 N_0 E_{\mathrm{p}}^{-\alpha}}{\pi^{3/2} R_{\mathrm{dif}}^3} \exp\left(-\frac{(R - R_{\mathrm{esc}})^2}{R_{\mathrm{dif}}^2}\right) , \tag{7.9}$$

where the diffusion length is

$$R_{\mathrm{dif}} \equiv R_{\mathrm{dif}}(E_{\mathrm{p}}, t) = \sqrt{4D(E_{\mathrm{p}})t'} , \tag{7.10}$$

where $t' = t - t_{\mathrm{esc}}(E_{\mathrm{p}})$ represents the time the particles spend in the ISM. For the above solution to be valid, the probability density function must satisfy the condition $\int_0^\infty f(E_{\mathrm{p}}, R, t)\, dV = \int_0^\infty f(E_{\mathrm{p}}, R, t) 4\pi R^2 dR = 1$. Therefore an extra term, f_0, is included, as defined by Equation 7.11 and derived in Section B.1.

$$f_0 = \frac{\sqrt{\pi} R_{\mathrm{dif}}^3}{(\sqrt{\pi} R_{\mathrm{dif}}^2 + 2\sqrt{\pi} R_{\mathrm{esc}}^2)|R_{\mathrm{dif}}| + 4 R_{\mathrm{esc}} R_{\mathrm{dif}}^2} \tag{7.11}$$

Equation 7.9 was also verified to be a solution to Equation 7.2 using the Green's function technique. As the particles are released at different times depending on their energy there are some particles which have not escaped the SNR shock radius, i.e. the 'bubble'. Particles of energy $E_{\mathrm{p}} < E_{\mathrm{p,esc}}$ and radius $R < R_{\mathrm{esc}}$ are confined within the SNR bubble. The distribution of CR particles in the bubble contains some uncertainty. Realistically, the CR particles would accumulate in the shock region leading to 'shell' brightening as explored by theoretical studies (Ptuskin and Zirakashvili, 2005; Celli et al., 2019; Brose et al., 2020). To obtain the realistic distribution involves solving again the transport equation where the diffusion term is neglected. This approach is complex and involves further assumptions about the distribution of gas that the SNR expands into, therefore we look for a simple solution. In this case, we choose to distribute the CR particles uniformly (see e.g. Atoyan et al., 1995; Zirakashvili and Aharonian, 2010) over the bubble volume, as we do not consider diffusion inside this region. The bubble emission is then described through:

$$f_{\mathrm{bubble}}(E_{\mathrm{p}}, R, t) = \frac{1}{(4/3)\pi R_{\mathrm{esc}}^3} . \tag{7.12}$$

7.3 Gamma-Ray Production

Kelner et al., 2006 provide analytical parameterisations for the spectra of γ-rays assuming they are created hadronically through the decay of neutral pions. These formulae are approximated from simulations of proton-proton collisions using the SIBYLL code (Fletcher et al., 1994). SIBYLL is a Monte Carlo simulation code

which provides a description of hadronic particle production. The analytical representation for the numerical simulations is accurate down to a few percent for γ-ray energies above $1\,\mathrm{GeV}$. For a proton with energy E_p the number of photons per collision for the interval from x to $x + dx$ is given by:

$$F_\gamma(x, E_\mathrm{p}) = B_\gamma \frac{\ln(x)}{x} \left(\frac{1 - x^{\beta_\gamma}}{1 + k_\gamma x^{\beta_\gamma}(1 - x^{\beta_\gamma})} \right)^4 \times$$
$$\left[\frac{1}{\ln(x)} - \frac{4\beta_\gamma x^{\beta_\gamma}}{1 - x^{\beta_\gamma}} - \frac{4k_\gamma \beta_\gamma x^{\beta_\gamma}(1 - 2x^{\beta_\gamma})}{1 + k_\gamma x^{\beta_\gamma}(1 - x^{\beta_\gamma})} \right] . \quad (7.13)$$

Here, the variable $x = E_\gamma / E_\mathrm{p}$. The parameters B_γ, β_γ and k_γ are estimated by taking the best least squares fit to the numerical calculation of the spectra, given by Equation 7.15.

$$\begin{aligned} B_\gamma &= 1.3 + 0.14L + 0.011L^2 \\ \beta_\gamma &= (1.79 + 0.11L + 0.008L^2)^{-1} \\ k_\gamma &= (0.801 + 0.049L + 0.014L^2)^{-1} , \end{aligned} \quad (7.14)$$

where $L = \ln(E_\mathrm{p}/1\,\mathrm{TeV})$. This is valid for incident protons of energy $0.1\,\mathrm{TeV} \leq E_\mathrm{p} \leq 10^5\,\mathrm{TeV}$. Using the above parameterisation, Kelner et al., 2006 calculate the production rate of γ-rays for some energy distribution of protons. The volume distribution of protons in the energy interval from E_p to $E_\mathrm{p} + dE_\mathrm{p}$ is $dN_\mathrm{p} = J_\mathrm{p}(E_\mathrm{p})\, dE_\mathrm{p}$. The γ-ray production rate in the energy interval from E_γ to $E_\gamma + dE_\gamma$ is then (Kelner et al., 2006):

$$\Phi_\gamma(E_\gamma) \equiv \frac{dN_\gamma}{dE_\gamma} = c\, n_\mathrm{H}(R) \int_{E_\gamma}^\infty \sigma_\mathrm{pp}(E_\mathrm{p})\, f(E_\mathrm{p}, R, t)\, F_\gamma \left(\frac{E_\gamma}{E_\mathrm{p}}, E_\mathrm{p} \right) \frac{dE_\mathrm{p}}{E_\mathrm{p}} , \quad (7.15)$$

where c is the speed of light, the ambient number density of hydrogen gas is n_H, the inelastic cross-section of proton-proton collisions is $\sigma_\mathrm{pp}(E_\mathrm{p})$ (Kafexhiu et al., 2014) and F_γ is the total γ-ray spectrum given by Equation 7.13.

The differential γ-ray spectrum, $\mathcal{F}$, is obtained by integrating the γ-ray production rate, Φ_γ, over the step size, dl, equal to the line of sight distance. The differential γ-ray flux $(\mathrm{TeV}^{-1}\,\mathrm{s}^{-1}\,\mathrm{cm}^{-2})$ is normalised to each cell in the map by accounting for the steradian of the cell, Ω.

$$\mathcal{F} = \frac{\Omega}{4\pi} \int_0^l \Phi_\gamma(E_\gamma)\, dl = \frac{\Phi_\gamma(E_\gamma)}{4\pi} \frac{A}{D^2} l , \quad (7.16)$$

where A is the area and D is the distance from the source to Earth. Combining the above with Equation 7.15, where $N_\mathrm{H} = n_\mathrm{H}\, l$, gives the differential γ-ray flux $(\mathrm{TeV}^{-1}\,\mathrm{cm}^{-2}\,\mathrm{s}^{-1})$:

$$\mathcal{F}_\gamma(E_\gamma, R, t) = \frac{N_\mathrm{H} A}{4\pi D^2} c \int\limits_{E_\gamma}^{\infty} \sigma_\mathrm{pp}(E_\mathrm{p}) \, J_\mathrm{p}(E_\mathrm{p}, R, t) \, F_\gamma \left(\frac{E_\gamma}{E_\mathrm{p}}, E_\gamma \right) \frac{dE_\mathrm{p}}{E_\mathrm{p}} \, . \tag{7.17}$$

Here, the volume distribution of CRs is:

$$J_\mathrm{p}(E_\mathrm{p}, R, t) = \frac{c}{4\pi} f(E, R, t) \, , \tag{7.18}$$

where $f(E_\mathrm{p}, R, t)$ is from Equation 7.3 for the point origin model and Equation 7.8 for the shell origin model.

7.4 The Modelling Software `mario`

We adopt a model in this thesis for the injection of CR protons from an SNR and their subsequent escape and transport through the ISM. For this purpose we developed a `Python` package called `mario` (**M**odelling g**A**lactic gamma-**R**ay emiss**IO**n[4]). This modelling software was used to obtain the results in Chapter 6. `mario` uses a 2D approach to model the diffusion of CR protons, which have escaped the SNR, over each pixel in the total column density map. The emission inside the bubble region is also modelled using the same pixel-by-pixel approach. These maps are then used to produce γ-ray flux maps towards HESS J1804$-$216, and compared with observations.

`mario` provides both the point origin and shell origin models as described by Equations 7.3 and 7.8, respectively. The point origin model involves particles being injected into the ISM isotropically from the centre of the SNR. The shell origin model consists of two different components. The particles which have been injected and diffuse into the ISM upon escaping the shell of the SNR and the particles which are still trapped within the 'bubble' described by Equation 7.12.

Figure 7.1 shows a comparison of the CR proton spectra from the point origin and shell origin models for the same model parameters. For the shell origin model the escape radius is $R_\mathrm{esc} = 25\,\mathrm{pc}$, therefore the proton fluxes at $R = 24\,\mathrm{pc}$ and $R = 26\,\mathrm{pc}$ are shown to represent both the bubble component and diffused component, respectively. The point origin model in Figure 7.1 shows only the diffused component, which is the same for both radii at higher energies ($> 1\,\mathrm{TeV}$). As the energy decreases further, the CR proton flux from the point origin model at $R = 26\,\mathrm{pc}$ (red curve) decreases more rapidly than the point origin model at $R = 24\,\mathrm{pc}$ (light red curve). For the shell origin model, there is a clear difference between the CR proton spectra from the diffused and bubble components. The light blue curve in Figure 7.1 (with $R = 24\,\mathrm{pc}$) shows the emission from inside the bubble, as the escape radius for

---

[4]mario code available at GitHub https://github.com/Astro-Kirsty/mario

this model is $R_{esc} = 25\,\mathrm{pc}$. This emission is only seen for energies below the escape energy of $E_{p,esc} \sim 2.5\,\mathrm{TeV}$, as this is a condition of the bubble (see Equation 7.8). At energies above the escape energy the diffused component of the CR proton flux at $R = 26\,\mathrm{pc}$ is present (as shown by the navy curve in Figure 7.1). This curve overlaps with the point origin model (shown by the red curve in Figure 7.1), as these are both the diffused component of the emission using the same model parameters.
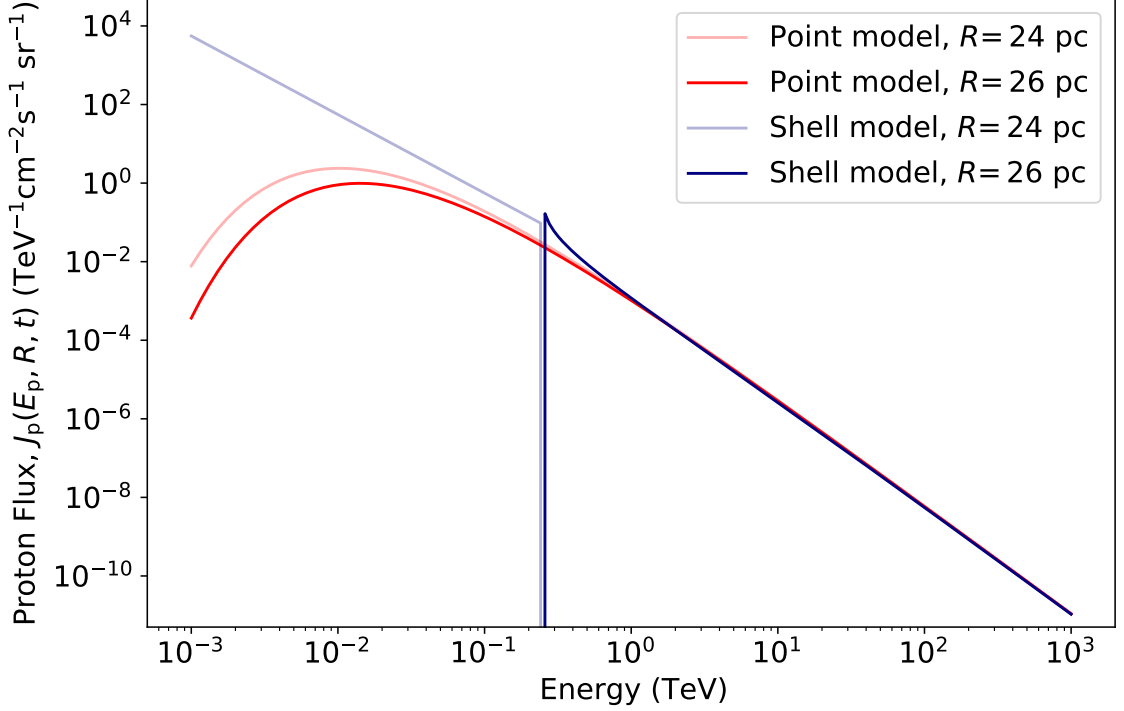
Figure 7.1: Comparison of the point origin and shell origin models for an arbitrary injection spectrum. The escape radius for the shell origin model is $R_{esc} = 25\,\mathrm{pc}$. The light red curve shows the point origin model using a radius of $R = 24\,\mathrm{pc}$ and the red curve shows the point origin model with $R = 26\,\mathrm{pc}$. The light blue curve shows the shell origin model inside the SNR bubble with a radius of $R = 24\,\mathrm{pc}$ and the dark blue curve shows the shell origin model outside the SNR bubble with a radius of $R = 26\,\mathrm{pc}$. For energies greater than the escape energy, $E_{p,esc} \sim 2.5\,\mathrm{TeV}$, both the point origin and shell origin models largely overlap, as this represents the diffused component of the CR flux. At energies below this, the shell origin model is described by a uniform distribution, whereas the point origin models are still described by the diffused emission.

The shell origin model is utilised throughout this thesis (see Equation 7.8). Figure 7.2 shows a schematic of the model in 2D, in which CRs leave the SNR bubble and interact with each pixel in the map, which has multiple characteristics. The column density, N_H, from the gas observations along with the volume distribution of CRs (Equation 7.18) are used to create a γ-ray flux, $\mathcal{F}(E_\gamma)$ (Equation 7.17), for each pixel in the map. The purple region of Figure 7.2 indicates the bubble component as described by Equation 7.12 where $E_p < E_{p,esc}$ and $R < R_{esc}$. The yellow region of Figure 7.2 indicates the region of diffused emission which is described by Equation 7.9.
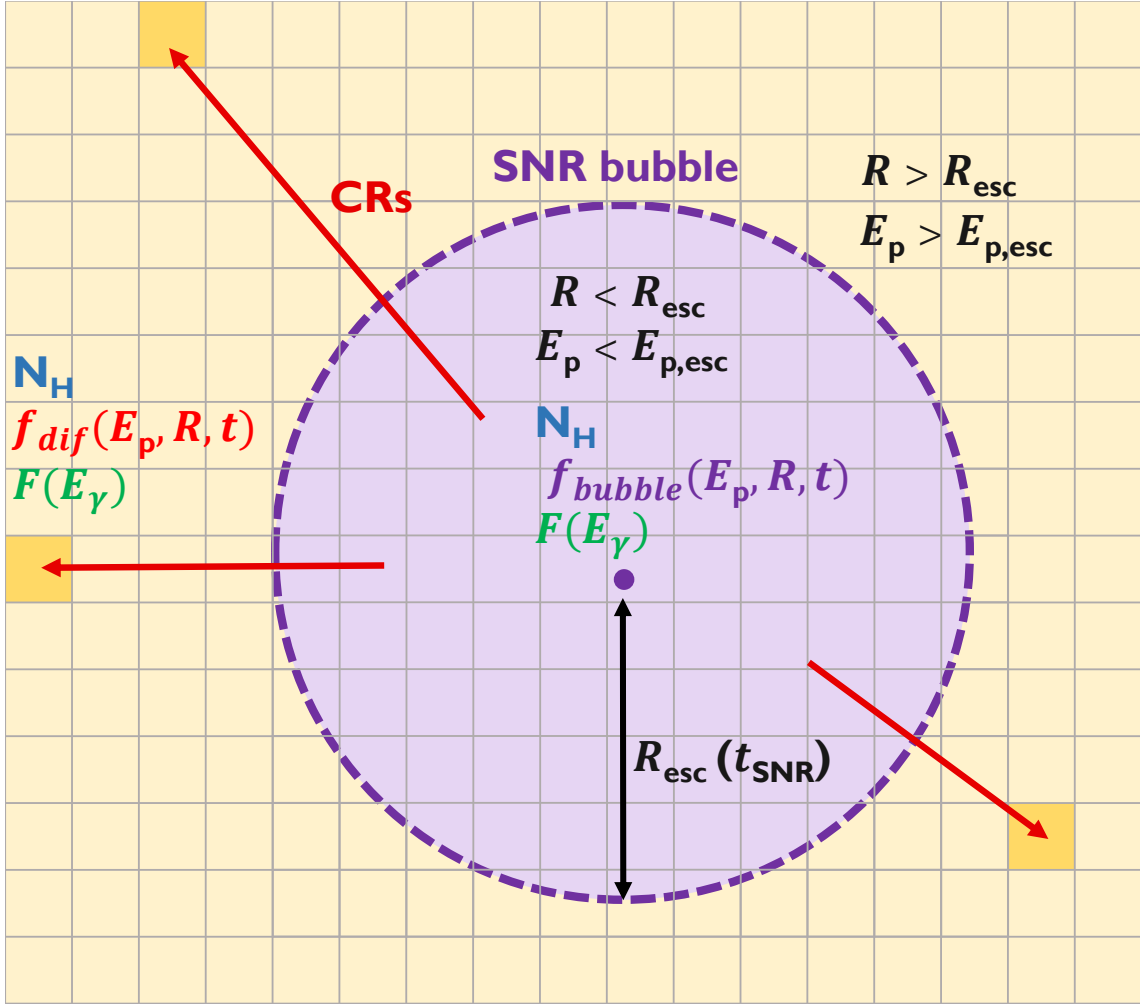
Figure 7.2: Schematic illustrating the release point of CRs from the SNR bubble (shown in purple) and their subsequent propagation to interact with the ISM to create γ-rays. Each pixel has characteristics of N_{H} and $\mathcal{F}(E_\gamma)$. The purple pixels inside the bubble have a PDF described by $f_{\mathrm{bubble}}(E_{\mathrm{p}}, R, t)$ and the yellow pixels outside of the bubble have a PDF described by $f_{\mathrm{dif}}(E_{\mathrm{p}}, R, t)$.

For the model, a proton flux map is created for every pixel in the map for a range of energies, giving a proton flux 'cube'. Combining this with the total column density map gives a γ-ray flux 'cube', again with energy along the third axis. This γ-ray flux cube means that each pixel in the map has an associated γ-ray spectra (an example shown in Figure 7.3). The γ-ray source spectra can also be obtained by taking a region around the γ-ray source and summing all fluxes within that region.

For the shell origin model there are two components: the diffused emission outside the bubble component and the uniformly described emission inside the bubble. To investigate the results for these components, the emission is investigated for two different pixels in the γ-ray flux map, one inside the bubble and another outside. Figure 7.3 shows a comparison between these two components for an arbitrary SNR accelerator. This figure shows a clear distinction between the bubble and diffused components, which are separated by the escape energy $E_{\mathrm{p,esc}} \sim 3.8\,\mathrm{TeV}$.
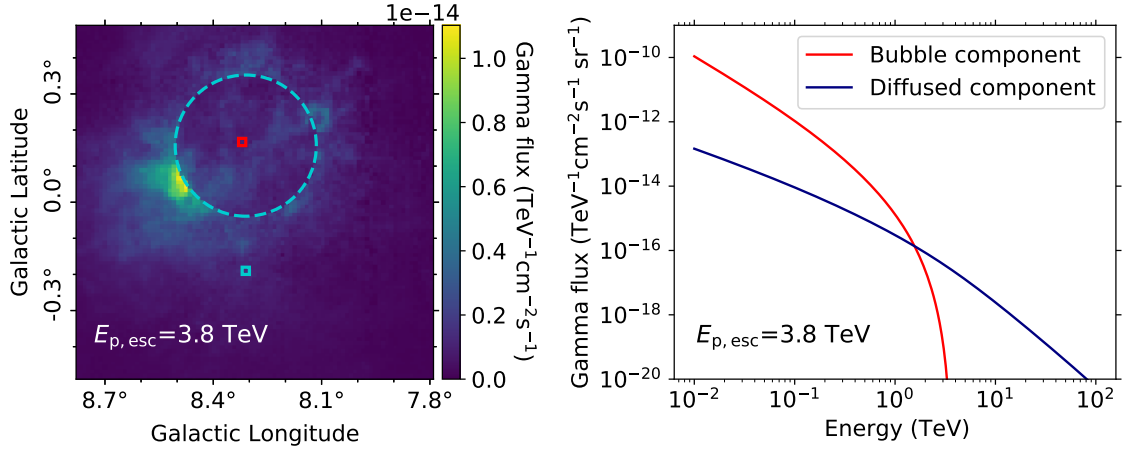
Figure 7.3: Comparison between the bubble and diffused emission as taken from a γ-ray map. The escape energy is $E_{\mathrm{p,esc}} \sim 3.8\,\mathrm{TeV}$. *Left*: the γ-ray flux map for an arbitrary source indicating the SNR bubble by the dashed cyan circle. The red pixel is inside the bubble and the cyan pixel is outside the bubble. *Right*: the diffused component of the γ-ray flux shown by the blue curve taken from the cyan pixel in the left panel. The bubble component taken from the red pixel in the left panel shown by the red curve. The flux from the bubble component rapidly drops off when the escape energy is reached, where the diffused component begins to dominate.

Figure 7.4 shows an example of the 2D approach used here. Panel A of Figure 7.4 shows the total column density map (N_{H}) for two example clouds with constant number density. The proton flux distribution, $J_{\mathrm{p}}(E_{\mathrm{p}}, R, t)$, at 2 TeV for an arbitrary source is shown in Panel B1 of Figure 7.4. This panel shows the component of the bubble emission where the escape energy is $E_{\mathrm{p,esc}} \sim 3\,\mathrm{TeV}$. Panel B2 shows the proton flux distribution for the diffused emission, at 10 TeV. Combining Panels A and B2 from Figure 7.4 through Equation 7.17 gives an example of the γ-ray flux map at 1 TeV (Panel C of Figure 7.4).

Panel B1 of Figure 7.4 shows a slice of the proton flux cube at 2 TeV. As this is lower than the escape energy, $E_{\mathrm{p,esc}} \sim 3\,\mathrm{TeV}$, this represents the bubble component and so is 'bubble-filled'. Panel B2 in Figure 7.4 shows the proton flux at 10 TeV which is higher than the escape energy, therefore this is the diffused component of the emission. This shows that the bubble is no longer filled and the proton flux is dominant outside the SNR bubble radius. Combining the proton flux map and the total column density map gives the γ-ray flux map, as shown at 1 TeV in Panel C of Figure 7.4. At this energy it is possible to see both the influence of the bubble and diffused components. The navy circle in the centre presents the contribution from the bubble component. Outside of this, the two gas clouds become clearly visible with the strongest emission just outside the bubble radius.
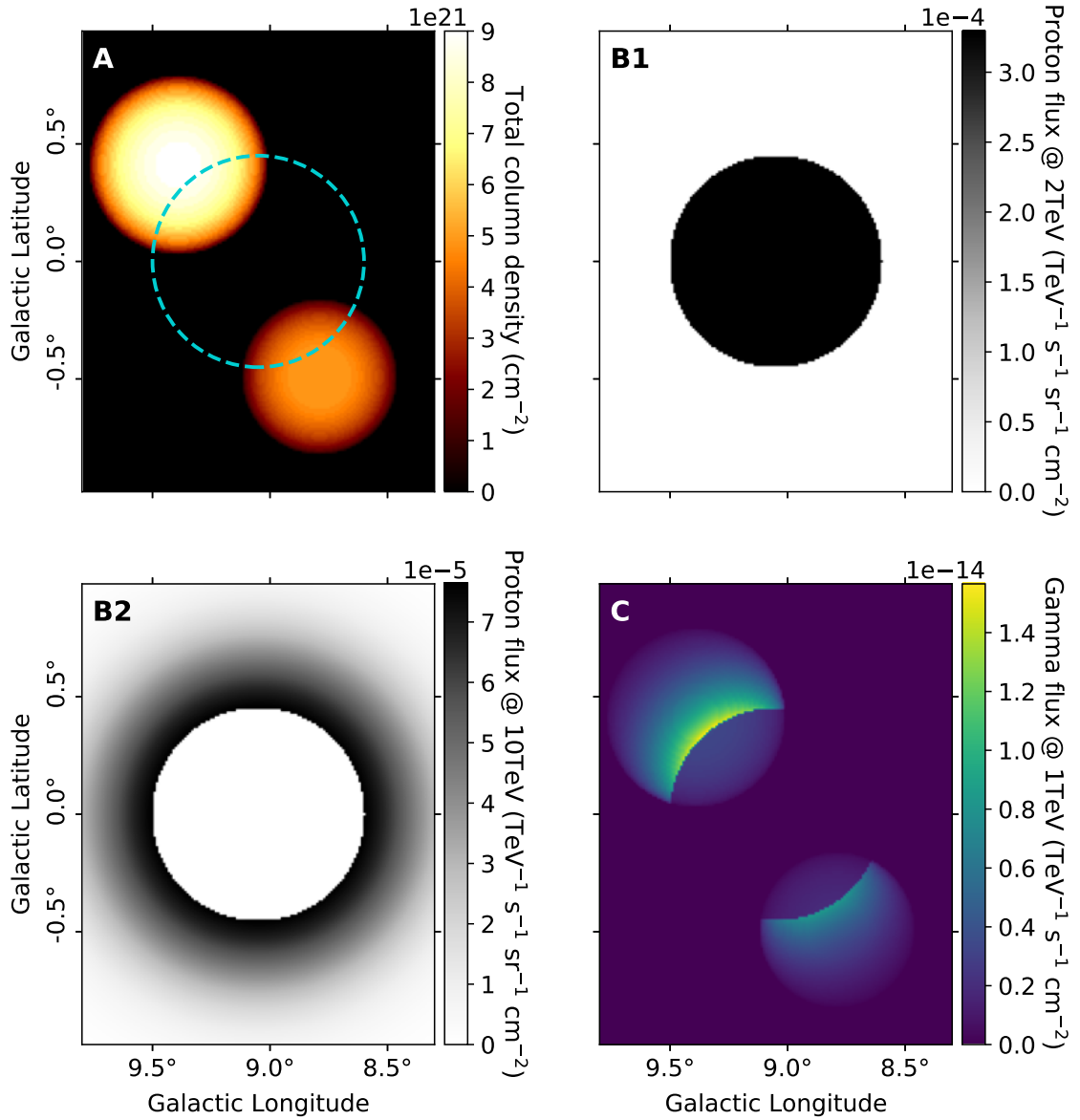
Figure 7.4: An example figure showing the 2D approach used in this thesis. **Panel A**: Total column density towards two example clouds for a constant number density throughout the clouds. **Panel B1**: The proton flux at $2\,\mathrm{TeV}$ for an arbitrary source, representing the bubble emission. This model has an escape energy of $E_{\mathrm{p,esc}} \sim 3\,\mathrm{TeV}$, therefore this panel is clearly dominated by the bubble emission. **Panel B2**: The proton flux at $10\,\mathrm{TeV}$, representing the diffused emission. This shows that the bubble component is not visible. The emission outside the bubble radius is strongest close to the bubble radius, and begins to decrease as you move away from this radius. **Panel C**: The γ-ray flux at $1\,\mathrm{TeV}$. The contribution from the two gas clouds is clearly visible.

7.5 Verification of `mario`

The following section outlines the verification of the `mario` code. This is done by comparing specific sections of the code with figures from other publications such as Aharonian and Atoyan, 1996; Kelner et al., 2006. In addition, the implementation of the code is verified.

7.5.1 Verification with other publications

To verify our model is producing accurate results several tests were performed. Firstly, to ensure each equation is implemented correctly, various figures from literature (i.e. Aharonian and Atoyan, 1996; Kelner et al., 2006) are reproduced. Figs 1a and b of Aharonian and Atoyan, 1996 are replicated using an energy budget of $W_\mathrm{p} = 10^{50}$ erg, spectral index of $\alpha = 2.2$, number density of $n_\mathrm{H} = 1\,\mathrm{cm}^{-3}$ and index of diffusion coefficient of $\delta = 0.5$, for various source ages and distances, as shown in Figure 7.5. The diffusion coefficient from Aharonian and Atoyan, 1996 is:

$$D(E_\mathrm{p}) = D_{10}(E_\mathrm{p}/10\,\mathrm{GeV})^{\delta}\,, \tag{7.19}$$

where D_{10} is the diffusion coefficient at $E_\mathrm{p} = 10\,\mathrm{GeV}$ given by $10^{28}\,\mathrm{cm}^2\,\mathrm{s}^{-1}$ for fast diffusion and $10^{26}\,\mathrm{cm}^2\,\mathrm{s}^{-1}$ for slow diffusion. This equation is equivalent to Equation 7.5 from Gabici et al., 2007 when $B = 3\,\mu\mathrm{G}$, D_0 takes the Galactic average value of $\sim 3 \times 10^{27}\,\mathrm{cm}^2\,\mathrm{s}^{-1}$ where $\chi = 1$ for fast diffusion and $\chi = 0.01$ for slow diffusion. Figure 7.5 replicates the Aharonian and Atoyan, 1996 figure, therefore the section of code for the distribution of protons from the point origin model is validated.

Modelling of the γ-ray production rate has been performed by Kelner et al., 2006. Fig 7 from Kelner et al., 2006 shows the energy spectra of γ-rays as produced by proton-proton interactions for three different initial CR proton energies, $E_\mathrm{p}=0.1$ TeV, 10 TeV[5], 1000 TeV. Using Equation 7.13 this plot is reproduced as shown in Figure 7.6. The reproduced plot matches the results from Kelner et al., 2006, so the implementation of the γ-ray equation from Equation 7.17 in `mario` is verified.

We are able to replicate both the proton distribution and the γ-ray flux spectra for the point origin model, verifying these sections of the `mario` code. It is not possible to compare the shell origin model from any figures in literature, however, as the curves from the point origin and shell origin models are the same for the diffused component (see Figure 7.1), we can be confident that the code is implemented well for the shell origin model. The physics behind the diffused component of the `mario` code is the same for both the point origin and shell origin models.

---

[5]There is a misprint in Fig 7 of Kelner et al., 2006, 100 TeV should be replaced by 10 TeV.
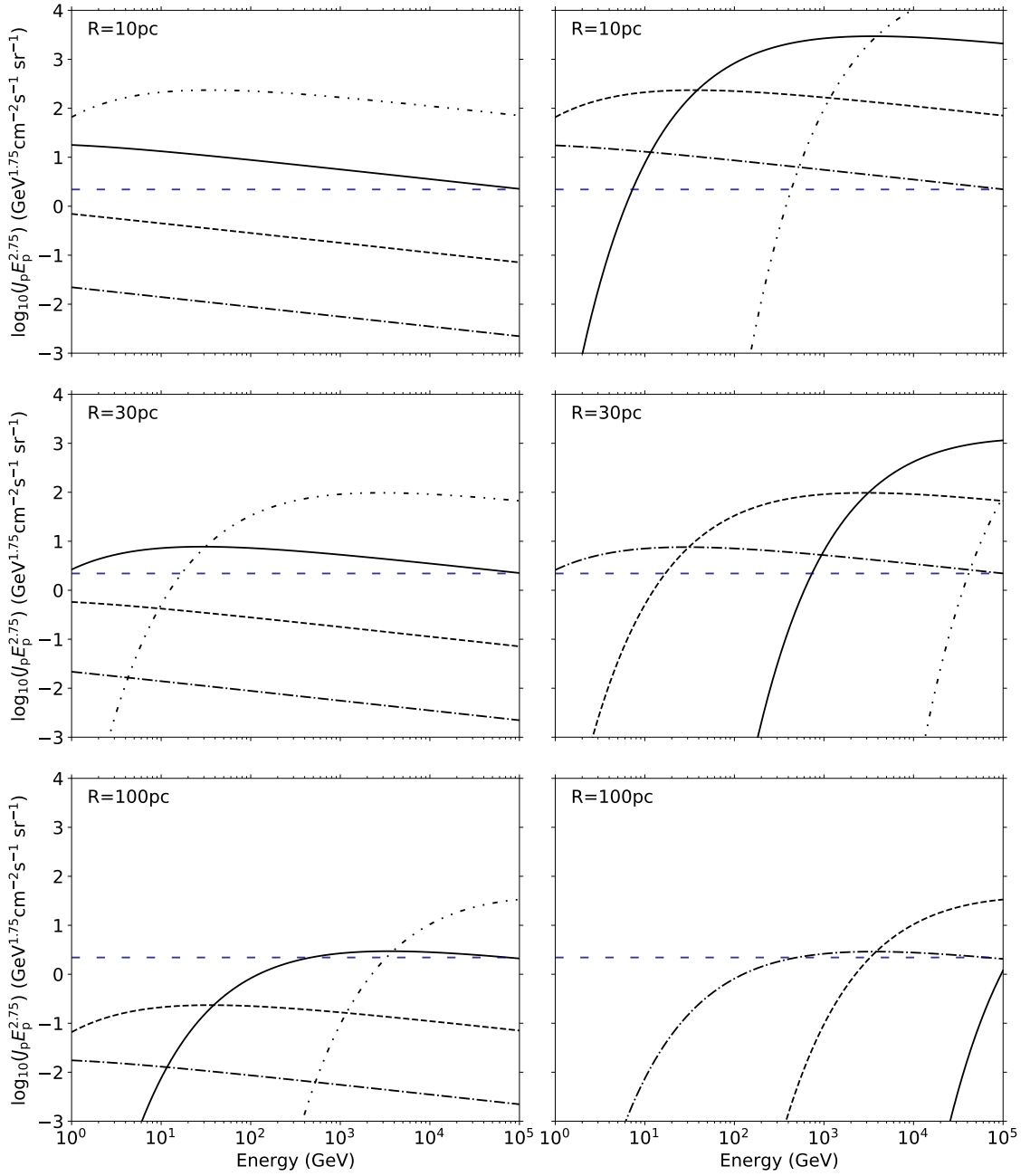
Figure 7.5: Evolution of escaping CRs from an impulsive accelerator using the point origin model. Curves show dash dot-dotted, solid, dashed and dot-dashed for ages of the source t=10^3 yr, 10^4 yr, 10^5 yr and 10^6 yr, respectively. The energy-dependent diffusion coefficient from Equation 7.19 has a power law index of $\delta = 0.5$ with $D_{10} = 10^{28}\,\mathrm{cm}^2\,\mathrm{s}^{-1}$ for fast diffusion (left panel) and $D_{10} = 10^{26}\,\mathrm{cm}^2\,\mathrm{s}^{-1}$ for slow diffusion (right panel). The spectral index is $\alpha = 2.2$ with an energy budget of $W_\mathrm{p} = 10^{50}\,\mathrm{erg}$. The dashed blue curve shows the CR flux at Earth. Image replicated from Aharonian and Atoyan, 1996.
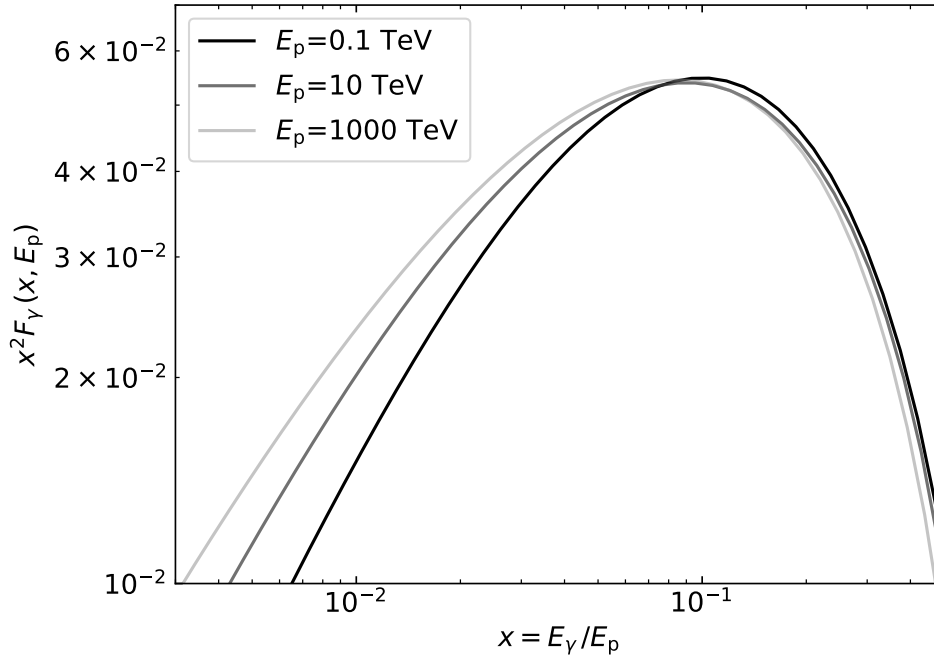
Figure 7.6: Energy spectra of γ-rays using the number of photons per collision F_γ from Equation 7.13 for different energy for the incident protons. The black, dark grey and light grey curves show proton energies of $0.1\,\mathrm{TeV}$, $10\,\mathrm{TeV}$ and $1000\,\mathrm{TeV}$, respectively. Image replicated from Kelner et al., 2006.

7.5.2   Verification of the implementation

Further validation of the model involves investigating the energy budget. It is expected that the volume integrated energy spectra after simulations will be the same as the injected spectrum of CRs. The volume integrated spectrum is obtained through $\int 4\pi R^2 f(E_\mathrm{p}, R, t)dR$, where $f(E_\mathrm{p}, R, t)$ is the PDF described by Equation 7.8. The injected spectrum of CRs is described by $N_0 E_\mathrm{p}^{-\alpha}$. Figure 7.7 shows this comparison for an arbitrary source, in which both spectra match.

For some arbitrary source with an energy budget of $W_\mathrm{p} = 10^{50}\,\mathrm{erg}$, it is expected this will equal the final energy budget after simulations, given by Equation 7.20.

$$W_\mathrm{p,final} = \int 4\pi R^2\, dR\, W_\mathrm{d} \qquad \mathrm{erg}\,, \qquad (7.20)$$

where $W_\mathrm{d} = \int E_\mathrm{p}\, f(E_\mathrm{p}, R, t)\, N_0\, E_\mathrm{p}^{-\alpha} dE_\mathrm{p}$ is the energy density $(\mathrm{erg\,cm^{-3}})$ for each distance, R. This can be visualised by the energy budget distribution with respect to the distance from the source, R, as shown in Figure 7.8. The left panel of Figure 7.8 shows the cumulative sum of the energy budget, $W_\mathrm{ps} = 4\pi R^2\, dR\, W_\mathrm{d}$, distributed over the space. The plots tends to plateau at an energy budget of $W_\mathrm{p,final} = 10^{50}\,\mathrm{erg}$ as expected from the input energy budget, W_p. The right hand panel of Figure 7.8 shows the energy density (W_d) distributed over all space. It is clear that most of the energy is distributed within the SNR radius, indicated by R_esc. Both panels of Figure 7.8 show that most of the energy in contained within $100\,\mathrm{pc}$ of the accelerator.
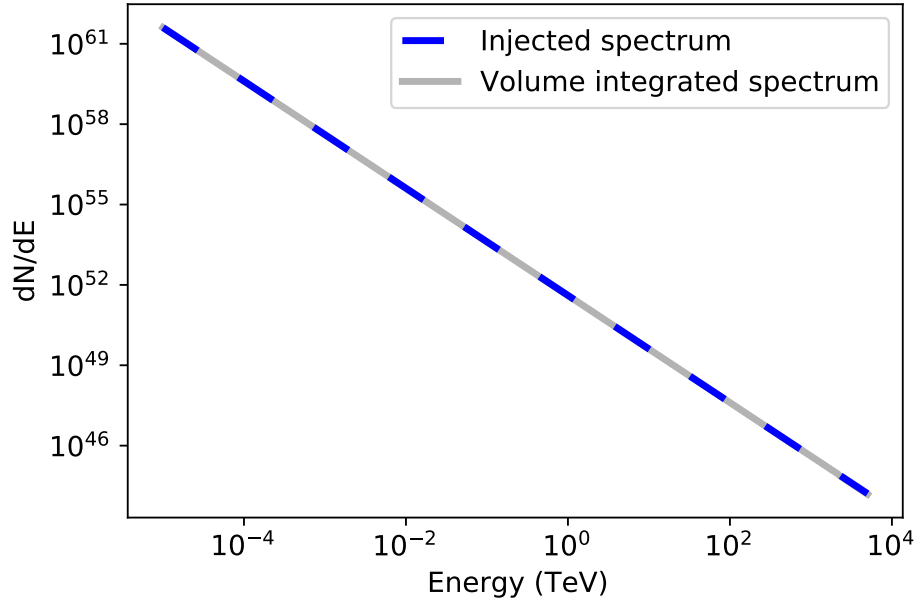
Figure 7.7: The injected spectrum, $N_0 E_{\mathrm{p}}^{-\alpha}$, of the CR protons is shown by the blue dashed curve. The CR proton spectrum from integrating over the volume, $\int 4\pi R^2 f(E_{\mathrm{p}}, R, t)\, dR$, is shown by the grey curve. Both of these curves match, therefore the input spectrum is the same as the output spectrum, as expected.
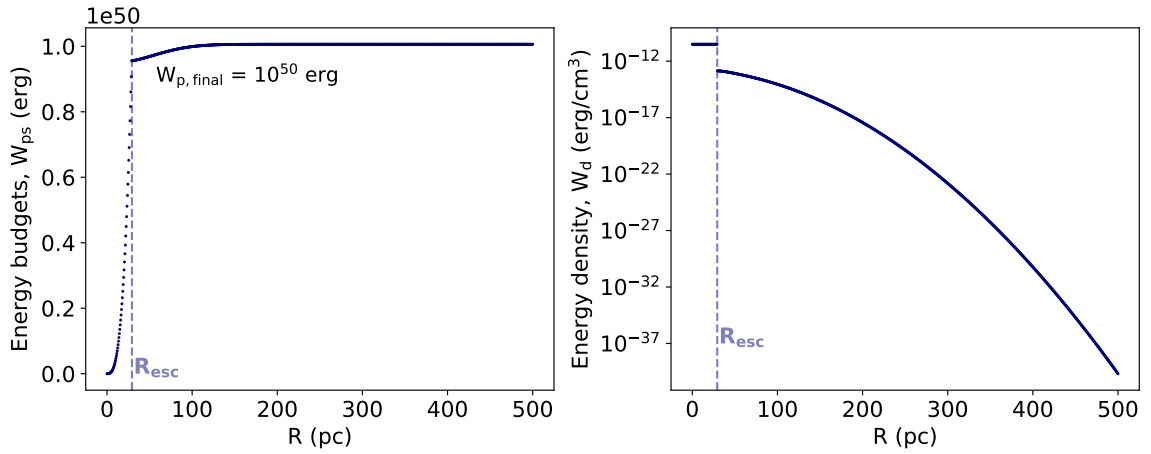
Figure 7.8: CR energy distributed over space from the accelerator to $500\,\mathrm{pc}$. The dashed blue line indicates the radius of the SNR also given by the escape radius, R_{esc}. *Left*: the cumulative sum of the energy budget, $W_{\mathrm{ps}} = 4\pi R^2\, dR\, W_{\mathrm{d}}$. *Right*: the energy density, W_{d}, as distributed over R. These plots show that the energy budget is mostly distributed within $100\,\mathrm{pc}$ of the accelerator.

7.6   Influence of Model Parameter Variation

It is important to investigate the parameter space of our model to ensure each parameter behaves as it is expected to. Figure 7.9 shows the effect of varying different parameters in the model. The parameter space is outlined in Table 1 of Chapter 6. The models shown in Figure 7.9 have an arbitrary base model with the parameters shown in Table 7.1. The parameters of this base model are then varied individually to see the effect of the model parameters on the spectra, as shown in Figure 7.9.

Table 7.1: Base model parameters for Figure 7.9.

χ	δ	$E_{p,max}$	δ_p	α	E_{SN}	t_{sedov}	M_{ej}
		(PeV)			(erg)	(yr)	$(M_\odot)$
0.01	0.5	1	2.5	1.8	10^{51}	1600	10

Figure 7.9 panel A and B, show that as the diffusion parameters δ and χ increase, the flux decreases at higher energies. A higher δ or χ value gives a higher diffusion coefficient (Equation 7.5) which means the particles are transported quickly. Equation 7.5 is inversely proportional to the γ-ray flux from Equation 7.17 resulting in a decrease in γ-ray flux as δ and χ increase. These plots also show that below the escape energy the γ-ray fluxes for the parameters start to match, which is attributed to the bubble component of the flux. Panel C shows the dependency of δ_p on the escape energy, $E_{p,esc}$. These parameters are related through Equation (5) in Chapter 6. As δ_p increases, the escape energy decreases rapidly. This is evident in Equation (5) where $t_{sedov} < t_{SNR}$ which makes δ_p and $E_{p,esc}$ indirectly proportional. This figure therefore shows how δ_p effects the energy at which the diffusion component dominates over the bubble component. This effect is seen for $\delta_p = 1.4$ and $\delta_p = 2.5$ as the corresponding escape energies are in the energy range shown in Figure 7.9. In Figure 7.9 panel D shows the effect of the maximum CR proton energy on the escape energy. There is only a slight variation in the curvature of the models, particularly at low energies and at $\sim 1\,\mathrm{TeV}$. The maximum proton energy, $E_{p,max}$, is proportional to the escape energy, $E_{p,esc}$, as shown by Equation (5) in Chapter 6, therefore as $E_{p,max}$ increases so too does $E_{p,esc}$. As the escape energy increases, more of the spectra is dominated by the bubble. In panel D of Figure 7.9, $E_{p,esc} = 15.8\,\mathrm{TeV}$ for $E_{p,max} = 5\,\mathrm{PeV}$, therefore the bubble component of the γ-ray emission extends to higher energies than for $E_{p,max} = 1\,\mathrm{PeV}$. The variation in curvature is attributed to the change between the bubble and diffused emission being at different energies. Panel E shows that as the spectral index α increases, the flux above $\sim 1\,\mathrm{TeV}$ decreases. This behaviour is due to these parameters being inversely proportional, as shown in Equation 7.18. This effect is most prominent at higher energies.
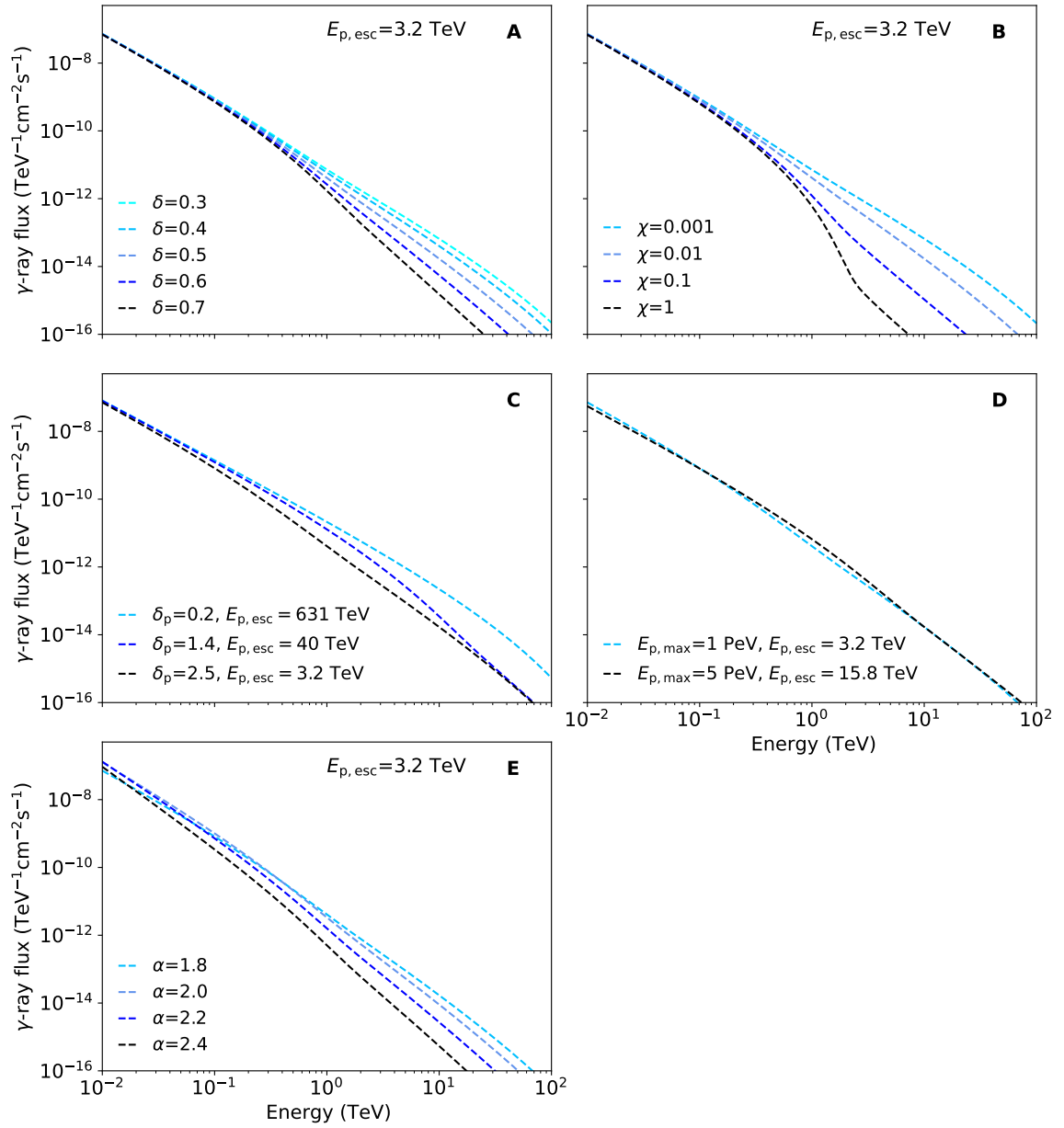
Figure 7.9: Modelled γ-ray spectra for different model parameters, with the base model described in Table 7.1. The escape energy, $E_{\mathrm{p,esc}}$, is shown for each parameter variation. **A**: As the index of the diffusion coefficient, δ, varies from 0.3 to 0.7 the flux decreases. **B**: By varying the diffusion suppression factor, χ, from 0.001 to 0.1 the flux begins to decrease. **C**: The γ-ray flux increases with lower values of the parameter for the energy-dependent release of CRs, δ_{p}. **D**: By varying the maximum CR proton energy, $E_{\mathrm{p,max}}$, there is only slight variation in the spectra. **E**: As the spectral index, α, increases from 1.8 to 2.4 the γ-ray flux above $\sim 1\,\mathrm{TeV}$ decreases.

7.7 Optimisation Procedure

The model described throughout this thesis has a range of model parameters. Multiple parameters have a similar effect on the model results, as outlined in Section 7.6, leading to a redundancy in the model solution. Therefore, a purely quantitative optimisation across all parameters is not possible. To overcome this, a systematic grid search over the parameter space is performed, in which each combination of parameters is modelled. Many parameters in the model have a parameter space which is defined from typical values in literature as determined through both experimental and theoretical studies. The energy budget ($W_{\mathrm{p}} = \eta E_{\mathrm{SN}}$), however, is scaled to fit the spectral data. The sum of the absolute value of the residuals, r, is minimised using the least absolute deviations method to determine the optimal η value which provides a match to the observations.

$$r = \sum_i \left(|F_{\mathrm{obs}} - \eta_i\, F_{\mathrm{model}}| \right), \tag{7.21}$$

where η_i is varied from 0.001 to 1, F_{obs} is the observed flux and F_{model} is the model flux. Each η_i value is evaluated until the residual is minimised by η. The energy budget, W_{p}, as determined from above will shift the spectrum up and down to match the observations.

To determine the best matching model to the GeV-TeV observations two different metrics are used for the spectral and spatial γ-ray distributions. The metric used here for the spectral analysis is given by Equation 7.22 which quantifies how well the model data fits the observations.

$$\frac{\chi^2}{m} = \left(\sum_i \frac{(F_{\mathrm{obs,i}} - F_{\mathrm{model,i}})^2}{\sigma_{\mathrm{model,i}}^2} \right) \frac{1}{m}, \tag{7.22}$$

where $F_{\mathrm{obs,i}}$ is the observed flux, $F_{\mathrm{model,i}}$ is the model flux, $\sigma_{\mathrm{model,i}}$ is the uncertainty in the observations, i denotes each spectral data point and m is the number of data points. For the model to match the observations well, χ^2/m is expected to be one.

For the spatial model we want the γ-ray flux values for the model inside the γ-ray source region to be similar to the observation values in the same region. The metric used to examine the spatial agreement with observations is the standard deviation which measures how far the spread of the model deviates from the mean (see Equation 7.23). The bubble component for this metric is excluded as the distribution of particles are not modelled in detail here.

$$S = \frac{\sum_i (R_i - \mu)^2}{N}, \tag{7.23}$$

where $R_i = F_{\mathrm{obs,i}} - F_{\mathrm{model,i}}$ is the residual from the integrated flux map from 1 TeV to 100 TeV (to match the H.E.S.S. Collaboration et al., 2018 observations) for each

pixel i in the residual map, μ is the mean of the residual map and N is the number of pixels in the residual map. To ensure this method is acceptable two different spatial models are considered, shown in Figure 7.10. The left panel of Figure 7.10 shows that the morphology matches observations well in comparison to the right panel where the morphology shows a peak in γ-ray emission offset from the position of the γ-ray observation peak. This clear distinction is quantitatively confirmed through the standard deviation values, where the lower value of S indicates the model matches the observations better.
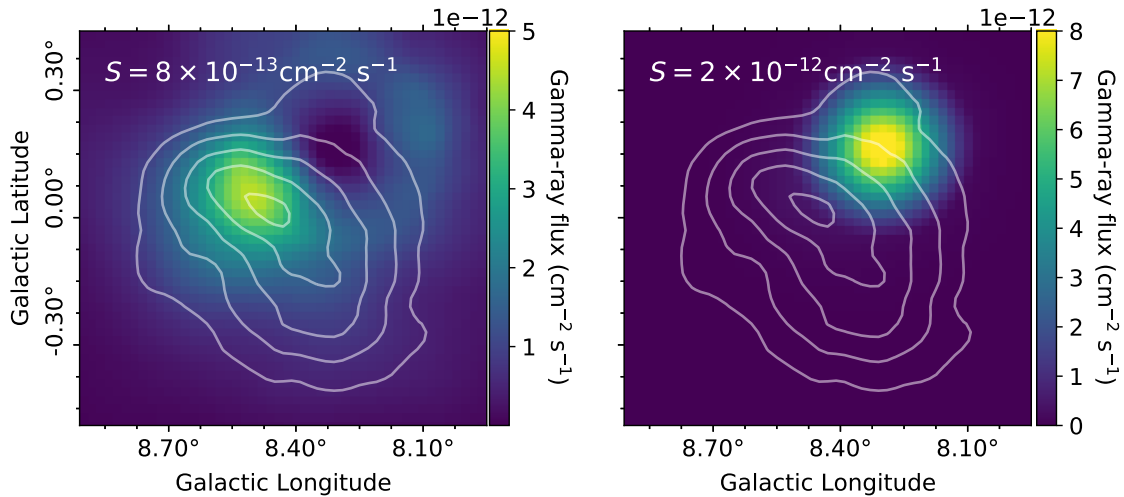
Figure 7.10: γ-ray flux maps for two different models for an arbitrary accelerator compared to observations shown by the solid white contours. *Left*: γ-ray flux for a standard deviation of $S = 8 \times 10^{-13}\,\mathrm{cm}^{-2}\,\mathrm{s}^{-1}$. *Right*: γ-ray flux for a standard deviation of $S = 2 \times 10^{-12}\,\mathrm{cm}^{-2}\,\mathrm{s}^{-1}$. This shows that the lower value of standard deviation (left panel) matches the observations better than the higher value (right panel).

In determining the best model there are a few criteria that must be met. Firstly, the modelled emission should not be 'bubble-filled' as the emission in that component is not modelled in great detail. The emission is considered bubble-dominated if the emission inside the bubble is 10 % greater than the emission outside the bubble region. Another criterion to be met is that the η value is less than 50% of the total kinetic energy (Ackermann et al., 2013; Berezhko and Völk, 1997; Berezhko and Völk, 2000). Once excluding these models, the best matching models for each accelerator are chosen by sorting the models in ascending order of the spectral criterion, Equation 7.22. The top 5 models are chosen based on this criterion as we are largely biased by the bubble component for the spatial emission. The best matching model should also have a well matched spatial morphology, therefore we take the lowest value of the spatial criterion (Equation 7.23) from the top 5 spectral models. This model then becomes the best matching model.

7.8   Discussion

Chapter 6 shows the results for the best matching spectral and spatial model for each accelerator. The best matching model is chosen by taking the 5 best matching spectral models (lowest values of χ^2/m from Equation 7.22), and choosing the lowest standard deviation from the spatial model (Equation 7.23). The top 5 models are chosen as they are within the tail of the χ^2/m distribution as shown for each accelerator in Figure 7.11.
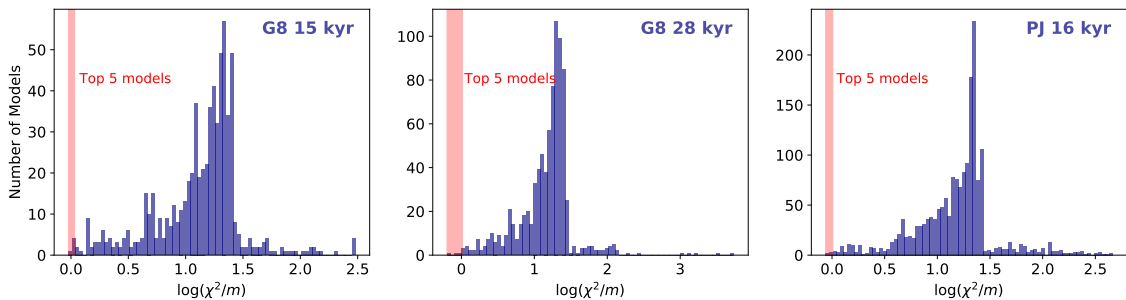
Figure 7.11: χ^2/m distribution for each accelerator. The red shaded regions indicate the 5 best matching models for the spectral criterion.

The spatial and spectral plots for the 5 best matching models are shown in this section. For completeness, the energy bands defined in Chapter 6 are also shown here for the 5 best matching models.

7.8.1   SNR G8.7−0.1: 15 kyr

The 5 best matching models for SNR G8.7−0.1 with an age of 15 kyr are shown in Figure 7.12. The morphology for the different energy bands defined in Chapter 6 are shown by Figures B.1 and B.2.

The 5 best matching spatial models of the integrated flux above 1 TeV for SNR G8.7−0.1 with an age of 15 kyr have similar morphology with a bright band of modelled γ-ray emission towards the southern edge of SNR G8.7−0.1. The top 5 models contain a range of δ, δ_p and $E_{\mathrm{p,max}}$ values and SN types (see Table D1 of Chapter 6), given the similarity in morphology means the models are not sensitive enough to the change in these parameters. The stronger emission does not overlap with the TeV peak of HESS J1804−216 from observations. For each model, the results are highly biased by the bubble component, due to its large size.

The spectral plots for SNR G8.7−0.1 show that the model matches the observations well at lower energies. At energies above 5 TeV, however, the model deviates from the spectral observations. The escape energy for SNR G8.7−0.1 with an age of 15 kyr is ∼15 TeV-19 TeV. This high value means the bubble component is dominating for each of the top 5 models, which is shown by splitting the spectra into their bubble and diffused components. The bubble component contains some uncertainty due to the uniform distribution of particles. Therefore, as the bubble dominates the γ-ray spectra there is some uncertainty associated with the figure.
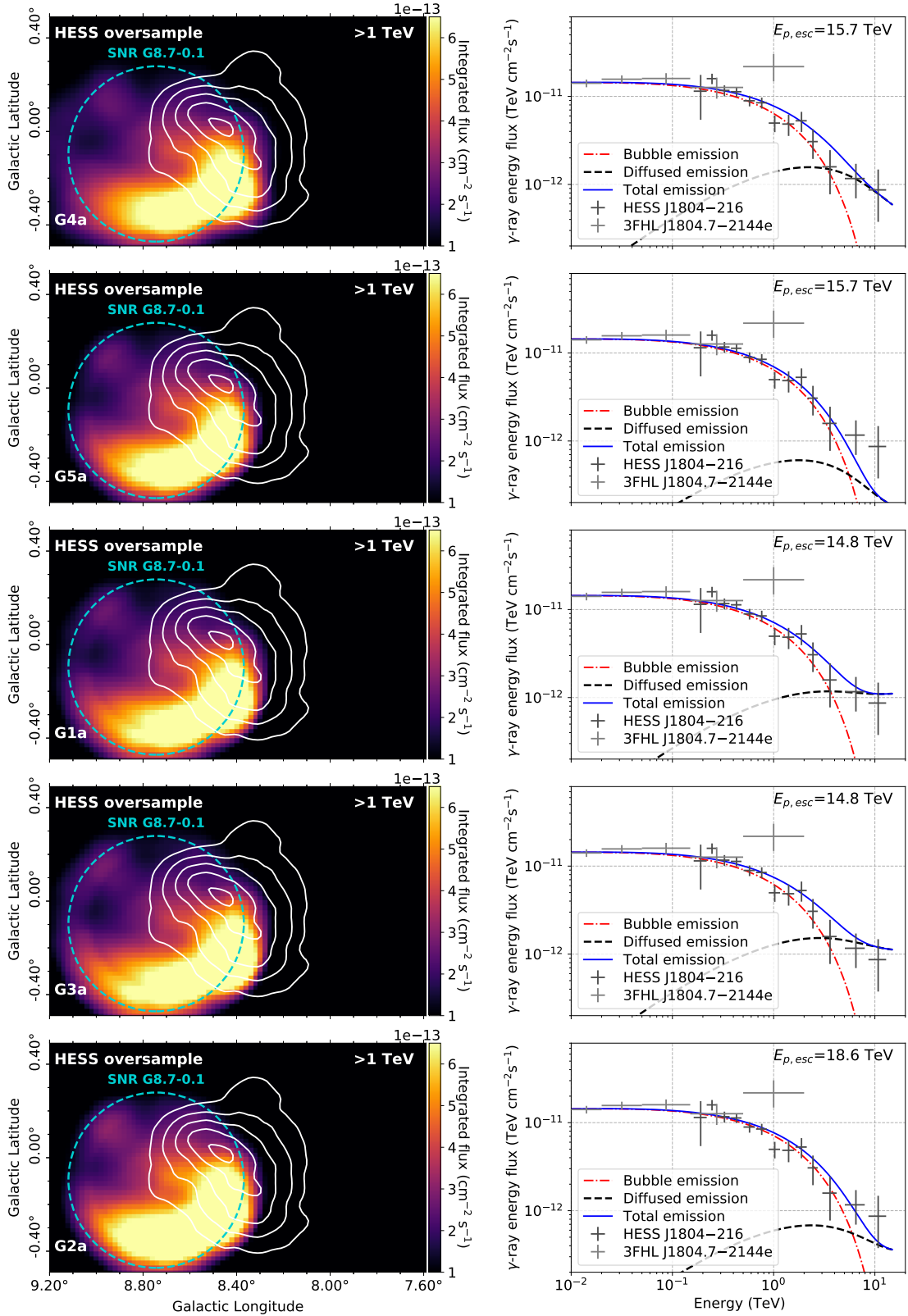
Figure 7.12: The top 5 best matching models for SNR G8.7−0.1 with an age of 15 kyr. The model parameters for each figure are given in Table E.1 of Chapter 6. Figure information same as Figure 4 in Chapter 6.

The top 5 models for SNR G8.7−0.1 with an age of 15 kyr have very similar morphology with a bright band of emission towards the southern edge of SNR G8.7−0.1 in their different energy bands (Figures B.1 and B.2). The bubble is typically dominant for the first three energy bands i.e. from 10 GeV to 10 TeV, as expected from the escape energy of $E_{\mathrm{p,esc}} \sim 15$ TeV. For the highest energy band (E_γ=10−100 TeV) the diffused emission starts to become more dominant. There is strong emission in a ring-like feature which follows the southern edge of SNR G8.7−0.1 with a peak in the modelled emission towards the Galactic south. This feature does not overlap with the TeV peak from the HESS J1804−216 observations.

7.8.2   SNR G8.7−0.1: 28 kyr

The 5 best matching models for SNR G8.7−0.1 with an age of 28 kyr are shown in Figure 7.13. The morphology for the different energy bands defined in Chapter 6 are shown by Figures B.3 and B.4.

The top 5 models for the integrated flux above 1 TeV for SNR G8.7−0.1 with an age of 28 kyr show very similar morphology to an age of 15 kyr. The bright ring of emission towards the southern edge of SNR G8.7−0.1 is present for both ages. The top 4 models for 28 kyr have a much lower escape energy ($E_{\mathrm{p,esc}} \sim 6 - 8$ TeV) than the top 4 models for 15 kyr ($E_{\mathrm{p,esc}} \sim 15$ TeV), leading to some differences in the morphology and spectral plots. The ring feature at the inner southern edge of SNR G8.7−0.1 is more prominent for 15 kyr, as more particles are still trapped in the bubble region. The models for 28 kyr tend to be less filled towards the northern edge of SNR G8.7−0.1, however, for 15 kyr the top 5 models have emission in this region. All the spatial morphology maps for 28 kyr show a peak of γ-ray emission towards the southern edge of SNR G8.7−0.1. This emission is seen as a small blob of emission in the first panel of Figure 7.13, then slowly grows to become a large band of strong emission which covers much of the southern part of SNR G8.7−0.1 in the final panel. This behaviour is attributed to the lower escape energy of ~ 6.2 TeV of the first two panels, therefore the bubble component is less dominant for these panels. As the emission in the southern part of the SNR increases so too does the escape energy (up to ~ 18 TeV), therefore more particles are trapped inside the bubble. The spectra for the top 3 models match well across all energies (top three panels of Figure 7.13). The spectra in the last two panels match the observations at lower energies but start to show differences between the model and observation at energies above 5 TeV.

The morphology in the different energy bands (Figures B.3 and B.4) for SNR G8.7−0.1 with an age of 28 kyr have similar behaviour to the 15 kyr age. In summary, the first three energy bands are typically dominated by bubble emission, and the emission in the last energy band becomes diffusion dominated.
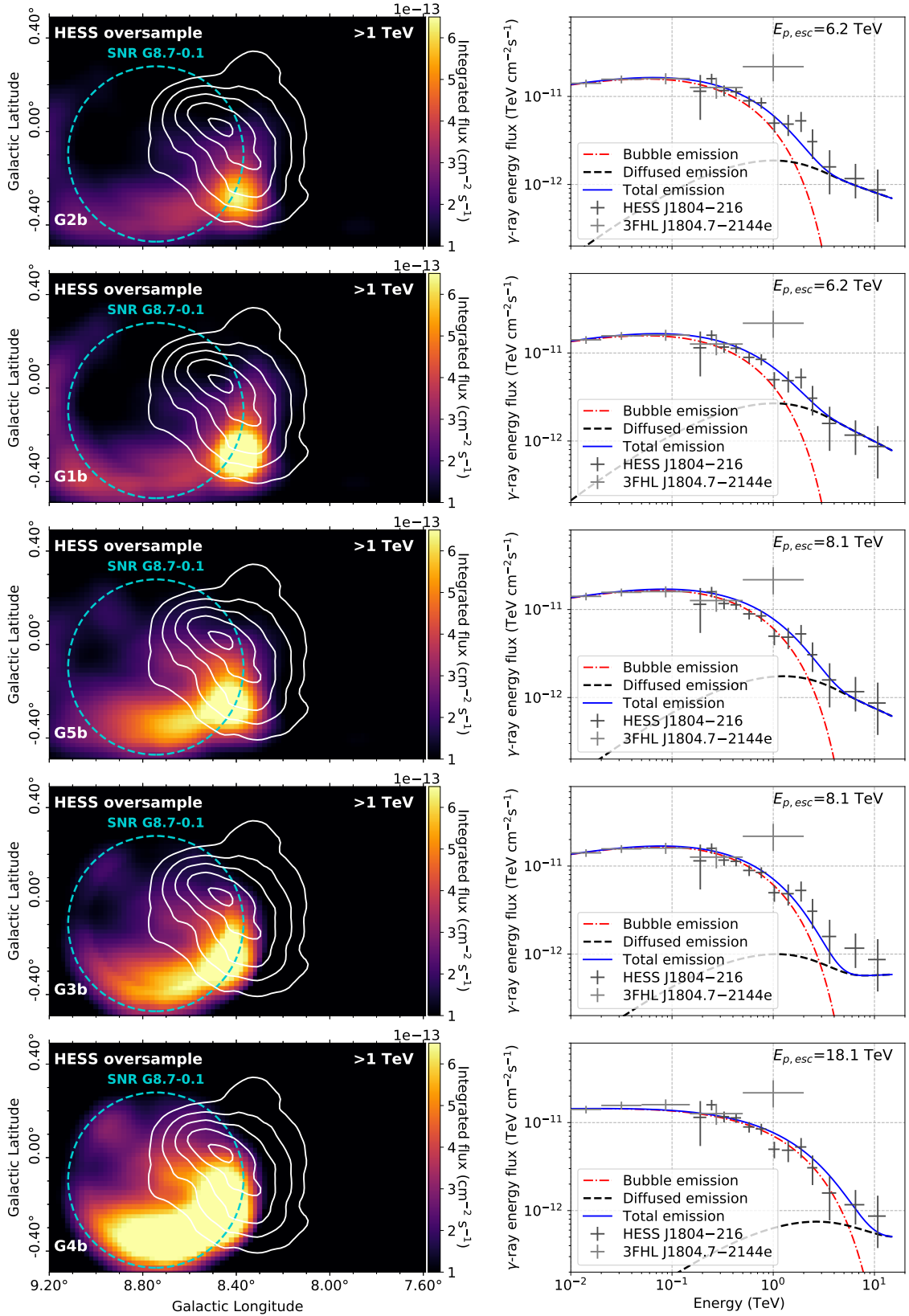
Figure 7.13: The top 5 best matching models for SNR G8.7−0.1 with an age of 28 kyr. The model parameters for each figure are given in Table E.2 of Chapter 6. Figure information same as Figure 5 in Chapter 6.

7.8.3   The Progenitor SNR of PSR J1803−2137: 16 kyr

The 5 best matching models for the progenitor with an age of 16 kyr are shown in Figure 7.14. The morphology for the different energy bands defined in Chapter 6 are shown by Figures B.5 and B.6.

The top 5 models for the progenitor SNR of PSR J1803−2137 have a changing escape radius, as the n_0 value changes for each model (noting P1 and P3 have the same initial number density, $n_0 = 20\,\mathrm{cm}^{-3}$). As this is a currently undetected progenitor SNR there is no known SNR radius, therefore the escape radius takes on a number of values. This was not an issue previously for SNR G8.7−0.1 as this has an associated SNR radius from radio observations. Due to the different escape radii there is some variation in each of the top 5 spatial models. The common feature in each of the top 5 morphology models is a peak of emission towards the outer western edge of the progenitor radius, which is due to the morphology of the ISM here. The escape energies for each model vary from 4 TeV to 13 TeV, which determines how dominant the bubble component is for the spatial maps. P5 and P3 are clearly dominated by the bubble component with very little diffused emission. P1, P2 and P4 however have a lower escape energy and therefore the diffused emission begins to dominate. Splitting the spectra into the bubble and diffused components shows how the escape energy effects the curvature of the spectra.

For the top 5 models of the progenitor the energy bands (Figures B.5 and B.6) show a bubble-filled morphology at lower energies, as expected from the high escape energy of the models. For P5 and P3 the emission is bubble-dominated for the first three energy bands, and for the highest energy band the emission is tightly constrained in a ring around the progenitor SNR radius. These two models do not match the spatial morphology from observations. The other 3 models (P1, P2 and P4) have bubble-dominated emission for the two lower energies panels (E_γ=10−100 GeV and E_γ=0.1−1 TeV), and diffusion dominated emission for the two higher energy panels (E_γ=1−10 TeV, and E_γ=10−100 TeV). The diffused emission in the two higher energy panels is well outside the bounds of HESS J1804−216.
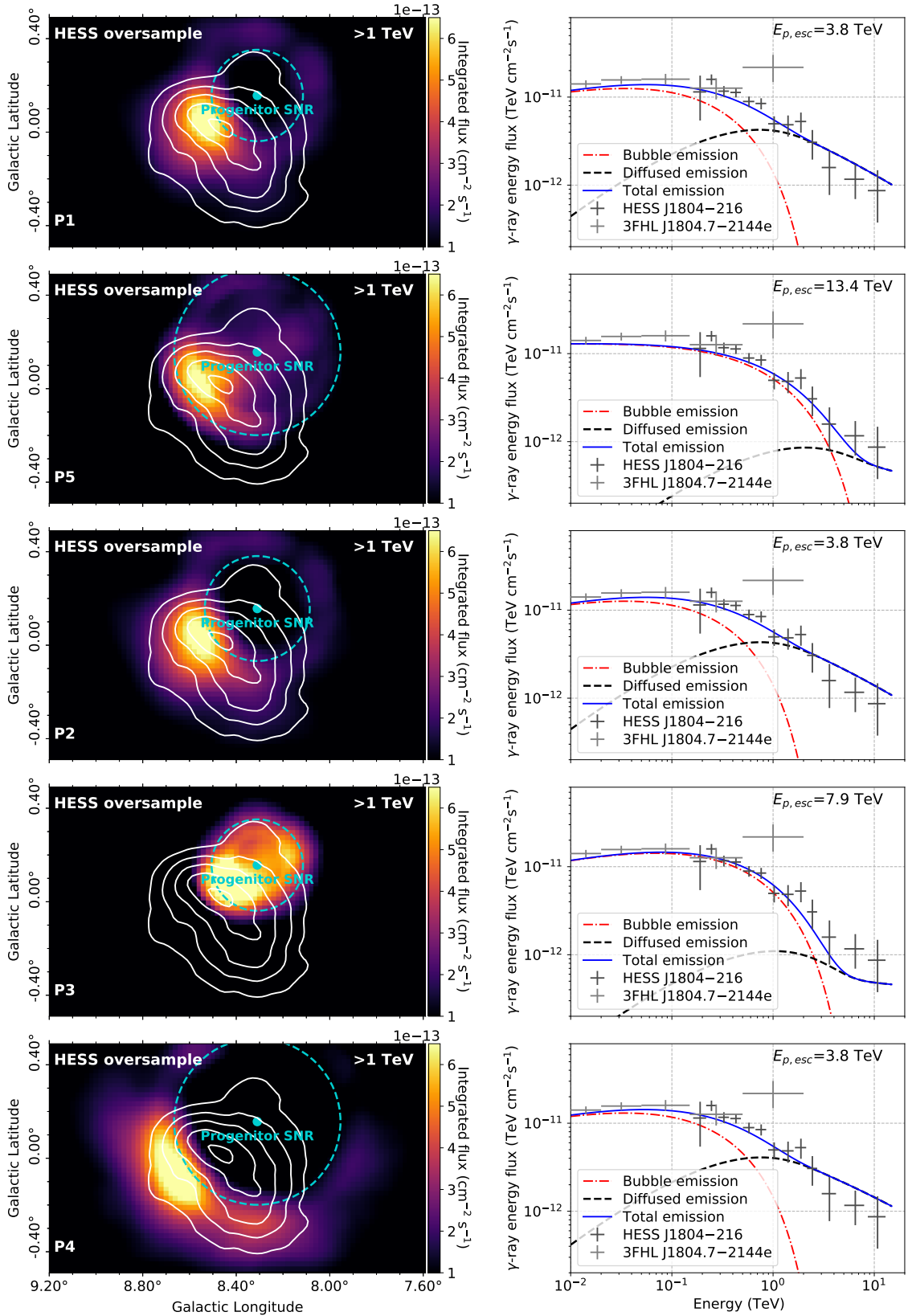
Figure 7.14: The top 5 best matching models for the progenitor SNR of PSR J1803−2137 with an age of 16 kyr. The model parameters for each figure are given in Table E.3 of Chapter 6. Figure information same as Figure 6 in Chapter 6.

8   Examining the morphology of HESS J1804−216 at different energies

> *Most of the fundamental ideas of science are essentially simple, and may, as a rule, be expressed in a language comprehensible to everyone.*
>
> — Albert Einstein, *German Physicist*

This chapter outlines the analysis of the H.E.S.S. observations using the γ-ray astronomy open-source `Python` package `gammapy` (Deil et al., 2020). The H.E.S.S. data used throughout this thesis is the publicly available H.E.S.S. Galactic Plane Survey (HGPS, H.E.S.S. Collaboration et al., 2018) which combines observations from January 2004 to January 2013. The HGPS includes observations carried out by the four H.E.S.S. Phase I telescopes (CT1-4, described in Section 3.1.5). Since 2013 however, HESS J1804−216 has been observed further with more data now available as compared to the HGPS. This extra data could provide further information about HESS J1804−216. The publicly available data also has limited FITS file survey sky maps and limited spectral information available. The sky maps include a 2D integrated flux map above 1 TeV and a 2D statistical significance map. By analysing the H.E.S.S. data again, it is possible to produce updated spectral plots and sky maps for multiple energy-bands. The aim of this chapter is to analyse all available H.E.S.S. data across different energy bands to perform an energy-dependent morphology study and inspect the γ-ray spectrum at the highest energies.

It is possible for γ-ray sources to exhibit energy-dependent morphology, in which the spatial morphology of the γ-rays are different for different energy bands. This is plausible for different source types including pulsar wind nebulae (PWNe) and SNRs. PWNe are expected to accelerate particles to high energies. The evolutionary phases of a PWNe (as described in Section 2.1.3) lead to a unique γ-ray morphology. Evolved PWNe detected by H.E.S.S. are seen to exhibit an energy-dependent morphology in γ-rays (e.g. Aharonian et al., 2006a; H.E.S.S. Collaboration et al., 2012). For PWNe, the emission is expected to be compact and close to the pulsar position at high energies, however, for lower energies the emission is expected to be more extended with an offset from the pulsar position.

HESS J1825−137 is a well-known example of a PWNe which shows a clear energy-dependent γ-ray morphology (Aharonian et al., 2006a; H.E.S.S. Collaboration et al., 2019; Principe et al., 2020). A compact nebula with an extended diffuse nebula was discovered in X-rays towards PSR B1823−13 with asymmetric morphology (Finley et al., 1996). Aharonian et al., 2005 discovered an extended very-high-energy γ-ray nebula towards this region, designated HESS J1825−137. The size of the nebula is seen to increase with decreasing energy (H.E.S.S. Collaboration et al., 2019), shown by Figure 8.1. This behaviour is indicative of the population of electrons in the nebula cooling as particles have travelled away from the pulsar position. At low energies (< 32 TeV) the emission nebula is extended with its peak offset from the position of PSR B1823−13. For higher energies (> 32 TeV), the emission is more

compact and close to the pulsar position. This behaviour is indicative that the γ-ray emission towards HESS J1825−137 originates from PSR B1823−13 as a PWNe.
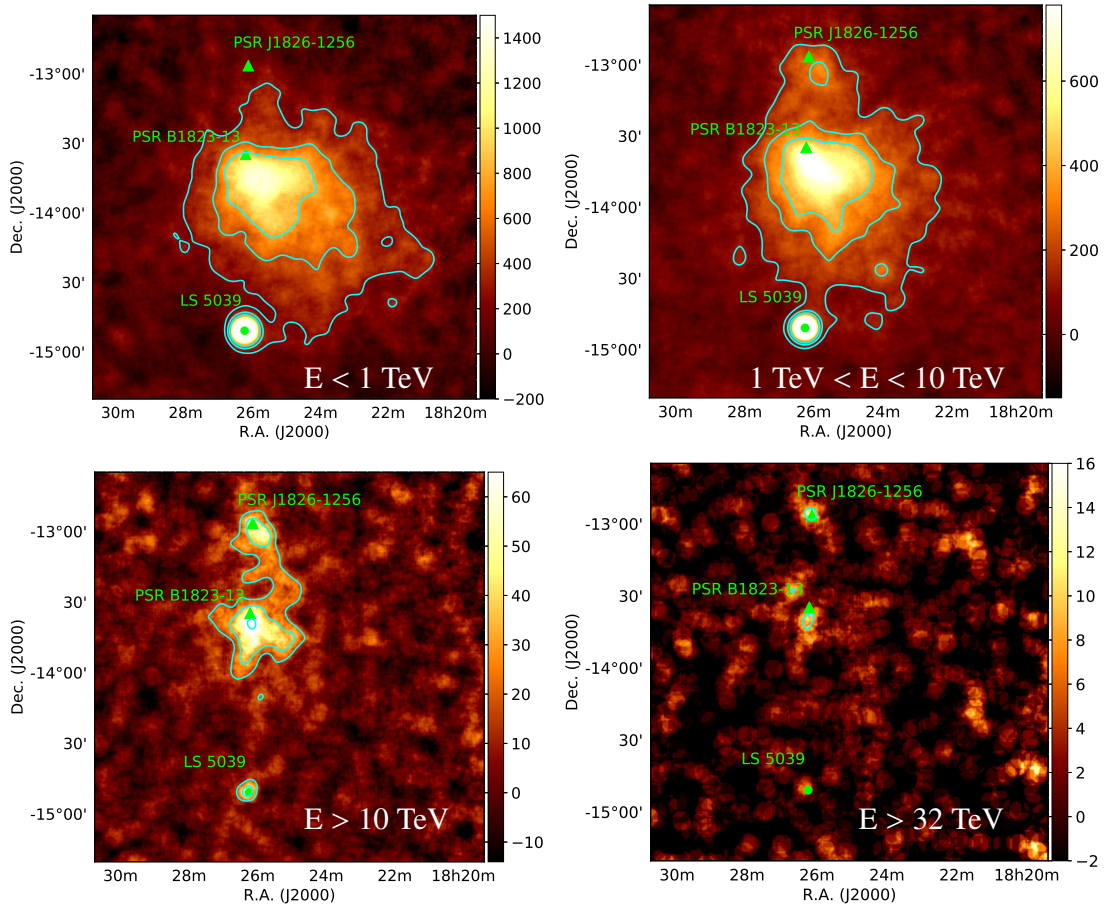
Figure 8.1: Excess counts maps of HESS J1825−137 in different energy bands. The nebula size increases with decreasing energy indicating energy-dependent morphology. This is indicated by the significance contours shown by the cyan curves for 5σ, 10σ, and 15σ for maps with $E < 10\,\text{TeV}$ and 3σ, 5σ, and 10σ for maps with $E > 10\,\text{TeV}$. The binary LS 5039 is another separate source within the field of view. Image taken from H.E.S.S. Collaboration et al., 2019.

Another example of a PWNe with energy-dependent morphology is HESS J1303−631 (H.E.S.S. Collaboration et al., 2012). The emission at high energies ($> 10\,\text{TeV}$) is compact and coincident with the position of PSR J1301−6305, however, at low energies ($< 2\,\text{TeV}$) the emission is extended. This is the typical behaviour seen for PWNe, in which the nebula size increases with decreasing energy (Aharonian et al., 2006a; H.E.S.S. Collaboration et al., 2012).

SNRs are also known to accelerate particles to high energies. In general for the SNR scenario, it is expected that higher energy particles have travelled further away from the source than lower energy ones. If we have a uniform gas density it is expected that the morphology at higher energies is away from the centre of the SNR. For lower energies the morphology should be closer to the SNR position. Investigating the possibility of energy-dependent morphology towards HESS J1804−216 is therefore an important step in helping determine whether a PWNe or SNR scenario is plausible.

It is also important to investigate the maximum energy that protons are accelerated to. Galactic accelerators are believed to accelerate particles up to the CR knee at energies of 10^{15} eV (PeV), as discussed in Section 2.2.1. These sources are called PeVatrons which would produce γ-rays of $\sim$100 TeV ($E_\gamma \sim 0.17E_\mathrm{p}$, Kelner et al., 2006). PeVatron candidates have a number of signatures (Celli et al., 2020; Cristofari, 2021). The γ-ray energy distribution is expected to extend beyond 10 TeV (Abdalla et al., 2021). These spectra are often relatively hard, characterised by a power law of $E^{-\Gamma} \sim E^{-2}$ (Abramowski et al., 2014; Kafexhiu et al., 2014). The proton spectra are expected to extend into the PeV energy range (Cao et al., 2021). SNRs are one of the current expected source populations to efficiently accelerate particles up to PeV energies (Bell et al., 2013; A. M. W. Mitchell et al., 2021). In this chapter, the spectrum of HESS J1804−216 using the most recent H.E.S.S. data will also be investigated to search for any sign of the source being a PeVatron candidate. This is also an important factor as the upcoming Cherenkov Telescope Array (CTA) has a Key Science Project dedicated to the search for CR PeVatrons (CTA Consortium et al., 2018).

8.1 Gamma-Ray Data Analysis Theory

For γ-ray telescopes, the initial data processing is referred to as low-level reconstruction. The raw data containing the signal is taken from the γ-ray telescopes and is calibrated to obtain the light intensity. This calibrated data contains the image of the Cherenkov light from the air shower and night sky background (NSB). Image cleaning is then performed, to remove pixels that do not contain Cherenkov light and exclude pixels containing (only or mostly preferably) NSB fluctuations (Aharonian et al., 2006b). The pixels that survive the image cleaning process also include NSB. The final step in low-level reconstruction is image parameterisation which describes the shower image. Typically the cleaned shower images are parametrised using the so-called Hillas parameters (see Section 3.1.3). Next, the high-level reconstruction is implemented which includes direction and energy reconstruction and the separation of gamma-like and hadron-like events. So-called event lists are obtains which are gathered to only include gamma-like events. As a user of H.E.S.S. or CTA these are the output files received. The next step of processing involves statistical analysis of the gamma-like events to obtain so-called science products.

The typical workflow for the data taken from γ-ray telescopes, in particular H.E.S.S., begins with event lists and IRFs (Instrument Response Functions). The Gamma Astro Data Format (GADF[6]) is the established format for the files which are obtained at this level. The Header Data Unit (HDU) index file contains information stored in binary tables and points to where each HDU is stored.

The HDU classes include:

- EVENTS - a binary FITS table containing the events list, which includes the event ID, reconstructed energy, arrival time, arrival direction and more.

---

[6] https://gamma-astro-data-formats.readthedocs.io/en/latest/index.html

- GTI - Good Time Interval indicating the validity of the data, including a start and stop time, to account for the instrument not being on or non-detection of photons.

The IRF components include:

- PSF - the radially symmetric Point Spread Function representing the response for a point source. In this case, it gives the probability distribution of reconstructed event positions.

- AEFF - the Effective Area, i.e. the collection area over the field of view (FoV) as a function of energy and offset angle.

- EDISP - the Energy Dispersion described by a probability density function (PDF) of energy migration Ereco/Etrue as a function of Etrue and FoV position.

- BKG - the differential background flux brightness as a function of reconstructed energy and FoV coordinates.

The data obtained from the H.E.S.S. collaboration is in the form of FITS files which contain event lists, effective area, energy dispersion, the point spread function and background. The latest FITS file data produced by the 'HESS FITS data - Task group' is called 'Prod05' (H.E.S.S. Collaboration, 2021a). These were initially released to the collaboration in 2019, but have since been updated (in November 2020). This dataset was produced using the 'Heidelberg calibration' (H.E.S.S. Collaboration, 2021b; Bolz, 2004), a method used in H.E.S.S. to produce the high-level data. Further information on these methods are found in Aharonian et al., 2004 and Aharonian et al., 2006b. The Prod05 FITS files include data from 2004 to 2020 with various cuts on the data. Table D.1 describes this dataset.

8.1.1   Signal Evaluation and Significance Computation

A number of methods are used in γ-ray astronomy for determining the background (from gamma-like events) for a γ-ray source region. Berge et al., 2007 provides an overview of various methods to determine the background. The ones of interest here are the ring background and reflected region background methods, in which the number of counts from the 'off' region are compared to the number of counts in the 'on' region. The 'off' region is defined where there is expected to be no emission from any γ-ray sources. An estimate of the γ-ray excess in the region of interest involves determining the background in that region, as shown by Equation 8.1.

$$N_{\text{exc}} = N_{\text{on}} - \alpha N_{\text{off}} \,, \tag{8.1}$$

where N_{on} is the number of counts in the 'on' region and N_{off} is the number of counts in the 'off' region. The normalisation factor is α, taken as the ratio of the 'on' source time (t_{on}) to the 'off' source time (t_{off}) given by $\alpha = t_{\text{on}}/t_{\text{off}}$.

The statistical significance, S (σ), is calculated through (T. P. Li and Ma, 1983):

$$S = \sqrt{-2\ln\lambda}$$

$$= \sqrt{2}\left\{N_{\mathrm{on}}\ln\left[\frac{1+\alpha}{\alpha}\left(\frac{N_{\mathrm{on}}}{N_{\mathrm{on}}+N_{\mathrm{off}}}\right)\right] + N_{\mathrm{off}}\ln\left[(1+\alpha)\left(\frac{N_{\mathrm{off}}}{N_{\mathrm{on}}+N_{\mathrm{off}}}\right)\right]\right\}^{1/2},$$

$$(8.2)$$

where ln is the natural logarithm, λ is the maximum likelihood ratio and N_{on}, N_{off} and α are defined previously. Equation 8.2 is formulated through the likelihood ratio method. Using statistical hypothesis testing, the null hypothesis is H_0: all observed photons originated in the background and the alternative hypothesis is H_a: all observed photons originated from a new source. The likelihoods are calculated for the null hypothesis, $\mathcal{L}_0$, and alternative hypothesis, $\mathcal{L}_a$. Taking the ratio of these $(\mathcal{L}_0/\mathcal{L}_a)$ gives the maximum likelihood, from which the statistical significance in Equation 8.2 is determined. Further information on the statistics and methods to obtain Equations 8.1 and 8.2 are outlined in T. P. Li and Ma, 1983.

The background estimations described in the following must exclude any regions of sky in which significant γ-ray emission is present. These regions are called 'exclusion' regions and are masked out for analysis (see Section 8.2.2).

8.1.2   Reflected Region Background Method

For the reflected region background the 'off' region is defined as a number of regions which have the same size and shape as the 'on' region, and an equal offset from the pointing position (Berge et al., 2007). This method gets its name as the 'on' region is 'reflected' with respect to the pointing position, to obtain each 'off' region. For this background technique the ring of regions are centred around the pointing position, however for the ring background method the ring is centred on the source region. As the offset is equal for the 'on' and 'off' regions, the radial acceptance correction is not required, unlike the ring background method. Therefore, this method is commonly used for spectral analysis. Figure 8.2 shows a schematic of this background technique.
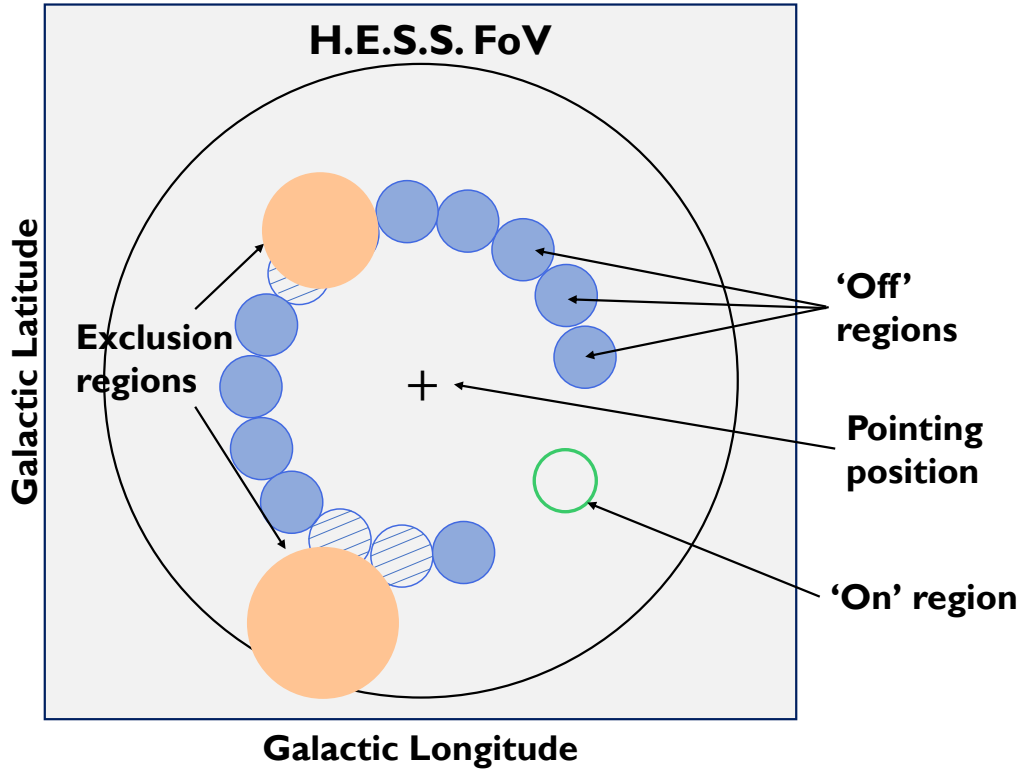
Figure 8.2: Schematic of the reflected regions background method. The black circle shows the H.E.S.S. FoV, the observation pointing position is shown by the black plus sign and the exclusion regions are shown by the orange circles. The green unfilled circle shows the 'on' region, the filled blue circles show the reflected 'off' regions and the dashed circles show the excluded reflected regions. Image adapted from H.E.S.S. Collaboration et al., 2018.

8.1.3   Ring Background Method

The ring background method involves taking a ring region for each pixel in the FoV where the counts inside each ring estimate the background. This is used to provide an estimate of the background for any point within the FoV, hence creating a map. As the ring covers areas which have a different offset from the pointing position, the acceptance inside the ring cannot be assumed to be constant. Therefore, for the determination of the normalisation factor, α, for each position on the ring requires an acceptance correction to take into account the difference in acceptance between these two regions. This method is insensitive to large-scale deviations between the acceptance profile from the actual dataset and the model, due to the method utilising the relative normalisation in a small ring extension compared to the entire FoV (Berge et al., 2007). Linear gradients in the system acceptance are also averaged out over the ring. Due to this, the ring background method is best suited to generating sky maps which show the entire FoV from the dataset. This method is disfavoured in determining energy spectra, due to the acceptance correction which is applied and the increase in the systematic error of flux calculations (Aharonian et al., 2006b; Berge et al., 2007), so a different method must be utilised (see Section 8.1.2). Figure 8.3 shows a schematic of this method.
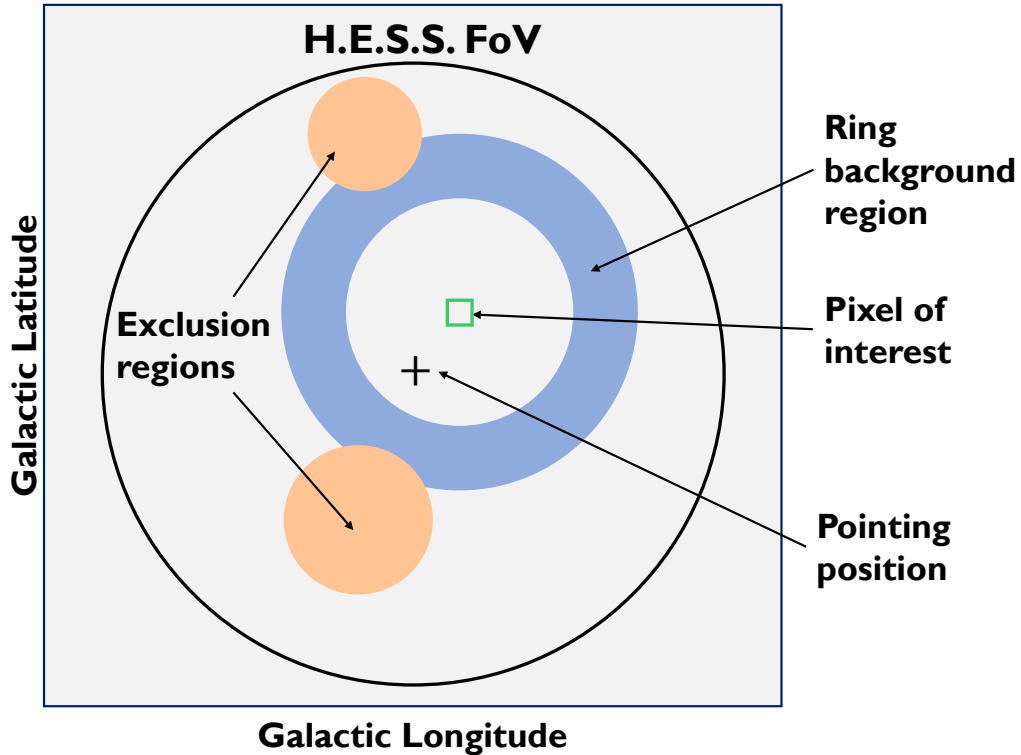
Figure 8.3: Schematic of the ring background method. The black circle shows the H.E.S.S. FoV, the observation pointing position is shown by the black plus sign and the exclusion regions are shown by the orange circles. The green square indicates the pixel of interest and the filled blue ring indicates the region which the 'off' counts are estimated from for this pixel. Image adapted from Berge et al., 2007.

8.1.4   Software - `gammapy` Package

`gammapy`[7] (Donath et al., 2015; Deil et al., 2017b) is an open-source software developed for the science analysis of γ-ray data from various γ-ray observatories. It consists of a number of existing scientific `Python` packages such as `numpy`, `matplotlib`, `scipy` and `astropy`. `gammapy` can be used to analyse data from existing γ-ray telescopes, including H.E.S.S., MAGIC and *Fermi*-LAT provided the data is in the FITS format. It has become the official software analysis tool of many observatories including the upcoming CTA (Deil et al., 2017a). This data is typically in the form of event lists and IRFs which are used to create a number of science products. The science products available include, but are not limited to, flux, significance and excess counts maps, spectral plots and light curves. The analysis of the H.E.S.S. data performed in this thesis will follow the workflow in Figure 8.4.

---

[7]Available at https://github.com/gammapy/gammapy
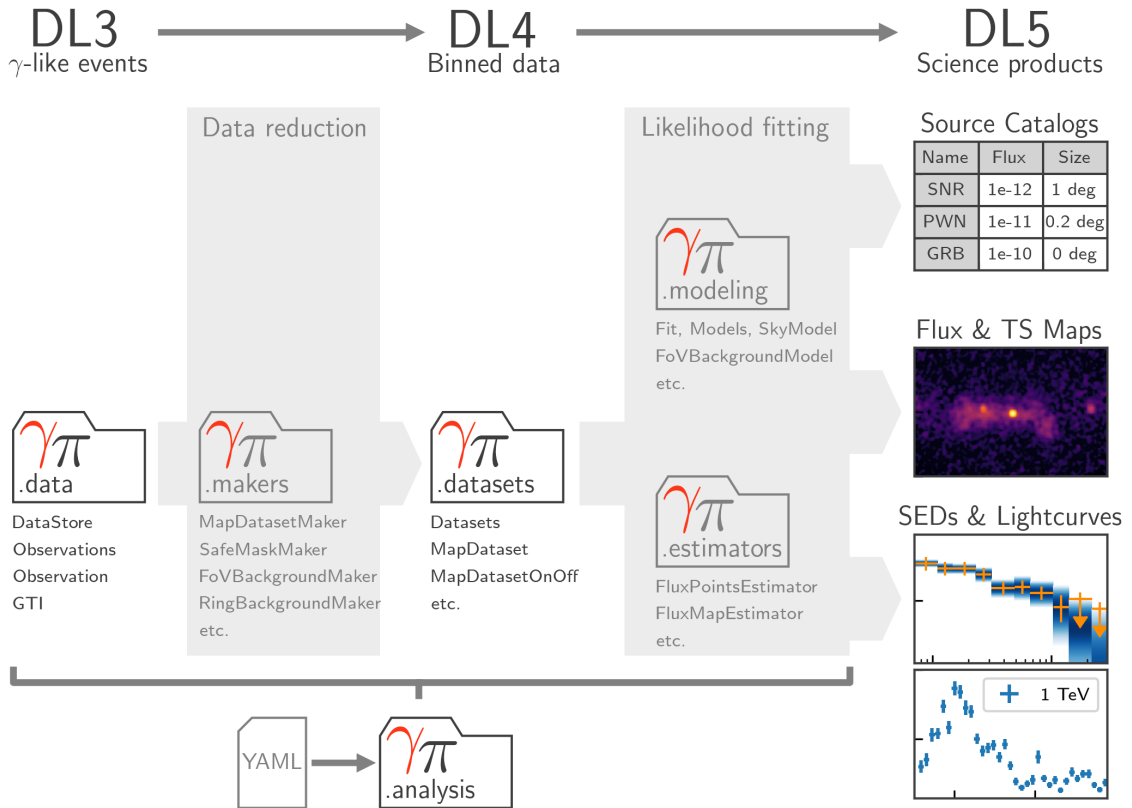
Figure 8.4: Analysis workflow and package structure for `gammapy`. The analysis performed in this thesis will follow this workflow. Image from The Gammapy developers, 2021.

8.2   H.E.S.S. Data Analysis

This section outlines the data analysis performed in this thesis, including how the data was selected. The results for both the spectral and spatial γ-ray distributions are presented here.

8.2.1   Data Selection

The H.E.S.S. data for the `gammapy` analysis consists of 'runs', which are observations typically with a duration of 28 minutes for a fixed position in the sky. These are identified using a unique observation number, called an 'OBS_ID', which has a specific date and time from when the observation was performed. The data used in this analysis is taken within a 2° region of HESS J1804−216 with a total of 195 observation runs and an observation time of 88 hours (outlined in Table 8.1). Comparing this to the data from H.E.S.S. Collaboration et al., 2018, which consists of a livetime of ∼44 hours, there is now double the amount of available data. The total observation lists for H.E.S.S. phase I, II and IU are shown in Tables D.4 to D.6.

Table   8.1:   Observations   towards   HESS J1804−216   for   the `std_ImPACT_fullEnclosure` configuration.

Phase	Number of runs	Observation Period	Telescopes	Observation Time (hours)
H.E.S.S. 1	141	2004-2010	CT1-4	64.6
H.E.S.S. 2	42	2013-2014	CT1-4	17.9
H.E.S.S. 1u	12	2017-2019	CT1-4	5.6
Total	195	2004-2019	CT1-4	88.1

8.2.2   Exclusion Regions

The analysis region is defined by a square geometry centred on the γ-ray source, HESS J1804−216 ($l = 8.37°$, $b = -0.03°$). A grid size of 0.02° (consistent with H.E.S.S. Collaboration et al., 2018 and a common analysis setting in H.E.S.S.) and a width of 3.2° to cover the source region is used. For the purpose of this analysis, the exclusion regions are defined by searching for any H.E.S.S. source within a 4° radius of the HESS J1804−216 centroid and excluding it by taking a circular region of radius $1.5R_s$, where R_s is the radius of the source. Applying an extra 1.5 factor to the radius is a conservative method, however it covers any significant γ-ray emission that could contaminate our background estimation. For HESS J1804−216 the regions outlined in Table 8.2 are excluded for the determination of the background. Figure 8.5 shows the exclusions regions from Table 8.2 towards HESS J1804−216 for this analysis.

Table 8.2: Regions excluded from the `gammapy` analysis within a 4° radius of HESS J1804−216.

Source name	Galactic Longitude (°)	Galactic Latitude (°)	Radius×1.5 (°)
HESS J1800−240	5.96	−0.42	0.75
HESS J1801−233	6.66	−0.27	0.3
HESS J1804−216*	8.38	−0.09	0.57
HESS J1808−204	10.01	−0.24	0.23
HESS J1809−193	11.11	−0.02	0.75

* Source of interest.
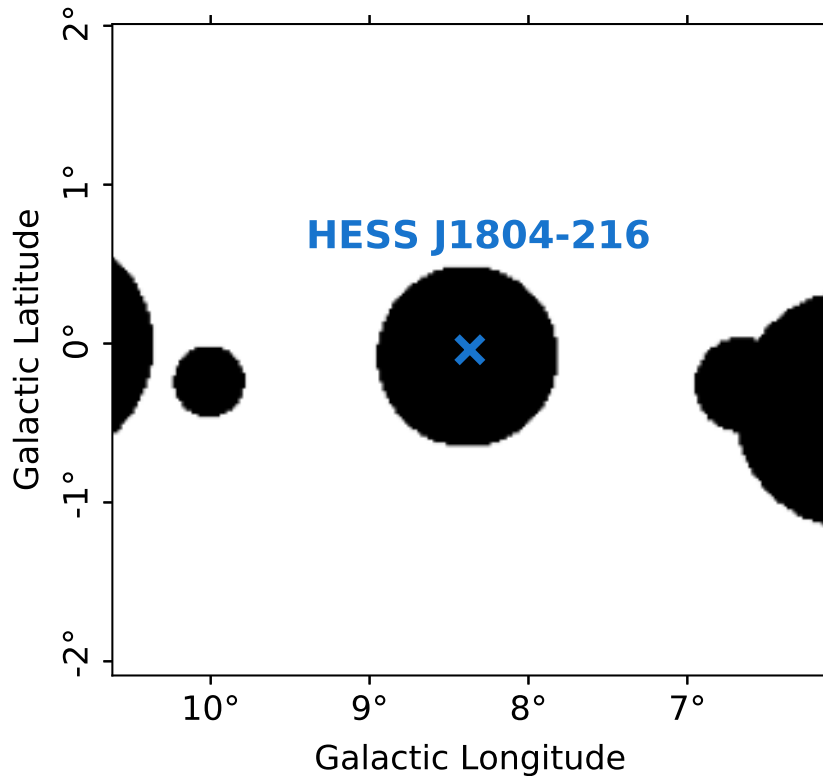
Figure 8.5: Exclusion regions within a 4° radius of HESS J1804−216, as described in Table 8.2. The blue cross indicates the position of the source of interest in this thesis, HESS J1804−216.

8.2.3   Results for the Spatial Morphology

This section outlines the methods used for obtaining the spatial plots for our analysis. The `gammapy` and analysis settings used for the spatial analysis are summarised in Table D.2 and described here. The ring background method described in Section 8.1.3 is used for analysing the spatial morphology of γ-rays towards HESS J1804−216. We define an annulus with an inner ring radius of $r_{\mathrm{inner}} = 0.7°$ and ring width of 0.44°, leading to an outer ring radius of $r_{\mathrm{outer}} = 1.14°$, following the method as described in H.E.S.S. Collaboration et al., 2018.

For analysing how the γ-ray morphology of HESS J1804−216 changes with energy, we want to look at different energy bands. To utilise the ring background method both the reconstructed energy and true energy must be defined. The true energy band spans a wide range of energies from 0.05 TeV to 20 TeV. The reconstructed energies for the `gammapy` analysis are defined by energy bands such that the uncertainty is equal in each band. The energy bands for the spatial analysis are: 0.2-0.32 TeV, 0.32-0.43 TeV, 0.42-0.56 TeV, 0.56-0.67 TeV, 0.67-0.95 TeV, 0.95-1.45 TeV and 1.45-12 TeV.

Firstly, a so-called map dataset is created using the geometry defined previously (see Table D.2). A 'safe' range is set for this dataset to exclude parts of data with high systematics of the IRF. To achieve this, the maximum offset value between the centre of observations and the data is set to 2° (Mohrmann et al., 2019), where data outside of this radius is excluded. A safe effective area of 10% of the maximum effective area is used (c.f. Mohrmann et al., 2019). A so-called observation dataset is defined for each run number in the list (see `OBS_ID` in Tables D.4 to D.6) which includes various information including effective area, energy dispersion, livetime, among others. Each observation file is combined to create a stacked dataset which contains the total counts, background counts and excess counts for the map region. Maps of N_{off}, N_{on} and α are also available.

We utilise the `ExcessMapEstimator` class which calculates the correlated flux and significance (σ) maps for a given map dataset. These maps are calculated using the number of 'on' and 'off' events along with methods outlined in T. P. Li and Ma, 1983. We use a correlation radius of 0.1°, standard for H.E.S.S (H.E.S.S. Collaboration et al., 2018), for the significance maps. The calculation of the γ-ray flux maps required an exposure map to be present in the dataset. The spatial results for the previously defined energy bands are shown in Figure 8.6 using the ring background technique (see Section 8.1.3).

Figure 8.6 shows the γ-ray significance (σ) maps for this analysis, where the black, grey and white contours indicates levels of significance at 8σ, 6σ and 4σ. This figure shows at a first look that the morphology of the γ-ray emission is similar over different energy bands. The flux maps for this analysis are shown in Figure D.3 for completeness.
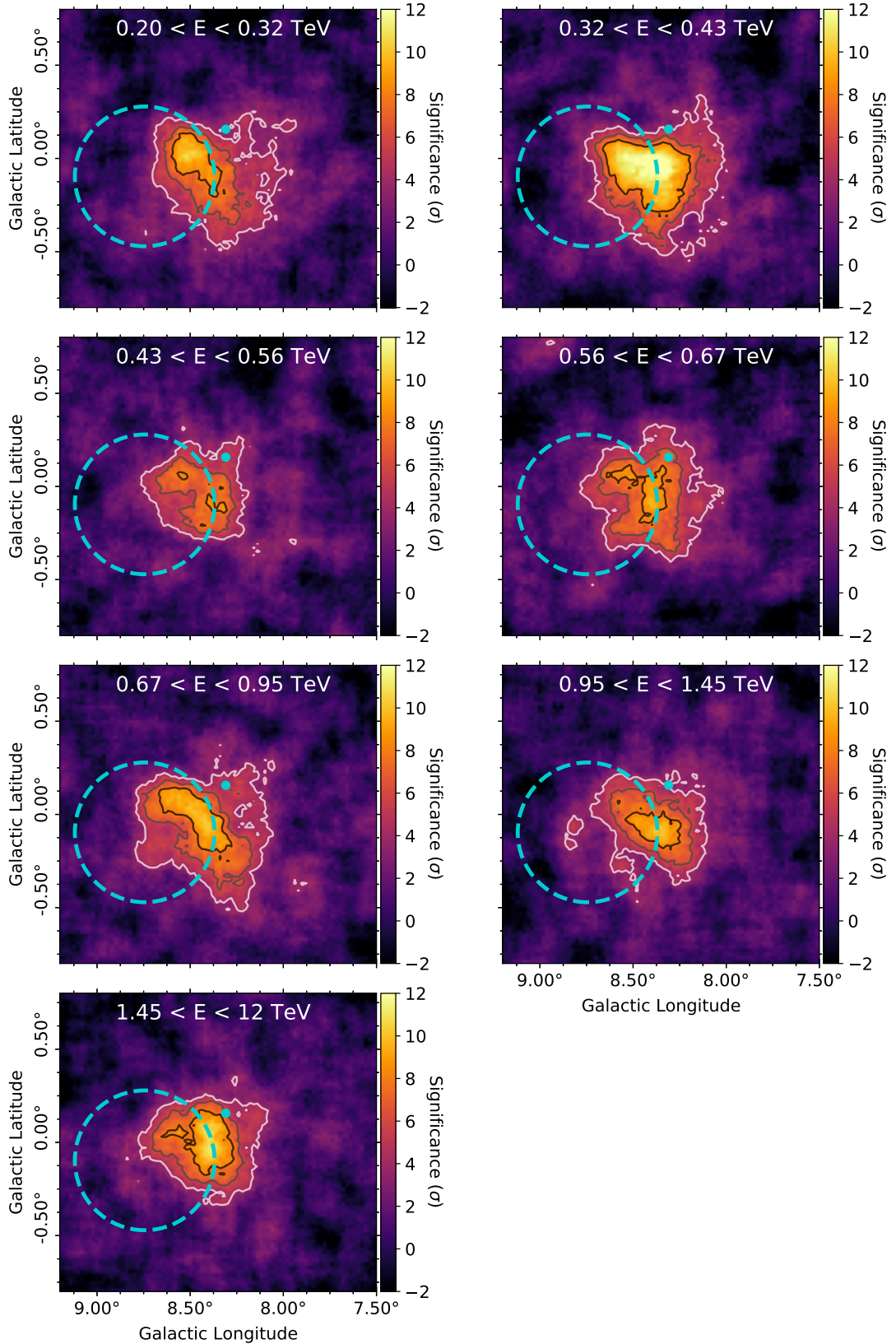
Figure 8.6: Gamma-ray significance maps towards HESS J1804−216. The contours indicate different levels of significance, where black is 8σ, grey is 6σ and white is 4σ. The cyan dashed circle indicates SNR G8.7−0.1 and the cyan dot indicates the position of the progenitor SNR of PSR J1803−2137.

8.2.4   Results for the Gamma-Ray Spectrum

This section explains the method for obtaining the spatial plots for our analysis. The `gammapy` and analysis settings used for this are summarised in Table D.3 and discussed here. For the spectral analysis the reflected regions background technique as described in Section 8.1.2 is used. To analyse the spectrum towards HESS J1804−216 the reflected regions background is utilised, similarly to the ring background method both the reconstructed energy and true energy must be defined. The reconstructed energy is defined for the energies of interest, in this case from 0.2 TeV to 100 TeV. The true energy band spans a wider range of energies than the reconstructed energy, from 0.05 TeV to 120 TeV, to allow for migration of events. An observation dataset is created using these energies which contain the counts, exposure and energy dispersion of the observations. Each observation is combined, using the previously defined 'safe' mask, to create a stacked dataset of 'on' and 'off' counts. As the name suggests this contains the 'on' and 'off' counts along with the background and excess counts.

We require each energy bin in the spectrum to have significance greater than 2σ, otherwise it is included as an upper limit. To ensure this, the last 4 energy bins were combined into one larger energy bin. Next, using the method described in Section 8.1.2, the energy spectrum is plotted for these energy bins. For a comparison to the observations from Aharonian et al., 2005 see Figure D.2.

For this thesis, two models (power law and exponential cutoff power law) are fit to the data to investigate the shape of the γ-ray spectrum. The power law has the form:

$$\phi_{\mathrm{PL}}(E) = \phi_0 \left(\frac{E}{E_0} \right)^{-\Gamma} , \tag{8.3}$$

where ϕ_0 is the amplitude, Γ is the index of the power law fit and E_0 is a normalisation energy taken here to be 1 TeV. The exponential cutoff power law is described by:

$$\phi_{\mathrm{ECO}}(E) = \phi_0 \left(\frac{E}{E_0} \right)^{-\Gamma} \exp\left(-E\lambda\right) , \tag{8.4}$$

where ϕ_0 is the amplitude, Γ is the spectral index and $\lambda = 1/E_{\mathrm{cutoff}}$ where E_{cutoff} is the 'cutoff' energy. The 'goodness-of-fit' measure used here for the spectral analysis is the reduced chi-square statistic which quantifies which model fits best to the observational data using the following criterion:

$$\frac{\chi^2}{\mathrm{ndf}} = \left(\sum_i \frac{(O_i - F_i)^2}{G_i^2} \right) \frac{1}{\mathrm{ndf}} , \tag{8.5}$$

where O_i is the observational flux, F_i is the model flux, G_i is the uncertainty in

the flux observations, i denotes each data point and ndf is the number degrees of freedom taken here as the number of data points minus the number of fit parameters. Table 8.3 shows the parameter values from each model fit along with the χ^2/ndf value. Figure 8.7 shows a comparison between the two different fits.

Table 8.3: Fit parameters for the power law (PL, Equation 8.3) spectral model and the exponential cutoff power law (ECPL, Equation 8.4) spectral model.

Spectral Model	ϕ $(10^{-12}\,\mathrm{cm}^{-2}\,\mathrm{s}^{-1}\,\mathrm{TeV}^{-1})$		Γ		λ (TeV^{-1})		E_0 (TeV)	χ^2/ndf
	Value	Error	Value	Error	Value	Error		
PL	5.9	0.15	2.69	0.03	-	-	1 (fixed)	0.74
ECPL	6.4	0.33	2.63	0.05	0.04^a	0.03^a	1 (fixed)	0.68

^{a} From error propagation, these values relate to $E_{\mathrm{cutoff}} = 24.7 \pm 18.4\,\mathrm{TeV}$.
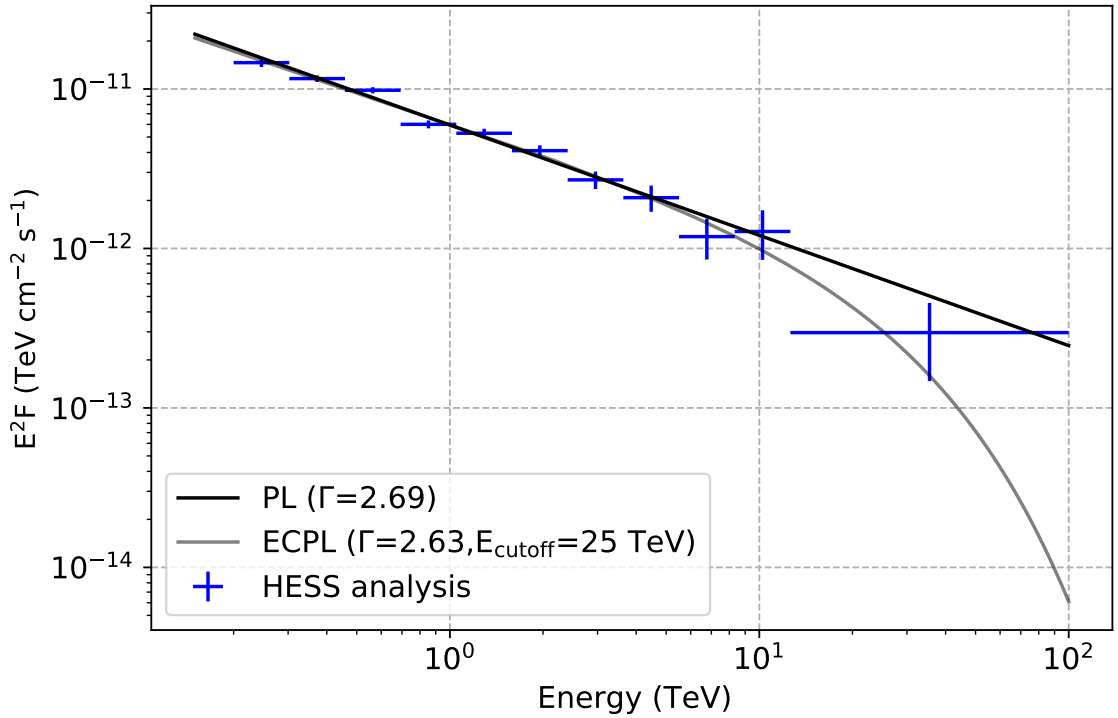
Figure 8.7: Spectral plot with a power law (PL) fit shown in black and the exponential cutoff power law (ECPL) fit shown in grey. The blue data points show the γ-ray spectrum for HESS J1804−216 from this analysis.

8.3 Discussion

The results presented in the previous section are considered here to discuss the possible mechanisms of CR acceleration and explanation for the observed TeV emission from HESS J1804−216. Using the new results from this analysis, the spectrum will be discussed in further detail here, including any evidence for acceleration of particles to PeV energies. The spatial analysis of HESS J1804−216 involves searching for any evidence of energy-dependent morphology. Both the PWNe and SNR scenario are investigated for any energy-dependent morphology. The observations for this analysis are compared with the SNR model defined in Chapter 6.

8.3.1 PeVatron Candidate

There are a number of potential candidates for accelerating CRs up to the highest energies, 10^{15} eV and above, including SNRs, PWNe and stellar clusters (Bell et al., 2013; Lemoine-Goumard, 2014; Aharonian et al., 2019; LHAASO Collaboration et al., 2021). Recent observations show the extension of γ-ray spectra to energies up to and above 100 TeV (HAWC Collaboration et al., 2020; Tibet ASγ Collaboration et al., 2021; Abdalla et al., 2021; Cao et al., 2021). The extension of the γ-ray spectrum above 100 TeV is considered observational indication of a PeVatron source due to $E_\gamma \sim 0.17 E_{\mathrm{p}}$ (Kelner et al., 2006). HESS J1804−216 currently has a γ-ray spectrum which extends to energies of tens of TeV with no sign of a cutoff. It is important to investigate the spectrum of HESS J1804−216 further with the data presented in this thesis to see if it is a plausible PeVatron candidate.

The γ-ray spectrum for HESS J1804−216 for this analysis is shown in Figure 8.7. The spectrum was fit with both a power law and exponential cutoff power law, with results shown in Table 8.3. To quantify which spectral function fits the data best we used a reduced chi-square measure, Equation 8.5. The best fit model for the γ-ray spectrum from HESS J1804−216 is the exponential cutoff power law as it has a lower χ^2/ndf value than that for the power law. For this model, the cutoff energy is $E_{\mathrm{cutoff}} = 24.7 \pm 18.4$ TeV with a spectral index of $\Gamma = 2.63$. The cutoff energy here gives an indication of the maximum γ-ray energy that is reached.

As discussed previously, for a source to be classified as a PeVatron candidate its spectrum must display a high energy cutoff, $E_{\mathrm{cutoff}} > 10$ TeV. Given the energy cutoff for this analysis on HESS J1804−216 is $E_{\mathrm{cutoff}} > 7$ TeV, it cannot be ruled out as being able to accelerate particles to PeV energies. HESS J1804−216 is therefore a PeVatron candidate. Further observations, for example with the next-generation Imaging Atmospheric Cherenkov Telescope (IACT) CTA which will have a better sensitivity to high-energy γ-rays (few arcmin at $\sim$100 TeV, see Section 3.1.6), would help to better understand the spectrum of HESS J1804−216 at high energies. CTA is expected to cover γ-ray energies up to 300 TeV, therefore leading to important understanding of PeVatrons. One of the Key Science Projects (KSPs) within CTA is Cosmic Ray PeVatrons (CTA Consortium et al., 2018). One of the goals of this KSP is to search for these Galactic PeVatrons and reveal their accelerator, to help solve the mystery of the origin of the highest energy Galactic CRs.

8.3.2   PWNe scenario: Energy-dependent Morphology Interpretation

The PWNe scenario is thought to have energy-dependent morphology in γ-rays, as discussed previously in the introduction of this chapter (Chapter 8). At high energies the emission is expected to be compact and close to the pulsars current position. At lower energies, however, the emission starts to become more extended and offset from the pulsar position. It is therefore important to look for any evidence of this energy dependence, to show any indication of a PWNe scenario. To investigate the possibility of energy-dependent γ-ray morphology radial excess profiles are produced for different energy bands. This is one method to visualise and quantify any features in the different energy bands. Firstly, the energy bands are defined so that we have sufficient statistics in each energy band for the radial profile. Requiring the significance to be roughly the same in each energy band we have chosen three γ-ray energy bands: $E_1 = 0.2 - 0.56 \, \mathrm{TeV}$, $E_2 = 0.56 - 0.97 \, \mathrm{TeV}$ and $E_3 = 0.97 - 12 \, \mathrm{TeV}$.

The emission around the current position of PSR J1803−2137 is of interest to us. The observed γ-ray emission is strongest towards the South-West of this position (see Figure 8.6), therefore instead of taking concentric rings from this position, a circular wedge geometry is utilised. The radial profile is obtained by summing the excess counts in each wedge annulus with a width of 0.08° out to a radius of 0.64°, with location of PSR J1803−2137 at the apex of the wedge (as shown by Figure 8.8).
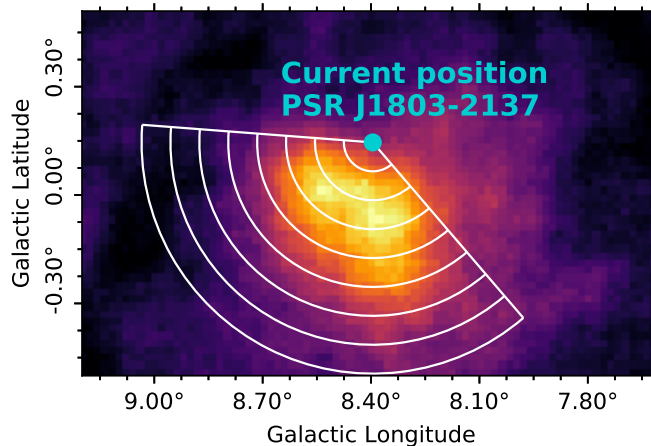
Figure 8.8: The observational excess counts map over the entire energy range. The circular wedge geometry with PSR J1803−2137 at the apex of the wedge (indicated by the cyan dot) is shown in white. The radial profiles are extracted from each wedge annulus which have a width of 0.08°.

The excess counts values in each wedge are calculated through:

$$N_{\mathrm{exc}} = \sum N_{\mathrm{on,i}} - \sum \left(\alpha_i N_{\mathrm{off,i}} \right), \qquad (8.6)$$

where $N_{\mathrm{on,i}}$, $N_{\mathrm{off,i}}$ and α_i (as defined in Equation 8.1) are the values in each wedge as taken from the uncorrelated maps from the ring background method in `gammapy`. The uncertainty for the excess counts measurements in each wedge annulus is given by:

$$\sigma(N_{\text{exc}}) = \sqrt{\sum N_{\text{on,i}} + \sum \left(\alpha_i^2 N_{\text{off,i}} \right)} \, . \tag{8.7}$$

The excess counts are normalised by dividing by the sum of the excess counts, N_{exc} from Equation 8.6, in each radial wedge bin for each energy band. These normalised radial wedge excess profiles are shown in Figure 8.9 for each energy band as defined in this section.
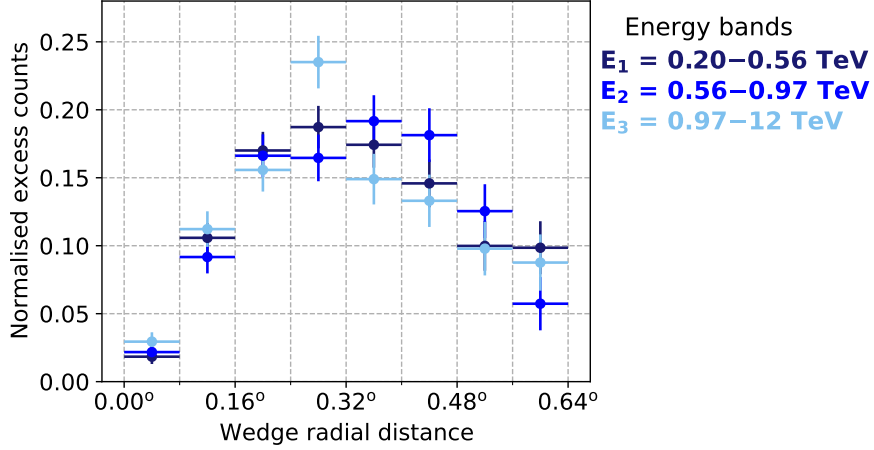
Figure 8.9: The radial wedge profile for each annulus (as defined in Figure 8.8) and energy band for the H.E.S.S. observations. This radial profile for each energy band is shown to increase out to a specific radius ($\sim 0.32°$) and then begins to decrease.

Figure 8.9 shows that the radial profile for each energy band increases out to a radius of $\sim 0.32°$ and then begins to decrease. This increase in normalised excess counts out to $\sim 0.32°$ is due to the area of each annulus increasing with radius. As the strongest emission is contained within this region, once the radial distance is greater than $0.32°$ the normalised excess counts begin to decrease. To investigate the possibility of energy-dependent morphology between the energy bands, we can look at the deviation plots between each of the energy bands. Using the definition of E_1, E_2 and E_3 in Figure 8.9, we take deviation profiles of E_1-E_2, E_2-E_3 and E_1-E_3, as shown in Figure 8.10.

Figure 8.10 shows no indication of an energy-dependent morphology, as each deviation plot is consistent with the blue zero line. For energy dependency in the PWNe scenario we would expect the deviations to be offset from zero, where the first few data points being negative and the next few positive. This behaviour is shown in the example of the PWNe scenario in Figure D.6. The features in Figure 8.10 indicate that a PWNe scenario is unlikely, as the emission is expected to be compact and close to the pulsar position at higher energies. For lower energies we would expect extended emission with the centroid offset from the pulsar position. If this were the case, we would expect a clear difference between each of the energy bands (as shown by deviation from the blue zero line in Figure 8.10), which is not seen. To quantify the level of difference, statistical tests can be applied. We will conduct the following tests at a 3σ level of significance, i.e., reject the null hypothesis when its p-value ≤ 0.003.
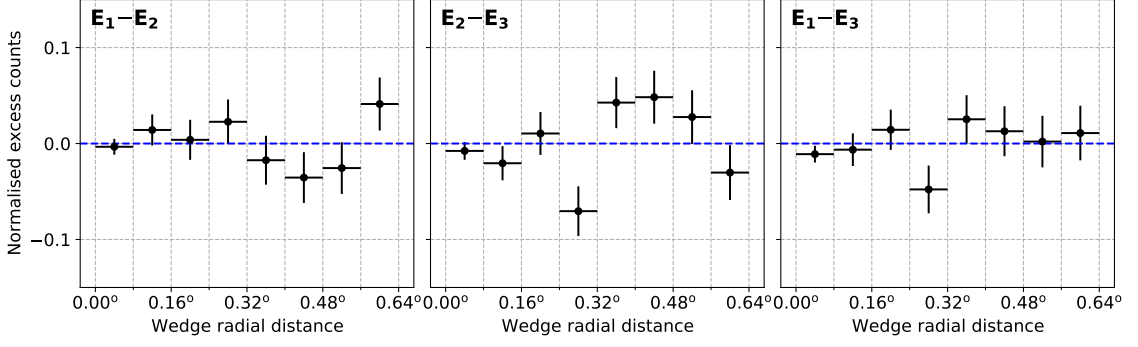
Figure 8.10: Deviation plots between the different energy bands indicated in Figure 8.9. The blue dashed line shows the expected zero value line to indicate no energy-dependent morphology.

The first test is the chi-square goodness of fit test (see Equation 8.8, Barlow, 1989; Bevington and Robinson, 1969) to evaluate how well the observations deviate from the expected value. The null hypothesis, H_0, assumes there is no significant deviation between the observed and expected values i.e., the morphology is energy-independent. The alternative hypothesis, H_a, proposes that there is deviation between these, i.e., the morphology is energy-dependent.

$$\chi^2 = \sum_i \frac{(D_i - G_i)^2}{\sigma_i^2} \, , \tag{8.8}$$

where D_i are the deviation values (E_1-E_2 or E_2-E_3 or E_1-E_3) with uncertainty values σ_i, G_i are the expected values and i denotes each radial bin. As we are testing for energy independence, the expected values, G_i, are all zero, as indicated by the blue lines in Figure 8.10. To calculate the p-value for this distribution we also need to know the number of degrees of freedom. This is calculated through $\nu = n-1$, where n is the number of data points. The p-value for the chi-square distribution can be found in a look-up table, for example from Barlow, 1989.

Another common test is the Wald-Wolfowitz Test (Barlow, 1989), also known as a run-test, which examines the randomness of a sequence of values. The chi-square test described above takes into account the deviation but not the signs, whilst the run-test takes into account the signs of the data points but not deviations from the reference value. Therefore the two statistical tests are quite complementary. The run-test takes the given dataset and marks the data with a '+' if the data is greater than the reference value or '−' if the data is less than. The reference value used here is zero, as this would indicate energy independence. The null hypothesis, H_0, for the run-test is that the data points are independent (with no preference for either '+' or '-') and similar to the reference value, i.e., energy-independence. The alternative hypothesis, H_a, is that the values do not follow the reference value, i.e., energy-dependence. The test-statistic for the run-test is given by the Z-score:

$$Z = \frac{|R - \mu_R|}{\sigma} \, , \tag{8.9}$$

where the mean (i.e., the expected number of runs) is given by:

$$\mu_R = \frac{2N_+ N_-}{N} + 1 \, . \tag{8.10}$$

Here, N_+ is the number of values above the line (in Figure 8.10), N_- is the number of values below the line and the total number of values is $N = N_+ + N_-$. The variance is:

$$\sigma^2 = \frac{2N_+ N_- (2N_+ N_1 - N)}{N^2(N-1)} = \frac{(\mu - 1)(\mu - 2)}{N - 1} \, . \tag{8.11}$$

A run is defined as a series of increasing or decreasing values. The total number of runs, R, is given by the number of increasing or decreasing values. For example, '$-++---++-+--$' consists of seven runs, three consisting of $+$'s and four consisting of $-$'s. The p-value here is taken from `Python`'s `scipy` package which utilises NIST, 2013.

Table 8.4 shows the results for both the chi-square and run-tests. The results for each energy band deviation for the chi-square test fail to reject the null hypothesis at the 3σ significance level, so we have no compelling evidence that energy-dependent morphology is present. From the run-test results in Table 8.4, the p-value indicates that we also do not achieve a statistically significant result (p-value> 0.003), therefore we fail to reject the null hypothesis that there is energy-independence. Therefore, the alternative hypothesis (for energy-dependent morphology) is not supported.

Table 8.4: Test results for the PWNe scenario with PSR J1803−2137 as the accelerator to quantify if any energy-dependent morphology is seen in the H.E.S.S. observations. The energy bands are E_1=0.2−0.56 TeV, E_2=0.56−0.97 TeV and E_3=0.97−12 TeV. The results here show that we fail to reject the null hypothesis (of energy-independence) as the p-value is always > 0.003.

Energy band	Chi-square		Run test	
	χ^2	p-value	Z-score	p-value
$E_1 - E_2$	7.3	0.40	0.76	0.22
$E_2 - E_3$	17.4	0.02	0.00	0.50
$E_1 - E_3$	7.3	0.40	0.62	0.27

In conclusion, this analysis has found that the morphology of HESS J1804−216 is not consistent with that expected of a mature PWNe with the current data. Further data with smaller uncertainties would help to confirm any energy-dependent or independent morphology. The emission at the highest energies (> 12 TeV) has very low significance ($< 2\sigma$), therefore CTA could be used to further probe the higher energies. The small-sized telescopes for CTA are expected to detect γ-rays of a few TeV up to 300 TeV with better sensitivity and angular resolution than current IACTs (CTA Consortium et al., 2018).

8.3.3   SNR Scenario: Energy-dependent Morphology Interpretation

In Chapter 6, a model was introduced for γ-rays created in the hadronic scenario from two different SNRs, SNR G8.7−0.1 and the progenitor SNR of PSR J1803−2137. The spatial morphology of the best matching models was presented in different energy bands, which can now be adjusted to compare with the analysis of the H.E.S.S. data towards HESS J1804−216 in this chapter. The energy bands are defined the same way as the PWNe investigation: E_1=0.2−0.56 TeV, E_2=0.56−0.97 TeV and E_3=0.97−12 TeV. The integrated γ-ray flux morphology maps of the best matching models for both SNR G8.7−0.1 and the progenitor SNR of PSR J1803−2137 are shown in the appendix for these energy bands (shown by Figure D.7).

The radial profile is taken in a wedge which comprises the stronger γ-ray emission from HESS J1804−216. This is different for each SNR, as outlined below. To determine the radial bands, it is important to consider the size of the SNR bubble for each SNR, to ensure we include radial bins both inside and outside the bubble radius. The radii for each SNR are chosen such that one radial ring lines up with the edge of the SNR bubble. For the progenitor SNR, the bubble radius is $R_{\rm esc} \sim 0.195°$, so we take wedge annuli with a width of $\sim 0.098°$. For SNR G8.7−0.1, the bubble radius is equal to the SNR radius of $R_{\rm esc} = 0.375°$, where the wedge annuli have a width of $\sim 0.094°$. The wedge annuli for each SNR, shown in Figure 8.11, has the birth position of each SNR at the apex of the wedge.
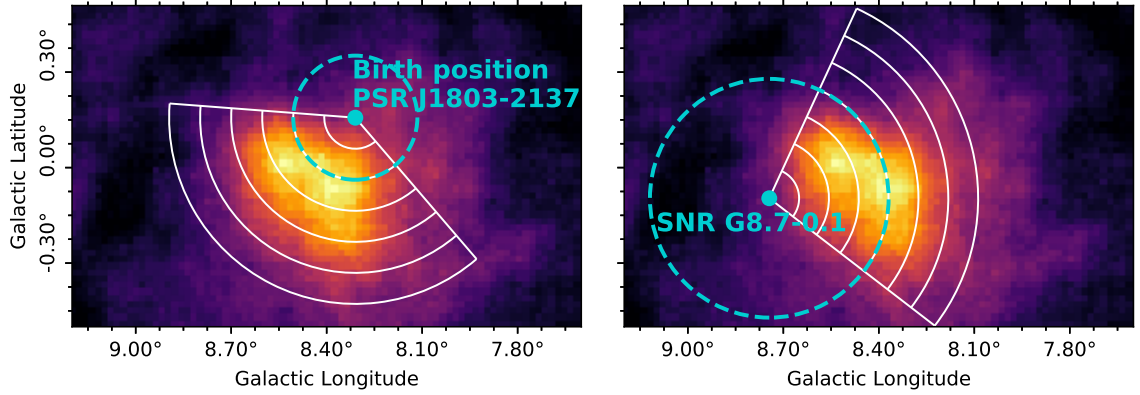
Figure 8.11: The observational excess counts map over the entire energy range. *Left*: The circular wedge geometry with the birth position of PSR J1803−2137 at the apex of the wedge (indicated by the cyan dot). *Right*: The circular wedge geometry with the position of SNR G8.7−0.1 at the apex of the wedge (indicated by the cyan dot). The radial profiles are extracted from each wedge annulus.

The integrated flux maps from the model, $F_{{\rm model},i}$, can be converted to counts maps through:

$$N_{{\rm exc,model},i} = F_{{\rm model},i}\, A_{\rm eff}\, t_{\rm live}\,, \tag{8.12}$$

where i indicates each pixel in the map, $A_{\rm eff}$ is the average effective area for the given energy band from all observation runs and $t_{\rm live}$ is the total livetime from all

observation runs. The excess counts for the model is obtained for each wedge annulus through:

$$N_{\text{exc,model}} = \sum N_{\text{exc,model,i}} \, . \tag{8.13}$$

Progenitor SNR of PSR J1803−2137

Figure 8.15 shows the wedge radial profile for the modelled progenitor SNR of PSR J1803−2137. For the best matching model for the progenitor SNR of PSR J1803−2137 the escape energy is 3.8 TeV for CR protons, therefore we expect energies less than this to be trapped inside the bubble and above this to have escaped. The escape radius is $R_{\text{esc}} \sim 0.195°$, therefore the first two radial bins in Figure 8.15 are from emission inside the bubble. The normalised excess counts for the first two radial bins increases, due to the emission inside the bubble being uniformly distributed and the increasing area of the radial bins as the wedge radial distance increases. For a first look, the modelled emission appears to exhibit some energy-dependent morphology, as the radial profiles in the energy bands are different.
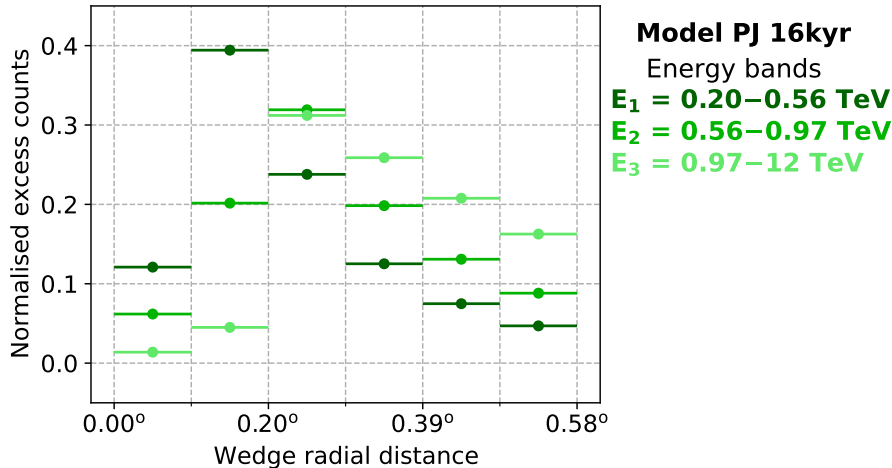
Figure 8.12: The radial wedge profile for each annulus for the modelled progenitor (PJ) SNR of PSR J1803−2137 (as defined in the left panel of Figure 8.11) and energy band. The normalised excess counts increase until the bubble radius is reached (∼0.195°), then begin to decrease.

In a similar method outlined in Section 8.3.2, the observed γ-ray emission in each energy band is investigated using the same radial bins as defined above. Figure 8.13 shows the radial profile of the H.E.S.S. observations using the wedges defined in the left panel of Figure 8.11. There is no clear indication of any energy-dependent morphology seen in this figure. To quantitatively investigate this further, we look at the deviation profiles as shown in Figure 8.14.

Figure 8.14 shows there is little difference between each of the energy bands for the observations. To quantify this, both the chi-square goodness of fit test (see Equation 8.8) and the run-test (see Equation 8.9) are utilised. The results for both of these tests using the wedge radial annuli defined in the left panel of Figure 8.11 is given in Table 8.5.
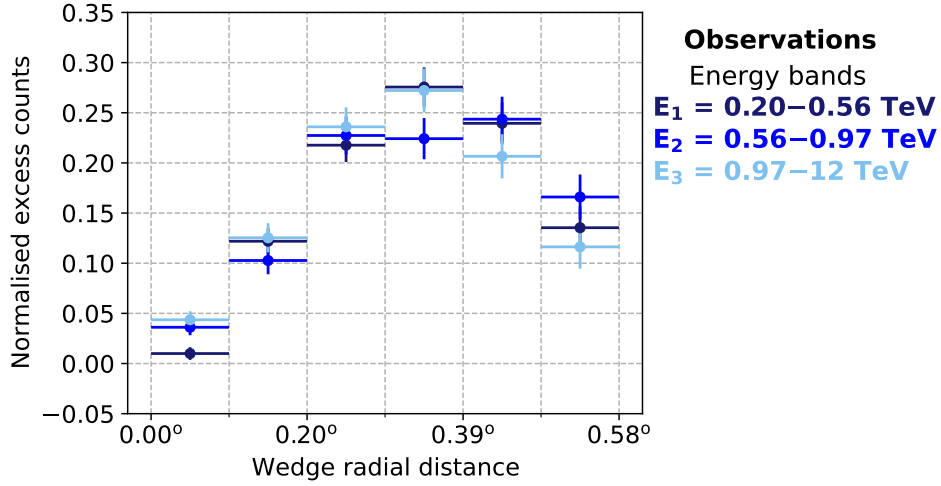
Figure 8.13: The radial wedge profile for each annulus and energy band for the observations as defined in the left panel of Figure 8.11. The deviation between each of the energy bands appears to be small.
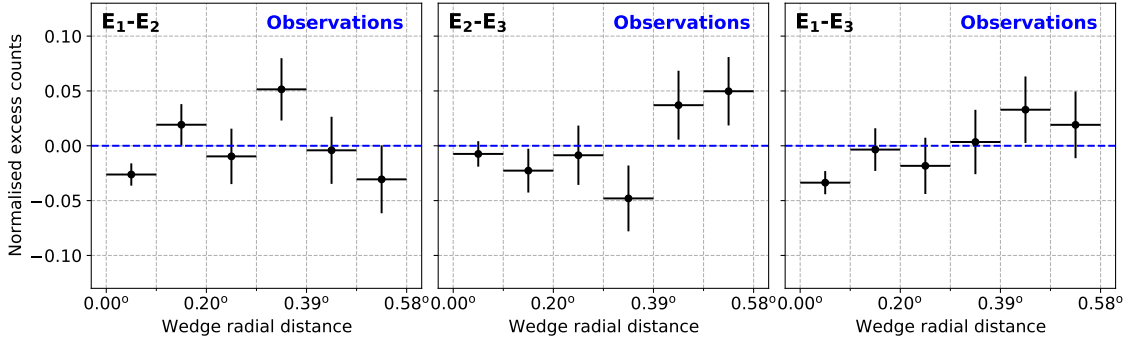
Figure 8.14: Deviation plots between the different energy bands indicated in Figure 8.13 for the observations centred on the birth position of the progenitor SNR of PSR J1803−2137. The blue dashed line shows the expected zero value line to indicate no energy-dependent morphology.

Table 8.5: Test results for the observations assuming the wedge annuli profile as defined in the left panel of Figure 8.11. This shows that the null hypothesis cannot be rejected at the 3σ significance level (i.e. p-value> 0.003).

Energy band	Chi-square		Run test	
	χ^2	p-value	Z-score	p-value
E_1-E_2	12.1	0.03	1.41	0.08
E_2-E_3	8.3	0.14	1.77	0.04
E_1-E_3	12.3	0.03	1.83	0.03

The results for both the chi-square and run-test in Table 8.5 indicate that we fail to reject the null hypothesis (p-value>0.003). Therefore, there is no compelling evidence that energy-dependent morphology is present in the observations.

It is also important to consider how the observations compare to the model. To do so, we take the radial wedge profiles for each energy band and compare the observations with the model. This is shown in Figure 8.15 for the progenitor SNR of PSR J1803−2137.
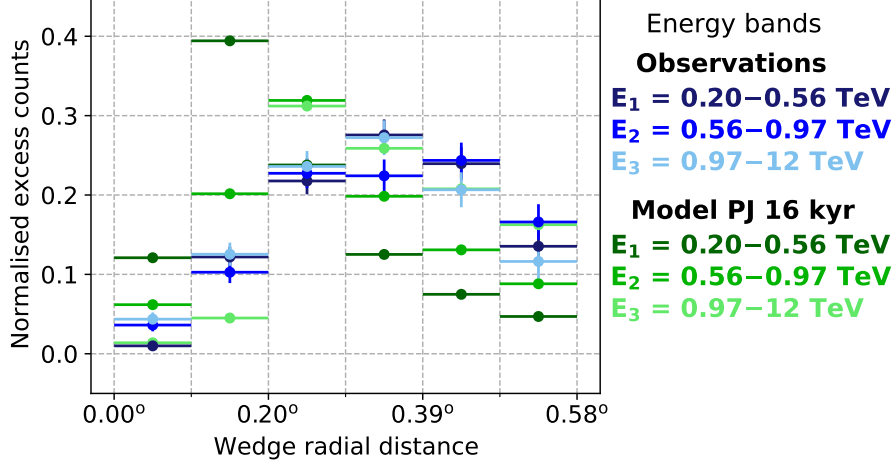
Figure 8.15: The radial wedge profile for each annulus and energy band for the observations and model for the progenitor SNR as defined in the left panel of Figure 8.11.

To quantify how well the observations and model match we used a reduced chi-square test:

$$\chi^2 = \left(\sum_i \frac{(O_i - M_i)^2}{\sigma_i^2} \right) , \tag{8.14}$$

where O_i indicates the observation for each deviation profile with uncertainty σ_i and M_i is the model deviation profile values. The null hypothesis, H_0, is that the observations and model show no significant difference. The alternative hypothesis, H_a, is that the observations and model are significantly different. The results for this test with the progenitor SNR wedge annuli definition (left panel of Figure 8.11) are shown in Table 8.6.

Table 8.6: Chi-square goodness of fit results for the SNR scenario with progenitor SNR of PSR J1803−2137 as the accelerator. The null hypothesis is rejected for all energy bands as p-value<0.003, therefore the model and observations are significantly different.

Energy band	χ^2	ndf	p-value
E_1	890	6	10^{-189}
E_2	125	6	10^{-24}
E_3	63	6	10^{-11}

Table 8.6 shows for all deviation combinations the p-value is < 0.003, so the null hypothesis is rejected, meaning the model and observations are significantly different. Therefore, the observations struggle to match the expected γ-ray morphology from the model with the progenitor SNR of PSR J1803−2137 as the accelerator of CR protons.

SNR G8.7−0.1

Figure 8.16 shows the wedge radial profile for both ages of SNR G8.7−0.1. For these models the SNR bubble radius is $R_{\mathrm{esc}} = 0.375°$, which means the first four radial bins are contained within the bubble. The normalised excess counts for both panels of Figure 8.16 increases until the bubble radius is reached, then it begins to decrease. This is typical behaviour as the area of the wedge annuli is increasing as the radius increases. Both ages of SNR G8.7−0.1 for the model data in Figure 8.16 show an interesting morphology, in which there appears to be a difference between the different energy bands.
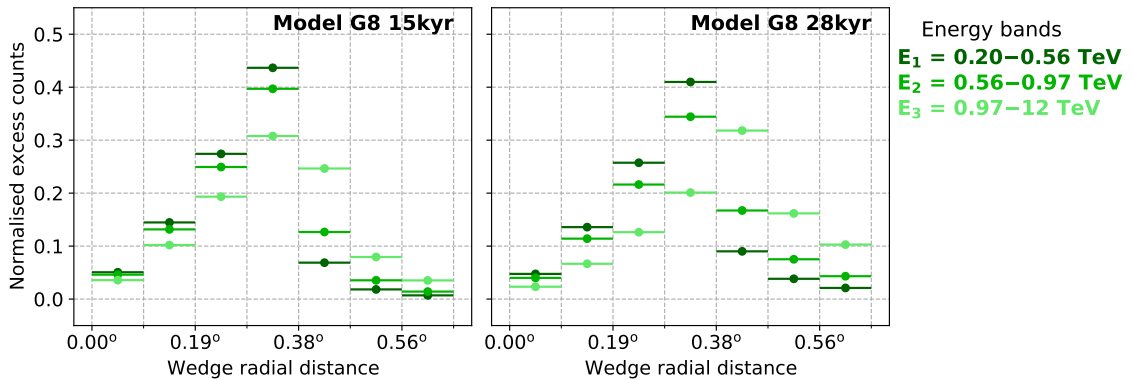
Figure 8.16: *Left*: The radial wedge profile for each annulus for SNR G8.7−0.1 with an age of 15 kyr (as defined in the right panel of Figure 8.11) for each energy band. *Right*: The radial wedge profile for each annulus for SNR G8.7−0.1 with an age of 28 kyr (as defined in the right panel of Figure 8.11) for each energy band.

The radial profiles for observations from the wedge annuli defined in the right panel of Figure 8.11 are presented in Figure 8.17. The observed emission here is the same when considering either age of SNR G8.7−0.1 as the radius is assumed to be the same.

The radial profiles in Figure 8.17 are shown to increase out to a radius of $\sim 0.47°$, then it begins to decrease. Again, this behaviour is typical as the area of the wedge annuli increase with increasing radius. It is not clear from this figure alone if energy-dependent morphology is seen, therefore we again look at the deviation profiles as shown in Figure 8.18.
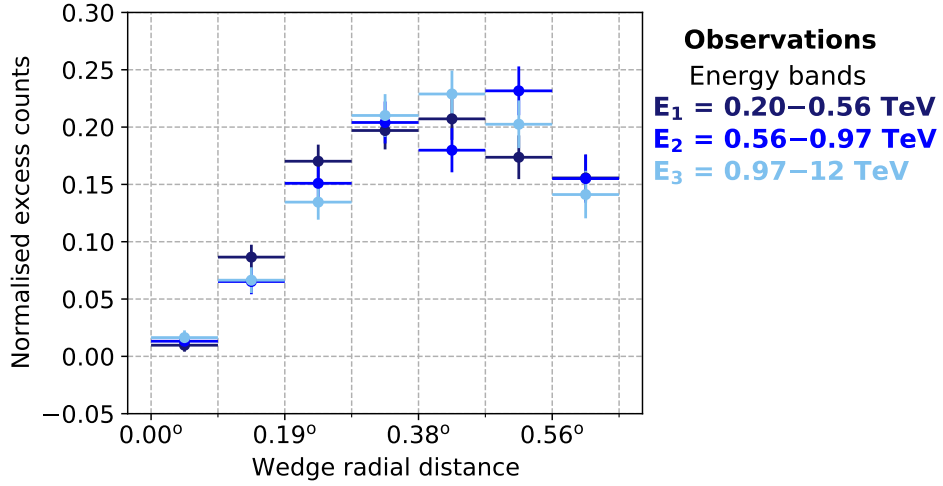
Figure 8.17: The radial wedge profile for each annulus and energy band for the observations as defined in the right panel of Figure 8.11. The energy bands tend to show smaller deviations from one another.
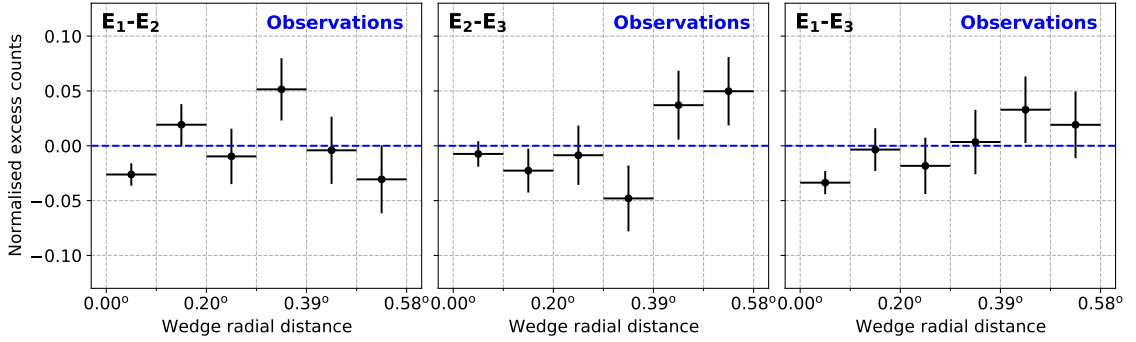
Figure 8.18: Deviation plots between the different energy bands indicated in Figure 8.17 for the observations centred on SNR G8.7−0.1. The blue dashed line shows the expected zero value line to indicate no energy-dependent morphology.

The deviation profiles in Figure 8.18 typically appear to follow the blue reference zero line well. To quantify this, the chi-square and run-tests are presented in Table 8.7. These results show that at a significance of 3σ we cannot reject the null hypothesis, therefore there is no compelling evidence, again, that the observations exhibit energy-dependent morphology. This is consistent with the other radial profiles obtained for the H.E.S.S. observations in this analysis.

A comparison between the observations and model is made using the radial profiles in the right panel of Figure 8.11 for the different energy bands. Figure 8.19 shows this comparison for the model with SNR G8.7−0.1 as the accelerator with an age of 15 kyr.

Table 8.7: Test results for the observations assuming the wedge annuli profile as defined in the right panel of Figure 8.11. At a significance level of 0.003 we fail to reject the null hypothesis for all deviation combinations.

Energy band	Chi-square		Run test	
	χ^2	p-value	Z-score	p-value
E_1-E_2	8.1	0.23	1.33	0.09
E_2-E_3	5.0	0.55	0.36	0.36
E_1-E_3	7.3	0.29	0.36	0.36
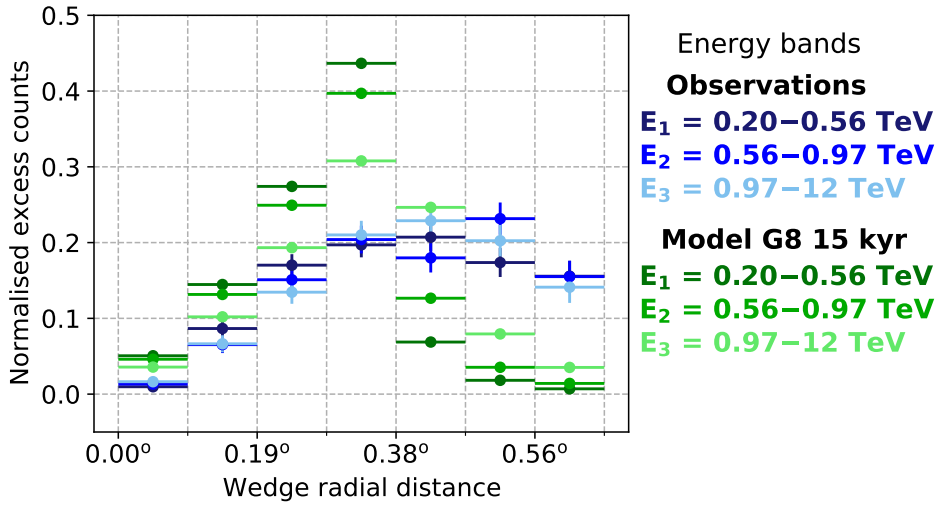
Figure 8.19: The radial wedge profile for each annulus and energy band for the observations and model for SNR G8.7−0.1 with an age of 15 kyr as defined in the right panel of Figure 8.11.

Using the chi-square measure defined in Equation 8.14 the observations are quantitatively compared to the model for both ages of SNR G8.7−0.1, under the null hypothesis that the observations and model are not significantly different. Table 8.8 shows the results of the reduced chi-square test for SNR G8.7−0.1 with an age of 15 kyr.

Table 8.8: Chi-square goodness of fit results for the SNR scenario with SNR G8.7−0.1 with an age of 15 kyr as the accelerator. The null hypothesis is rejected for all energy bands as p-value<0.003, therefore the model and observations are significantly different.

Energy band	χ^2	ndf	p-value
E_1	521	7	$\sim 10^{-108}$
E_2	354	7	$\sim 10^{-72}$
E_3	123	7	$\sim 10^{-23}$

The chi-square results in Table 8.8 allow us to reject the null hypothesis, for the all the energy bands, in favour of the alternative hypothesis, that the observation and model are significantly different (at the 0.003 significance level).

Figure 8.20 shows the radial profiles for the comparison between the observations and model with SNR G8.7−0.1 as the accelerator with an age of 28 kyr.
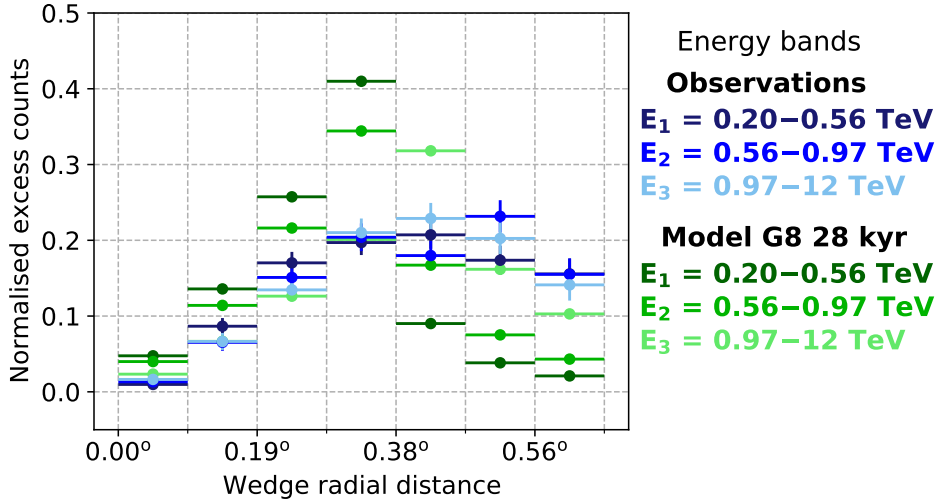
Figure 8.20: The radial wedge profile for each annulus and energy band for the observations and model for SNR G8.7−0.1 with an age of 28 kyr as defined in the right panel of Figure 8.11.

Table 8.9 shows the chi-square results for SNR G8.7−0.1 with an age of 28 kyr. These results give good ground to reject the null hypothesis in favour of the alternative hypothesis for all three energy bands, meaning the observations and model are significantly different.

Table 8.9: Chi-square goodness of fit results for the SNR scenario with SNR G8.7−0.1 with an age of 28 kyr as the accelerator. The null hypothesis is rejected in favour of the alternative hypothesis for all three energy bands. Hence, the observations and model are significantly different.

Energy band	χ^2	ndf	p-value
E_1	404	7	$\sim 10^{-83}$
E_2	198	7	$\sim 10^{-39}$
E_3	28	7	$\sim 10^{-4}$

The key aspect to note for both ages of SNR G8.7−0.1 is that the energy bands for the model tend to exhibit different morphology. From the chi-square and run-test results for the observations (Table 8.7), we could not reject the null hypothesis. Therefore there is no convincing evidence for or against energy-dependent morphology for the observations.

Upon comparing the model to observations through the chi-square test, it is shown that the wedge radial profile from observations are significantly different from the model results. The observations therefore struggle to match the expected γ-ray morphology from the `mario` model assuming SNR G8.7−0.1 is the accelerator of CR protons.

The results presented in this section show that the model and observations struggle to match within each of their energy bands. Previously, in Chapter 6 we determined the best matching models for each accelerator using the spatial morphology of γ-rays above 1 TeV. This was shown to provide a similar match to the γ-ray observations. However, the morphology in different energy bands is shown to be quite different, indicated here through the radial profile plots. This is likely attributed to the uncertainties of our model (see in Discussion of Chapter 6).

9 Conclusions and Future Work

> *We must have perseverance and above all confidence in ourselves. We must believe that we are gifted for something and that this thing must be attained.*
>
> — Marie Curie, *Polish-French Physicist*

This thesis focused on studying the unidentified TeV γ-ray source HESS J1804$-$216 to constrain the nature of emission. Supernova remnants (SNRs) and Pulsar Wind Nebulae (PWNe) are two prominent candidates for accelerating cosmic rays (CRs) to high energies, see Section 2.1. HESS J1804$-$216 has several of these plausible counterparts within 1°: SNR G8.7$-$0.1, SNR 8.3$-$0.1, PSR J1803$-$2137, PSR J1803$-$2149 and PSR J1806$-$2125. The interstellar medium (ISM) towards HESS J1804$-$216 was investigated in detail in an attempt to unveil its origin.

The Mopra radio telescope in all three wavelength bands (3 mm, 7 mm and 12 mm) was utilised along with the HI data from the Southern Galactic Plane Survey (SGPS). These observations provided a useful way to probe the intriguing features of the ISM, in addition to studying the potential CR accelerators towards this source. Carbon monoxide (CO) is the typical tracer of hydrogen as it is abundant and easily detected in the ISM. However, due to its abundance, it quickly becomes optically thick, therefore we need to consider tracers of dense gas ($n > 10^4 \, \mathrm{cm}^{-3}$) to overcome this. Dense gas tracers have a higher critical density and lower abundance compared to ^{12}CO(1-0), so are able to probe the internal dynamics of dense cloud cores. The five dense gas tracers used in this thesis are carbon monosulfide (CS(1-0)), silicon monoxide, methanol, cyanopolyyne and ammonia (see Section 4.6). The clumps of emission in CS(1-0), particularly, confirmed the presence of dense gas.

Gas was seen to overlap the TeV source at multiple velocity components along the line of sight (Chapter 5). There was a substantial amount of gas seen in Components C ($\mathrm{v_{lsr}} = 8$ to $26 \, \mathrm{km \, s}^{-1}$) and D ($\mathrm{v_{lsr}} = 26$ to $56 \, \mathrm{km \, s}^{-1}$) towards HESS J1804$-$216. In Component C, there was morphological matches between the ^{12}CO(1-0) and ^{13}CO(1-0) interstellar gas data and the TeV γ-ray emission towards HESS J1804$-$216. A depletion of gas in the southern peak of the TeV source is present in Component C (Chapter 5). Component D showed dense gas clouds overlapping the Galactic-South of HESS J1804$-$216 and SNR G8.7$-$0.1. These clouds are also consistent with several HII regions.

Total column density maps were used to calculate various characteristics of the gas including mass and density. These were utilised to test the validity of both the purely hadronic and purely leptonic scenarios for the potential CR accelerators towards HESS J1804$-$216 (c.f. Chapter 5). For the purely leptonic scenario, it is possible for PSR J1803$-$2137 to accelerate highly energetic electrons as a PWNe. This is supported by the high spin down luminosity, leading to a TeV γ-ray efficiency of 3%, typical of a PWNe-driven TeV source. SNR G8.7$-$0.1 or the progenitor SNR of PSR J1803$-$2137 is expected to accelerate CR protons in the purely hadronic

scenario. Modelling of the CR proton spectra for these SNRs showed matches to the observed GeV and TeV CR enhancement factors (see Chapter 5). This in-depth gas analysis allowed us to identify that either a middle-aged SNR or PSR can produce the TeV γ-ray emission towards HESS J1804−216.

The hadronic scenario is investigated further for both SNR G8.7−0.1 and the progenitor SNR of PSR J1803−2137 as plausible counterparts (see Chapter 6). The spatial and spectral distributions of CR protons are generated by modelling the energy-dependent escape and diffusion of these particles into the ISM. The accelerated CR protons interact with the ISM to produce γ-rays. The spatial and spectral distributions of γ-rays for a range of model parameters are produced (Chapter 6). To produce this 2D approach to modelling the γ-ray emission, we developed a Python package called `mario`. Comparing the best matching models with the GeV to TeV γ-ray observations revealed that the progenitor SNR of PSR J1803−2137 was the most prominent candidate, however, we are limited by the bubble component.

There are various known limitations of this model, which come from assuming a 2D propagation of CR protons and 2D distribution of the ISM. The 2D proton model means we do not consider particles which diffuse along our line of sight, which becomes problematic for an accelerator which is close to the gas clouds (both accelerators we consider are within the bounds of HESS J1804−216). In addition to this, we do not model the diffusion inside the bubble component, therefore the results are biased (c.f. Chapter 6). A similar issue arises by assuming a 2D distribution of the ISM in which all gas has been integrated over. Again, there could be gas that is foreground/background to the accelerator, which is included that may not physically be able to interact with the CR protons. Another limitation of the model is the simple assumptions of the bubble component, for example the uniform distribution of CR protons and ISM. Realistically, we expect the particle distribution inside the bubble to be complex with CRs built up at the shock front. The ISM inside the bubble could also be up to ∼4 times denser from diffusive shock acceleration theory or be less dense as the ISM is dissociated by the SNR shock.

The final study for this thesis was to analyse all the possible available H.E.S.S. data using the open-source `Python` package `gammapy` (see Chapter 8). The γ-ray spectra is investigated at the highest energies to access the possibility of particles being accelerated to PeV energies. The HESS J1804−216 spectra for this analysis was shown to follow an exponential cutoff power law spectra model, with a cutoff energy of $E_{\text{cutoff}} = 25^{+73}_{-11}$ TeV (see Section 8.3.1). This gives indication that HESS J1804−216 is a PeVatron candidate. The upcoming CTA would be able to probe the emission at the highest energies further. The morphology of γ-rays towards HESS J1804−216 was investigated at different energies. Firstly, assuming a PWNe scenario for PSR J1803−2137, the H.E.S.S. observations do not appear to exhibit energy-dependent morphology (see Section 8.3.2). This is not consistent with the expected morphology of a mature PWNe. More data from the upcoming CTA could help investigate this further. The morphology in different energy bands is also investigated for the SNR scenario using the model defined in Chapter 6. The model for both the progenitor SNR of PSR J1803−2137 and SNR G8.7−0.1 shows a clear difference to the observations (see Section 8.3.3). There is no compelling evidence of energy-dependent morphology for the observations according to the statistical tests

performed. It is shown that the observations and model results for each accelerator are significantly different (see results from the chi-square in Section 8.3.3). Further observations at higher energies would allow us to investigate the morphology here further.

9.1   Future work

As mentioned previously, the method adopted to model the γ-rays towards HESS J1804$-$216 in the hadronic scenario has a number of limitations. Future work would involve adaptations to the model, to make it more realistic. Firstly, to implement a 3D proton distribution which describes particles diffusing along our line of sight. This would involve using the number density and volume in the γ-ray flux calculation (Equation 7.17) instead of the 2D version in which we use the column density and area of the source. Another modification to the model would be to adapt the diffusion such that it is no longer constant and changes with changing magnetic field. The magnetic field is taken as a constant in our model, however the distribution of the magnetic field is expected to change within the ISM with varying number density. This would lead to a decrease in diffusion length as the number density and thus magnetic field increase. Using a constant number density for the SNR evolution leads to spherical uniformity of the particle escape radius. The evolution of the SNR is also dependent upon $\delta_{\rm p}$, which describes the energy dependent release of CRs. A future version of the model would involve tracing the evolution of the SNR shock in further detail, including the escape radius as it changes with ISM density. For example, we expect the escape radius to decrease as it encounters larger number densities.

The hadronic model described in this thesis for SNRs can be extended for leptonic production of γ-rays, to model sources such as PWNe. This would involve modelling the distribution of high-energy electrons emanating from pulsars as a PWNe. The addition of modelling the magnetic field structure, would allow the electrons to be closely traced, such that the magnetic field is stronger at the pulsar position and decreases at distances away from the pulsar. Allowing for different injection spectrum types to be modelled, such as a broken power law, would extend the model for a source which cannot be described by a single power law. A broken power law is expected to be able to explain the acceleration for low-energy electrons or to explain the spectral break from synchrotron losses (Bucciantini et al., 2010; Amato, 2014). Creating a model from these fundamentals, would help in better determining other PWNe candidates along the Galactic plane.

The work presented in this thesis forms a basis for comparisons between the ISM and next-generation ground based γ-ray telescopes, such as the Cherenkov Telescope Array (CTA). CTA is expected to have angular resolution comparable to the ISM data from the Mopra radio telescope. The finer details of this upcoming γ-ray data will allow for better comparison between the TeV γ-ray emission and ISM. CTA will also have higher sensitivity with an extended energy range from 10's of GeV to $\sim$300 TeV, to potentially unveil a number of currently undetected sources.

Implementing the adaptations to the model would make the model more realistic. This would allow the model to be transferred to other PWNe and SNR systems. In addition, comparing the γ-ray data from CTA with the arcminute scale γ-ray data from the updated model would allow the nature of other unidentified sources to be constrained further.

A   Spectrum of Diffusive Shock Acceleration

The probability of a cosmic ray (CR) particle crossing the shock (i.e. escaping downstream) and the probability of returning from the shock is given by Equation A.1.

$$
\begin{aligned}
P_{\text{escape}} &= \frac{4 v_{\text{shock}}}{R v} \\
P_{\text{return}} &= 1 - P_{\text{escape}} = 1 - \frac{4 v_{\text{shock}}}{R v}
\end{aligned}
\tag{A.1}
$$

The probability of a CR particle returning from the shock k times is then $P(> k) = (P_{\text{return}})^k$, where the energy after k crossings is:

$$
E = E_0 \left(1 + \frac{\Delta E}{E} \right)^k .
\tag{A.2}
$$

Here, E_0 is the initial energy of the particle. The integral energy spectrum, $Q(> E)$, is then proportional to the probability of crossing the shock k times, as shown by Equation A.3.

$$
Q(> E) = (P_{\text{return}})^k
\tag{A.3}
$$

By rearranging Equation A.2 we can obtain an expression for k:

$$
k = \frac{\ln(E/E_0)}{\ln(1 + \Delta E/E)} .
\tag{A.4}
$$

Taking the logarithm of Equation A.3 gives:

$$
\begin{aligned}
\ln(Q(> E)) &= A + k \ln(P_{\text{return}}) \\
&= A + \frac{\ln(E/E_0)}{\ln(1 + \Delta E/E)} \ln[P_{\text{return}}] \\
&= A + \frac{\ln[P_{\text{return}}]}{\ln(1 + \Delta E/E)} (\ln(E) - \ln(E_0)) .
\end{aligned}
\tag{A.5}
$$

The energy spectrum is then defined as:

$$
\ln(Q(> E)) = B - \Gamma \ln(E) ,
\tag{A.6}
$$

where B and Γ are constants, defined as:

$$\Gamma = \frac{-\ln(P_{\text{return}})}{\ln(1 + \Delta E/E)}.$$ (A.7)

Combining the fractional energy change from Equation 2.16 and the probability of escape from Equation A.1 in the limit where $v_{\text{shock}} \gg c$ gives:

$$\Gamma \approx \frac{P_{\text{escape}}}{\Delta E/E} = \frac{\dfrac{4v_{\text{shock}}}{Rv}}{\dfrac{4}{3}\dfrac{R-1}{R}\dfrac{v_{\text{shock}}}{c}} \approx \frac{3}{R-1} \qquad \text{for v} \rightarrow \text{c}.$$ (A.8)

The integral form of the spectrum is therefore (from Equation A.6):

$$Q(> E) \propto E^{-\Gamma} = E^{-\frac{3}{R-1}}.$$ (A.9)

The differential form of the spectrum is given by Equation 2.17.

B   Additional `mario` information

B.1   Normalising the PDF

The PDF equation must satisfy the condition, $\int_0^\infty f(E, R, t)\, dV = 1$. For the model in 3D, the coordinates are transformed from cartesian coordinates (x, y, z) to spherical coordinates (r, θ, ϕ) in volume through:

$$dV = \int_0^{2\pi} \int_0^\pi \int_0^\infty f(R, \theta, \phi) \sin\theta R^2 \, dR \, d\theta \, d\phi \,. \tag{B.1}$$

By evaluating each integral this equation is reduced to:

$$dV = 4\pi \int_0^\infty f(R)\, R^2 \, dR \,. \tag{B.2}$$

Applying this equation to our definition for both the bubble and diffused PDF:

$$4\pi \int_0^{R_{\text{esc}}} f_{\text{bubble}}(E, R, t)\, R^2 \, dR = 1 \qquad \text{and} \qquad 4\pi \int_{R_{\text{esc}}}^\infty f_{\text{dif}}(E, R, t)\, R^2 \, dR = 1 \,. \tag{B.3}$$

Evaluating the above for the bubble PDF:

$$\begin{aligned} 4\pi \int_0^{R_{\text{esc}}} f_{\text{bubble}}(E, R, t)\, R^2 \, dR &= 4\pi \int_0^{R_{\text{esc}}} \frac{R^2}{(4/3)\pi R_{\text{esc}}^3} \, dR \\ &= \int_0^{R_{\text{esc}}} \frac{3R^2}{R_{\text{esc}}^3} \, dR \\ &= 1 \,. \end{aligned} \tag{B.4}$$

Evaluating Equation B.3 for the diffused PDF:

$$\begin{aligned} f_0 &\equiv 4\pi \int_{R_{\text{esc}}}^\infty f(E, R, t) R^2 \, dR \\ &= \int_{R_{\text{esc}}}^\infty \frac{4\pi R^2}{\pi^{3/2} R_{\text{dif}}^3} \exp\left(-\frac{(R - R_{\text{esc}})^2}{R_{\text{dif}}^2}\right) dR \\ &= \frac{(\sqrt{\pi} R_{\text{dif}}^2 + 2\sqrt{\pi} R_{\text{esc}}^2)|R_{\text{dif}}| + 4R_{\text{esc}} R_{\text{dif}}^2}{\sqrt{\pi} R_{\text{dif}}^3} \,. \end{aligned} \tag{B.5}$$

However, this equation should be equal to 1, to satisfy the conditions of a PDF. Therefore, normalising the PDF using this factor gives:

$$f_{\text{dif}}(E, R, t) = \frac{1}{\pi^{3/2} R_{\text{dif}}^3} \exp\left(-\frac{(R - R_{\text{esc}})^2}{R_{\text{dif}}^2}\right) \frac{1}{f_0}$$

$$= \frac{1}{\pi^{3/2} R_{\text{dif}}^3} \exp\left(-\frac{(R - R_{\text{esc}})^2}{R_{\text{dif}}^2}\right) \frac{\sqrt{\pi} R_{\text{dif}}^3}{(\sqrt{\pi} R_{\text{dif}}^2 + 2\sqrt{\pi} R_{\text{esc}}^2)|R_{\text{dif}}| + 4 R_{\text{esc}} R_{\text{dif}}^2} .$$

$$(\text{B.6})$$

B.2   Top 5 Best Matching Models

This section shows the top 5 best matching models for each accelerator for completeness, as outlined in Tables E.1 to E.3 in Chapter 6.
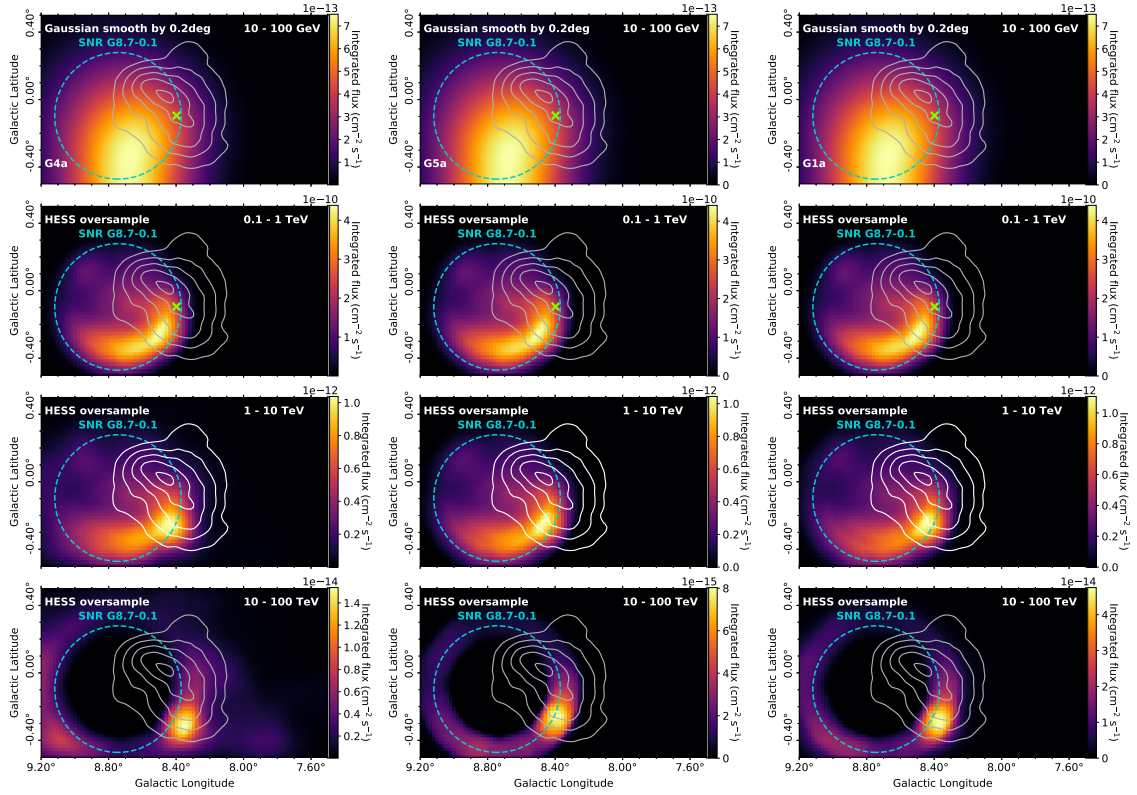
Figure B.1: γ-ray flux maps for various energy bands towards HESS J1804$-$216 for SNR G8.7$-$0.1 with an age of 15 kyr. The escape radius, R_{esc}, is shown by the cyan dashed circle. The green cross indicates the centroid of 3FHL J1804.7$-$2144e. The TeV γ-ray emission above 1 TeV from H.E.S.S. Collaboration et al., 2018 is shown by the solid white contours in the third panel and by grey contours in the other panels as a reference for where the γ-ray emission is expected. Model parameters are described in Table E.1 of Chapter 6.
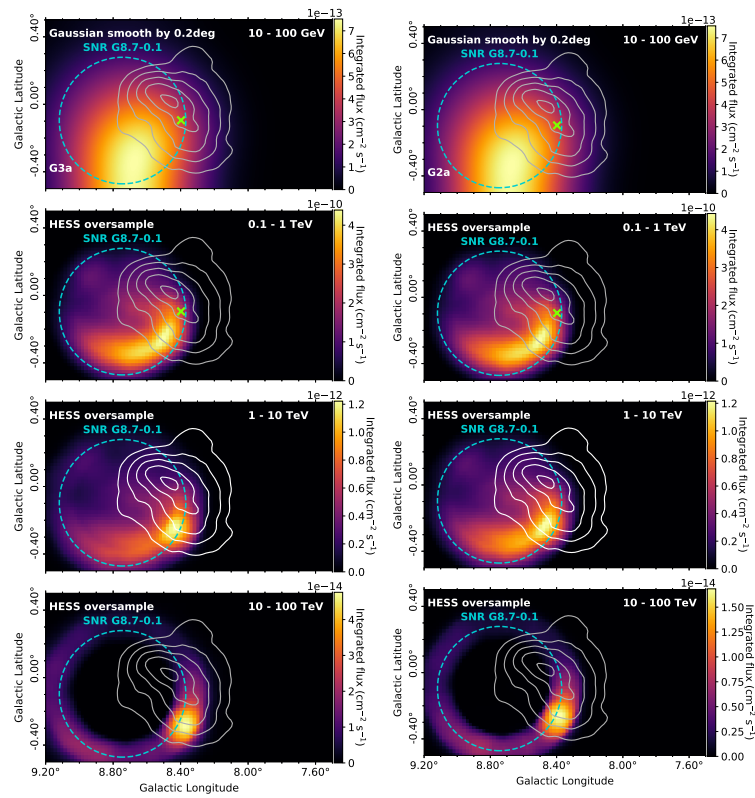
Figure B.2: γ-ray flux maps for various energy bands towards HESS J1804−216 for SNR G8.7−0.1 with age of 15 kyr, information for plots described in Figure B.1.
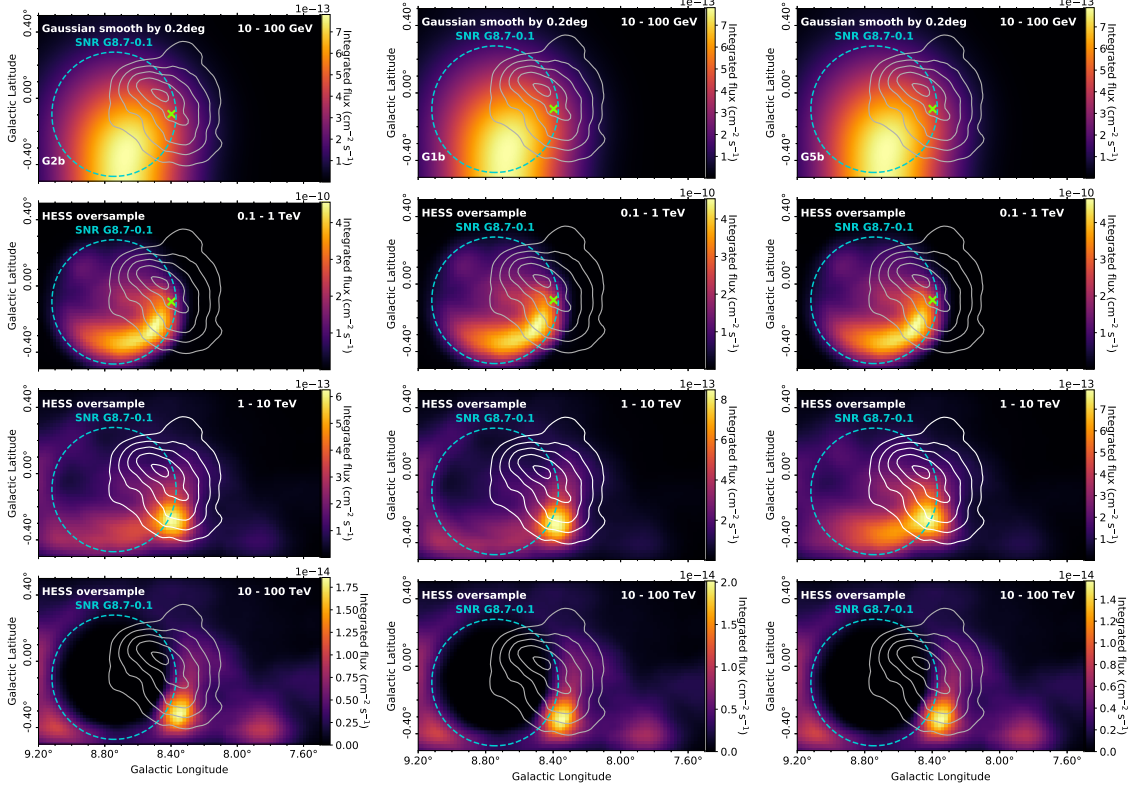
Figure B.3: γ-ray flux maps for various energy bands towards HESS J1804$-$216 for SNR G8.7$-$0.1 with an age of 28 kyr. The escape radius, R_{esc}, is shown by the cyan dashed circle. The green cross indicates the centroid of 3FHL J1804.7$-$2144e. The TeV γ-ray emission above 1 TeV from H.E.S.S. Collaboration et al., 2018 is shown by the solid white contours in the third panel and by grey contours in the other panels as a reference for where the γ-ray emission is expected. Model parameters are described in Table E.2 of Chapter 6.
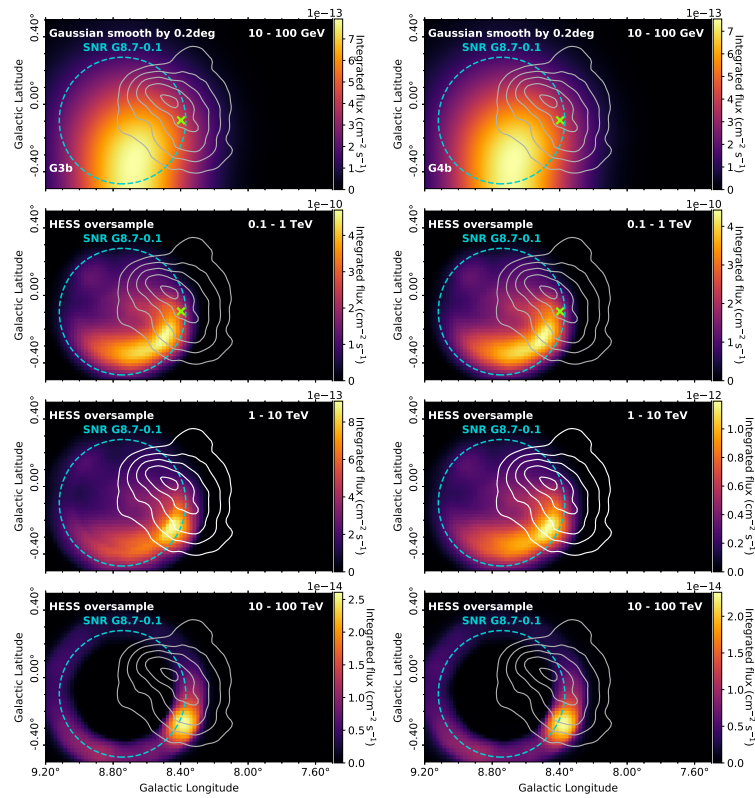
Figure B.4: γ-ray flux maps for various energy bands towards HESS J1804−216 for SNR G8.7−0.1 with age of 28 kyr, information for plots described in Figure B.3.
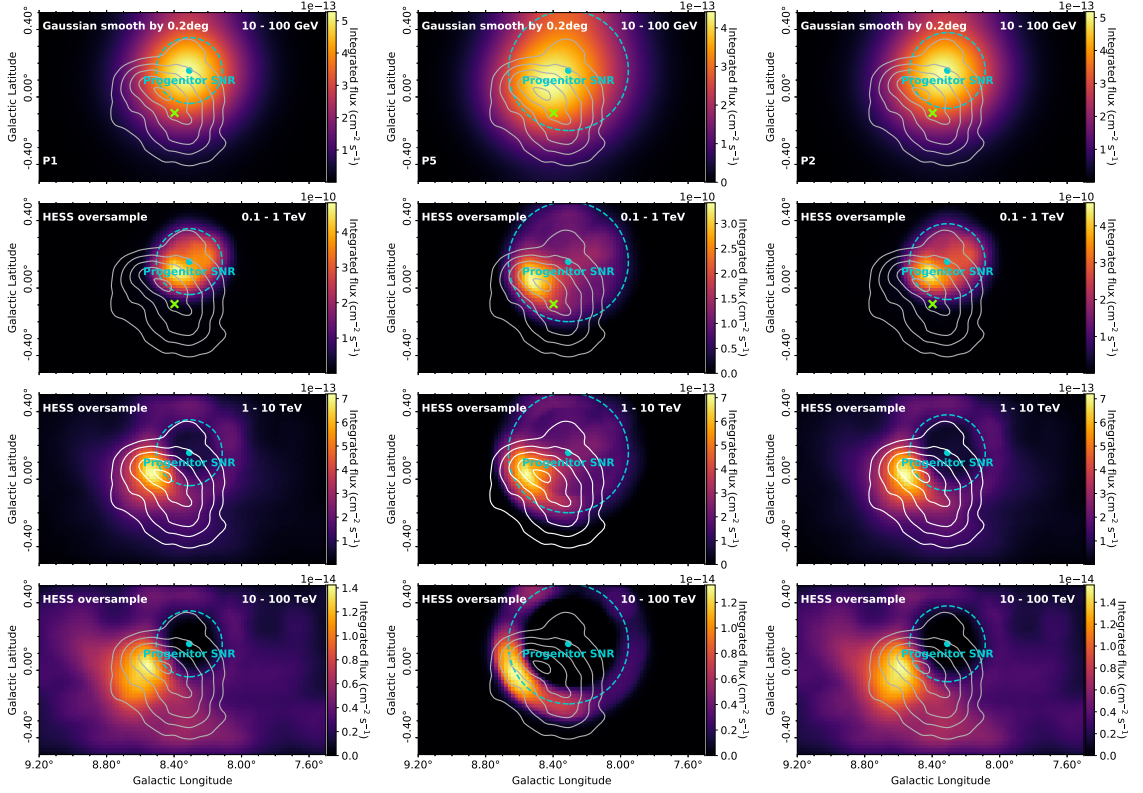
Figure B.5: γ-ray flux maps for various energy bands towards HESS J1804$-$216 for the progenitor SNR of PSR J1803$-$2137. The escape radius, R_{esc}, is shown by the cyan dashed circle. The green cross indicates the centroid of 3FHL J1804.7$-$2144e. The TeV γ-ray emission above 1 TeV from H.E.S.S. Collaboration et al., 2018 is shown by the solid white contours in the third panel and by grey contours in the other panels as a reference for where the γ-ray emission is expected. Model parameters are described in Table E.3 of Chapter 6.
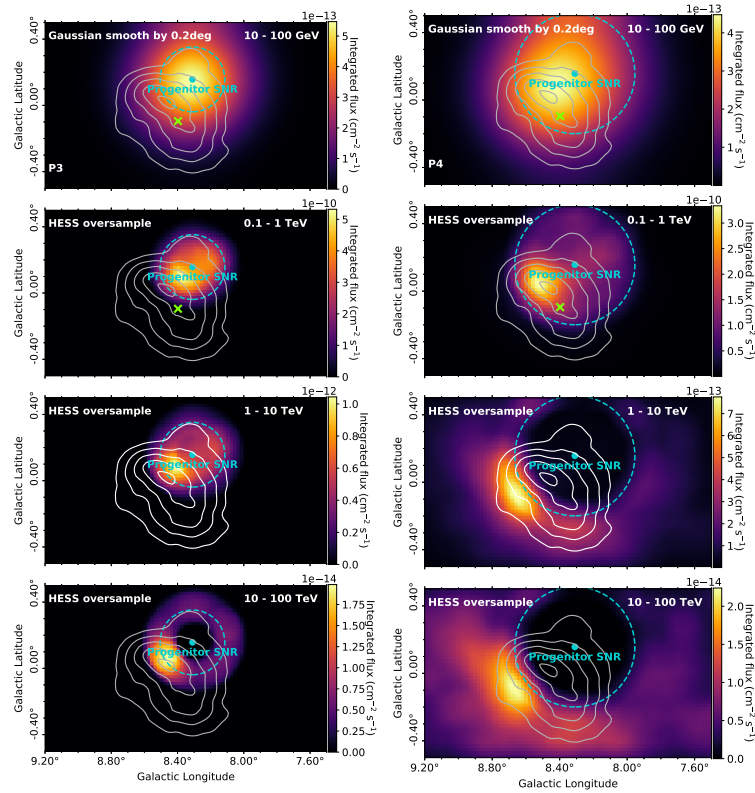
Figure B.6: γ-ray flux maps for various energy bands towards HESS J1804$-$216 for the progenitor SNR of PSR J1803$-$2137, information for plots described in Figure B.5.

C   Leptonic Scenario - First Look

For the leptonic scenario, it was found that the TeV emission being produced by highly energetic electrons from PSR J1803−2137 as a Pulsar Wind Nebula (PWN) is supported given the energetics of the system (Feijen et al., 2020). These electrons are able to diffuse the 30 pc distance to create a TeV source of this size, hence PSR J1803−2137 could potentially contribute to the TeV γ-ray emission from HESS J1804−216.

The following section describes the simulated γ-ray emission produced through leptonic interactions. SNRs are able to produce γ-rays leptonically through the inverse-Compton effect (e.g. SN1006, Koyama et al., 1995). We look at the impulsive accelerator case for the leptonic scenario here.

C.1   Electron Flux

We model the spectrum of CR electrons injected into the surrounding ISM. High energy electrons suffer significant synchrotron radiation losses due to the enhanced magnetic field strength in molecular clouds. We assume the dominant cause of energy losses is synchrotron radiation and inverse compton radiation, given by p_2. Equation C.1 gives the distribution of CR electrons in units of cm^{-3}, from Atoyan et al., 1995.

$$f(\gamma, R, t) = \frac{N_0 \gamma^{-\alpha}}{\pi^{3/2} R_{\text{dif}}^3} \left(1 - \gamma p_2 t\right)^{\alpha - 2} \exp\left[\frac{-R^2}{R_{\text{dif}}^2}\right] , \tag{C.1}$$

where the diffusion radius is

$$R_{\text{dif}}(\gamma, t) = 2\sqrt{D(\gamma) t \frac{1 - (1 - \gamma/\gamma_{\text{cut}})^{1-\delta}}{\gamma/\gamma_{\text{cut}}(1 - \delta)}} . \tag{C.2}$$

The Lorentz factor is $\gamma = E_e/m_e c^2$, where $m_e = 511 \, \text{keV/c}^2$. The 'energy cut-off' is $\gamma_{\text{cut}} = (p_2 t)^{-1}$. If $\gamma > \gamma_{\text{cut}}$ then $f = 0$. p_2 is the term due to synchrotron and inverse Compton losses:

$$p_2 = 5.2 \times 10^{20} \frac{w_o}{\text{eV/cm}^3} \text{s}^{-1} , \tag{C.3}$$

where $w_o = w_B + w_{\text{MBR}} + w_{\text{opt}}$. $w_{\text{MBR}} = 0.25 \text{eV/cm}^3$ is the microwave background radiation energy density, $w_{\text{opt}} = 0.5 \text{eV/cm}^3$ is the optical-IR radiation energy density and $w_B = 0.5 \text{eV/cm}^3$ is energy density of the magnetic field (at $B = 5 \mu \text{G}$).

The diffusion coefficient is:

$$D(\gamma) = D_0(1 + \gamma/\gamma_*)^\delta \,, \tag{C.4}$$

where $D_0 = D_{10}/(1 + \gamma/\gamma_*)^\delta$ for D_{10} defined as the diffusion coefficient at $10\,\mathrm{GeV}$, γ is at $10\,\mathrm{GeV}$ and γ_* is defined at $3\,\mathrm{GeV}$. Figure C.1 shows the electron spectra injected by an impulsive source.
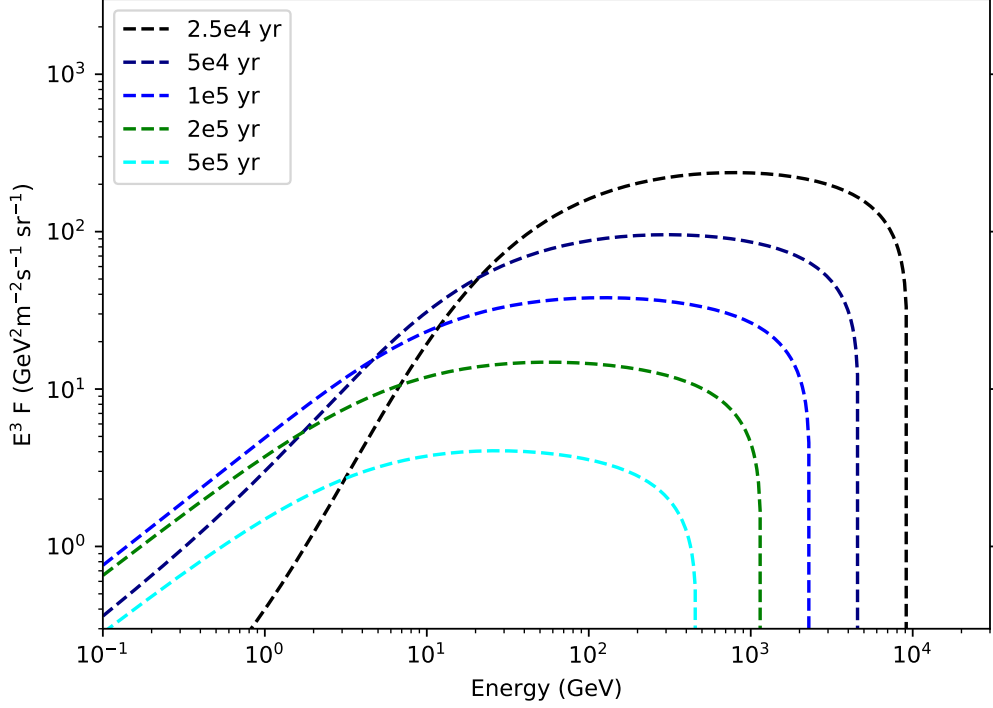
Figure C.1: Modelled energy spectra of CR electrons (Equation C.1) escaping from an impulsive accelerator, with an energy budget of $E_{\mathrm{budget}} = 10^{48}\,\mathrm{erg}$ and power law spectral index of $\alpha = 2.2$. Distance to the source, R, is taken at $100\,\mathrm{pc}$. Index of diffusion coefficient is $\delta = 0.6$. The curves cyan, green, blue, navy and black correspond to the age of the source (t) $5 \times 10^5\,\mathrm{yr}$, $2 \times 10^5\,\mathrm{yr}$, $10^5\,\mathrm{yr}$, $5 \times 10^4\,\mathrm{yr}$ and $2.5 \times 10^4\,\mathrm{yr}$ respectively.

D   H.E.S.S. Analysis

D.1   Prod05 FITS files

The Prod05 FITS files include data from 2004 to 2020 with various cuts on the data. Table D.1 describes the entire available dataset.

Table D.1: The Prod05 FITS file information for different H.E.S.S. phases with their respective dates, run numbers and configuration types.

Phase	Dates	Run Numbers	Configuration	Telescopes
H.E.S.S. I	2004–2013	18361–85392	std_fullEnclosure	CT1-4
			std_zeta_fullEnclosure	CT1-4
			hard_zeta_fullEnclosure	CT1-4
			std_ImPACT_fullEnclosure	CT1-4
H.E.S.S. II	2013–2016	85000–123729	std_fullEnclosure	CT1-4
			std_zeta_fullEnclosure	CT1-4
			hard_zeta_fullEnclosure	CT1-4
			std_ImPACT_fullEnclosure	CT1-4
			std_zeta_hybrid_fullEnclosure	CT1-5
			std_ImPACT_hybrid_fullEnclosure	CT1-5
H.E.S.S. IU	2017–2020	127720–154768	std_zeta_fullEnclosure	CT1-4
			hard_zeta_fullEnclosure	CT1-4
			std_ImPACT_fullEnclosure	CT1-4
			std_zeta_hybrid_fullEnclosure	CT1-5

D.2 `gammapy` Analysis Settings

The analysis settings used for the `gammapy` analysis of the spatial distribution of
HESS J1804−216 is shown in Table D.2. These settings are used to obtain the
results in Section 8.2.3.

Table D.2: The `gammapy` and analysis settings used for the spatial analysis.

Setting	Value
Gammapy version	v0.18.2
Map size	$3.2° \times 3.2°$
Pixel size	0.02°
Maximum event offset	2°
Correlation radius	0.1°
True Energy Axis	0.05 TeV to 20 TeV
Energy bins	0.2, 0.32, 0.43, 0.56, 0.67, 0.95, 1.45, 12 TeV
Analysis Configuration	`std_ImPACT_fullEnclosure`
Energy thresholds	Maximum 10% energy bias at 2° offset
Gammapy Background Method	RingBackgroundMaker
Inner Ring Radius	0.7°
Ring Width	0.44°

The analysis settings used for the `gammapy` analysis of the spectral distribution of
HESS J1804−216 is shown in Table D.3. These settings are used to obtain the results
in Section 8.2.4.

Table D.3: The `gammapy` and analysis settings used for the spectral analysis.

Setting	Value
Gammapy version	v0.18.2
Maximum event offset	2°
True Energy Axis	0.05 TeV to 120 TeV
Reconstructed Energy Axis	0.2 TeV to 100 TeV
Analysis Configuration	`std_ImPACT_fullEnclosure`
Energy thresholds	Maximum 10% energy bias at 2° offset
Gammapy Background Method	ReflectedRegionsBackgroundMaker

D.3   Significance in energy bands

Figure D.1 shows the significance of each energy band is roughly the same, as determined by Equation 8.2.
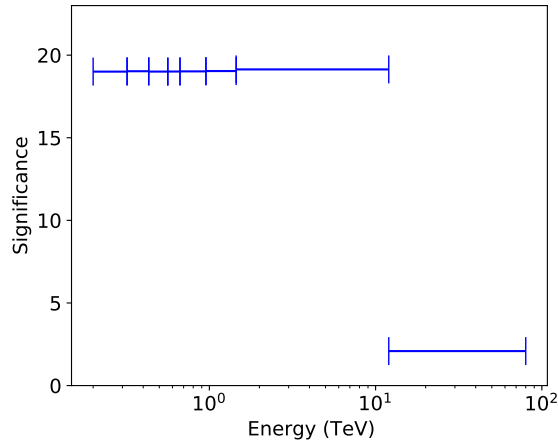
Figure D.1: Significance in each energy band for the H.E.S.S. data analysis performed in this thesis (see Section 8.1.1).

D.4   Spectral Comparison

Figure D.2 shows the spectral comparison between the H.E.S.S. 2006 survey of the inner galaxy (Aharonian et al., 2006c) and the H.E.S.S. data analysis performed in this thesis towards HESS J1804−216. The observations from Aharonian et al., 2006c are between May and July of 2004 with 11.7 hr of observation time. The data used in this analysis was collected from May 2004 until November 2020 with ∼88 hr of observations. The analysis used here provides an extra energy bin at higher energies, which indicates emission to PeV energies.
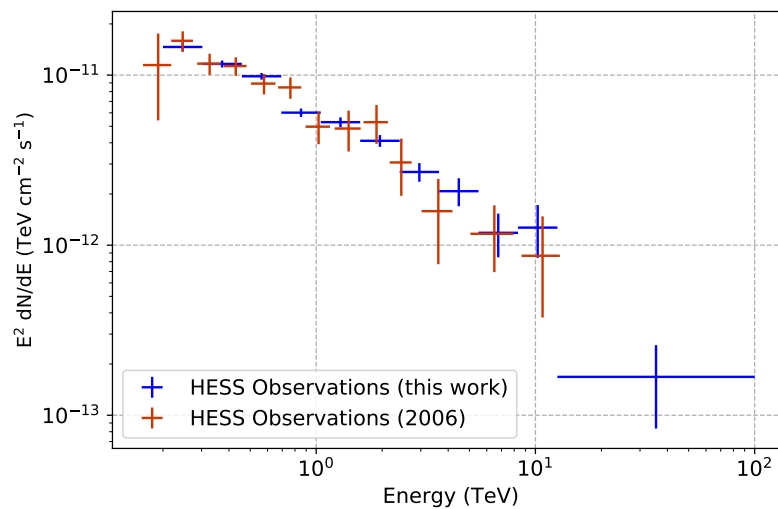
Figure D.2: TeV γ-ray spectra towards HESS J1804−216 from Aharonian et al. (2006c) in red and the data from this analysis shown in blue.

D.5   Gamma-ray Flux Maps

The γ-ray flux maps obtained using the methods described in Section 8.2.3 are shown in Figure D.3 for completeness.
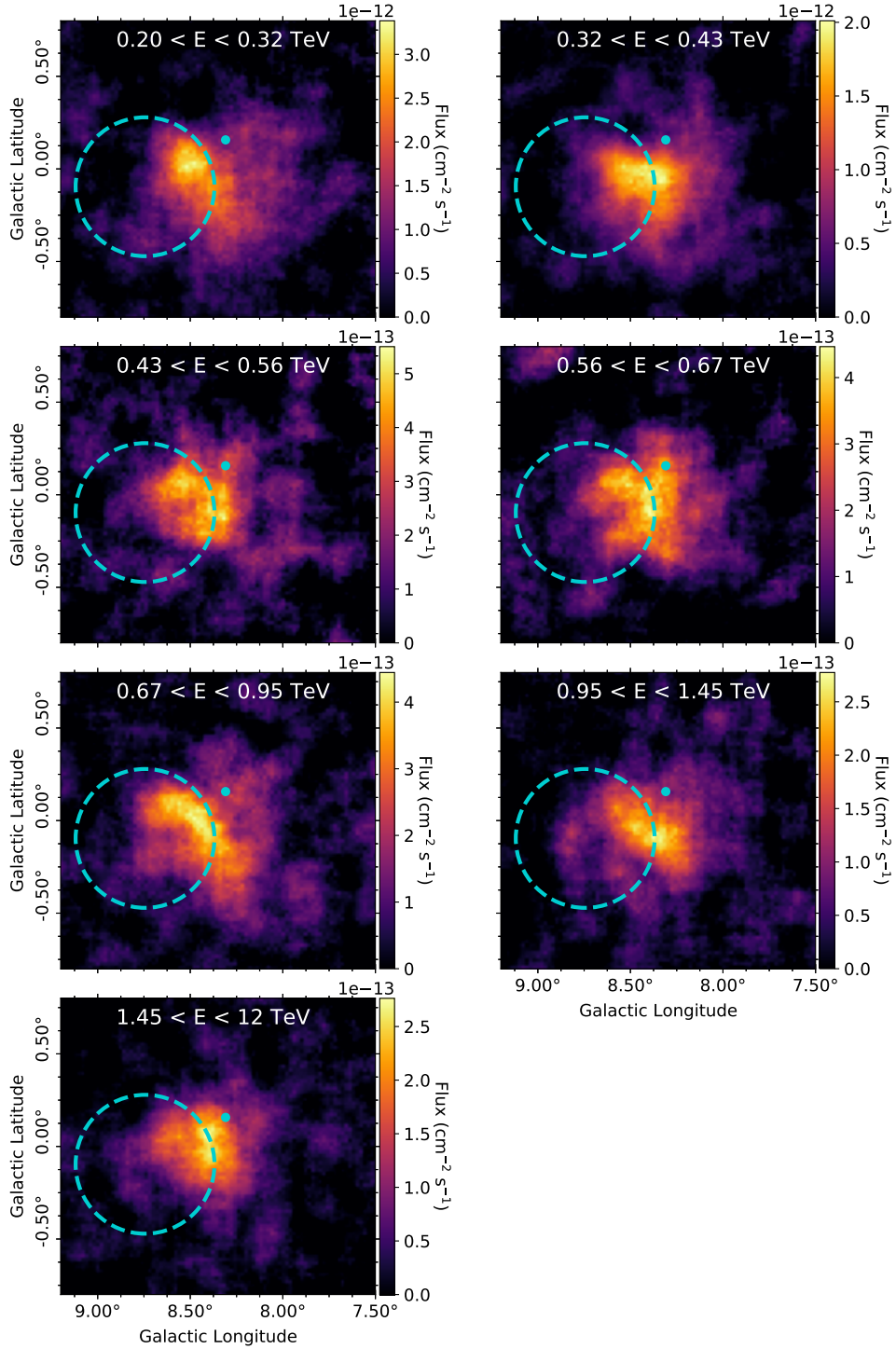
Figure D.3: Gamma-ray flux maps towards HESS J1804−216. The cyan dashed circle indicates SNR G8.7−0.1 and the cyan dot indicates the position of the progenitor SNR of PSR J1803−2137.

D.6   Significance maps

To ensure the exclusion regions are large enough for the analysis, it is important to plot the distribution of significance in both the off bins and all bins. This is to ensure that the background estimation has not been contaminated with γ-ray like events. It is expected that the off-distribution follows a normal distribution. Figure D.4 shows the distribution of significance, in which the off-bins show a clear normal distribution, therefore our exclusion regions are large enough to cover any γ-ray signal.
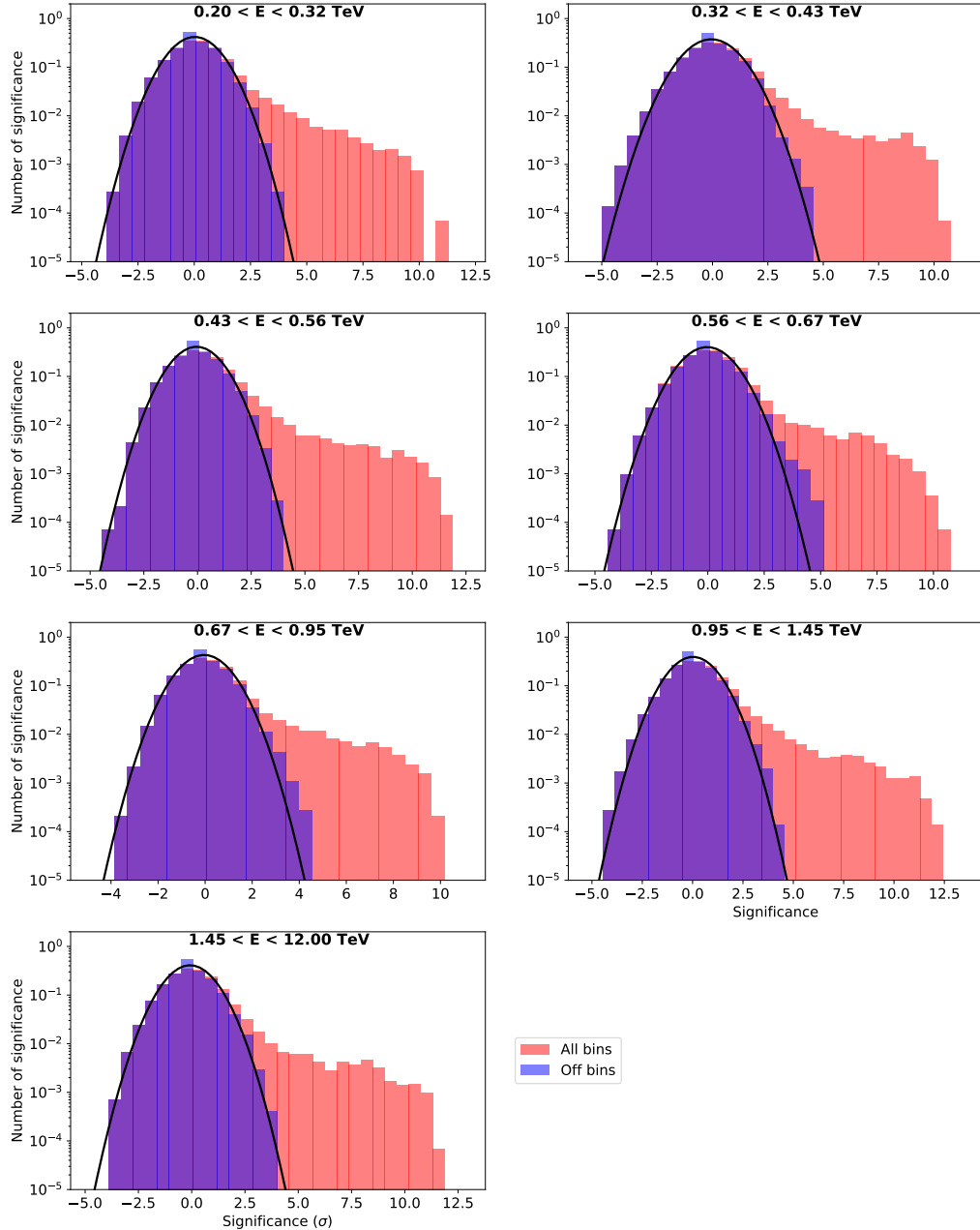
Figure D.4: Significance histogram for each energy band showing the off distribution in purple follows a normal distribution.

D.7   Pulsar Wind Nebula Morphology Example

As discussed in Chapter 8, PWNe are expected to exhibit energy-dependent morphology. At higher energies the emission is expected to the compact and close to the pulsars position, however, at lower energies the emission is extended and offset from the position of the pulsar. An example of this behaviour is shown in Figure D.5.
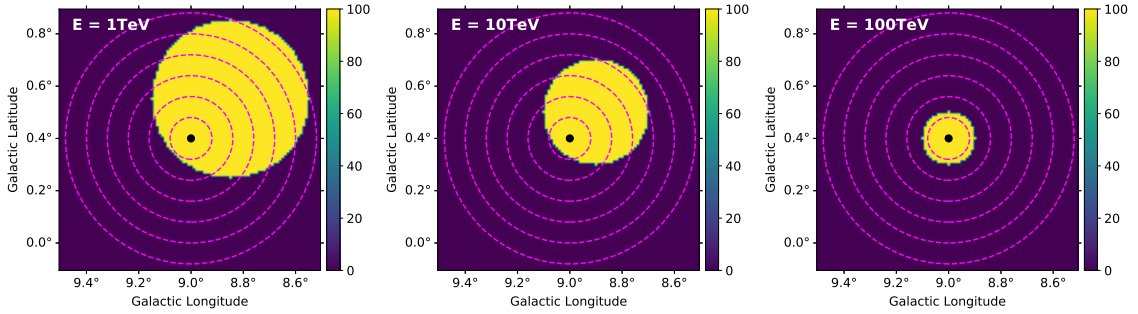
Figure D.5: Example of PWNe scenario with nebula size increasing with decreasing energy.

The radial profiles in Figure D.6 are taken from the concentric rings shown in Figure D.5.
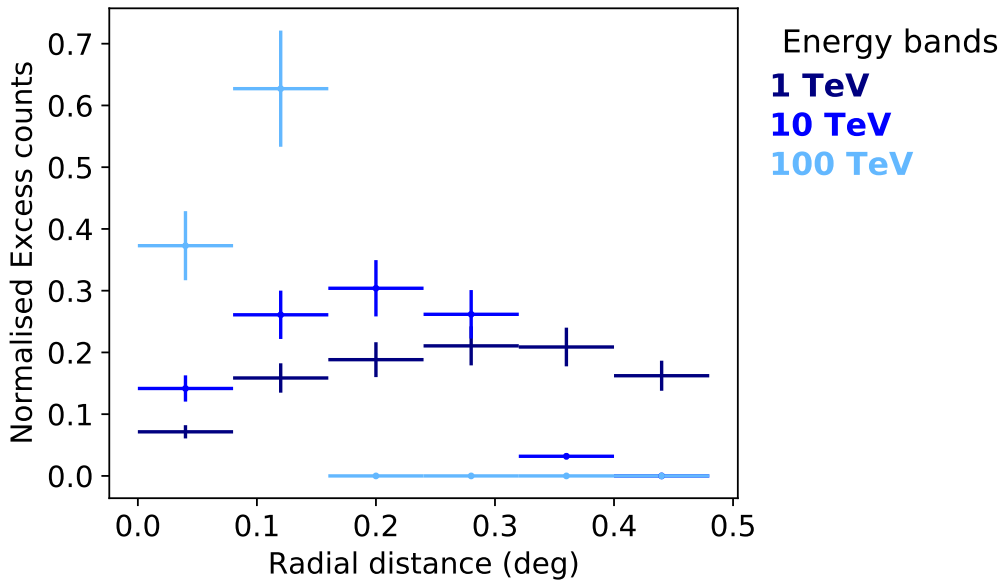
Figure D.6: Radial profiles for an example of PWNe scenario.

D.8   Energy bands for the best matching models

These integrated flux maps from the model are compared with the energy bands defined in Chapter 8 for the H.E.S.S. observations.
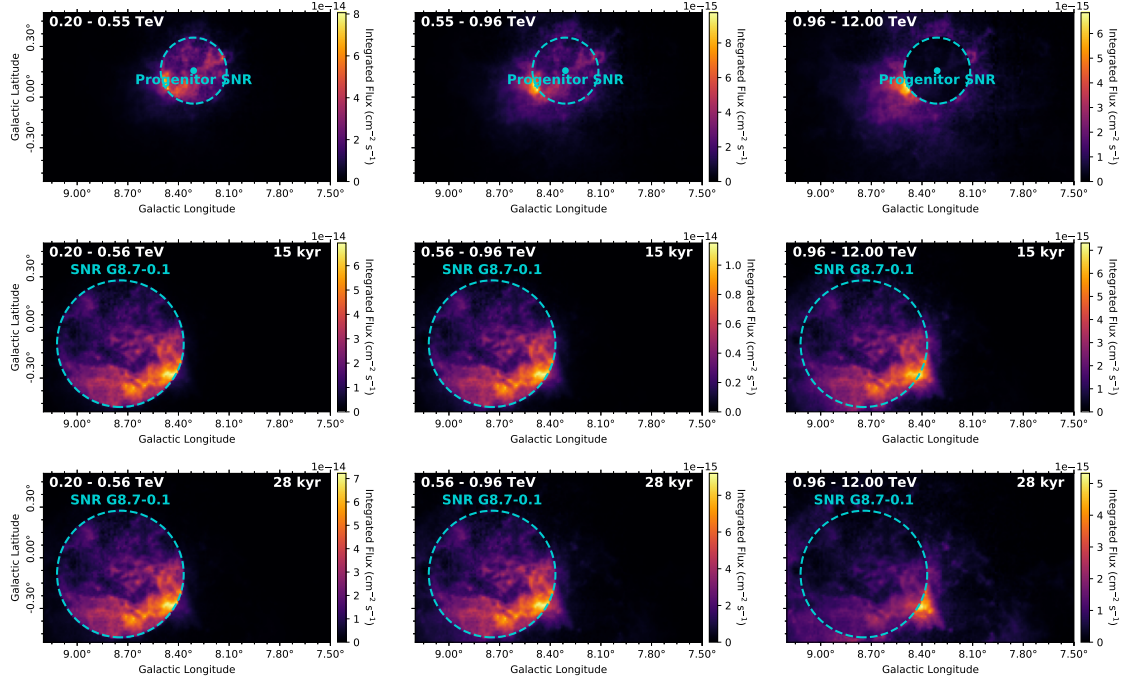
Figure D.7: γ-ray flux map in the different energy bands towards HESS J1804−216 for the best matching spectral and spatial models. *Top*: the best matching model (P1) for the progenitor SNR of PSR J1803−2137. The progenitor SNR of PSR J1803−2137 is indicated by the cyan dot. *Middle*: the best matching model (G4a) for SNR G8.7−0.1 with an age of 15 kyr. *Bottom*: the best matching model (G2b) for SNR G8.7−0.1 with an age of 28 kyr. The escape radius, R_{esc}, is shown by the cyan dashed circle.

D.9   Observations list

The full list of observations used in Chapter 8 for H.E.S.S. I, H.E.S.S. II and H.E.S.S. IU are shown in Tables D.4 to D.6.

Table D.4: Full table of observations for the H.E.S.S. I phase with the `std_ImPACT_fullEnclosure` configuration. `OBS_ID` is the identifier for the observation. The observation time is listed along with the object which the observations are for. The pointing position is given by `GLON_PNT` and `GLAT_PNT`, for the telescopes listed in `TELLIST`.

OBS_ID	Date	Observation Time (min)	Object	GLON_PNT (deg)	GLAT_PNT (deg)	TELLIST
20877	2004-05-21	28.0	G009.9+0.0	9.9	0.0	1,2,3,4
20902	2004-05-22	28.0	G007.8+0.0	7.8	0.0	1,2,3,4
20963	2004-05-25	28.0	G005.0+0.0	5.0	0.0	1,2,3,4
20969	2004-05-25	28.0	G011.3+0.0	11.3	0.0	1,2,3,4
20982	2004-05-26	28.0	G009.2+0.0	9.2	0.0	1,2,3,4
20983	2004-05-26	28.0	G008.5+0.0	8.5	0.0	1,2,3,4
21122	2004-06-11	28.0	G005.7+0.0	5.7	0.0	1,2,3,4
21124	2004-06-11	28.0	G006.4+0.0	6.4	0.0	1,2,3,4
21125	2004-06-11	28.0	G007.1+0.0	7.1	0.0	1,2,3,4
21171	2004-06-14	28.1	G011.3-1.0	11.3	-1.0	1,2,3,4
21183	2004-06-14	28.0	W 28	7.0	-0.5	1,2,3,4
21184	2004-06-14	28.0	W 28	6.5	0.4	1,2,3,4
21185	2004-06-14	10.1	W 28	7.1	0.2	1,2,3,4
21186	2004-06-14	18.0	W 28	7.1	0.2	1,2,3,4
21189	2004-06-14	28.0	W 28	6.3	-0.3	1,2,3,4
21267	2004-06-17	28.0	W 28	6.5	0.4	1,2,3,4
21268	2004-06-17	28.0	W 28	7.0	-0.5	1,2,3,4
21293	2004-06-18	28.0	W 28	7.1	0.2	1,2,3,4
21294	2004-06-18	28.0	W 28	6.3	-0.3	1,2,3,4
21297	2004-06-18	22.0	W 28	6.5	0.4	1,2,3,4
21317	2004-06-19	28.0	W 28	6.3	-0.3	1,2,3,4
21320	2004-06-19	25.0	W 28	7.1	0.2	1,2,3,4
21440	2004-06-26	28.0	G005.7-1.0	5.7	-1.0	1,2,3,4
21529	2004-07-10	28.1	G8.4+0.0	7.9	0.0	1,2,3,4
21530	2004-07-10	28.0	G8.4+0.0	8.9	0.0	1,2,3,4

21534	2004-07-10	28.0	G008.5-1.0	8.5	-1.0	1,2,3,4
21535	2004-07-10	28.0	G007.8+1.0	7.8	1.0	1,2,3,4
21544	2004-07-11	28.0	G8.4+0.0	8.9	0.0	1,2,3,4
21546	2004-07-11	28.0	G8.4+0.0	7.9	0.0	1,2,3,4
21547	2004-07-11	28.0	G8.4+0.0	8.9	0.0	1,2,3,4
21550	2004-07-11	28.0	G009.2-1.0	9.2	-1.0	1,2,3,4
21562	2004-07-12	28.0	G8.4+0.0	7.9	0.0	1,2,3,4
21565	2004-07-12	28.0	G8.4+0.0	8.9	0.0	1,2,3,4
21569	2004-07-12	28.0	G008.5+1.0	8.5	1.0	1,2,3,4
21570	2004-07-12	28.0	G009.9-1.0	9.9	-1.0	1,2,3,4
21585	2004-07-13	28.0	G005.0+0.0	5.0	0.0	1,2,3,4
21586	2004-07-13	28.0	G007.8+0.0	7.8	0.0	1,2,3,4
21587	2004-07-13	28.0	G008.5+0.0	8.5	0.0	1,2,3,4
21588	2004-07-13	28.0	G009.2+0.0	9.2	0.0	1,2,3,4
21600	2004-07-14	28.0	G005.7+0.0	5.7	0.0	1,2,3,4
21601	2004-07-14	25.8	G009.9+0.0	9.9	0.0	1,2,3,4
21602	2004-07-14	28.0	G8.4+0.0	8.4	0.5	1,2,3,4
21603	2004-07-14	28.0	G8.4+0.0	8.4	-0.5	1,2,3,4
21606	2004-07-14	28.0	G8.4+0.0	8.4	-0.5	1,2,3,4
21607	2004-07-14	28.0	G8.4+0.0	8.4	0.5	1,2,3,4
21609	2004-07-14	28.0	G009.9+0.0	9.9	0.0	1,2,3,4
21626	2004-07-15	28.0	G009.2+1.0	9.2	1.0	1,2,3,4
21627	2004-07-15	28.0	G010.6-1.0	10.6	-1.0	1,2,3,4
21628	2004-07-15	28.1	G009.9+1.0	9.9	1.0	1,2,3,4
21651	2004-07-17	28.0	G010.6+1.0	10.6	1.0	1,2,3,4
21696	2004-07-18	17.9	G011.3+1.0	11.3	1.0	1,2,3,4
22354	2004-09-08	28.0	G8.4+0.0	8.4	0.5	1,2,3,4
22355	2004-09-08	28.0	G8.4+0.0	8.4	-0.5	1,2,3,4
22372	2004-09-09	28.0	G8.4+0.0	7.9	0.0	1,2,3,4
22373	2004-09-09	23.9	G8.4+0.0	8.9	0.0	1,2,3,4
22387	2004-09-10	25.7	G8.4+0.0	8.9	0.0	1,2,3,4
26155	2005-06-07	28.2	J1809-193	11.7	0.3	1,2,3,4
26156	2005-06-07	28.2	J1809-193	10.4	-0.3	1,2,3,4
26202	2005-06-09	28.2	J1809-193	11.4	-0.6	1,2,3,4
26235	2005-06-10	28.2	J1809-193	10.4	-0.3	1,2,3,4

26236	2005-06-10	28.2	J1809-193	11.7	0.3	1,2,3,4
26419	2005-06-14	28.2	J1809-193	10.4	-0.3	1,2,3,4
26420	2005-06-14	28.2	J1809-193	11.7	0.3	1,2,3,4
26932	2005-07-03	28.3	J1809-193	11.4	-0.6	1,2,3,4
26933	2005-07-03	28.2	J1809-193	10.7	0.6	1,2,3,4
26961	2005-07-04	28.2	J1809-193	10.4	-0.3	1,2,3,4
26962	2005-07-04	28.2	J1809-193	11.7	0.3	1,2,3,4
31622	2006-05-02	28.2	W28 HS midway	6.0	0.2	1,3,4
31623	2006-05-02	28.1	W28 HS midway	6.7	-1.0	1,2,3,4
31624	2006-05-02	28.1	W28 HS midway	6.0	0.2	1,2,3,4
31625	2006-05-02	28.1	W28 HS midway	6.7	-1.0	1,2,3,4
31670	2006-05-03	28.1	W28 HS midway	6.0	0.2	1,3,4
31671	2006-05-03	28.2	W28 HS midway	6.7	-1.0	1,2,3,4
31672	2006-05-03	28.1	W28 HS midway	6.0	0.2	1,2,3,4
31673	2006-05-03	17.2	W28 HS midway	6.7	-1.0	1,2,3,4
31701	2006-05-04	28.1	W28 HS midway	6.0	0.2	1,2,3,4
31702	2006-05-04	28.2	W28 HS midway	6.7	-1.0	1,2,3,4
31703	2006-05-04	28.2	W28 HS midway	6.0	0.2	1,2,3,4
31704	2006-05-04	28.1	W28 HS midway	6.7	-1.0	1,2,3,4
31705	2006-05-04	13.8	W28 HS midway	6.0	0.2	1,2,3,4
31727	2006-05-05	28.2	W28 HS midway	6.0	0.2	1,2,3,4
31728	2006-05-05	28.2	W28 HS midway	6.7	-1.0	1,2,3,4
31729	2006-05-05	28.1	W28 HS midway	6.0	0.2	1,2,3,4
31730	2006-05-05	28.1	W28 HS midway	6.7	-1.0	1,2,3,4
31731	2006-05-05	23.1	W28 HS midway	6.0	0.2	1,2,3,4
31757	2006-05-06	28.1	W28 HS midway	6.7	-1.0	1,2,3,4
31786	2006-05-07	28.2	W28 HS midway	6.0	0.2	1,2,3,4
31787	2006-05-07	28.2	W28 HS midway	6.7	-1.0	1,2,3,4
31788	2006-05-07	28.2	W28 HS midway	6.0	0.2	1,2,3,4
31789	2006-05-07	28.1	W28 HS midway	6.7	-1.0	1,2,3,4
31790	2006-05-07	28.1	W28 HS midway	6.0	0.2	1,2,3,4
31801	2006-05-08	28.1	W28 HS midway	6.0	0.2	1,2,3,4
31802	2006-05-08	28.2	W28 HS midway	6.7	-1.0	1,2,3,4
31803	2006-05-08	28.2	W28 HS midway	6.0	0.2	1,2,3,4
31804	2006-05-08	16.1	W28 HS midway	6.7	-1.0	1,2,3,4

31839	2006-05-09	28.2	W28 HS midway	6.7	-1.0	1,2,3,4
31840	2006-05-09	28.1	W28 HS midway	6.0	0.2	1,2,3,4
31841	2006-05-09	28.1	W28 HS midway	6.7	-1.0	1,2,3,4
31842	2006-05-09	28.1	W28 HS midway	6.0	0.2	1,2,3,4
31897	2006-05-10	24.9	W 28	7.0	-0.5	1,2,3,4
32257	2006-05-21	28.1	W28 HS midway	6.7	-1.0	1,2,3
32258	2006-05-21	28.2	W28 HS midway	6.0	0.2	1,2,3
32259	2006-05-21	28.1	W28 HS midway	6.7	-1.0	1,2,3
32260	2006-05-21	28.2	W28 HS midway	6.0	0.2	1,2,3
32261	2006-05-21	26.3	W28 HS midway	6.7	-1.0	1,2,3
32290	2006-05-22	28.1	W28 HS midway	6.0	0.2	1,2,3
32291	2006-05-22	28.2	W28 HS midway	6.7	-1.0	1,2,3
32292	2006-05-22	28.2	W28 HS midway	6.0	0.2	1,2,3
32293	2006-05-22	28.2	W28 HS midway	6.7	-1.0	1,2,3
32321	2006-05-23	28.1	W28 HS midway	6.0	0.2	1,2,3,4
32323	2006-05-23	28.2	W28 HS midway	6.0	0.2	1,2,3,4
32324	2006-05-23	28.1	W28 HS midway	6.7	-1.0	1,2,3,4
32325	2006-05-23	28.2	W28 HS midway	6.7	-1.0	1,2,3,4
32330	2006-05-24	28.1	W28 HS midway	6.0	0.2	1,2,3,4
32331	2006-05-24	28.2	W28 HS midway	6.7	-1.0	1,2,3,4
32384	2006-05-26	28.2	W28 HS midway	6.0	0.2	1,2,3,4
33520	2006-07-18	28.2	J18100-1920	11.8	-0.0	1,2,3,4
33537	2006-07-19	28.2	J18100-1920	11.1	-0.7	1,2,3,4
33538	2006-07-19	28.2	J18100-1920	11.1	0.7	1,2,3,4
33560	2006-07-20	28.2	J18100-1920	11.1	0.7	1,2,3,4
33561	2006-07-20	28.2	J18100-1920	11.1	-0.7	1,2,3,4
33562	2006-07-20	28.2	J18100-1920	11.8	-0.0	1,2,3,4
33563	2006-07-20	28.1	J18100-1920	10.4	-0.0	1,2,3,4
33564	2006-07-20	28.2	J18100-1920	11.1	0.7	1,2,3,4
33580	2006-07-21	28.2	J18100-1920	10.4	-0.0	1,2,3,4
33581	2006-07-21	28.2	J18100-1920	11.8	-0.0	1,2,3,4
33582	2006-07-21	28.2	J18100-1920	11.1	-0.7	1,2,3,4
33583	2006-07-21	28.1	J18100-1920	11.1	0.7	1,2,3,4
33584	2006-07-21	28.1	J18100-1920	10.4	-0.0	1,2,3,4
33605	2006-07-22	28.2	J18100-1920	11.8	-0.0	1,2,3,4

33606	2006-07-22	28.1	J18100-1920	10.4	-0.0	1,2,3,4
33607	2006-07-22	28.2	J18100-1920	11.1	0.7	1,2,3,4
33629	2006-07-23	28.2	J18100-1920	11.1	-0.7	1,2,3,4
33630	2006-07-23	13.1	J18100-1920	11.1	0.7	1,2,3,4
33631	2006-07-23	28.1	J18100-1920	11.1	-0.7	1,2,3,4
33632	2006-07-23	28.2	J18100-1920	11.1	0.7	1,2,3,4
33633	2006-07-23	28.2	J18100-1920	10.4	-0.0	1,2,3,4
33656	2006-07-24	28.1	J18100-1920	11.1	0.7	1,2,3,4
33657	2006-07-24	28.2	J18100-1920	11.1	-0.7	1,2,3,4
33659	2006-07-24	28.1	J18100-1920	11.1	0.7	1,2,3,4
33660	2006-07-24	28.2	J18100-1920	11.1	-0.7	1,2,3,4
33685	2006-07-25	28.2	J18100-1920	10.4	-0.0	1,2,3,4
33686	2006-07-25	28.1	J18100-1920	11.8	-0.0	1,2,3,4
33687	2006-07-25	28.2	J18100-1920	11.1	-0.7	1,2,3,4
33688	2006-07-25	28.2	J18100-1920	11.1	0.7	1,2,3,4
33689	2006-07-25	28.1	J18100-1920	10.4	-0.0	1,2,3,4
33690	2006-07-25	28.1	J18100-1920	11.8	-0.0	1,2,3,4
41320	2007-08-30	28.1	HESS J1809-193	11.3	-0.5	1,2,3,4
41347	2007-08-31	28.2	HESS J1809-193	10.6	0.7	1,2,3,4
41348	2007-08-31	28.2	HESS J1809-193	11.5	0.4	1,2,3,4
41370	2007-09-01	28.2	HESS J1809-193	10.3	-0.3	1,2,3,4
41403	2007-09-02	22.3	HESS J1809-193	11.3	-0.5	1,2,3,4
41421	2007-09-03	28.2	HESS J1809-193	10.6	0.7	1,2,3,4
41442	2007-09-04	28.1	HESS J1809-193	11.5	0.4	1,2,3,4
41443	2007-09-04	28.2	HESS J1809-193	10.3	-0.3	1,2,3,4
41463	2007-09-05	28.1	HESS J1809-193	11.3	-0.5	1,2,3,4
41464	2007-09-05	28.1	HESS J1809-193	10.6	0.7	1,2,3,4
41487	2007-09-06	28.2	HESS J1809-193	11.5	0.4	1,2,3,4
41488	2007-09-06	28.2	HESS J1809-193	10.3	-0.3	1,2,3,4
41513	2007-09-07	28.1	HESS J1809-193	11.3	-0.5	1,2,3,4
41540	2007-09-08	28.2	HESS J1809-193	10.6	0.7	1,2,3,4
41541	2007-09-08	28.1	HESS J1809-193	11.5	0.4	1,2,3,4
41935	2007-09-29	28.2	HESS J1809-193	10.3	-0.3	1,2,3,4
41954	2007-09-30	28.1	HESS J1809-193	11.5	0.4	1,2,3,4
41955	2007-09-30	28.2	HESS J1809-193	10.6	0.7	1,2,3,4

41975	2007-10-01	28.1	HESS J1809-193	11.3	-0.5	1,2,3,4
41976	2007-10-01	28.1	HESS J1809-193	11.5	0.4	1,2,3,4
41992	2007-10-02	28.1	HESS J1809-193	10.3	-0.3	1,2,3,4
41993	2007-10-02	28.2	HESS J1809-193	11.3	-0.5	1,3,4
42076	2007-10-04	28.1	HESS J1809-193	10.6	0.7	1,2,3,4
42077	2007-10-04	28.1	HESS J1809-193	11.5	0.4	1,2,3,4
42117	2007-10-05	28.1	HESS J1809-193	10.3	-0.3	1,2,3,4
42147	2007-10-06	28.2	HESS J1809-193	11.3	-0.5	1,2,3,4
42170	2007-10-07	28.1	HESS J1809-193	10.6	0.7	1,2,3,4
42210	2007-10-08	28.2	HESS J1809-193	11.5	0.4	1,2,3,4
42237	2007-10-09	28.1	HESS J1809-193	10.3	-0.3	1,2,3,4
52498	2009-07-18	28.1	SGR 1806-20	10.3	-0.9	1,2,3,4
52530	2009-07-19	28.2	SGR 1806-20	9.7	0.4	1,2,3,4
52552	2009-07-20	28.1	SGR 1806-20	10.6	0.1	1,2,3,4
52555	2009-07-20	28.1	SGR 1806-20	9.4	-0.6	1,2,3,4
52578	2009-07-21	28.2	SGR 1806-20	10.3	-0.9	1,2,3,4
52579	2009-07-21	28.2	SGR 1806-20	9.7	0.4	1,2,3,4
52580	2009-07-21	28.2	SGR 1806-20	10.6	0.1	1,2,3,4
52599	2009-07-22	28.1	SGR 1806-20	9.4	-0.6	1,2,3
52604	2009-07-22	28.1	SGR 1806-20	10.3	-0.9	1,2,3,4
52628	2009-07-23	28.1	SGR 1806-20	9.7	0.4	1,2,3,4
52629	2009-07-23	28.2	SGR 1806-20	10.6	0.1	1,2,3,4
52654	2009-07-24	28.1	SGR 1806-20	9.4	-0.6	1,2,3,4
52655	2009-07-24	28.1	SGR 1806-20	10.3	-0.9	1,2,3,4
52656	2009-07-24	28.2	SGR 1806-20	9.7	0.4	1,2,3,4
52675	2009-07-25	28.1	SGR 1806-20	10.6	0.1	1,2,3
52676	2009-07-25	28.2	SGR 1806-20	9.4	-0.6	1,2,3,4
52698	2009-07-26	28.1	SGR 1806-20	10.3	-0.9	1,2,3,4
52699	2009-07-26	28.1	SGR 1806-20	9.7	0.4	1,2,3,4
52700	2009-07-26	28.1	SGR 1806-20	10.6	0.1	1,2,3,4
52716	2009-07-27	28.2	SGR 1806-20	10.3	-0.9	1,3,4
52718	2009-07-27	28.2	SGR 1806-20	9.4	-0.6	1,2,3,4
52954	2009-08-11	28.2	SGR 1806-20	10.3	-0.9	1,2,3,4
52955	2009-08-11	28.2	SGR 1806-20	9.7	0.4	1,2,3,4
52956	2009-08-11	28.1	SGR 1806-20	10.6	0.1	1,2,3,4

52968	2009-08-12	28.2	SGR 1806-20	9.4	-0.6	1,2,3,4
52969	2009-08-12	28.1	SGR 1806-20	10.3	-0.9	1,2,3,4
52970	2009-08-12	28.2	SGR 1806-20	9.7	0.4	1,2,3,4
53008	2009-08-13	28.2	SGR 1806-20	10.6	0.1	1,2,3,4
53009	2009-08-13	28.1	SGR 1806-20	9.4	-0.6	1,2,3,4
53010	2009-08-13	28.2	SGR 1806-20	10.3	-0.9	1,2,3,4
53026	2009-08-14	28.1	SGR 1806-20	9.7	0.4	1,2,3,4
53027	2009-08-14	28.1	SGR 1806-20	10.6	0.1	1,2,3,4
53028	2009-08-14	28.1	SGR 1806-20	9.4	-0.6	1,2,3,4
53048	2009-08-15	28.2	SGR 1806-20	10.3	-0.9	1,2,3,4
53074	2009-08-16	28.1	SGR 1806-20	10.3	-0.9	1,2,3,4
53075	2009-08-16	28.2	SGR 1806-20	9.7	0.4	1,2,3,4
53076	2009-08-16	28.1	SGR 1806-20	10.6	0.1	1,2,3,4
53098	2009-08-17	28.1	SGR 1806-20	9.4	-0.6	1,2,3,4
53100	2009-08-17	28.1	SGR 1806-20	9.4	-0.6	1,2,3,4
53125	2009-08-18	28.1	SGR 1806-20	10.3	-0.9	1,2,3,4
53126	2009-08-18	28.1	SGR 1806-20	9.7	0.4	1,2,3,4
53146	2009-08-19	28.1	SGR 1806-20	10.6	0.1	1,2,3,4
53175	2009-08-20	28.1	SGR 1806-20	9.4	-0.6	1,2,3,4
53206	2009-08-21	28.1	SGR 1806-20	10.3	-0.9	1,2,3,4
53228	2009-08-22	28.2	SGR 1806-20	9.7	0.4	1,2,3,4
58082	2010-06-05	28.1	SGR 1806-20	10.6	0.1	1,2,3,4
58121	2010-06-06	28.2	SGR 1806-20	9.4	-0.6	1,2,3,4
58122	2010-06-06	25.1	SGR 1806-20	10.3	-0.9	1,2,3,4
58145	2010-06-07	28.2	SGR 1806-20	9.7	0.4	1,2,3,4
58146	2010-06-07	28.2	SGR 1806-20	10.6	0.1	1,2,3,4
58147	2010-06-08	28.1	SGR 1806-20	10.3	-0.9	1,2,3,4
58167	2010-06-08	28.2	SGR 1806-20	9.7	0.4	1,2,3,4
58168	2010-06-08	28.1	SGR 1806-20	9.4	-0.6	1,2,3,4
58169	2010-06-09	28.2	SGR 1806-20	10.6	0.1	1,2,3,4
58197	2010-06-09	28.2	SGR 1806-20	10.3	-0.9	1,2,3,4
58198	2010-06-09	28.1	SGR 1806-20	9.7	0.4	1,2,3,4
58223	2010-06-10	28.1	SGR 1806-20	9.4	-0.6	1,2,3,4
58224	2010-06-10	28.1	SGR 1806-20	10.6	0.1	1,2,3,4
58256	2010-06-11	10.3	SGR 1806-20	10.3	-0.9	1,2,3,4

58257	2010-06-11	28.1	SGR 1806-20	10.3	-0.9	1,2,3,4
58258	2010-06-12	28.1	SGR 1806-20	9.7	0.4	1,2,3,4
58286	2010-06-12	28.1	SGR 1806-20	9.4	-0.6	1,2,3,4
58287	2010-06-12	28.2	SGR 1806-20	10.6	0.1	1,2,3,4
58288	2010-06-12	28.2	SGR 1806-20	10.3	-0.9	1,2,3,4
58290	2010-06-13	28.1	SGR 1806-20	9.7	0.4	1,2,3,4
58315	2010-06-13	28.1	SGR 1806-20	9.4	-0.6	1,2,3,4
58316	2010-06-13	28.2	SGR 1806-20	10.6	0.1	1,2,3,4
58317	2010-06-13	28.1	SGR 1806-20	10.3	-0.9	1,2,3,4
58318	2010-06-14	28.2	SGR 1806-20	9.7	0.4	1,2,3,4
58319	2010-06-14	28.1	SGR 1806-20	9.4	-0.6	1,2,3,4
58348	2010-06-14	28.2	SGR 1806-20	10.6	0.1	1,2,3,4
58349	2010-06-14	28.2	SGR 1806-20	10.3	-0.9	1,2,3,4
58350	2010-06-14	28.2	SGR 1806-20	9.7	0.4	1,2,3,4
58351	2010-06-15	28.1	SGR 1806-20	9.4	-0.6	1,2,3,4
58352	2010-06-15	28.2	SGR 1806-20	10.6	0.1	1,2,3,4
58373	2010-06-15	28.2	SGR 1806-20	10.3	-0.9	1,2,3,4
58374	2010-06-15	28.1	SGR 1806-20	9.7	0.4	1,2,3,4
58375	2010-06-15	28.2	SGR 1806-20	9.4	-0.6	1,2,3,4
58376	2010-06-16	28.1	SGR 1806-20	10.6	0.1	1,2,3,4
58377	2010-06-16	28.1	SGR 1806-20	10.3	-0.9	1,2,3,4
58396	2010-06-16	28.1	SGR 1806-20	9.7	0.4	1,2,3,4
58397	2010-06-16	28.1	SGR 1806-20	9.4	-0.6	1,2,3,4
58398	2010-06-16	28.1	SGR 1806-20	10.6	0.1	1,2,3,4
58399	2010-06-17	28.1	SGR 1806-20	10.3	-0.9	1,2,3,4
58423	2010-06-17	28.1	SGR 1806-20	9.7	0.4	1,2,3,4
58448	2010-06-18	28.1	SGR 1806-20	9.4	-0.6	1,2,3,4
58450	2010-06-18	28.1	SGR 1806-20	10.6	0.1	1,2,3,4
58467	2010-06-19	28.2	SGR 1806-20	10.3	-0.9	1,2,3,4
59206	2010-07-30	28.1	SGR 1806-20	9.4	-0.6	1,2,3,4
59223	2010-07-31	28.1	SGR 1806-20	10.6	0.1	1,2,3,4
59224	2010-07-31	28.2	SGR 1806-20	9.7	0.4	1,2,3,4
59225	2010-07-31	28.1	SGR 1806-20	10.3	-0.9	1,2,3,4
59226	2010-07-31	13.1	SGR 1806-20	9.4	-0.6	1,2,3,4
59237	2010-08-01	28.1	SGR 1806-20	9.4	-0.6	1,2,3,4

59238	2010-08-01	28.1	SGR 1806-20	10.6	0.1	1,2,3,4
59239	2010-08-01	27.8	SGR 1806-20	9.7	0.4	1,2,3,4
59240	2010-08-01	28.2	SGR 1806-20	10.3	-0.9	1,2,3,4
59255	2010-08-02	28.1	SGR 1806-20	9.4	-0.6	1,2,3,4
59256	2010-08-02	28.2	SGR 1806-20	10.6	0.1	1,2,3,4
59257	2010-08-02	28.1	SGR 1806-20	9.7	0.4	1,2,3,4
59258	2010-08-02	28.2	SGR 1806-20	10.3	-0.9	1,2,3,4
59272	2010-08-03	28.1	SGR 1806-20	9.4	-0.6	1,2,3,4
59273	2010-08-03	28.1	SGR 1806-20	10.6	0.1	1,2,3,4
59274	2010-08-03	28.1	SGR 1806-20	9.7	0.4	1,2,3,4
59275	2010-08-03	28.2	SGR 1806-20	10.3	-0.9	1,2,3,4
59297	2010-08-04	28.2	SGR 1806-20	9.4	-0.6	1,2,4
59298	2010-08-04	28.2	SGR 1806-20	10.6	0.1	1,2,3,4
59299	2010-08-04	28.1	SGR 1806-20	9.7	0.4	1,2,3,4
59300	2010-08-04	28.2	SGR 1806-20	10.3	-0.9	1,2,3,4
59301	2010-08-04	28.2	SGR 1806-20	9.4	-0.6	1,2,3,4
59320	2010-08-05	28.2	SGR 1806-20	10.6	0.1	1,2,3,4
59321	2010-08-05	28.2	SGR 1806-20	9.7	0.4	1,2,3,4
59322	2010-08-05	28.1	SGR 1806-20	10.3	-0.9	1,2,3,4
59345	2010-08-06	28.1	SGR 1806-20	9.4	-0.6	1,2,3,4
59346	2010-08-06	28.2	SGR 1806-20	10.6	0.1	1,2,3,4
59347	2010-08-06	28.2	SGR 1806-20	9.7	0.4	1,2,3,4
59348	2010-08-06	28.1	SGR 1806-20	10.3	-0.9	1,2,3,4
59369	2010-08-07	28.2	SGR 1806-20	9.4	-0.6	1,2,3,4
59376	2010-08-07	28.2	SGR 1806-20	10.6	0.1	1,2,3,4
59403	2010-08-08	28.1	SGR 1806-20	9.7	0.4	1,2,3,4
59404	2010-08-08	28.1	SGR 1806-20	10.3	-0.9	1,2,3,4
59405	2010-08-08	28.1	SGR 1806-20	9.4	-0.6	1,2,3,4
59427	2010-08-09	28.2	SGR 1806-20	9.7	0.4	1,2,3,4
59428	2010-08-09	28.1	SGR 1806-20	10.3	-0.9	1,2,3,4
59429	2010-08-09	28.1	SGR 1806-20	9.4	-0.6	1,2,3,4
59430	2010-08-09	28.1	SGR 1806-20	10.6	0.1	1,2,3,4
59431	2010-08-09	28.1	SGR 1806-20	9.7	0.4	1,2,3,4
59432	2010-08-09	28.1	SGR 1806-20	10.3	-0.9	1,2,4
59433	2010-08-09	28.1	SGR 1806-20	9.4	-0.6	1,2,3,4

59434	2010-08-09	28.1	SGR 1806-20	10.6	0.1	1,2,3,4
59435	2010-08-09	28.2	SGR 1806-20	9.7	0.4	1,2,3,4
59436	2010-08-09	28.1	SGR 1806-20	10.3	-0.9	1,2,3,4
59456	2010-08-10	28.1	SGR 1806-20	10.6	0.1	1,2,3,4
59457	2010-08-10	28.1	SGR 1806-20	9.4	-0.6	1,2,3,4
59483	2010-08-11	28.1	SGR 1806-20	10.3	-0.9	1,2,3,4
59513	2010-08-12	28.2	SGR 1806-20	9.7	0.4	1,2,3,4

Table D.5: Full table of observations for the H.E.S.S. II phase with the `std_ImPACT_fullEnclosure` configuration. `OBS_ID` is the identifier for the observation. The observation time is listed along with the object which the observations are for. The pointing position is given by `GLON_PNT` and `GLAT_PNT`, for the telescopes listed in `TELLIST`.

`OBS_ID`	Date	Observation Time (min)	Object	`GLON_PNT` (deg)	`GLAT_PNT` (deg)	`TELLIST`
86512	2013-07-13	28.0	FermiPSR J1809-2332	7.6	-2.4	1,2,3,4
86513	2013-07-13	28.0	FermiPSR J1809-2332	7.2	-1.6	1,2,3,4
86514	2013-07-13	28.0	FermiPSR J1809-2332	7.8	-1.8	1,2,3,4
86917	2013-07-26	25.2	FermiPSR J1809-2332	7.0	-2.2	1,2,3,4
86965	2013-07-28	28.0	FermiPSR J1809-2332	7.8	-1.8	1,2,3,4
86966	2013-07-28	28.0	FermiPSR J1809-2332	7.2	-1.6	1,2,3,4
86967	2013-07-28	28.0	FermiPSR J1809-2332	7.6	-2.4	1,2,3,4
87056	2013-07-31	28.0	FermiPSR J1809-2332	7.0	-2.2	1,2,3,4
87057	2013-07-31	28.0	FermiPSR J1809-2332	7.8	-1.8	1,2,3,4
87058	2013-07-31	17.4	FermiPSR J1809-2332	7.2	-1.6	1,2,3,4
87080	2013-08-01	28.0	FermiPSR J1809-2332	7.6	-2.4	1,2,3,4
87081	2013-08-01	28.0	FermiPSR J1809-2332	7.0	-2.2	1,2,3,4
87118	2013-08-02	28.0	FermiPSR J1809-2332	7.2	-1.6	1,2,3,4
87119	2013-08-02	28.0	FermiPSR J1809-2332	7.6	-2.4	1,2,3,4
87120	2013-08-02	18.8	FermiPSR J1809-2332	7.8	-1.8	1,2,3,4
87149	2013-08-03	28.0	FermiPSR J1809-2332	7.8	-1.8	1,2,3,4
87150	2013-08-03	28.0	FermiPSR J1809-2332	7.2	-1.6	1,2,3,4
87151	2013-08-03	28.0	FermiPSR J1809-2332	7.6	-2.4	1,2,3,4
87191	2013-08-04	28.0	FermiPSR J1809-2332	7.0	-2.2	1,2,3,4

87192	2013-08-04	28.0	FermiPSR J1809-2332	7.8	-1.8	1,2,3,4
87343	2013-08-08	28.0	FermiPSR J1809-2332	7.2	-1.6	1,2,3,4
87846	2013-08-24	18.1	FermiPSR J1809-2332	7.8	-1.8	1,3,4
87847	2013-08-24	28.0	FermiPSR J1809-2332	7.0	-2.2	1,2,3,4
87893	2013-08-25	28.0	FermiPSR J1809-2332	7.6	-2.4	1,2,3,4
87926	2013-08-26	15.4	FermiPSR J1809-2332	7.2	-1.6	1,2,3,4
87927	2013-08-26	28.0	FermiPSR J1809-2332	7.8	-1.8	1,2,3,4
88032	2013-08-28	28.0	FermiPSR J1809-2332	7.2	-1.6	1,3,4
88033	2013-08-28	28.0	FermiPSR J1809-2332	7.6	-2.4	1,2,3,4
88230	2013-09-01	28.0	FermiPSR J1809-2332	7.0	-2.2	1,2,3,4
88231	2013-09-01	28.0	FermiPSR J1809-2332	7.8	-1.8	1,2,3,4
89005	2013-09-21	28.1	FermiPSR J1809-2332	7.8	-1.8	1,2,3,4
89030	2013-09-22	18.0	FermiPSR J1809-2332	7.0	-2.2	1,2,3,4
89031	2013-09-22	28.0	FermiPSR J1809-2332	7.6	-2.4	1,2,3,4
89038	2013-09-22	21.9	FermiPSR J1809-2332	7.2	-1.6	1,2,3,4
96233	2014-06-24	28.0	HESS J1804-216	7.8	-0.4	1,2,3,4
96320	2014-06-26	11.9	HESS J1804-216	9.0	0.3	1,2,3
96400	2014-06-28	28.0	HESS J1804-216	9.0	0.3	1,2,3,4
96468	2014-06-30	27.6	HESS J1804-216	8.1	0.6	1,2,3,4
96498	2014-07-01	28.0	HESS J1804-216	8.7	-0.6	1,2,3,4
97173	2014-07-22	28.0	HESS J1804-216	9.0	0.3	1,2,3,4
97483	2014-07-29	28.0	NGC 6440	8.1	3.2	1,2,3,4
97616	2014-08-03	27.4	HESS J1804-216	7.8	-0.4	1,2,3,4
98298	2014-08-24	28.0	HESS J1804-216	8.1	0.6	1,2,3,4
98299	2014-08-24	28.0	HESS J1804-216	8.7	-0.6	1,2,3,4
98439	2014-08-27	14.9	HESS J1804-216	7.8	-0.4	1,2,3,4
99135	2014-09-10	16.7	NGC 6440	8.1	3.2	2,3,4
99174	2014-09-11	28.0	HESS J1804-216	7.8	-0.4	2,3,4
99190	2014-09-11	28.0	HESS J1804-216	9.0	0.3	1,2,3,4
99203	2014-09-11	21.7	HESS J1804-216	8.1	0.6	1,2,3,4
99406	2014-09-17	28.0	HESS J1804-216	8.7	-0.6	2,3,4
99567	2014-09-20	24.9	HESS J1804-216	7.8	-0.4	2,3,4
99685	2014-09-25	18.7	NGC 6440	8.1	3.2	2,3,4
100043	2014-10-11	28.0	HESS J1804-216	8.1	0.6	1,2,3,4
100085	2014-10-12	28.0	HESS J1804-216	8.7	-0.6	1,2,3,4

100213	2014-10-16	28.0	HESS J1804-216	7.8	-0.4	1,2,3,4
100247	2014-10-17	28.0	HESS J1804-216	9.0	0.3	1,2,3,4
100288	2014-10-18	28.0	HESS J1804-216	8.1	0.6	1,2,3,4
100316	2014-10-19	18.4	HESS J1804-216	8.7	-0.6	1,2,3,4
100343	2014-10-20	20.4	HESS J1804-216	7.8	-0.4	2,3,4
100378	2014-10-21	28.0	HESS J1804-216	9.0	0.3	1,2,3,4

Table D.6: Full table of observations for the H.E.S.S. IU phase with the `std_ImPACT_fullEnclosure` configuration. `OBS_ID` is the identifier for the observation. The observation time is listed along with the object which the observations are for. The pointing position is given by `GLON_PNT` and `GLAT_PNT`, for the telescopes listed in `TELLIST`.

`OBS_ID`	Date	Observation Time (min)	Object	`GLON_PNT` (deg)	`GLAT_PNT` (deg)	`TELLIST`
129975	2017-05-04	28.0	ToO20170503A	11.4	-1.1	1,2,3
149655	2019-05-30	27.3	W28 region center	6.8	0.1	1,2,3,4
149766	2019-06-01	28.0	W28 region center	5.6	-0.6	1,2,3,4
149767	2019-06-01	28.0	W28 region center	6.5	-0.9	1,2,3,4
149768	2019-06-01	28.0	W28 region center	5.8	0.3	1,2,3,4
149769	2019-06-01	28.1	W28 region center	6.8	0.1	1,2,3,4
149770	2019-06-01	28.0	W28 region center	5.6	-0.6	1,2,3,4
149814	2019-06-02	28.0	W28 region center	5.8	0.3	2,3,4
149815	2019-06-02	28.0	W28 region center	6.8	0.1	2,3,4
149858	2019-06-03	28.0	W28 region center	6.5	-0.9	1,2,3,4
149859	2019-06-03	28.0	W28 region center	5.8	0.3	1,2,3,4
149860	2019-06-03	28.0	W28 region center	5.6	-0.6	1,2,3,4
149861	2019-06-03	28.0	W28 region center	6.8	0.1	1,2,3,4
149862	2019-06-03	22.3	W28 region center	6.5	-0.9	1,2,3,4
149863	2019-06-03	11.2	W28 region center	6.5	-0.9	1,2,3,4
149898	2019-06-04	28.0	W28 region center	6.5	-0.9	1,2,3,4
149899	2019-06-04	28.0	W28 region center	5.6	-0.6	1,2,3,4
149900	2019-06-04	28.0	W28 region center	5.8	0.3	1,2,3,4
149901	2019-06-04	28.0	W28 region center	6.5	-0.9	1,2,3,4
149902	2019-06-04	24.6	W28 region center	5.6	-0.6	1,2,3,4

149950	2019-06-05	28.0	W28 region center	6.8	0.1	1,2,3,4
149951	2019-06-05	28.0	W28 region center	5.8	0.3	1,2,3,4
149952	2019-06-05	28.0	W28 region center	6.5	-0.9	1,2,3,4
149953	2019-06-05	28.0	W28 region center	5.6	-0.6	1,2,3,4
149954	2019-06-05	28.0	W28 region center	6.8	0.1	1,2,3,4
150008	2019-06-06	28.0	W28 region center	5.8	0.3	2,3,4
150009	2019-06-06	28.0	W28 region center	6.5	-0.9	2,3,4
150010	2019-06-06	28.0	W28 region center	5.6	-0.6	2,3,4
150065	2019-06-07	28.0	W28 region center	6.8	0.1	1,2,3,4
150066	2019-06-07	28.0	W28 region center	5.8	0.3	1,2,3,4
150067	2019-06-07	28.0	W28 region center	6.5	-0.9	1,2,3,4
150069	2019-06-07	28.0	W28 region center	5.6	-0.6	1,2,3,4
150107	2019-06-08	28.0	W28 region center	6.8	0.1	1,2,3,4
150108	2019-06-08	28.0	W28 region center	5.8	0.3	1,2,3,4
150109	2019-06-08	28.0	W28 region center	6.5	-0.9	1,2,3,4
150143	2019-06-09	21.0	W28 region center	5.6	-0.6	1,2,3,4
150144	2019-06-09	28.0	W28 region center	6.8	0.1	1,2,3,4
150145	2019-06-09	23.0	W28 region center	5.8	0.3	1,2,3,4
150147	2019-06-09	28.0	W28 region center	6.5	-0.9	1,2,3,4
150189	2019-06-10	28.0	W28 region center	5.6	-0.6	1,2,3,4
150190	2019-06-10	28.0	W28 region center	6.8	0.1	1,2,3,4
150191	2019-06-10	28.0	W28 region center	5.8	0.3	1,2,3,4
150192	2019-06-10	28.0	W28 region center	6.5	-0.9	1,2,3,4
150193	2019-06-10	28.0	W28 region center	5.6	-0.6	1,2,3,4
150194	2019-06-10	28.0	W28 region center	6.8	0.1	1,2,3,4
150244	2019-06-11	28.0	W28 region center	5.8	0.3	1,2,3,4
150245	2019-06-11	28.0	W28 region center	6.5	-0.9	1,2,3,4
150308	2019-06-12	28.0	W28 region center	5.6	-0.6	1,2,3,4
150309	2019-06-12	28.0	W28 region center	6.8	0.1	1,2,3,4
150310	2019-06-12	28.0	W28 region center	6.5	-0.9	1,2,3,4
150362	2019-06-13	28.0	W28 region center	5.8	0.3	1,2,3,4
150363	2019-06-13	28.0	W28 region center	6.5	-0.9	1,2,3,4

Bibliography

Aartsen, M. G. et al. (Mar. 2017). "The IceCube Neutrino Observatory: instrumentation and online systems". In: *Journal of Instrumentation* 12.3, P03012.

Abdalla, H. et al. (Sept. 2021). "Evidence of 100 TeV γ-ray emission from HESS J1702-420: A new PeVatron candidate". In: A&A 653, A152, A152.

Abeysekara, A. U. et al. (May 2012). "On the sensitivity of the HAWC observatory to gamma-ray bursts". In: 35.10, pp. 641–650.

Abeysekara, A. U. et al. (July 2018). "A Very High Energy γ-Ray Survey toward the Cygnus Region of the Galaxy". In: ApJ 861.2, 134, p. 134.

Abramowski, A. et al. (Jan. 2012). "Discovery of extended VHE γ-ray emission from the vicinity of the young massive stellar cluster Westerlund 1". In: A&A 537, A114, A114.

Abramowski, A. et al. (Oct. 2014). "Discovery of the Hard Spectrum VHE γ-Ray Source HESS J1641-463". In: ApJ 794.1, L1, p. L1.

Ackermann, M. et al. (Feb. 2013). "Detection of the Characteristic Pion-Decay Signature in Supernova Remnants". In: *Science* 339.6121, pp. 807–811.

Ackermann, M. et al. (July 2017). "Search for Extended Sources in the Galactic Plane Using Six Years of Fermi-Large Area Telescope Pass 8 Data above 10 GeV". In: ApJ 843.2, 139, p. 139.

Aharonian, F. A. (2004). *Very high energy cosmic gamma radiation : a crucial window on the extreme Universe.*

Aharonian, F. A. and A. M. Atoyan (May 1996). "On the emissivity of π_0-decay gamma radiation in the vicinity of accelerators of galactic cosmic rays." In: A&A 309, pp. 917–928.

Aharonian, F. A., A. M. Atoyan, and T. Kifune (Oct. 1997a). "Inverse Compton gamma radiation of faint synchrotron X-ray nebulae around pulsars". In: MNRAS 291.1, pp. 162–176.

Aharonian, F. A., J. Buckley, T. Kifune, and G. Sinnis (Sept. 2008). "High energy astrophysics with ground-based gamma ray detectors". In: *Reports on Progress in Physics* 71.9, 096901, p. 096901.

Aharonian, F. A., W. Hofmann, A. K. Konopelko, and H. J. Völk (Mar. 1997b). "The potential of ground based arrays of imaging atmospheric Cherenkov telescopes. I. Determination of shower parameters". In: *Astroparticle Physics* 6.3-4, pp. 343–368.

Aharonian, F. A., R. Yang, and E. de Oña Wilhelmi (Mar. 2019). "Massive stars as major factories of Galactic cosmic rays". In: *Nature Astronomy* 3, pp. 561–567.

Aharonian, F. A. et al. (2004). "Calibration of cameras of the H.E.S.S. detector". In: *Astropart. Phys.* 22, pp. 109–125.

Aharonian, F. A. et al. (Mar. 2005). "A New Population of Very High Energy Gamma-Ray Sources in the Milky Way". In: *Science* 307.5717, pp. 1938–1942.

Aharonian, F. A. et al. (Dec. 2006a). "Energy dependent γ-ray morphology in the pulsar wind nebula HESS J1825-137". In: A&A 460.2, pp. 365–374.

Aharonian, F. A. et al. (Oct. 2006b). "Observations of the Crab nebula with HESS". In: A&A 457.3, pp. 899–915.

Aharonian, F. A. et al. (Jan. 2006c). "The H.E.S.S. Survey of the Inner Galaxy in Very High Energy Gamma Rays". In: ApJ 636.2, pp. 777–797.

Aharonian, F. A. et al. (June 2007). "Detection of extended very-high-energy γ-ray emission towards the young stellar cluster Westerlund 2". In: A&A 467.3, pp. 1075–1080.

Ajello, M. et al. (Oct. 2017). "3FHL: The Third Catalog of Hard Fermi-LAT Sources". In: ApJS 232.2, 18, p. 18.

Albert, A. et al. (Dec. 2020). "3HWC: The Third HAWC Catalog of Very-high-energy Gamma-Ray Sources". In: ApJ 905.1, 76, p. 76.

Amato, E. (2014). "The Theory of Pulsar Wind Nebulae". In: *International Journal of Modern Physics: Conference Series* 28, p. 1460160.

Amenomori, M. et al. (Mar. 1990). "Development and performance test of a prototype air shower array for search for gamma ray point sources in the very high energy region". In: *Nuclear Instruments and Methods in Physics Research A* 288.2-3, pp. 619–631.

Atoyan, A. M., F. A. Aharonian, and H. J. Völk (Sept. 1995). "Electrons and positrons in the galactic cosmic rays". In: Phys. Rev. D 52.6, pp. 3265–3275.

Atwood, W. B. et al. (June 2009). "The Large Area Telescope on the Fermi Gamma-Ray Space Telescope Mission". In: ApJ 697.2, pp. 1071–1102.

Axford, W. I., E. Leer, and G. Skadron (Jan. 1977). "The Acceleration of Cosmic Rays by Shock Waves". In: *International Cosmic Ray Conference*. Vol. 11. International Cosmic Ray Conference, p. 132.

Baade, W. and F. Zwicky (1934). "Cosmic Rays from Super-Novae". eng. In: *Proceedings of the National Academy of Sciences* 20.5, pp. 259–263.

Barlow, R. J. (1989). *Statistics: A Guide to the Use of Statistical Methods in the Physical Sciences*. Manchester Physics Series. Wiley.

Bell, A. R. (Feb. 1978). "The acceleration of cosmic rays in shock fronts - II." In: MNRAS 182, pp. 443–455.

Bell, A. R., K. M. Schure, B. Reville, and G. Giacinti (May 2013). "Cosmic-ray acceleration and escape from supernova remnants". In: MNRAS 431.1, pp. 415–429.

Berezhko, E. G. and H. J. Völk (Aug. 1997). "Kinetic theory of cosmic rays and gamma rays in supernova remnants. I. Uniform interstellar medium". In: *Astroparticle Physics* 7.3, pp. 183–202.

– (May 2000). "Kinetic theory of cosmic ray and gamma-ray production in supernova remnants expanding into wind bubbles". In: A&A 357, pp. 283–300.

Berezinskii, V. S., S. V. Bulanov, V. A. Dogiel, and V. S. Ptuskin (1990). *Astrophysics of cosmic rays.*

Berge, D., S. Funk, and J. Hinton (May 2007). "Background modelling in very-high-energy γ-ray astronomy". In: A&A 466.3, pp. 1219–1229.

Bernlöhr, K. et al. (Nov. 2003). "The optical system of the H.E.S.S. imaging atmospheric Cherenkov telescopes. Part I: layout and components of the system". In: *Astroparticle Physics* 20.2, pp. 111–128.

Bevington, P. R. and D. K. Robinson (1969). *Data Reduction and Error Analysis for the Physical Sciences*. 3rd ed. McGraw-Hill.

Blandford, R. and D. Eichler (Oct. 1987). "Particle acceleration at astrophysical shocks: A theory of cosmic ray origin". In: Phys. Rep. 154.1, pp. 1–75.

Blandford, R. and J. P. Ostriker (Apr. 1978). "Particle acceleration by astrophysical shocks." In: ApJ 221, pp. L29–L32.

Blondin, J. M., R. A. Chevalier, and D. M. Frierson (Dec. 2001). "Pulsar Wind Nebulae in Evolved Supernova Remnants". In: ApJ 563.2, pp. 806–815.

Blondin, J. M., E. B. Wright, K. J. Borkowski, and S. P. Reynolds (June 1998). "Transition to the Radiative Phase in Supernova Remnants". In: *The Astrophysical Journal* 500.1, pp. 342–354.

Blumenthal, G. R. and R. J. Gould (Apr. 1970). "Bremsstrahlung, Synchrotron Radiation, and Compton Scattering of High-Energy Electrons Traversing Dilute Gases". In: *Rev. Mod. Phys.* 42 (2), pp. 237–270.

Bogovalov, S. V. and F. A. Aharonian (Apr. 2000). "Very-high-energy gamma radiation associated with the unshocked wind of the Crab pulsar". In: MNRAS 313.3, pp. 504–514.

Bolatto, Alberto D., Mark Wolfire, and Adam K. Leroy (Aug. 2013). "The CO-to-H_2 Conversion Factor". In: ARA&A 51.1, pp. 207–268.

Bolz, O. (2004). "Absolute Energiekalibration der abbildenden Cherenkov-Teleskope des H.E.S.S. Experiments und Ergebnisse erster Beobachtungen des Supernova Überrests RX J1713.7−3946." PhD thesis. Ruprecht-Karls-Universität Heidelberg.

Braiding, C. et al. (May 2015). "The Mopra Southern Galactic Plane CO Survey - Data Release 1". In: PASA 32, e020, e020.

Braiding, C. et al. (Aug. 2018). "The Mopra Southern Galactic Plane CO Survey—Data Release 3". In: PASA 35, e029, e029.

Brand, J. and L. Blitz (Aug. 1993). "The velocity field of the outer galaxy." In: A&A 275, pp. 67–90.

Brose, R., M. Pohl, I. Sushch, O. Petruk, and T. Kuzyo (Feb. 2020). "Cosmic-ray acceleration and escape from post-adiabatic supernova remnants". In: A&A 634, A59, A59.

Bucciantini, N., J. Arons, and E. Amato (Dec. 2010). "Modelling spectral evolution of pulsar wind nebulae inside supernova remnants". In: *Monthly Notices of the Royal Astronomical Society* 410.1, pp. 381–398.

Burton, M. G. et al. (Aug. 2013). "The Mopra Southern Galactic Plane CO Survey". In: PASA 30, e044, e044.

Canto, J. (Dec. 1977). "On the density and energy of supernova remnants." In: A&A 61.5, pp. 641–645.

Cao, Z. et al. (May 2019). "Introduction to Large High Altitude Air Shower Observatory (LHAASO)". In: *Chinese Astronomy and Astrophysics* 43.4, pp. 457–478.

Cao, Z. et al. (June 2021). "Ultrahigh-energy photons up to 1.4 petaelectronvolts from 12 γ-ray Galactic sources". In: Nature 594.7861, pp. 33–36.

Casanova, S. et al. (Oct. 2010). "Modeling the Gamma-Ray Emission Produced by Runaway Cosmic Rays in the Environment of RX J1713.7-3946". In: PASJ 62, pp. 1127–1134.

Celli, S., F. A. Aharonian, and S. Gabici (Nov. 2020). "Spectral Signatures of PeVatrons". In: ApJ 903.1, 61, p. 61.

Celli, S., G. Morlino, S. Gabici, and F. A. Aharonian (Dec. 2019). "Exploring particle escape in supernova remnants through gamma rays". In: MNRAS 490.3, pp. 4317–4333.

Čerenkov, P. A (1934). "Visible Emission of Clean Liquids by Action of γ Radiation". In: *Dokl. Acad. Sci. URSS*. Vol. 2, pp. 451–457.

Cheng, K.S. and G.E. Romero (2004). *Cosmic Gamma-Ray Sources.* Astrophysics and Space Science Library, 304. Springer Netherlands.

Chevalier, R. A. (Jan. 1977). "The interaction of supernovae with the interstellar medium." In: ARA&A 15, pp. 175–196.

Cioffi, D. F., C. F. McKee, and E. Bertschinger (Nov. 1988). "Dynamics of Radiative Supernova Remnants". In: ApJ 334, p. 252.

Cornils, R., K. Bernlöhr, G. Heinzelmann, W. Hofmann, and M. Panter (Jan. 2005). "The optical system of the H.E.S.S. II telescope". In: *29th International Cosmic Ray Conference (ICRC29), Volume 5.* Vol. 5. International Cosmic Ray Conference, p. 171.

Cristofari, P. (Aug. 2021). "The Hunt for Pevatrons: The Case of Supernova Remnants". In: *Universe* 7.9, p. 324.

Crutcher, R. M., B. Wandelt, C. Heiles, E. Falgarone, and T. H. Troland (Dec. 2010). "Magnetic Fields in Interstellar Clouds from Zeeman Observations: Inference of Total Field Strengths by Bayesian Analysis". In: ApJ 725, pp. 466–479.

CSIRO (2021a). *Mopra radio telescope.* URL: https://www.csiro.au/en/about/facilities-collections/atnf/mopra-radio-telescope. Accessed: 15-5-2021.

– (2021b). *Parkes radio telescope.* URL: https://www.csiro.au/en/about/facilities-collections/atnf/parkes-radio-telescope. Accessed: 7-12-2021.

CTA Collaboration (2016). *Cherenkov Telescope Array. Exploring the Universe at the Highest Energies.* URL: https://www.cta-observatory.org/. Accessed: 25-11-2021.

– (2021). *CTAO Performance.* URL: https://www.cta-observatory.org/science/ctao-performance/. Accessed: 25-11-2021.

CTA Consortium et al. (2018). *Science with the Cherenkov Telescope Array.*

Dame, T. M., Dap Hartmann, and P. Thaddeus (Feb. 2001). "The Milky Way in Molecular Clouds: A New Complete CO Survey". In: ApJ 547.2, pp. 792–813.

Dawson, J. R. et al. (Apr. 2014). "SPLASH: the Southern Parkes Large-Area Survey in Hydroxyl - first science from the pilot region". In: MNRAS 439.2, pp. 1596–1614.

de Wilt, P. et al. (June 2017). "Dense molecular gas at 12 mm towards Galactic TeV gamma-ray sources". In: MNRAS 468.2, pp. 2093–2113.

Deil, C. et al. (Jan. 2017a). "Gammapy - A prototype for the CTA science tools". In: *35th International Cosmic Ray Conference (ICRC2017)*. Vol. 301. International Cosmic Ray Conference, p. 766.

Deil, C. et al. (Jan. 2017b). "Open high-level data formats and software for gamma-ray astronomy". In: *6th International Symposium on High Energy Gamma-Ray Astronomy*. Vol. 1792. American Institute of Physics Conference Series, p. 070006.

Deil, C. et al. (Nov. 2020). *gammapy/gammapy: v.0.18.2*. Version v0.18.2.

Dickey, J. M. and F. J. Lockman (Jan. 1990). "H I in the galaxy." In: ARA&A 28, pp. 215–261.

Donath, A. et al. (July 2015). "Gammapy: An open-source Python package for gamma-ray astronomy". In: *34th International Cosmic Ray Conference (ICRC2015)*. Vol. 34. International Cosmic Ray Conference, p. 789.

Drury, L. O'C., F. A. Aharonian, and H. J. Voelk (July 1994). "The gamma-ray visibility of supernova remnants. A test of cosmic ray origin". In: A&A 287, pp. 959–971.

Drury, L. O'C., W. J. Markiewicz, and H. J. Voelk (Nov. 1989). "Simplified models for the evolution of supernova remnants including particle acceleration". In: A&A 225.1, pp. 179–191.

Einecke, S. (2017). "The Data Mining Guide to the Galaxy: Active Galactic Nuclei in a Multi-Wavelength Context". PhD thesis. technische universitat dortmund.

Engel, R., D. Heck, and T. Pierog (Nov. 2011). "Extensive Air Showers and Hadronic Interactions at High Energy". In: *Annual Review of Nuclear and Particle Science* 61.1, pp. 467–489.

Feijen, K. et al. (Dec. 2020). "Arcminute-scale studies of the interstellar gas towards HESS J1804-216: Still an unidentified TeV γ-ray source". In: PASA 37, e056, e056.

Fermi, E. (Apr. 1949). "On the Origin of the Cosmic Radiation". In: *Physical Review* 75.8, pp. 1169–1174.

Finley, J. P., R. Srinivasan, and S. Park (Aug. 1996). "The Morphology of Young Neutron Stars: PSR B1823-13, Its Compact Nebula, and Its Interstellar Neighborhood". In: ApJ 466, p. 938.

Fletcher, R. S., T. K. Gaisser, Paolo Lipari, and Todor Stanev (Nov. 1994). "sibyll: An event generator for simulation of high energy cosmic ray cascades". In: Phys. Rev. D 50.9, pp. 5710–5731.

Frail, D. A. and G. F. Mitchell (Dec. 1998). "OH (1720 MHz) Masers as Signposts of Molecular Shocks". In: ApJ 508.2, pp. 690–695.

Frater, R. H., J. W. Brooks, and J. B. Whiteoak (June 1992). "The Australia Telescope - Overview". In: *Journal of Electrical and Electronics Engineering Australia* 12.2, pp. 103–112.

Frerking, M. A., R. W. Wilson, R. A. Linke, and P. G. Wannier (Aug. 1980). "Isotopic abundance ratios in interstellar carbon monosulfide". In: ApJ 240, pp. 65–73.

Fukui, Y. and A. Kawamura (Sept. 2010). "Molecular Clouds in Nearby Galaxies". In: ARA&A 48, pp. 547–580.

Fukui, Y. et al. (Feb. 2012). "A Detailed Study of the Molecular and Atomic Gas toward the γ-Ray Supernova Remnant RX J1713.7-3946: Spatial TeV γ-Ray and Interstellar Medium Gas Correspondence". In: ApJ 746.1, 82, p. 82.

Fukui, Y. et al. (Jan. 2015). "Optically Thick H I Dominant in the Local Interstellar Medium: An Alternative Interpretation to "Dark Gas"". In: ApJ 798.1, 6, p. 6.

Furlanetto, S. R. (2016). "The 21-cm Line as a Probe of Reionization". In: *Understanding the Epoch of Cosmic Reionization: Challenges and Progress.* Ed. by Andrei Mesinger. Vol. 423. Astrophysics and Space Science Library, p. 247.

Gabici, S., F. A. Aharonian, and P. Blasi (June 2007). "Gamma rays from molecular clouds". In: Ap&SS 309, pp. 365–371.

Gaensler, B. M. and P. Slane (Sept. 2006). "The Evolution and Structure of Pulsar Wind Nebulae". In: ARA&A 44.1, pp. 17–47.

Gaisser, T. K. (1990). *Cosmic rays and particle physics.*

Giacinti, G. et al. (Apr. 2020). "Halo fraction in TeV-bright pulsar wind nebulae". In: A&A 636, A113, A113.

Ginzburg, V. L. and S. I. Syrovatskii (1964). *The Origin of Cosmic Rays.*

Green, D. A. (Aug. 2019). "A revised catalogue of 294 Galactic supernova remnants". In: *Journal of Astrophysics and Astronomy* 40.4, 36, p. 36.

Greisen, K. (Apr. 1966). "End to the Cosmic-Ray Spectrum?" In: Phys. Rev. Lett. 16.17, pp. 748–750.

Gusdorf, A., S. Cabrit, D. R. Flower, and G. Pineau Des Forêts (May 2008). "SiO line emission from C-type shock waves: interstellar jets and outflows". In: A&A 482.3, pp. 809–829.

H.E.S.S. Collaboration (2021a). *HESS FITS data.* URL: https://hess-confluence. desy.de/confluence/display/HESS/HESS+FITS+data. Accessed: 12-12-2021.

– (2021b). *HESS FITS data.* URL: https://hess-confluence.desy.de/confluence/ display/HESS/HD+Calibration. Accessed: 14-12-2021.

H.E.S.S. Collaboration et al. (Dec. 2012). "Identification of HESS J1303-631 as a pulsar wind nebula through γ-ray, X-ray, and radio observations". In: A&A 548, A46, A46.

H.E.S.S. Collaboration et al. (Apr. 2018). "The H.E.S.S. Galactic plane survey". In: A&A 612, A1, A1.

H.E.S.S. Collaboration et al. (Jan. 2019). "Particle transport within the pulsar wind nebula HESS J1825-137". In: A&A 621, A116, A116.

Habart, E. et al. (Aug. 2005). "Molecular Hydrogen". In: *SSR* 119, pp. 71–91.

Haungs, A., H. Rebel, and M. Roth (July 2003). "Energy spectrum and mass composition of high-energy cosmic rays". In: *Reports on Progress in Physics* 66.7, pp. 1145–1206.

HAWC Collaboration et al. (Jan. 2020). "Multiple Galactic Sources with Emission Above 56 TeV Detected by HAWC". In: *Phys. Rev. Lett.* 124 (2).

Heck, D., J. Knapp, J. N. Capdevielle, G. Schatz, and T. Thouw (1998). *CORSIKA: a Monte Carlo code to simulate extensive air showers.*

Heitler, W. (1954). *The quantum theory of radiation.* 3rd ed. International series on monographs on physics. Clarendon Press Oxford.

Herbst, E., T. J. Millar, S. Wlodek, and D. K. Bohme (Sept. 1989). "The chemistry of silicon in dense interstellar clouds." In: A&A 222, pp. 205–210.

Hess, V. (1912). "Uber Beobachtungen der durchdringenden Strahlung bei sieben Freiballonfahrten". In: *Phys. Z.* 13, pp. 1084–1091.

Heyer, M. and T. M. Dame (Aug. 2015). "Molecular Clouds in the Milky Way". In: ARA&A 53, pp. 583–629.

Hillas, A. M. (Jan. 1984). "The Origin of Ultra-High-Energy Cosmic Rays". In: ARA&A 22, pp. 425–444.

Hillas, A. M. (Aug. 1985). "Cerenkov Light Images of EAS Produced by Primary Gamma Rays and by Nuclei". In: *19th International Cosmic Ray Conference (ICRC19), Volume 3*. Vol. 3. International Cosmic Ray Conference, p. 445.

– (Jan. 1996). "Differences between Gamma-Ray and Hadronic Showers". In: Space Sci. Rev. 75.1-2, pp. 17–30.

Hinton, J. A. and W. Hofmann (Sept. 2009). "Teraelectronvolt Astronomy". In: ARA&A 47.1, pp. 523–565.

Ho, P. T. P. and C. H. Townes (1983). "Interstellar ammonia". In: ARA&A 21, pp. 239–270.

Hofmann, W. (July 2012a). *The H.E.S.S. Telescopes*. URL: https://www.mpi-hd.mpg.de/hfm/HESS/pages/about/telescopes/. Accessed: 5-5-2021.

– (2012b). *The H.E.S.S. Telescopes - images*. URL: https://www.mpi-hd.mpg.de/hfm/HESS/pages/press/2012/HESS_II_first_light/. Accessed: 15-5-2021.

Hofmann, W. et al. (Nov. 1999). "Comparison of techniques to reconstruct VHE gamma-ray showers from multiple stereoscopic Cherenkov images". In: *Astroparticle Physics* 12.3, pp. 135–143.

Jelley, J. V. (1958). *Čerenkov Radiation, and Its Applications*. United Kingdom Atomic Energy Authorit.

Jennings, R. E. (1962). "Čerenkov Radiation". In: *Science Progress* 50.199, pp. 364–375.

Jogler, T. and S. Funk (Jan. 2016). "Revealing W51C as a Cosmic Ray Source Using Fermi-LAT Data". In: ApJ 816.2, 100, p. 100.

Jokipii, J. R. and G. Morfill (Jan. 1987). "Ultra–High Energy Cosmic Rays in a Galactic Wind and Its Termination Shock". In: ApJ 312, p. 170.

Kafexhiu, E., F. A. Aharonian, A.M. Taylor, and Gabriela S. Vila (Dec. 2014). "Parametrization of gamma-ray production cross sections for pp interactions in a broad proton energy range from the kinematic threshold to PeV energies". In: Phys. Rev. D 90.12, 123014, p. 123014.

Kaspi, V. M., M. S. E. Roberts, and A. K. Harding (2006). "Isolated neutron stars". In: *Compact stellar X-ray sources*. Vol. 39, pp. 279–339.

Kelner, S. R., F. A. Aharonian, and V. V. Bugayov (Aug. 2006). "Energy spectra of gamma rays, electrons, and neutrinos produced at proton-proton interactions in the very high energy regime". In: Phys. Rev. D 74.3, 034018, p. 034018.

Keohane, J. W., R. Petre, E. V. Gotthelf, M. Ozaki, and K. Koyama (July 1997). "A Possible Site of Cosmic Ray Acceleration in the Supernova Remnant IC 443". In: ApJ 484.1, pp. 350–359.

Kerr, F. J. and D. Lynden-Bell (Aug. 1986). "Review of galactic constants." In: MNRAS 221, pp. 1023–1038.

Konopelko, A. (Oct. 2005). "STEREO ARRAY of 30 m imaging atmospheric Čerenkov telescopes: A next-generation detector for ground-based high energy gamma-ray astronomy". In: *Astroparticle Physics* 24.3, pp. 191–207.

Kotera, K. and A. V. Olinto (Sept. 2011). "The Astrophysics of Ultrahigh-Energy Cosmic Rays". In: ARA&A 49.1, pp. 119–153.

Koyama, K. et al. (Nov. 1995). "Evidence for shock acceleration of high-energy electrons in the supernova remnant SN1006". In: Nature 378.6554, pp. 255–258.

Ladd, N., C. Purcell, T. Wong, and S. Robertson (Jan. 2005). "Beam Size, Shape and Efficiencies for the ATNF Mopra Radio Telescope at 86-115 GHz". In: PASA 22.1, pp. 62–72.

Lau, J. C. et al. (Jan. 2017). "Interstellar gas towards the TeV γ-ray sources HESS J1640-465 and HESS J1641-463". In: MNRAS 464.3, pp. 3757–3774.

Leibundgut, B. (Jan. 2000). "Type Ia Supernovae". In: A&A Rev. 10.3, pp. 179–209.

Lemoine-Goumard, M. (Jan. 2014). "Gamma-ray observations of supernova remnants". In: *Supernova Environmental Impacts*. Ed. by Alak Ray and Richard A. McCray. Vol. 296, pp. 287–294.

LHAASO Collaboration et al. (July 2021). "Peta-electron volt gamma-ray emission from the Crab Nebula". In: *Science* 373, pp. 425–430.

Li, H. and Y. Chen (Nov. 2010). "γ-rays from molecular clouds illuminated by accumulated diffusive protons from supernova remnant W28". In: *Monthly Notices of the Royal Astronomical Society: Letters* 409.1, pp. L35–L38.

Li, T. P. and Y. Q. Ma (Sept. 1983). "Analysis methods for results in gamma-ray astronomy." In: ApJ 272, pp. 317–324.

Lockett, P., E. Gauthier, and M. Elitzur (Jan. 1999). "OH 1720 Megahertz Masers in Supernova Remnants: C-Shock Indicators". In: ApJ 511.1, pp. 235–241.

Longair, M. S. (2011). *High Energy Astrophysics*.

Marcowith, A., M. Lemoine, and G. Pelletier (July 2006). "Turbulence and particle acceleration in collisionless supernovae remnant shocks. II. Cosmic-ray transport". In: A&A 453.1, pp. 193–202.

Martin, B.R. and G. Shaw (2009). *Particle physics.* 3rd ed. Manchester physics series. Wiley.

Martin-Pintado, J., R. Bachiller, and A. Fuente (Feb. 1992). "SiO emission as a tracer of shocked gas in molecular outflows." In: A&A 254, pp. 315–326.

Matthews, J. (Jan. 2005). "A Heitler model of extensive air showers". In: *Astroparticle Physics* 22.5-6, pp. 387–397.

McClure-Griffiths, N. M. et al. (June 2005). "The Southern Galactic Plane Survey: H I Observations and Analysis". In: ApJS 158.2, pp. 178–187.

Mirzoyan, R. et al. (Dec. 1994). "The first telescope of the HEGRA air Cherenkov imaging telescope array". In: *Nuclear Instruments and Methods in Physics Research A* 351.2-3, pp. 513–526.

Mitchell, A. M. W., G. P. Rowell, S. Celli, and S. Einecke (May 2021). "Using interstellar clouds to search for Galactic PeVatrons: gamma-ray signatures from supernova remnants". In: MNRAS 503.3, pp. 3522–3539.

Moderski, R., M. Sikora, P. S. Coppi, and F. A. Aharonian (Nov. 2005). "Klein-Nishina effects in the spectra of non-thermal sources immersed in external radiation fields". In: MNRAS 363.3, pp. 954–966.

Mohrmann, L. et al. (Dec. 2019). "Validation of open-source science tools and background model construction in γ-ray astronomy". In: A&A 632, A72, A72.

Moriguchi, Y. et al. (Oct. 2005). "A Detailed Study of Molecular Clouds toward the TeV Gamma-Ray Supernova Remnant G347.3-0.5". In: ApJ 631.2, pp. 947–963.

Naito, T. and F. Takahara (Mar. 1994). "High energy gamma-ray emission from supernova remnants". In: *Journal of Physics G Nuclear Physics* 20.3, pp. 477–486.

NASA/DOE/Fermi LAT Collaboration (2013). *Fermi's Five-year View of the Gamma-ray Sky.* URL: https://svs.gsfc.nasa.gov/11342. Accessed: 15-5-2021.

Nicholas, B. (2011). "Cloudy Ammonia: A multi-wavelength molecular line survey of the molecular clouds surrounding the W28 supernova remnant." PhD thesis. The University of Adelaide.

NIST (2013). *NIST/SEMATECH e-Handbook of Statistical.* URL: https://doi.org/10.18434/M32189. Accessed: 1-2-2022.

Ohira, Y., R. Yamazaki, N. Kawanaka, and K. Ioka (Nov. 2012). "Escape of cosmic-ray electrons from supernova remnants". In: MNRAS 427.1, pp. 91–102.

Padmanabhan, T. (2001). *Theoretical Astrophysics - Volume 2, Stars and Stellar Systems*. Vol. 2.

Penzias, A. A., P. M. Solomon, R. W. Wilson, and K. B. Jefferts (Sept. 1971). "Interstellar Carbon Monosulfide". In: ApJ 168, p. L53.

Persic, M., P. Salucci, and F. Stel (July 1996). "The universal rotation curve of spiral galaxies — I. The dark matter connection". In: MNRAS 281.1, pp. 27–47.

Porter, N. A. and T. C. Weekes (Nov. 1977). "Gamma Ray Astronomy from 10^{11} to 10^{14} eV Using the Atmospheric Cerenkov Technique". In: *SAO Special Report* 381.

Principe, G. et al. (Aug. 2020). "Energy dependent morphology of the pulsar wind nebula HESS J1825-137 with Fermi-LAT". In: A&A 640, A76, A76.

Protheroe, R. J. and R. W. Clay (Jan. 2004). "Ultra High Energy Cosmic Rays". In: PASA 21.1, pp. 1–22.

Protheroe, R. J. and A. P. Szabo (Nov. 1992). "High energy cosmic rays from active galactic nuclei". In: *Phys. Rev. Lett.* 69 (20), pp. 2885–2888.

Ptuskin, V. S. and V. N. Zirakashvili (Jan. 2005). "On the spectrum of high-energy cosmic rays produced by supernova remnants in the presence of strong cosmic-ray streaming instability and wave dissipation". In: A&A 429, pp. 755–765.

Rebolledo, D. et al. (Mar. 2016). "The Carina Nebula and Gum 31 molecular complex - I. Molecular gas distribution, column densities, and dust temperatures". In: MNRAS 456.3, pp. 2406–2424.

Reid, M. J. et al. (Mar. 2014). "Trigonometric Parallaxes of High Mass Star Forming Regions: The Structure and Kinematics of the Milky Way". In: ApJ 783.2, 130, p. 130.

Reynolds, S. P. (Sept. 2008). "Supernova Remnants at High Energy". In: *Annual Review of Astronomy and Astrophysics* 46.1, pp. 89–126.

Rice, T. S., A. A. Goodman, E. A. Bergin, C. Beaumont, and T. M. Dame (May 2016). "A Uniform Catalog of Molecular Clouds in the Milky Way". In: ApJ 822.1, 52, p. 52.

Russeil, D. et al. (May 2017). "The Milky Way rotation curve revisited". In: A&A 601, L5, p. L5.

Rybicki, G. B. and A. P. Lightman (1986). *Radiative Processes in Astrophysics*.

Sano, H. et al. (May 2019). "Possible Evidence for Cosmic-Ray Acceleration in the Type Ia SNR RCW 86: Spatial Correlation between TeV Gamma-Rays and Interstellar Atomic Protons". In: ApJ 876.1, 37, p. 37.

Schmidt, F. (May 2021). *CORSIKA – an Air Shower Simulation Program*. URL: https://www.iap.kit.edu/corsika/. Accessed: 26-11-2021.

Schröder, F. G. et al. (May 2019). "High-Energy Galactic Cosmic Rays". In: *Bulletin of the AAS* 51.3.

Sedov, L. I. (1959). *Similarity and Dimensional Methods in Mechanics*.

Simon, R., J. M. Jackson, D. P. Clemens, T. M. Bania, and M. H. Heyer (Apr. 2001). "The Structure of Four Molecular Cloud Complexes in the BU-FCRAO Milky Way Galactic Ring Survey". In: ApJ 551.2, pp. 747–763.

Sinnis, G. (May 2009). "Air shower detectors in gamma-ray astronomy". In: *New Journal of Physics* 11.5, 055007, p. 055007.

Slane, P. et al. (Nov. 1999). "Nonthermal X-Ray Emission from the Shell-Type Supernova Remnant G347.3-0.5". In: ApJ 525.1, pp. 357–367.

Slane, P. et al. (Feb. 2001). "RX J0852.0-4622: Another Nonthermal Shell-Type Supernova Remnant (G266.2-1.2)". In: ApJ 548.2, pp. 814–819.

Sofue, Y. (2013). "Mass Distribution and Rotation Curve in the Galaxy". In: *Planets, Stars and Stellar Systems. Volume 5: Galactic Structure and Stellar Populations*. Ed. by Terry D. Oswalt and Gerard Gilmore. Vol. 5, p. 985.

Staveley-Smith, L. et al. (Nov. 1996). "The Parkes 21 CM multibeam receiver". In: PASA 13.3, pp. 243–248.

Strong, A. W., I. V. Moskalenko, and V .S. Ptuskin (Nov. 2007). "Cosmic-Ray Propagation and Interactions in the Galaxy". In: *Annual Review of Nuclear and Particle Science* 57.1, pp. 285–327.

Strong, A. W., I. V. Moskalenko, O. Reimer, S. Digel, and R. Diehl (July 2004). "The distribution of cosmic-ray sources in the Galaxy, γ-rays and the gradient in the CO-to-H_2 relation". In: A&A 422, pp. L47–L50.

Swordy, S. P. (Oct. 2001). "The Energy Spectra and Anisotropies of Cosmic Rays". In: Space Sci. Rev. 99, pp. 85–94.

Tafalla, M., P. C. Myers, P. Caselli, and C. M. Walmsley (Aug. 2004). "On The Internal Structure Of Starless Cores. Physical and Chemical Properties of L1498 and L1517B". In: Ap&SS 292.1, pp. 347–354.

Taylor, G. (Mar. 1950). "The Formation of a Blast Wave by a Very Intense Explosion. I. Theoretical Discussion". In: *Proceedings of the Royal Society of London Series A* 201.1065, pp. 159–174.

The Gammapy developers (2021). *Package Structure.* URL: https://docs.gammapy. org/dev/overview/package.html. Accessed: 20-10-2021.

The Pierre Auger Collaboration (2015). "The Pierre Auger Cosmic Ray Observatory". In: *Nuclear Instruments and Methods in Physics Research* 798, pp. 172–213.

Thoudam, S. et al. (Oct. 2016). "Cosmic-ray energy spectrum and composition up to the ankle: the case for a second Galactic component". In: A&A 595, A33, A33.

Tibet ASγ Collaboration et al. (Jan. 2021). "Potential PeVatron supernova remnant G106.3+2.7 seen in the highest-energy gamma rays". In: *Nature Astronomy* 5, pp. 460–464.

Townes, C. H. and A. L. Schwalow (1955). *Microwave spectroscopy.* International series in pure and applied physics. McGraw-Hill Book Company, Inc.

Truelove, J. K. and C. F. McKee (Feb. 1999). "Evolution of Nonradiative Supernova Remnants". In: ApJS 120.2, pp. 299–326.

Urquhart, J. S. et al. (Sept. 2010). "Characterisation of the Mopra Radio Telescope at 16-50GHz". In: PASA 27.3, pp. 321–330.

Vallée, J. P. (July 2014). "The Spiral Arms of the Milky Way: The Relative Location of Each Different Arm Tracer within a Typical Spiral Arm Width". In: AJ 148.1, 5, p. 5.

Voisin, F. J. et al. (Mar. 2019). "Connecting the ISM to TeV PWNe and PWN candidates". In: PASA 36, e014, e014.

Völk, H. J. and K. Bernlöhr (Aug. 2009). "Imaging very high energy gamma-ray telescopes". In: *Experimental Astronomy* 25.1-3, pp. 173–191.

Wakely, S. P. and D. Horan (2021). *TeVCat.* URL: tevcat.uchicago.edu. Accessed: 9-11-2021.

Walsh, A. J., S. N. Longmore, S. Thorwirth, J. S. Urquhart, and C. R. Purcell (Nov. 2007). "New ammonia masers towards NGC6334I". In: MNRAS 382.1, pp. L35–L38.

Walsh, A. J. et al. (Apr. 2011). "The H2O Southern Galactic Plane Survey (HOPS) – I. Techniques and H2O maser data". In: *Monthly Notices of the Royal Astronomical Society* 416.3, pp. 1764–1821.

Weekes, T. C. (Jan. 1988). "Very high energy gamma-ray astronomy." In: Phys. Rep. 160.1, pp. 1–121.

Weekes, T. C. et al. (July 1989). "Observation of TeV Gamma Rays from the Crab Nebula Using the Atmospheric Cerenkov Imaging Technique". In: ApJ 342, p. 379.

Weekes, T. C. et al. (May 2002). "VERITAS: the Very Energetic Radiation Imaging Telescope Array System". In: *Astroparticle Physics* 17.2, pp. 221–243.

Wilson, T. L., H. Rohlfs, and S. Huettemeister (2010). *Tools of Radio Astronomy.* 5th ed. Astronomy and Astrophysics Library. Springer Berlin Heidelberg.

Wilson, T. L. and P. Schilke (1993). "Ammonia masers in the interstellar medium." In: *Astrophysical Masers.* Ed. by Andrew W. Clegg and Gerald E. Nedoluha. Springer Berlin Heidelberg.

Woosley, S. E. and T. A. Weaver (Jan. 1986). "The physics of supernova explosions." In: ARA&A 24, pp. 205–253.

Zatsepin, G. T. and V. A. Kuz'min (Aug. 1966). "Upper Limit of the Spectrum of Cosmic Rays". In: *Soviet Journal of Experimental and Theoretical Physics Letters* 4, p. 78.

Zirakashvili, V. N. and F. A. Aharonian (Jan. 2010). "Nonthermal Radiation of Young Supernova Remnants: The Case of RX J1713.7-3946". In: ApJ 708.2, pp. 965–980.